Evaluation of Chemical and Electronic Properties of Photovoltaic Materials at Interfaces in Solar Cell Devices

by

Amira Ramadan Alghamdi

Thesis

Submitted to Flinders University

for the degree of

Doctor of Philosophy

College of Science and Engineering

March 2023

"Praise be to Allah, the Cherisher and Sustainer of the worlds"

If I say [electrons] behave like particles I give the wrong impression; also, if I say they behave like waves. They behave in their own inimitable way, which technically could be called a quantum mechanical way. They behave in a way that is like nothing that you have seen before.

Richard P. Feynman

Abstract

Organic photovoltaics (OPVs) and perovskite solar cells (PSCs) have come a long way in recent years, reaching power conversion efficiencies of ~19% and 25.7%, respectively, for a single cell test. This advance was brought about by concurrent progress in materials design and synthesis and interfacial engineering. Interfaces formed between different layers in solar cells dictate device characteristics and degradation. This thesis is dedicated to interfacial engineering and the investigation of a range of materials and modifications with OPV and PSC applications front of mind. In particular, the focus is on studying the electronic properties and energy band structures at the interface's layers in OPVs and PSCs and discovering the impact of the interface on device performance. In this thesis, in terms of OPV structure, a novel potential of organic interface layers was deployed with a range of active materials as a replacement for an inorganic interface layer due to its flexibility, ease of fabrication and potentially more cost-effective design than the conventional inorganic interfaces. The electronic structure and the charge transfer mechanism at the polymer cathode interface layer (CIL)/active layers interface are discussed. A powerful combination of experimental techniques was applied to gain fundamental understanding of the chemical and electronic properties and engineering of the interfaces formed with polymer CIL and active materials. The valance electron structure of new polymer (CIL) of P(NDI3N-T-Br) with TQ1 and N2200 active layers were first investigated where a mixing of phases at the interface was determined. The results show that the dipole formation between the donor, acceptor and P(NDI3N-T-Br) was observed, which enhanced electronic structure at the interfaces and facilitated charge transport over the interface. This energy level alignment meets the expectation of using P(NDI3N-T-Br) as an interface layer in blocking the hole transfer to the interface layer while TQ1:N2200 is used as the photovoltaic active layer. Consequently, another new CIL, P(NDI3N-F8-Br), with PTB7-Th and ITIC is investigated. A comprehensive study of the energy structure of P(NDI3N-F8-Br) with PTB-Th: ITIC deposited in the case of

inverted devices is constructed. The results show that P(NDI3N-F8-Br) can work as a hole-blocking layer. Simultaneously, however, the electrons transferring from ITIC were blocked by the P(NDI3N-F8-Br) interface. Investigating the electronic structure of new organic cathode materials thus lead to a better understanding of the charge energetics at the interface and down-selection of the device structure. To achieve a comprehensive understanding, comparison has been made to the interface of PTB7-Th: ITIC–incorporated zinc oxide (ZnO) as a conventional inorganic interface layer. The results show that the active layers worked proficiently with ZnO. As a result, ZnO blocks the holes and extracting the electrons from the ITIC layer, which is desired. Overall, dipole formation was observed at the interfaces of P(NDI3N-F8-Br) and ZnO with active layers. Finally, the distribution of the charge transport component of PTB7-Th: ITIC has been studied to fill the knowledge gap on this type of study in this field. Thus, the component distribution at the surface region of the PTB7-Th: ITIC blend was investigated with the effect of the additive p-anisaldehyde (AA) on the components, which formed one side of the interface of the blend with the MoO_x electrode. This finding contributes to an understanding of the interaction between the donor material and the high work function electrode/interface material. Following our research on OPVs, another study on PSCs is conducted. In PSCs, sputtered NiOx (sp-NiOx) is used as hole transport material in PSCs due to the mobility of its holes, compatibility of the stability, easy fabrication and Fermi level position suitable for hole extraction. However, unavoidable defects in sp-NiOx or perovskite films can affect solar efficiency. Thus, self-assembled monolayer (SAM) MeO-2PACz was inserted between the sp-NiO_x and perovskite film, which can contribute to reducing defects and improving the device's performance. The results showed that the MeO-2PACz interface enhances perovskite film quality by reducing charge recombination at the sp-NiOx/perovskite interface. It also passivates defects in the sp-NiOx surface and perovskite layer. The overall outcome resulted in an improvement in the device efficiency from 11.9% to 17.2%.

Table of Contents

Declaration

I certify that this thesis:

1. does not incorporate without acknowledgement any material previously submitted for a degree or diploma in any university
2. the research within will not be submitted for any other future degree or diploma without the permission of Flinders University; and
3. to the best of my knowledge and belief, does not contain any material previously published or written by another person except where due reference is made in the text.

Signed: Amira Ramadan Alghamdi

Date: 21 March 2023

Acknowledgements

The years of my PhD have been an incredible phase of my life, which witnessed a transition of my skills and knowledge. My PhD journey was full of stirring experiences with fascinating science around me. As this enriching and unique PhD journey comes to an end, I would first and foremost like to thank Allah (God) almighty for blessing me with the determination, health and wisdom to complete this thesis. I would also like to take this opportunity to acknowledge and thank all those who helped me either towards the completion of this thesis or those who made my PhD a memorable journey.

Firstly, I am deeply thankful to my supervisor, Prof. Gunther Andersson, for the constant encouragement to challenge myself and so much more. But I am especially grateful for him letting me follow my own path, make mistakes and learn, which let me grow into the role of a researcher. Thanks are also owed for his invaluable guidance and advices throughout my PhD journey and for his intellectual help that helped me compile this work, which would not have been completed without him. I have worked with Gunther ever since I started my Master's and it has been an absolute honour to learn from such a committed professional and to work closely with a good person. I sincerely appreciate him for inspiring me and supporting me not only academically but also through the emotional ups and downs of a PhD life, and for showing empathy and understanding in difficult situations. His wisdom and support always kept me going. I also appreciated his support during the COVID-19 time while I was in Japan, which I will never forget. Thanks a lot, Gunther. You are the best supervisor I have ever worked with. I would like to equally thank my co-supervisor, Prof. Mats Andersson, for his scientific discussions in all-polymer projects and for guiding me in the right direction through my PhD to carry out my research successfully. I'm grateful for providing all the polymer materials that I need and for visiting me in the laboratory to check on my progress. Thanks a lot, Mats. Throughout my PhD milestones, Prof. David Lewis and Prof. Jamie Quinton provided me with valuable advice—my sincere thanks to them.

I would like to thank the people I worked with them during my fellowship visit at National Institute of Material Sciences (NIMS), Japan. I owe my deepest gratitude to my supervisors, Dr Yasuhiro Shirai and Dr Masatoshi Yanagida, and their Photovoltaic Materials group in Japan (NIMS) for hosting me and training me in the fabrication of perovskite solar cells. Working independently in their group imparted much knowledge about the perovskite solar cell.

I express my sincere thanks to our head at Photovoltaic Materials group, Prof. Kenjiro Miyano, who I met with every week. I would also like to thank Dr Dhruba B. Khadka for his useful discussion and support. Thanks to all people I got to know at WPI-MANA building. My deepest gratitude to thank the head of the Centre for Green Research on Energy and Environmental Materials, Prof. Kohei Uosaki, for his support. It was a pleasure to meet and talk with him.

My heartiest thanks to Prof. Tomonobu Nakayam for his genteel manner. I appreciate his hospitality and generosity to me in Japan. It has really meant a lot. I am grateful to you, Tomo-san, with lots of respect.

I am thankful for all the people I have met and worked with them at NIMS. I feel privileged to have had the opportunity to work at NIMS and gain invaluable experience at one of the world's most accomplished research institutes. I would like to extend my special thanks to Osawa Yukiko-san and Yoshio Sakka-San from NIMS for their support during my fellowship visit.

My special thanks go to my senior, Dr Yanting Yin, who discussed with me the theory of the organic solar cell when I had just started my PhD, and Dr Jonas Bjuggren, who synthesised the novel polymers and collaborated with me and taught me the film fabrication of a polymer solar cell. I also would like to extend my special thanks to Bradley Kirk for his great collaboration. Also, thanks to Dr The Duong for his feedback on the introduction of the perovskite chapter.

I would like also to thank Dr. Benjamin Chambers for sharing his expertise and knowledge during the time that we used to work on the NICISS maintenance.

My warmest thanks to my colleagues in Andersson's group for their guidance and assistance throughout my project. I enjoyed not only working in the lab with them but also spending time discussing science, which made this time both informative and enjoyable.

I gratefully acknowledge the funding sources that made my PhD work possible. I am very grateful to Immam Abdulrahman bin Fisal University, Dammam, Saudi Arabia, for giving me the opportunity to continue postgraduate study in Australia. Thanks to all my friends and colleagues for providing me with endless support.

Last but not least, to my family, lovely sisters and brothers, thanks for all their love and encouragement. I know it was a long time that I spent away from my lovely family. To my mum, whose supplication was the secret of my success, and my dad (may Allah have mercy on him), who used to guide me and support me in various capacities. From the depth of my heart, thank you to my parents for supporting and caring for me to see me succeed in my life.

My sincere gratitude goes to my loving husband, Mahfooz Alghamdi—your hard work has always inspired me, and your sacrifices have helped me achieve my dream. I appreciate you patiently bearing with me during the stressful years of my PhD, listening to my concerns about my PhD for an immense number of hours and supporting me all the way. I love you so much.

To my two eyes, Adeeb and Elias. Your birth during my journey in Australia added joy and pleasure to our life, and I know that this period was also hard for both of you, especially while my husband and I were studying a PhD and when I was working late in the lab or my office. May Allah protect both of you for a heart that lives from your heartbeat and a mother who sees her present and her future in both of you.

I am grateful to all my Adelaide Friends for their support throughout my journey; thank you from the bottom of my heart.

Amira Ramadan Alghamdi

March 2023

List of Publications

The following articles have been published or submitted in peer-reviewed journals as part of this thesis.

1. **Alghamdi, A. R**.; Yanagida, M.; Shirai, Y.; Andersson, G. G.; Miyano, K. Surface Passivation of Sputtered NiO x Using a SAM Interface Layer to Enhance the Performance of Perovskite Solar Cells. *ACS omega* **2022**, *7* (14), 12147–12157.

2. **Alghamdi, A. R.**; Bjuggren, J. M.; Pan, X.; Andersson, M. R.; Andersson, G. G. Dipole Formation at Active Materials/P(NDI3N-T-Br) Interface in Organic-based Photovoltaic. *Macromolecular Materials and Engineering* **2022**, *307* (10), 2200303.

3. **Alghamdi, A. R.**; Kirk, B. P.; Kocak, G.; Andersson, M. R.; Andersson, G. G. Modification of the Surface Composition of PTB7-Th: ITIC Blend Using an Additive. *Molecules* **2022**, *27* (19), 6358. doi: 10.3390/molecules27196358. PMID: 36234895.

4. **Alghamdi, A. R.**; Kirk, B. P.; Kocak, G.; Andersson, M. R.; Andersson, G. G. Electronic Structure and the Dipole Formation at the ITIC: PTB7-Th on ZnO Interface. (Ready for submission).

5. **Alghamdi, A. R.**; Kirk, B. P.; Yin, Y.; Bjuggren, J. M.; Andersson, M. R.; Andersson, G. G. The Effect of the Thickness of Conjugated Polymer P(NDI3N-T8-Br) on the Device Performance of Organic Solar. (Ready for submission).

Publications not presented in this thesis.

1. Sumiya, M.; Takahara, Y.; **Alghamdi, A.**; Nakayama, Y.; Uesugi, F.; Harada, Y.; ... Imanaka, Y. Growth of AlxGa1-xN/InyGa1-yN Hetero Structure on AlN/Sapphire Templates Exhibiting Shubnikov-de Haas Oscillation. *Journal of Crystal Growth* **2021**, *574*, 126324.

2. Pandian, M. G. M.; Khadka, D. B.; Shirai, Y.; Yanagida, M.; Kitamine, S.; **Alghamdi, A. R.**; Subashchandran, S.; Miyano, K.. Effect of Surface Treatment of Sputtered Nickel Oxide in Inverted Perovskite Solar Cells. *Thin Solid Films* **2022**, 139486.

3. Alharbi, T. M. D.; **Alghamdi, A. R. M**.; Vimalanathan, K.; Raston, C. L. Continuous Flow Photolytic Reduction of Graphene Oxide. *Chemical Communications* **2019**, *55* (76), 11438–11441.

4. **Alghamdi, A. R. M.**; Kloo, L.; Andersson, G. G. The Influence of Three Modified Versions of Z907 on the Adsorption Kinetic on Titania. (In progress).

5. **Alghamdi, A. R. M.**; Kloo, L.; Andersson, G. G. The Effect of the Co-Adsorbent DPA on the Adsorption Kinetics and the Performance of the Dye Solar Cell under Different Immersion Times. (In progress).

6. **Alghamdi, A. R. M.**; Yanagida, M.; Shirai, Y.; Andersson, G. G.; Miyano K. Ion Migration of B and X in Mixed Cation Perovskite Solar Cell. (In progress).

Conference and Presentation

1. **Alghamdi, A. R. M.**, Lars Kloo and Gunther G. Andersson*, The Effect of the Co-Adsorbent DPA on the Adsorption Kinetics and the Performance of the Dye Solar*, [Poster] presented at the Second College of Science and Engineering Higher Degree Research conference (2018), Flinders University, Australia (27–28 November 2018).

2. **Alghamdi, A. R. M.**, Mats R. Andersson and Gunther G. Andersson, *Material Intermixing and Dipole Formation at TQ1/P(NDI3N-T-Br) Interface in Organic-based Photovoltaic*, Australasian Community for Advanced Organic Semiconductors (AUCAOS), Hahndorf, Adelaide (2018).

3. **Alghamdi, A. R. M.**, Mats R. Andersson and Gunther G. Andersson, *Dipole Formation at Active Materials/P(NDI3N-T-Br) Interface in Organic-based Photovoltaic*, [Poster] presented at the Advanced Materials and Nanotechnology (AMN9), Wellington, New Zealand (10–14 February 2019).

4. **Alghamdi, A. R. M.**, Mats R. Andersson and Gunther G. Andersson, *The Effect of the Co-Adsorbent DPA on the Adsorption Kinetics and the Performance of the Dye Solar*, [Poster] presented at the Nanoscale Science & Technology's 9th Annual Conference, Flinders University, Australia (June 2019).

5. **Alghamdi, A. R. M.**, Mats R. Andersson and Gunther G. Andersson, *Material Intermixing and Dipole Formation at TQ1/P(NDI3N-T-Br) Interface in Organic-based Photovoltaic*, [Poster] presented at the Third College of Science and Engineering Higher Degree Research conference, Flinders University, Australia (26–27 November 2019).

6. **Alghamdi, A. R. M.**, Mats R. Andersson and Gunther G. Andersson, *Dipole Formation at the Active Materials/Conjugated Polymer P(NDI3N-T-Br) Interface*, [Poster] presented virtually at the MANA International Symposiums Conference, NIMS, Japan (2022).

7. **Alghamdi, A. R. M.**, Mats R. Andersson and Gunther G. Andersson, *Surface Passivation of Sputtered NiOx using a SAM Interface Layer to Enhance the*

Performance of Perovskite Solar Cells, [Poster] presented at the Nanoscale Science & Technology's 10th Annual Conference, Flinders University, Australia (June 2021).

8. **Alghamdi, A. R. M.**, Jonas M Bjuggren, Mats R. Andersson and Gunther G. Andersson, *Electronic Structure at the TQ1:N2200/Conjugated Polymer P(NDI3N-T-Br) Interface*, [Poster] presented at the 2021 Australian Institute of Physics Summer Meeting, Queensland University of Technology (QUT), Australia (6–9 December 2021).

9. **Alghamdi, A. R. M.**, Mats R. Andersson and Gunther G. Andersson, *Materials Intermixing and the Dipole Formation at the active Layer/Conjugated Polymer P(NDI3N-T-Br) Interface*, [Presentation] presented at the Australasian Community for Advanced Organic Semiconductors (AUCAOS) Symposium, New South Wales, Australia (March 2022).

10. **Alghamdi, A. R. M.**, Mats R. Andersson and Gunther G. Andersson, *Electronics Structure of ITIC and PTB7-Th on Conjugated Polymer P(NDI3N-F8-Br) Interface for Organic Solar Cell*, [Poster] presented at the Nanoscale Science & Technology's 11th Annual Conference, Flinders University, Australia (June 2022).

11. **Alghamdi, A. R. M.**, Mats R. Andersson and Gunther G. Andersson, *Modification of the Surface Composition of PTB7-Th: ITIC Blend Using an Additive*, [Poster] presented at the 17th Conference of the International Association of Colloid and Interface Scientists (IACIS), Brisbane, Australia (June 2022).

12. **Alghamdi, A. R. M.**, Mats R. Andersson and Gunther G. Andersson, *Electronics Structure of ITIC and PTB7-Th on Conjugated Polymer P(NDI3N-F8-Br) Interface for Organic Solar Cell*, [Poster] presented virtually at the 33rd Australian Colloid and Surface Science Student Conference (33ACSSSC), Brisbane, Australia (January 2022).

13. **Alghamdi, A. R. M.** [Attending] at Australian Institute of Physics (AIP) Congress, Adelaide (December 2022).

Awards

- National Institute for Materials Science (NIMS) Fellowship, from January 2020 to April 2021.

- Horizon Professional Development Award Certificate, Silver: 2019, Flinders University, Australia.
- Horizon Professional Development Award Certificate, Bronze & Gold: 2020, Flinders University, Australia.
- Best Poster (People's Choice). Presented at the 2021 Australian Institute of Physics Summer Meeting, Queensland University of Technology (QUT), Australia, 6–9 December 2021.

Activities

- Attended the American Chemical Society ACS event on Campus at Adelaide University on 25 July 2019.
- Participated in 3MT competition, 2021.
- Attended the Australian National Fabrication Facility's Microengineering School, 20–23 September 2022.
- Attended the Australian Synchrotron Microscopy Workshop, 2022.

List of Figures

List of Tables

Abbreviation List of Chemicals and Symbols

AA	Anisaldehyde
AFM	Atomic Force Microscopy
ARXPS	Angle Resolved X-ray Photoelectron Spectroscopy
AZO	Aluminium-doped Zinc Oxide
BHJ	Bulk Heterojunction
CB	Conduction Band
CIL	Cathode Interface Layer
CT	Charge Transport
diBrDANDI	dibromo-2,7-bis[3-(dimethylamino)propyl]benzo[lmn][3,8]phenanthroline-1,3,6,8(2H,7H)-tetrone
ECB	Conduction Band Energy
E_f	Fermi Level Energy
E_g	Energy Gap
EQE	External Quantum Efficiency
ETL	Electron Transport Layer
EVB	Valence Band Energy
FF	Fill Factor
FWHM	Full Width at Half Maximum
HOMO	Highest Occupied Molecular Orbital
HTL	Hole Transport Layer
IPES	Inverse Photoemission Spectroscopy
IQE	Internal Quantum Efficiency
IPCE	Incident Photon-to-Electron Conversion Efficiency
I_{sc}	Short-Circuit Current
ITIC	3,9-bis(2-methylene-(3-(1,1-dicyanomethylene)-indanone))-5,5,11,11-tetrakis(4-hexylphenyl)-dithieno[2,3-d:20 ,30 -d0]-s-indaceno[1,2-b:5,6-b0]-dithiophene
ITO	Indium Tin Oxide
J_{sc}	Short-Circuit Current Density
J-V	Current Density-Voltage
LUMO	Lowest Unoccupied Molecular Orbital
MeO-2PACz	[2-(3,6-dimethoxy-9H-carbazol-9-yl)ethyl]phosphonic acid
MIES	Metastable Impact Electron Spectroscopy
MoO_x	Molybdenum Trioxide
N2200	poly[[N,N′-bis(2-octyldodecyl)-naphthalene-1,4,5,8-bis(dicarboximide) 2,6-diyl]-alt-5,5′-(2,2′-bithiophene)]

NDI	Naphthalene Diimide
NICISS	Neutral Impact Collision Ion Scattering Spectroscopy
OPV	Organic Photovoltaic
P(NDI3N-F8-Br)	poly[(N,N'-bis(3-(N,N-dimethyl)-N-ethylammonium)propyl)naphthalene-1,4,5,8-bis(dicarboximide)-2,6-diyl)-alt-2,7-(9,9’ dihexylfluorene))]dibromide
P(NDI3N-T-Br)	poly[(*N,N'*-bis(3-(*N,N*-dimethyl)-*N* ethylammonium)propyl)naphthalene-1,4,5,8-bis(dicarboximide)-2,6-diyl)-alt-2,5-thiophene)]dibromide
PCE	Power Conversion Efficiency
PES	Photoelectron Spectroscopy
PTB7-Th	poly[4,8-bis(5-(2-ethylhexyl)thiophen-2-yl)benzo[1,2-b; 4,5-b]dithiophene-2,6-diyl-alt-(4-(2-ethylhexyl)-3-fluorothieno[3,4-b]thiophene-)-2-carboxylate-2-6-diyl)]
R_s	Series Resistance
R_{sh}	Shunt Resistance
SAM	Self-Assembling Monolayer
SC	Solar Cell
SEM	Scanning Electron Microscopy
sp-NiOx	Sputtered Nickel Oxide
SVD	Singular Value Decomposition
TOF	Time Of Flight
TQ1	Poly[[2,3-bis(3-octyloxyphenyl-5,8-quinoxalinediyl]-2,5-thiophenediyl]
UHV	Ultra-High Vacuum
UPS	Ultraviolet Photoelectron Spectroscopy
VB	Valence Band
VL	Vacuum Level
V_{oc}	Open-Circuit Voltage
WF/ϕ	Work Function
XPS	X-Ray Photoelectron Spectroscopy
ZnO	Zinc Oxide

Chapter 1: Background

1.1 Introduction

1.1.1 The significance of renewable energy research

In the last decades, we have witnessed steadily advancing socio-economic conditions in different regions of the world, which corresponds to a significant growth in energy demand. Globally, the consumption of electricity is rampantly increasing due to continued electrification. Nearly 70% of our energy production goes towards electricity generation, be it from non-renewable (coal, oil and gas) or renewable (solar, wind and biomass) sources.[1] Fossil fuels—coal, oil and gas—still make up over 70% of the primary energy, which is used to generate electricity. Even with the introduction of new energy sources, it is expected that their share will only drop to 60% by 2040 (see Figure 1-1A).[2] Still, the impact of climate change and the rise in average global temperature, compounded by the rise in pollution levels in urban areas, cast overreliance on fossil fuels and is emphasised as the quintessential global problem of our century. Part of the solution to the rapid rise in energy demand and severe environmental pollution is to reliably raise the portion of renewable energy in the energy mix to above 40% of electricity generation by 2050.[3] According to a recent report by BP, 'BP Energy Outlook – 2018',[4] around 50% of newly installed power generation units use renewable sources, and, at this rate, it is projected that the share of energy coming from renewables will rise from a meagre 7% to roughly 25% by 2040.

Wind and solar energy are becoming increasingly competitive, which explains the rapid growth in renewable energy. Our closest star is the sun, which provides us with clean energy without any negative effects (pollution, greenhouse gas emissions [CO_2/CH_4]). An over 150% increase in electricity production from solar power is expected in 2022 when compared to a benchmark 2015 production (see Figure 1-1B). The huge increase in

solar power electricity generation is due to a larger-than-expected drop in production prices, which has made solar cells affordable by the 2020s.[5]

Figure 1-1. (A) Primary energy sources in power generation and (B) Renewable energy mix. Images removed due to copyright restriction. Available online from.[3,4]

These promising initial results are the outcome of growing photovoltaic (PV) development and their successful implementation worldwide, which is encouraged by sufficient research funding, advancement of low-cost PV technologies and support from policymakers. Solar power generation has not reached its colossal potential, as there are still limitations in the efficiency of the materials and the design of the PV cell. Additionally, the cost of energy from PV still outweighs fossil fuels, presenting a major challenge to the extensive worldwide deployment of PV cells. This work will focus on PV technology. We studied the internal mechanisms of a solar cell (SC) and the possible avenues for increasing their conversion efficiency.

1.1.2 Types of SCs and their historical timeline

The first discovery of PV effect was by French scientist Edmond Becquerel in 1839,[6] in a liquid-based system. After the initial almost 40-year discovery, the first operational device harnessing PV effect was described on selenium by Charles Fritts in 1883.[7] Almost a century later, in 1953, a chance discovery by Gerald Pearson and Calvin Fuller showed that doped silicon interacts with light in a similar fashion. Discovery was quickly followed by a silicon-based SC (designed by Chaplin et al. 1954[8]) and the first silicon SC for electricity generation outdoors in 1955.[9] The next 20 years saw spacecraft as the main protagonist for PV application.[9] SCs' full potential was established and its position cemented when NASA launched a satellite using SCs to power its operation.[10] The 1970s oil crisis prompted a renewal of interest in the technology and, in conjunction with the application of PVs in telecommunication systems, resulted in the device's modern concept in 1976.[9]

Based on the technology used for their design and fabrication, SCs can be classified into several types. Usually, a development stage is used to discern three generations of PV technologies. The first generation is based on crystalline silicon, a well-established technology with well-known characteristics and controllability, accounting for most panels (94%) produced today. The efficiency of the first silicon SC was only about 6%[8] and has since increased to over 26% in a laboratory setting.[11] Thin film structure defines the second generation of SCs, usually formed by copper indium gallium selenide, amorphous silicon or cadmium telluride. The film's thickness can range from a couple of nanometres to a few microns with the adjective 'thin' stemming from comparison to crystalline silicon SCs. Second generation SCs are characterised by lower efficiency vs crystalline silicon SCs; however, the use of small amounts of material in a thin film makes them considerably cheaper. Both technologies have now been upscaled from a laboratory to industrial level and are commercially available. Drawbacks of these technologies are coupled with the use of high temperatures and/or a vacuum in the manufacturing process (first generation cells) and the use of toxic and costly materials (second generation cells). These disadvantages have instigated the development of the third generation PVs, which promise to be lightweight, semi-transparent and compatible with the roll-to-roll production methods.

The third generation SCs, 'emerging' PV technologies, is still in the research and development phase and consists of organic PVs (OPVs), perovskite solar cells (PSCs), dye sensitised (DSSC), copper zinc tin sulphide, quantum dots and SCs. The efficiency vs time of different types of emerging PVs is shown in Figure 1-2, which shows an overview of current development. December 2020 witnessed record efficiencies being reported for OPVs of 18.2% and 25.5% for PSCs.[12] Additionally, a remarkable feat of surpassing the crystalline silicon single-junction cells was reported for perovskite/Si tandem cells, with a 29.1% efficiency.[13]

Figure 1-2. Best research-cell efficiencies chart. Image removed due to copyright restriction. Available online from.[12]

Among third generation SCs, OPVs present a class of devices that use inexpensive materials, such as polymers and small molecules, and also deliver high efficiencies. The use of organic solvents to manufacture the developed materials could result in a low-cost upscaling process. Recent research into OPVs has clarified underlying working principles, presenting possible electrode materials that optimise the cell design. PSCs present an even newer addition to the PVs with ever-increasing efficiency over the past decade, yet the main focus remains on optimising the individual layers within the cell.

The most important part in any SC is how the interfacial layers play several roles in both OPVs and PSCs. They, for example, provide a conductive contact between the metal and semiconductor interfaces, charging collection at the electrodes and forming a chemical and physical barrier between the electrodes and the photoactive materials. In OPVs, optimising the interfacial layers is the key to altering device performance and is the focus of current research. For the PSCs, defect level alteration at the interface and its effect on device performance is under this study.

This thesis investigates the interfacial processes in OPVs and PSCs and addresses the issues relevant to the interfaces to optimise the energy level and performance of such devices. In particular, we attempt to understand how interface engineering can help reduce energy losses in a SC, thereby enhancing its efficiency.

1.2 OPV-Based SCs: Background

Numerous advantages of OPVs, such as substrate interchangeability, ease of fabrication and cheap large-scale production, are driving the interest for this type of PVs.[14,15] Versatility of chemical synthesis routes for modification of organic semiconductors is what drives research in industry and academia.[16,17] Additionally, OPVs are highly flexible, readily recyclable, lightweight and the band gap can be tailored by careful manipulation on the molecular level. Polymer-based OPVs present an ideal alternative to

semiconductors based on inorganic materials in renewable energy production. Pochettino was the first to observe photoconductivity in anthracene as early as 1906, followed later by a report from Volmer in 1913.[18] These reports prompted substantial effort to understand and push the OPVs technology forward, as evidenced by a number of major review papers.[19–24]

1.2.1 History of OPVs

Work on photoconductivity of organic species has had a long research tradition, starting at the beginning of the twentieth century by seminal papers on anthracene by Pochettino and Volmer.[25,26] Later, in the 1960s, dyes were widely available (e.g., pinacyanol, methylene blue and phthalocyanines) and were shown to have semiconducting properties. These findings prompted research on their PV properties, as they were ideal candidates for this purpose. Organic charge transfer (CT) complexes and electrical conductivity in organic polymers have been sporadically debated;[27,28] however, the field of organic semiconductors only truly developed after the discovery (by Alan J. Heeger, Alan MacDiarmid and Hideki Shirakawa) of highly conductive polyacetylene film formed upon exposure to halogens.[29] Their seminal work on the development of conductive polymers saw them nominated for the Nobel Prize in Chemistry in 2000. Despite these remarkable developments, OPVs demonstrated extremely low efficacies of less than 0.1% in the 1980s.[30] Breakthroughs developed in 1986, when Tang et al.[31] put forward a bi-layered device structure made from an electron donor and an acceptor, with the reported efficiency of 1% being significantly higher than any of the previous reports. In Figure 1-3, different schemes of OPVs are shown. Bulk heterojunction (BHJ) was the next major innovation with the ‘active layer design’, an interwoven network of co-deposited electron donor/acceptor materials. It was possible to produce these structures by sublimation[32] and spin coating method.[33]

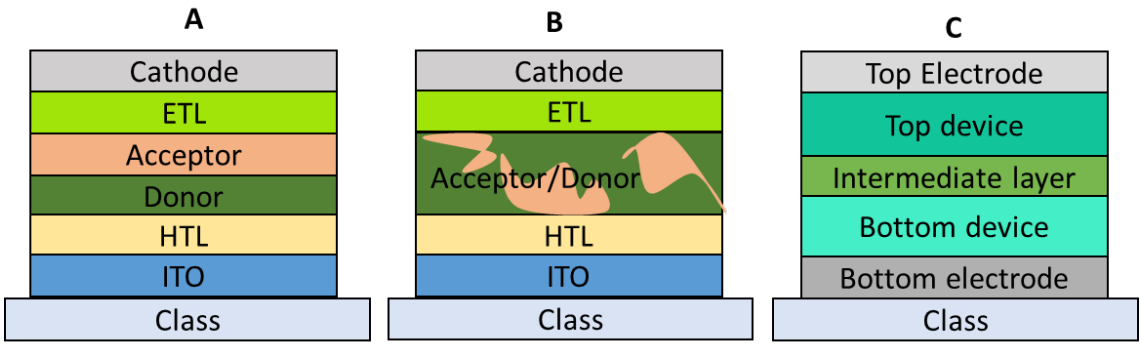

Figure 1-3. Typical structures of OPSs. (A) Bilayer system, (B) BHJ system and (C) tandem system. Adapted from.[36]

From that period, OPVs efficiency characteristics have improved tremendously to over 18%[34] and above 17% for a tandem device in recent years.[35] These advances included synthesis of new absorbing materials and device architecture optimisation, mainly through the modification of the hole/electron transportation layers. Adapted from [36].

1.2.2 Excitonic significance of OPVs and the concept of heterojunction

The value of the dielectric constant, ε_r, is the key differing characteristic between organic and inorganic semiconductors. Dielectric constant values for organic semiconductors lay between 2 and 4, whereas for pure silicon ε_r is 11.7,[36] which translates to two charges being intensely bound by Columbic forces when immersed in a medium (equation 1.1).

$$F\,(r)\frac{q_1 q_2}{4\pi\varepsilon_0\varepsilon_r\, r^2} \tag{1.1}$$

Where q_1 and q_2 are magnitudes of the charges, ε_0 is the dielectric constant, ε_r is the permittivity of the medium and r is the distance between the charges.

Upon electronic-magnetic excitation, silicon forms a pair of free, opposite charges, whereas these charges remain bound in organic material at room temperature. Electron-hole pairs made in this way have binding energy within a 0.3–1 eV range,[36] significantly greater than 0.025 eV at room temperature. A heterojunction model was effectively applied in the OPV case to circumvent the respective problem,[31,33] with two organic

semiconductors with inherently differing energy levels providing the driving force for the electron-hole pair separation.

1.2.3 OPV devices: their structures

It has been widely observed that bilayers and BHJ architecture are commonly used designs for single-junction OPVs, despite many different device architectures having been developed and investigated to date. A typical design consists of two electrodes, a cathode and an anode, the active layer and two types of transport materials for the holes and electrons. The most common substrates are glass or plastics. Usually, one of the electrodes should be a transparent conductive oxide, such as ITO or FTO, and the second electrode is usually a thermally evaporated metal (e.g., aluminium, gold or silver). The position in which holes and electrons are collected determines whether the design is a conventional device or an inverted device. Thus, if the holes enter the ITO side, we designate the system as being 'conventional', while if holes enter the metal side, it is called 'inverted'. The earliest design of the active layer was known as the 'bilayer', as shown in Figure 1-3A. In this case, the donor and acceptor were stacked on top of each other, while the later BHJ concept[33] introduced the blend of two materials forming an interwoven structure, as seen in Figure 1-3B. The later model offered a significant increase of the donor/acceptor interface surface, resulting in more excitons being successfully separated with sufficiently short pathways for free charge carriers to reach their intended collecting electrode. The morphology of the active layer is essential, as it must provide photogenerated excitons short path to the donor-acceptor junction comparable to their mean diffusion path, which typically needs to be on the order of 10–20 nm.[37] Thus, one of the easiest methods of producing such layers is the evaporation of the donor and the acceptor precursors, which, when evaporated concurrently, form the desired intertwined morphology. However, the most practised method is deposition from homogenous solution, where a single layer is formed by techniques such as spin coating, inkjet printing, etc.

A more physics-based approach to improving the performance of the device is in combining numerous devices parallel or in series to boost the output current/voltage. The typical tandem cell is shown in Figure 1-3C, where the active layers are separated by an intermediate layer. In this system, the voltage is the sum of voltages from individual cells, with the requirement for the currents of the two cells to be the same in magnitude.

This thesis focuses on the inverted architecture of BHJ devices.

1.2.4 The principle of operation of OPVs

The operating principle of a standard OPV consists of four main steps: charge extraction at the electrode layer, photo-excitation and generation of exciton, carrier transport and exciton dissociation and subsequent diffusion. Each of these concepts will be discussed in further detail in the following paragraphs. The overall scheme of essential processes during SC operation is shown in Figure 1-4.

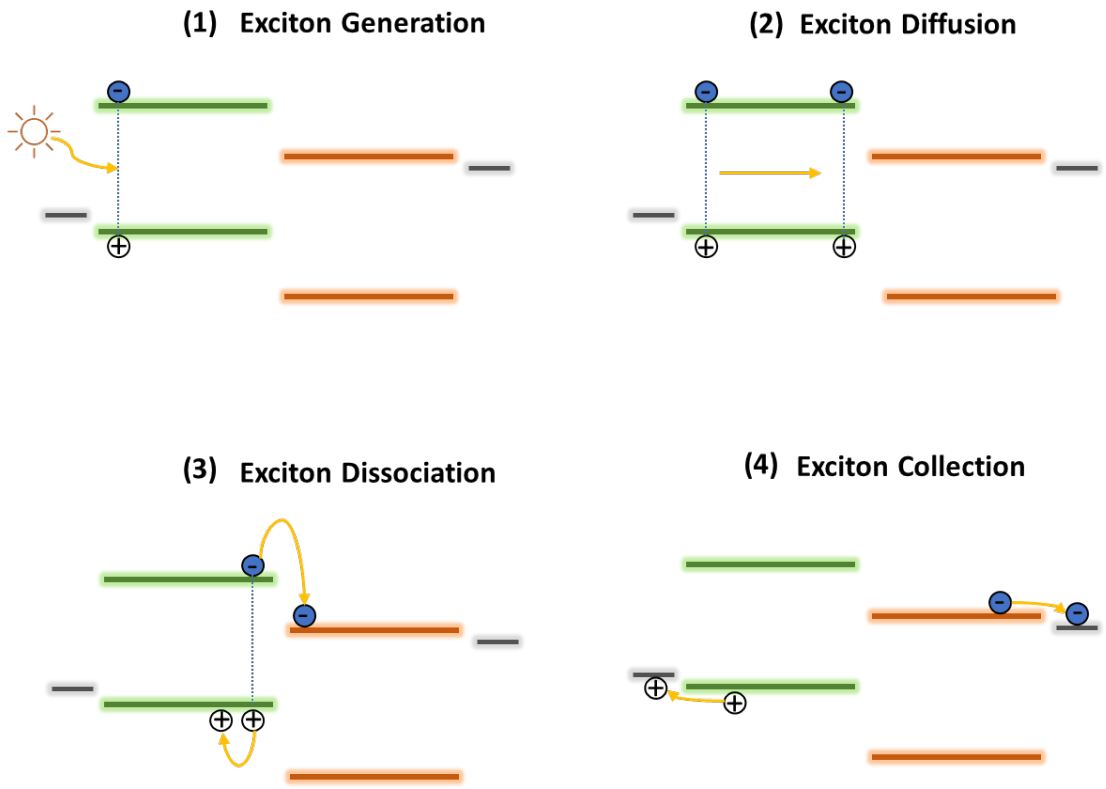

Figure 1-4. The working principle of the OPV. Adapted from.[36]

i. Photo-excitation and generation of exciton

When an incident photon is absorbed by an organic semiconductor, the electron is transferred to the lowest unoccupied molecular orbital (LUMO) from its initial state in the highest occupied molecular orbital (HOMO), both levels being the characteristic of the organic molecule. Process is analogous to the one in inorganic SCs, where the valence band (VB) to the conduction band (CB) take the role of HOMO and LUMO. Distinction lays in the formation of an exciton in organic materials instead of a free electron-hole pair in the inorganic case. High absorption coefficient (around 10^5 cm^{-1} [138]) is typical for many organic materials. It is a unique property that makes the fabrication of effective, ultra-thin (less than 1 micrometre thick) SCs possible, as enough light will be absorbed even in these thin structures.

ii. Exciton and subsequent diffusion

Following photo-excitation of the electron in the active organic material, dissociation of the formed strongly bound excitons needs to happen. Otherwise, recombination will occur and there will be no contribution to the photocurrent.

Exciton presents an electro-neutral entity and can diffuse through the material via arbitrary thermal motion. The distance excitons can traverse before recombination has a finite length and is known as diffusion length, described by equation 1.2.

$$l = \sqrt{D\tau} \tag{1.2}$$

Where D stands for the diffusion coefficient and τ is the lifetime of the exciton. In organic materials, the diffusion length is fairly short and tends to be in the nanometre range.[39]

Tang et al. were the first to demonstrate that by careful choice of organic materials, based on the difference in energy levels, the separation of the electron-hole pair is achievable, which was a prerequisite for efficient OPVs.[31] Contact surface between the two active

materials is known as heterojunction. The heterojunction concept and architecture have dominated the progress of the OPVs ever since. Formed exciton, with its nanometre range diffusion path, needs to arrive at the heterojunction for successful free charge carrier formation and current generation. Conversely, the diffusion path of the free charge carrier in silicon can reach even hundreds of microns.[40,41]

iii. Exciton dissociation

Figure 1-5 shows the energy levels of two materials (A and B) when placed in close contact. When the photo-excitation event takes place in A, within a close proximity of the A/B interface, exciton can diffuse to this junction. The spontaneous process occurs when the $LUMO_A$ and $LUMO_B$ energy differences are less than the potential energy of the exciton; thus, the electron is relocated from $LUMO_A$ energy level to $LUMO_B$ but the hole remains in $LUMO_A$. The resulting charge separation forms the CT state, with A and B designated as donor and acceptor materials. The CT event is instantaneous and happens on the timescale of femtoseconds.[42]

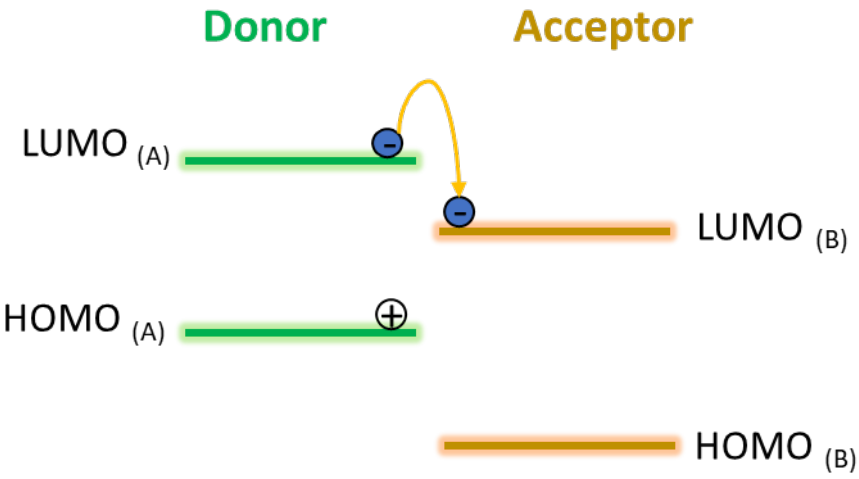

Figure 1-5. Energy level alignment of donor-acceptor heterojunction. Adapted from.[36]

iv. Charge transport (CT)

A common designation for dissociated exciton is a geminate pair. These pairs need a conductive medium to reach their respective electrodes for collection: electrons gather at the cathode and holes at the anode. The mechanism is hopping and following a gradient in electric potential, which results in diffusion and drift. Diffusion and drift are two main mechanisms of transference. As dissociation of excitons happens at the donor-acceptor interface, charge carrier concentration becomes high in its vicinity. Newly formed concentration gradient hinders hole and electron movement towards a heterojunction, resulting in motion known as diffusion. Diffusion is predominant when the potential is applied and strengths of the formed internal electric fields are balanced. The second relevant mechanism is drift, which is caused by the gradient in potential and is mainly determined by the choice of electrode materials. Every material has its own intrinsic work function (WF). When two different materials are contacted, they form biased potential (V_{bi}), positively affecting the open-circuit potential of the SC. Large internal electric fields cause the charge carriers to drift towards the collecting electrodes.

CT is remarkably different in organic and inorganic materials. The periodic structure of atoms in the crystal lattice and the covalent bonding between them in crystalline silicon allow relatively easy movement of free carriers of the charges in the VB and CB in the material. This is reflected in the high mobility of charge carriers in crystalline silicon: 0.1 $m^2 V^{-1} s^{-1}$ for electrons and $\sim 4.5\times10^{-2}$ $m^2 V^{-1} s^{-1}$ [43] for holes. The situation is considerably different in semiconductors based on organic materials, where conjugated π-bonds in molecules and van der Waal's forces between molecules determine these values. Additionally, these bond types provide certain advantages to organic materials, such as flexibility and lightweight; however, the downside is a considerably different CT mechanism due to the absences of long-range periodicity. The structure of organics is the absence of bands, which results in comparably lower mobility in the range of 10^{-2}–10^{-6} $m^2 V^{-1} s^{-1}$ [44]. Reaching comparable mobility of electrons and holes is significant in OPVs

because uneven mobility may cause 'space charge' limited current.[45] If the mobility of one charge carrier is noticeably larger, that species will reach the electrode much faster (i.e., in shorter time span). At the same time, the second type (i.e., the slower charge carriers) will reach its respective electrode with some delay. Misbalance in these processes causes accumulation of faster charge carriers and the generating of the 'space charge' lowering the current of the device's output. Therefore, both the mobility of the charge carriers and maintaining the balance between them are crucial for optimal SCs operation.

1.2.5 Energy level alignment at interfaces

This section will describe the CT at the surface (interface) formed by two layers of active materials. First, the contact surface will be discussed, followed by interpretation of energy values corresponding to energy bands.

1.2.5.1 Interfaces: chemistry and electronics

The interface is a thin layer at the contact point of two different materials, which may be conductive or semiconductive. Significant research efforts have been undertaken to understand the processes at the interface of different layers of polymer SCs, and it is these investigations that reveal the underlying mechanisms of the device's operation. Chemical intermixing and phases forming the interface, in conjunction with their electrical properties, determine the CT properties and, in turn, the series and shunt resistances (R_s and R_{sh}) of the devices.

The intermixing structure defined by BHJ architecture raises the donor/acceptor contact surface area and offers an accessible network route for exciton diffusion and dissociation, which contribute to the short-circuit current density (J_{sc}).[46,47] However, experimental results are limited about the interface energy level distribution in BHJ, despite their importance for the efficiency of the device, since it is difficult to obtain reliable data at the nanoscale, especially in the nanoscale–intermixing structure of a BHJ layer. It is possible that the mixing of two organic semiconductors produces physical blends where

HOMO/LUMO levels of each component remain unchanged or are only marginally modified. Conversely, combining another set of organic semiconductors can considerably shift HOMO/LUMO energies as a result of long-range Coulomb interactions[48] or intermolecular orbital hybridisation.[49]

These shifts influence the differences between energy levels at the donor/acceptor interface and the energy of the transport states (i.e., the mobility), which all results in the change in the open-circuit voltage (V_{oc}) of the device. Chemical incompatibility can sometimes cause separation of one component at the electrode interface, which changes local electric fields[50] that may advance/hinder charge extraction. Therefore, developing an understanding on how nanoscale intermixing affects donor/acceptor energy levels and, consequently, the electronic structures of the BHJs are paramount. We will discuss in Chapters 5, 6 and 7 the intermixing of donor-acceptor at the interfaces.

Alongside chemical distribution, understanding the electrical properties of the interface is of considerable importance for understanding the CT and device efficiency, which has been a focus of numerous research. Diverse arguments have been proposed over the years, with researchers like Chen,[51] Li,[52] Pietrick[53] and Wang[54] noting that the interfacial energy arrangement can be explained by taking into account the vacuum levels (E_{vac}) of each component. The argument was sound in the case of WF not shifting with respect to Fermi level (E_f) in both materials forming the junction, and could explain the behaviour of inorganic devices, such as silicon-based homo-junctions. However, this model still could not address the formation of electrostatic field at the interface.

Research by Seki[55] on the interface between metals and long-chain alkane organic proposed a different model. As a result of energy difference between the E_f of the metal and alkane organic, the equilibration of E_f occurred. This was then followed by electrons transferred from the organic, with a low WF, to the metal, with a higher WF, which created an electrostatic field at the interface. We have followed this approach, and it is further described in Chapter 4.

The conclusion is that the CT across the organic interface happens as a result of E_f alignment between the semiconductor materials forming the interface. Ultraviolet (UV) photoelectron spectroscopy (UPS)[56] is a technique that can be used to measure the HOMO (binding energy) relative to the E_f. Energy level alignment at the organic interface has been probed by other methods[57] such as capacitance–voltage and the Kelvin probe measurement.

1.2.5.2 Energy band parameters

E_f, ionisation energy (IE) and electron affinity (EA) belong to a set of properties that describe the electric behaviour of a material. Underlying theory is postulated by approximating the quantum state of a solid, which can then be used to derive the energies by examining the quantum mechanical wave functions for charges in a periodic model of atoms or molecules. The band theory is well suited to describe the properties of a material: electrical conductivity, the optical absorption, the photoelectric and the electroluminescent effects.[58] It is also very useful in describing the CT at the interface.

i. Vacuum level (E_{vac})

Vacuum level is the energy level of a free electron, with no kinetic energy, located at a sufficient distance so it experiences no binding force. Electrons can be explained as being beyond reach or 'infinitely' distant from a surface. Other energy levels are usually defined with respect to the vacuum level.

ii. Fermi level

There are many definitions of E_f, but in Fermi-Dirac statistics it is the highest occupied energy level in a material at absolute zero.

Following the Pauli exclusion theory,[59] fermions (to which electrons belong) can only occupy certain states. This level is the level with the lowest energy, which electrons are able to occupy at absolute zero. E_f plays a key role in the description of electrical and

thermal properties of a solid-state material. Fermi-Dirac statistic estimates the probability for an electron to occupy a given state and is given by the following function:[60]

$$(E) = \frac{1}{e^{(E-Ef)/kT} + 1} \tag{1.3}$$

E: point on the energy scale

E_F: Fermi level on the energy scale

kT: a product of Boltzmann constant and the absolute temperature T (K)

iii. Work function (WF)

WF represents the energy difference between E_F and E_{vac} in a solid material. By definition, the WF is the minimum amount of energy needed by an electron to leave a solid surface and reach a vacuum level outside the solid. In the case of contact between two semiconductors, alignment of E_F is expected because of the boundary condition (equal population of occupied states), which is indeed the case, and we see a matching of E_F at the interface of two discrete materials. The WF can be measured directly from the cut-off of secondary electron peak by UPS[61] and Kelvin probe microscopy.[62]

iv. Conduction Band

The CB consists of low-lying vacant electronic energy states. Electrons that obtain the necessary energy can overcome the gap between the VB and CB and populate the CB. The structure of these orbitals and their energy allow for free electron movement that can be used to conduct electric current. Abbreviation LUMO is frequently used in description of organic solids and has similar properties to CB. In organic chemistry, molecular orbitals are formed by a linear combination of atomic orbitals, which can be populated by electrons along the molecular conjugated chain. This can be used to define EA as the energy difference from the CB (or LUMO) to the E_{vac}.

v. Valence band

The VB is defined as the highest energy orbital that electrons populate at absolute zero and is located below the E_f in a semiconductor. In organic materials, the energy associated with HOMO has a similar meaning to VB.

vi. Band gap

The band gap (Eg) is of great importance in describing the behaviour of semiconductors and insulators. It is defined as the difference in energy between the CB/LUMO and the VB/HOMO. In semi-metals and metals, no band gap exists due to the overlap of VB/CB. It is worth noting that no energy states are available within the band gap. Wide band gap in a material signifies that a substantial amount of energy is needed to excite the electron from VB to CB (HOMO to LUMO), with lower probability of free electrons populating the conduction states.[63] A larger value of the band gap is a good indicator of a low conductivity material, and thus the R_s can be increased. However, the intrinsic current in a PV device is reduced due to a lower chance of intrinsic recombination.[64]

1.2.5.3 Interface electrical dipole: dipole formation

When two materials combine to establish the hypothetical model,[55] provided in Figure 1-6, one can observe general energy level rearrangement. The electron flow resulting from E_f adjustment originates from differences in the WF of materials A and B. In this case, an interface dipole is formed due to the establishment of an electric field. Thus, the energy band within a dipole moment are shifted due to its ability to extract charges.

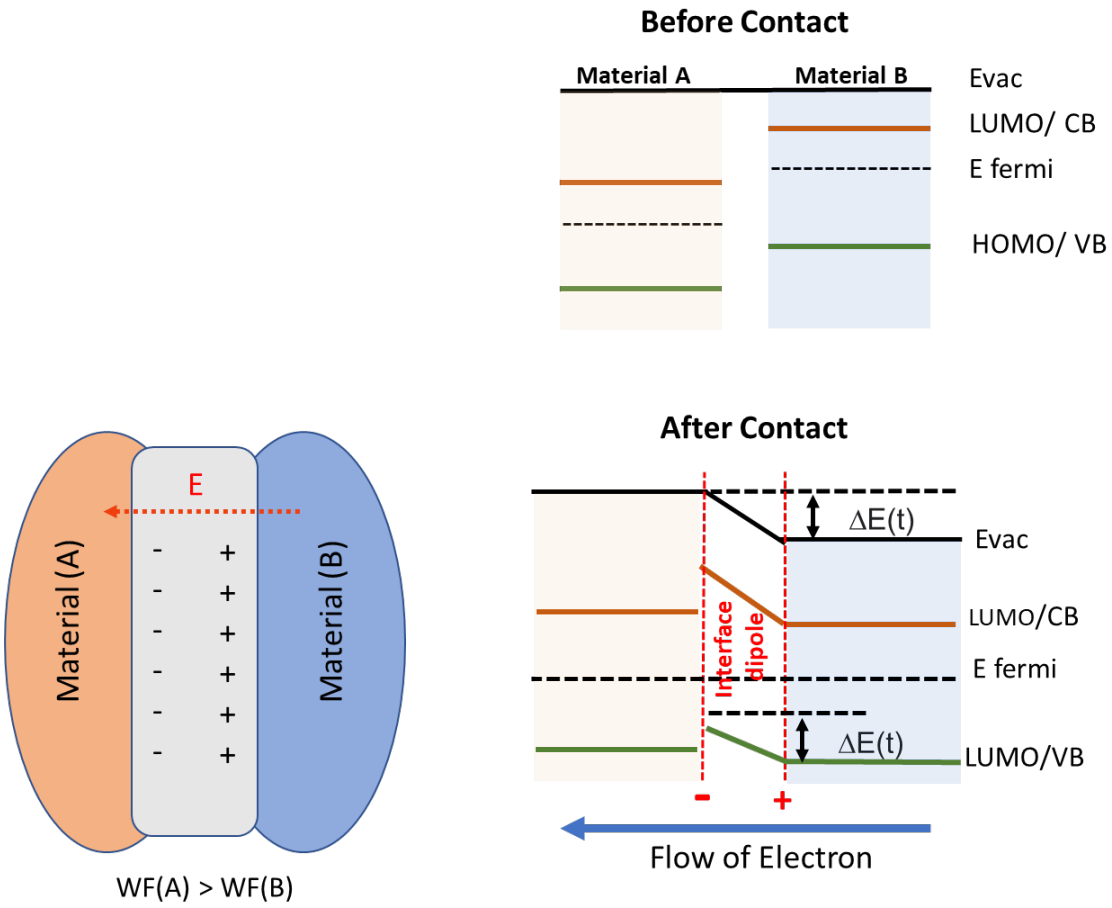

Figure 1-6. Different materials' energy levels when aligned at the interface. Fermi level is Fermi's energy level.

If we consider the boundary surface between two materials, which consists of a number of dipoles between molecules, then we can speak of an interface dipole. The vector sum of the individual local dipoles is distributed at the phase boundary. Thus, the intermediate dipole is formed from a sum of local dipoles, which are oriented parallel and directed normal to the surface.

The estimated value of the dipole formed at the boundary between the metal and the organic phase was reported in 1998 by Eisuki[55] on the basis of dipoles that occur in inorganic materials. In other words, the change in the WF of Ag that is being covered by the layer of organics leads to the formation of a dipole. Cho et al. also studied the TiO_2/electrolyte interface in DSSC.[65] The interface layer was evaluated, the dipole moment was analysed as a function of the WF difference, and the boundary layer was

evaluated. The observed TiO_2 CB shift is associated with a negative dipole moment oriented towards TiO_2 based on the increase in the energy difference between CB of TiO_2 and the redox state of the electrolyte. The V_{oc} also increased. Khan et al. explored similar results.[66]

A detailed characterisation of dipole between two organic layers—poly[4,8-bis(5-(2-ethylhexyl)thiophen-2-yl)benzo[1,2-b;4,5-b]dithiophene-2,6-diyl-alt-(4-(2-ethylhexyl)-3-fluorothieno[3,4-b]thiophene-)-2-carboxylate-2-6-diyl)] (PTB7) and [6,6]-Phenyl C71 butyric acid methyl ester ($PC_{71}BM$)—was also reported.[67] The change in WF was observed across different deposition thicknesses for $PC_{71}BM$/PTB7 arrangement based on the UPS secondary electron cascade. HOMO obtained from the valence electron peak was also demonstrated. Therefore, the dipole was calculated from the HOMO shift and WF change concerning various deposition extents. In 2017, an investigation of the dipole strength within interlayer Al/MEH-PPV was reported.[68] Different characterisation techniques were employed, such as X-ray photoelectron spectroscopy (XPS). Here, XPS was used to measure layer growth of Al deposited on MEH-PPV, which is angled mask controlled. It was reported that the WF derived from the KP increases by increasing the thickness of the Al and consequently changing the strength of the dipole, corresponding to the change of WF.

In 2020, bathophenanthroline (BPhen) showed a shift in the vacuum level of nearly 1.4 eV when incorporated in the electrode/BPhen interlayer interface. This shift was attributed to a double interfacial step formed by the dipole that is responsible for the evidenced shift, which, therefore, is used for the estimation of interfacial dipole and WF change.[69]

The method of WF change for determining the dipole strength at the interface layer has several issues, as discussed in more detail below.

a) The formation of dipoles at the interface surface cannot be directly related to the measured changes in the WF but can be an indication for their formation at such interfaces.[70] The WF is a measure for the dipole at the surface of the samples and not for the dipole formed at a buried interface. It could be argued that a dipole formed at a buried interface should carry through to the surface; however, if the surface has a mixture of two organic materials, as we did in our work in this thesis, it is difficult to predict which component will then dominate the secondary electron cut-off.

b) Direct dipole measurement would need to take into consideration changing/stable chemical composition. With that information, further deconvolution of signals can be done, delivering quantitative dipole measurements. The formation of a dipole at a buried interface will influence the electronic properties in the same way as an electronic bias. The UPS data can only provide information concerning a reference and only a change can be noted. However, the absolute values for XPS provide the information on which interface is subject to a dipole (or electric bias).

The penetration depth of the UPS is considerably large when it approaches exact interface thickness. Obtained valence electron spectra are a linear combination of the valence states[71] of materials making up an interface. By deconvolution of the spectra, contributions from the individual components can be recognised and will be described further in Chapter 2. Moreover, by combining the results from secondary electron spectra and ion scattering energy loss spectra, a deeper insight into energy levels and chemistry of the interfaces will be obtained.

1.2.5.4 Interface layer in the inverted structure

The inverted structure is shown in Figure 1-7. An active layer is placed between the transparent indium tin oxide (ITO) electrode and the upper metal electrode, which can be, for example, Al or Ag. However, the energy barrier for charge extraction can be created by the energy level mismatch between the electrodes and the active layer. Additionally, when there is no charge selectivity, the free charge carriers tend to recombine at the active

layer/electrode interface.[72] To overcome these problems, an interface layer is placed between the active layer and the electrodes, either as electron transport layers (ETLs), which assist in electron transport and holes block, or act as hole transport layers (HTLs), which assist in holes transport and electrons trapping. This selectivity of the layers enables the reduction of unfavourable charge recombination between the active layer and the electrodes. Additionally, an ohmic contact can form between the active layer and the electrodes by inserting ETLs and HTLs, which reduces the energy barrier for CT and improves device efficiency and sustainability.

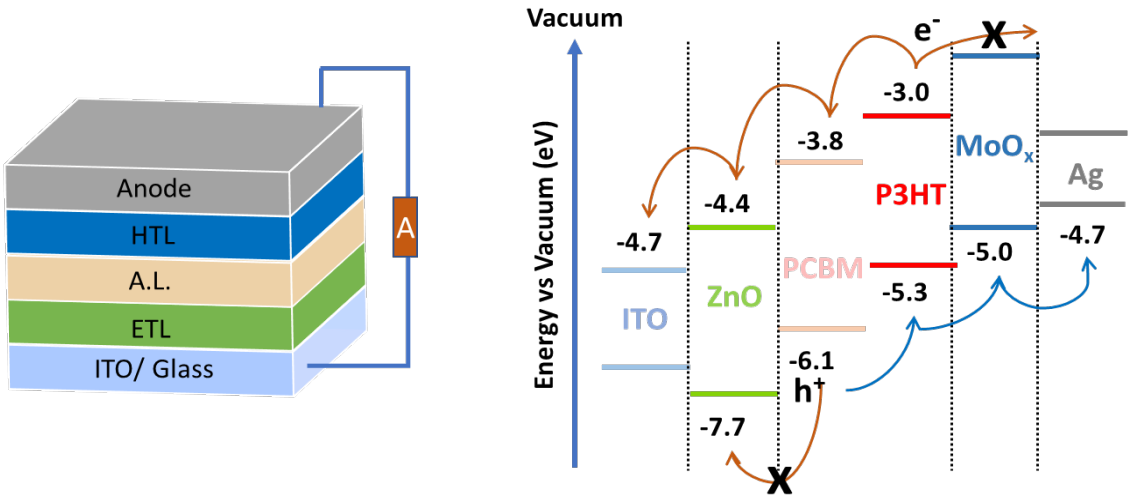

Figure 1-7. Inverted OPV device and associated energy levels.

The inverted sandwich structure is configured as ITO/ETL/active layer/HTL/Metal. For the poly(3-hydroxythiophene) (P3HT):phenyl-C-butyric acid methyl ester (PCBM) system, electrons travel from P3HT to PCBM, then are transported by zinc oxide (ZnO) (ETL) and finally extracted by the ITO cathode, as shown in Figure 1-7. Holes in P3HT domains are selectively transported by MoO_x (HTL) to the top anode for charge deposition. To reduce the energy barrier, solution-processed ZnO, TiO_2 and SnO_2 oxides can be used as ETLs, to obtain structures with high electron selectivity.[73] On top of the active layer, HTL, such as MoO_x and VO_3[74], is deposited. As alternatives to these materials, different organics, conjugated or non-conjugated polymers can be used. More

details are discussed further below. The advantage of using the inverted structure is that PEDOT: PSS on ITO can be prevented and replaced with a stable high WF metal as anode, thus reducing its degradation. In terms of efficiency, there is almost no difference between the conversion and the inverted device architectures, but if stability is considered, the inverted architecture is a far better choice for future applications.[75]

Extensive research has been directed towards the design of the donor-acceptor structure to optimise the energy levels and efficiency of the overall device. High-performance OPVs have been investigated for higher power conversion efficiency (PCE) compared to those based on fullerene acceptors. The non-fullerene acceptor (NFA), with an acceptor/donor/acceptor structure, consists of a rigid indacenodithieno[3,2-b]thiophene (IDTT) electron donor centre, with end groups of 2-(3-oxo-2,3-dihydroinden-1-ylidene) malononitrile (INCN). The broad and intense absorption of ITIC occurs in the 500–800 nm region with a maximum of 702 nm. The absorption profile corresponds to the push-pull structure of ITIC, which clear the way for intramolecular CT between IDTT and INCN. The HOMO is estimated to be –5.48 eV, while the LUMO energy levels of the ITIC films correspond to the value of –3.83 eV, so a narrow optical gap of 1.59 eV is observed. Device optimisation results in a PCE of 6.58% when using an ITIC-based design blended with PTB7-Th donor polymer, thus device energy levels, optical and electrical properties can be compared with a fullerene-based device with a PCE of 7.29%.[76]

Zhao et al. reported a system comprising poly[(2,6-(4,8-bis(5-(2-ethylhexyl)thiophen-2-yl)-benzo[1,2-b:4,5-b′]dithiophene))-alt-(5,5-(1′,3′-di-2-thienyl-5′,7′-bis(2-ethylhexyl) benzo[1′,2′-c:4′,5′-c′]dithiophene-4,8-dione))] (PBDB-T): ITIC is designed to give a PCE of 10.68%, since such architecture allows broad absorption and well-matched energy levels of the given PBDB-T: ITIC mixture.[77]

A new NFA was further developed by replacing the phenyl side chains with thienyl side chains in ITIC-Th. Lower values of LUMO and HOMO, –3.93 eV and –5.66 eV, can be

obtained in comparison with the ITIC values. This corresponds to good suitability of the PTB7-Th narrow-bandgap donor with band gap of 1.58 eV and the PDBT-T1 wide-bandgap donor with optimal band gap of 1.85 eV, which produces PCEs of 8.5% and 9.3%, in that order.[77]

i. Inorganic interface layer

The ETL, or cathode interface layer (CIL), enables sufficient mobility of electrons and their transfer across the layer since it acquires higher electrons than acceptor affinity.[78] To reduce charge recombination and interface defects, it is preferable to use ETL between the cathode and the active layer. The choice of ETL material should enable better compatibility with the active layer and the electrode, thus representing a phase boundary that facilitates electron extraction and improves light absorption.[79] SCs that include ETL are far more stable and long-lasting than those that do not.

Various TiO_x,[80] caesium carbonate (Cs_2CO_3)[81] and lithium fluoride (LiF)[82] materials have been investigated as highly efficient hole-blocking layers on ITO that permit electronic charge separation. However, due to its exceptional CT characteristic and suitable band gap, the most commonly used ETL material is ZnO.[83] The long-term stability of ZnO has placed it at the forefront of materials for these purposes, especially since it can be obtained through a low-temperature spin coating procedure. Further processing of the resulting film, which can increase crystallinity and thus enhance the device parameters, is an annealing procedure. For these reasons, ZnO is widely applied as a CBL in various donor-acceptor systems due to its ease of processing and stability.[84]

A liquid phase ZnO processing can introduce surface defects into the material and produce a charge recombination barrier. Passivation of the ZnO surface may be a way to overcome these issues. Defect reduction was proposed by Pandi et al.,[85] where reduced graphene oxide (rGO) sheets were employed to improve CT. Jiang et al. also investigated triethanolamine passivated ZnO film, which has lower trap density, improved

recombination time and higher electron mobility, affecting the comprehensive device performance.

In the tandem cell, when an 80 nm active layer of PBDTS-TDZ: ITIC is applied in the front and 125 nm PTB7-Th: O6T4F:$PC_{71}BM$ in the back cell, the OPV efficiency reaches a value of 18%, while ZnO was used as CIL.[86] Also, two terminal tandem cells were optimised using ZnO/p-type quaternary amine based on fluorene (PFN)-Br as CBL and a high PCE of 17.36% was achieved. There are other OPV devices in which ZnO or its composites were used as CBL as well (e.g., ZnO: PFN-Br[87]).

ii. Organic interface layer

Various organic materials and non-conjugated/conjugated polymers can be tested as CILs. Special classes of compounds with numerous favourable properties in OPVs are polymers, fullerenes and their derivatives.[88,89] Considering the contact made between the intermediate layer and the photoactive layer, one must take into account the reactions at the phase boundary and the stability of these two layers that can affect the stability and lifetime of the device itself. For this reason, good contact between the two layers is necessary because the accumulation of charge at the interface must be avoided. In this case, in PV devices, the stimulation of photoelectric conversion can be ensured; therefore, the research on polymer CIL has been provided special attention.

Non-conducting polymers with functionalities on side chain amino groups, such as poly(4-vinylpyridine) and polyethyleneimine (PEI), can modify ITO WF.[90,91] Control of the layer thickness must be performed, since these polymers have no intrinsic conductivity and thus behave as insulators at any thickness greater than the tunnelling threshold. Comparatively, the advantage of synthesising such materials in bulk is that solution-processed polymers can be fabricated using green solvents and are cheaper polymers compared to semiconducting polymers. One of the first semiconducting polymers used in OPVs was the PFN.[92] The search for polymers as ETL proceeded with

conjugated polymers where the tertiary replaced the quaternary amine, with Br serving as a counter ion.[93] It was found that the photo-response of such a material containing a tertiary amine increases in the presence of light, while a quaternary amine gives a constant high-level conductivity. The explanation for this behaviour can be found in the doping mechanism that allows the tertiary amine to undergo a photo-response while the quaternary amine is constantly doped.[94]

Materials that contain an n-oxide side group and have good solubility in water and alcohol can also be used in SCs. Such materials have a lone electron pair available for WF alternations and have been investigated in a perovskite-based PSC. Zwitterions NDIO and PDINO[95–97] were tested along with other organic interlayers that contribute to the high efficiency of the device, such as PFS,[98] NDI,[99] PFN[91] and NDI-N.[99]

The focus of this thesis is on a class of naphthalene diimide (NDI)-based materials. NDI is intended to be used as a core polymer for SCs and will be used in this thesis as polymer CIL to address its effects on the energy level (Chapter 5). Additionally, spin-coated ZnO will be employed as an inorganic CIL for comparison (Chapter 6).

1.3 Perovskite-Based SC: Background

1.3.1 Crystal structures of perovskite

Photon absorption in the PSC is dependent on the perovskite structured material and thus crucially effects the efficiency of the device. Russian crystallographer (Lev Perovskite)[100] is credited in the name of the family of compounds after establishing its structure in the mineral calcium titanate ($CaTiO_3$). In the structures of the ABX_3 chemical formula, A and B are considered as cations and X is the anion. Figure 1-8 shows the idealised cubic structure for a perovskite material, in which eight ‘A’ cations (blue) are positioned at the corners of the cube, one ‘B’ cation (black) occupies the cube’s centre, and six ‘X’ anions

(yellow) are placed in the middle of each of cube's sides. Various reports suggest that anions are loosely bound and can move easily throughout the perovskite structure.[101]

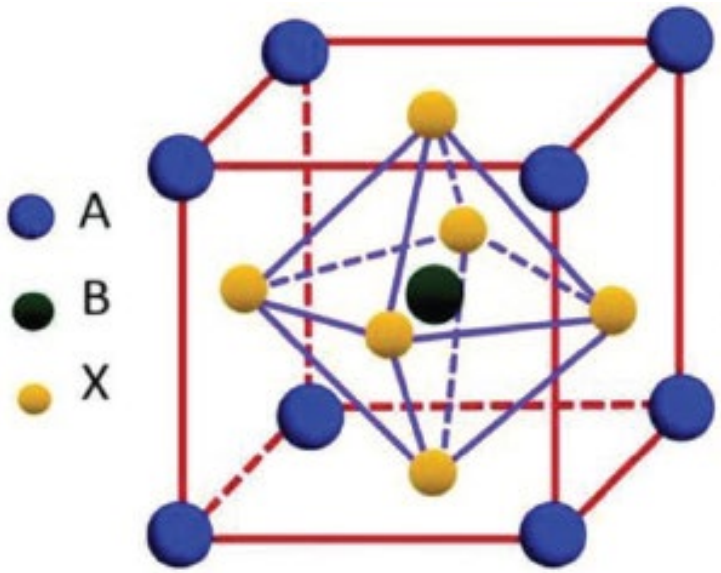

Figure 1-8. The cubic crystal structure of ideal perovskite.[102]

Initial findings of $CaTiO_3$ led to the discovery that many inorganic metal oxides adopt from perovskite structures (e.g., $BiFeO_3$, $SrTiO_3$, $BaTiO_3$ and $NaTiO_3$). A commonly studied perovskite is methylammonium lead iodide ($CH_3NH_3PbI_3$), which is known as an organic-inorganic hybrid. The organic $CH_3NH_3^+$ cation takes up the role of the 'A' cation, while the inorganic Pb^{2+} cation takes up the role of the 'B' cation.

By varying atoms and groups, in positions A, B and X of the perovskite cubic structure, the band arrangement of the perovskite crystal can be fine-tuned. The band gap (~1.5–1.6 eV) found in $CH_3NH_3PbI_3$ is near the ideal/desired value. Adjustment of the band gap to the optimum value of 1.4 eV can be achieved by replacing the methylammonium by formamidinium (FA) to form $FAPbI_3$. This expands the range of wavelength that can be efficiently absorbed by the material and considerably increasing the J_{sc}.[103] Larger ethylammonium ($CH_3CH_2NH_2$) was used in the A site (see again Figure 1-8), which raises the band gap to around 2.2 eV.[104] Further, replacing organic functional groups with inorganic cation forms a completely inorganic perovskite with similar E_g energies (e.g., $CsPbI_3$ =1.73 eV).[105] Based on extensive results, formation criteria can be proposed for

the ABX_3 structure for fine-tuning the band gap by changing the A site group. A Goldschmidt tolerance factor is used to estimate the likelihood and stability of the formation of a perovskite crystal, as shown in equation 1.4:

$$t = \frac{r_{A+} r_X}{\sqrt{2}(r_{B+} r_X)} \tag{1.4}$$

With r_A, r_B and r_X signifying the radii of the species in A, B and X. For a stable perovskite structure, the Goldschmidt tolerance factor should vary between 0.8 and 1.0, as listed in Table 1-1. Below are the conditions, with respect to radii of cation in A site (1.6–2.5 Å),[106] needed for successful preparation of Pb^{2+}-based perovskite in B site, for various halogens.

Table 1-1

Range of Radii for Cation in A Position in $APbX_3$ Structure

rB	rX	rA for t = 0.8	rA for t = 1.0
Pb2+ (1.19 Å)	Cl– (rCl = 1.81 Å)	1.58 Å	2.43 Å
Pb2+ (1.19 Å)	Br– (rBr = 1.96 Å)	1.60 Å	2.50 Å
Pb2+ (1.19 Å)	I–(rI = 2.20 Å)	1.64 Å	2.59 Å

Note. Obtained from Park.[106]

The most studied is $CH_3NH_3PbI_3$, with methylammonium radii of 1.8 Å. That gives 0.83 for the tolerance factor, indicating a somewhat distorted cubic structure is likely. Various reports show that $CH_3NH_3PbI_3$ is formed in tetragonal structure at ambient conditions with phase transformation to cubic at 54 °C.

Perovskites seem almost ideal for SC applications. Materials themselves are effecient,[107,108] with tuneable E_g,[109,110] sufficient exciton diffusion path,[111,112] low exciton binding energy[113] and high charge carrier mobilities.[114] From the upscaling perspective, preparing them from solution makes them cheap and simple. Roll-to-roll coating techniques have also been tried and tested and appear suitable for PSCs manufacturing. For example, it is also possible to make tandem SCs with silicon by adding a coating step.[115]

1.3.2 An overview of PSCs

As previously stated, the perovskite type of materials was discovered over a century ago. From the initial discovery in 1839, much work has been devoted to the study of their properties, especially to the oxide perovskites. Since the middle of the last century (1950s), perovskites have been applied in various applications, which includes their use in condensers, electrochemical transducers, multilayer capacitors, catalysts, etc. Still, it is only recently that organic-inorganic mixed perovskites have been used in thin-film SCs. Initial design of the Gretzel DSSC serves as the basis for modern dye-sensitised PSCs. Three critical components make up the DSSC: mesoporous TiO_2, light-absorbing dye attached to the TiO_2 and the redox-active electrolyte.

The first stage in their improvement was to replace the liquid electrolytes with solid-state compounds with equal or similar properties. At the same time, thin and flexible materials were being developed that could replace organic dyes for absorption of light over a wider range of wavelengths. For that purpose, Miyasaka et al. developed $CH_3NH_3PbI_3$ and $CH_3NH_3PbBr_3$ as light-absorbing substances in liquid electrolytes and solid-state. Their first report on the sensitised perovskite SC was published in 2009, which reported a remarkable 3.8% efficiency,[116] but with stability of only a couple of minutes due to the use of liquid electrolytes.

The next step was executed by Park et al. in 2011, who reached 6.5% efficiency by increasing the amount of perovskite in the cell design.[117] However, they faced the same problem: perovskite decomposition in the liquid electrolyte. In 2012, Snaith Group provided replacement of the liquid electrolyte with a recently developed solid-state hole conductor: 2,2′,7,7′-tetrakis (N, N-di-p-methoxyphenylamino)-9,9′-spirobifluorene (spiro-OMeTAD). By using perovskite, in combination with spiro-OMeTAD, stability was significantly improved with obtained efficiencies reaching 10%,[118] which was a noteworthy breakthrough as it improved the efficiency of solid-state DSSCs by almost 7%.[119]

The next development came with the use of non-conducting mesoporous Al_2O_3 instead of mesoporous TiO_2, resulting in cells providing 200–300 mV larger V_{oc} and efficiencies of over 10%.[120] This was the pinnacle in PSCs development as it established that perovskites could serve as both electron and hole conductors, which subsequently opened the door for the use of thin-film planar architecture in PSCs.[121]

After these discoveries, interest in PSCs increased considerably, seen through a firm rise in the number of publications with a special focus on new fabrication processes and techniques, which enhanced both efficiencies and stability of PSCs. For instance, Liu et al. used vapour deposition technique[122] and achieved around 15% efficiency in a planar PSC. In 2014, anti-solvent technique was employed where rate of perovskite crystallisation was carefully tuned by use of dimethyl sulfoxide solvent to produce thin films of high quality.[123–125] Since its publication, many researchers have started using this technique. Other techniques were developed by Burschka et al. in 2013,[126] whereby deposition is conducted in two subsequent steps. The first step is to deposit PbI_2 on the surface of porous TiO_2 while the conversion to perovskite is done in the second step, exposing the surface to methylammonium iodide. As with the anti-solvent technique, a two-step procedure enhanced perovskite layer quality to a respectable 15% cell efficiency.[126] Additionally, a well-known doctor-blade technique was employed in PSCs by Deng et al.[127] with a reported 18.3% efficiency.

The race for the highest PCE has since started. Bi et al. make use of poly(methyl methacrylate) to guide perovskite crystal nucleation and growth[128] and obtained a PCE of 21.02%. Simultaneously, scientists from KRICT and UNIST developed a single-junction PSC with 22.1% PCE.[5] This result was outdone in 2018 by researchers at the CAS, who published a PSC with a certified 23.3% PCE.[5] The latest entry is from June 2020, with NERL[5] announcing PSC with a PCE of 25.2%. PSCs are now on par with well-established PV devices like those using cadmium telluride and copper indium gallium selenide. Additionally, both researchers and industries are now moving towards using perovskite

in tandem devices. Consequently, in 2020 a new efficiency maximum, with a PCE of 29.15%, for a perovskite-silicon tandem SC[129] was reported, outclassing even the single-junction cells.[5] Perovskites are now finding their way into other similar applications that include building-integrated PVs, LED, lasers, photo-catalysts and photodetectors, among others.

1.3.3 PSC devices: their structures

The architecture of a PSC device predominantly dictates overall performance and indirectly affects which electrode materials will be used, their mutual compatibility and their method of preparation. The main architectures of PSCs distinguish between mesoscopic and planar. The mesoscopic design was employed first, and in this arrangement, oxide framework is covered by a layer of perovskite material with two possible routes:

1. Oxide framework is covered by a thin film of perovskite with the film penetrating every pore, as shown in Figure 1-9A.

2. Oxide framework is fully filled and covered by perovskite layer, as shown in Figure 1-9B.

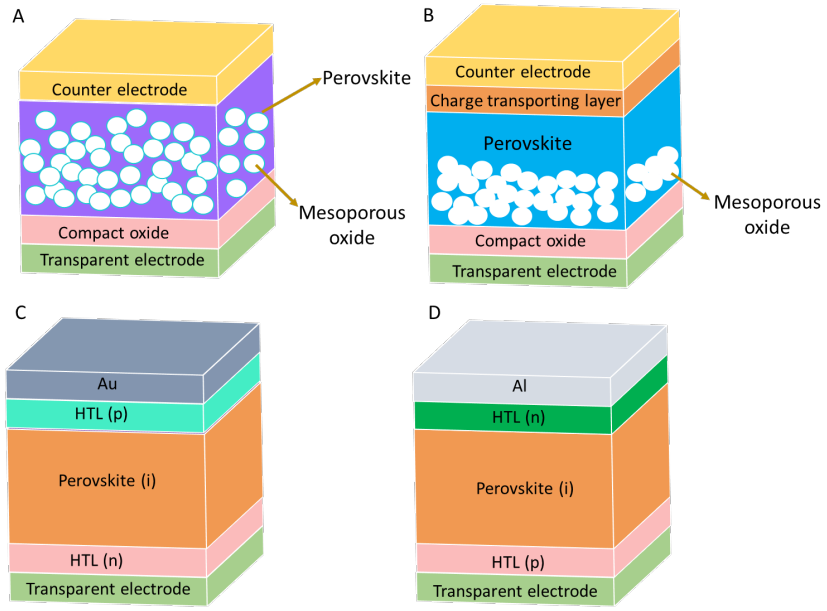

Figure 1-9. PSCs structures. (A) Mesoscopic PSCs and oxide framework covered by a thin layer. (B) Mesoscopic PSCs and oxide framework covered by a layer on the top. Planar PSCs structure: (C) the n–i–p architecture and (D) the p–i–n architecture. Adapted from.[153]

The critical breakthrough in PSCs development was the elucidation of perovskites ambipolar nature, which opened the door for effective application of the planar architecture. Several advantages of planar compared to mesoporous architecture include 1) preparation at relatively low temperatures (<150 °C), 2) use of flexible substrates, 3) possibility of incorporation in tandem SC, 4) multitude of deposition processes and 5) ease of preparation.

Planar PSC circumvents the use of underlying oxide framework, which is substituted with a thin layer of electron- or hole-conducting material. Similar to the case in OPVs, in planar architecture, we distinguish between 'conventional' or 'inverted', depending on the direction of the current flow. PSCs assembled in a 'conventional' mode collect electrons at the respective transparent electrode ('n–i–p' system), whereas in the 'inverted' mode electrons are captured at the metal ('p–i–n' system). Both are illustrated in Figures 1-9C and 1-9D. The experiments carried out in this thesis use a planar architecture arranged in a 'p–i–n' structure. Jeng et al. were the first to employ 'inverted' configuration in 2013,[130]

which was later shown to offer lower preparation temperatures and, more importantly, only a slight hysteresis when compared to the 'conventional' architecture.[131]

1.3.4 Interfacial engineering in PSC

The structure of the PSC is made up of several layers with a distinct interface. Each layer has its own characteristics. The interface properties are particularly important since charge carriers (electrons or holes) can pass from the perovskite layer to be collected at the perspective CT layer (CTL). To control these properties, when the interface is engineered, it is typically done by employing four main methods.

The first method deals with the passivation of defects, which, when formed at the CTL/perovskite interface, reduce the efficiency and stability of the PSC. Interface defects/traps mainly consist of oxygen or halide vacancies and low-coordinated metal atoms[132] with energy states that assist recombination at the interface. Sherkar et al.'s[133] simulations showed that defect/trap-assisted recombination can be sidestepped by passivation of defects/traps at the transport layer/perovskite interface in PSC, with an associated 40% rise in PCE versus the non-passivated device.[133]

The second method of interfacial engineering is through energy level shifting and aligning the energies between the transport and perovskite layer.[134] The aim is to create easier extraction and CT as a barrier height at the interface that exceeds 0.1 eV and prevents carrier extraction. This high barrier energy causes the accumulation of charge carriers, which results in undesirable recombination processes.

The third method involves increasing the perovskite film quality. Poly[bis(4-phenyl)(2,4,6-trimethylphenyl)amine (PTAA) causes punctures of the perovskite film during its preparation due to the difference in wettability.[134] However, using a buffer layer is one way to improve the wettability of the CTL, leading to an even more compact perovskite film with reduced defect formation. Further, controlling the perovskite's and substrate's thermal expansion coefficients by proper interface engineering can alleviate

the lattice strain caused by the mismatch in atomic positions and orientations between layers.[135]

The fourth method involves lowering the UV-degradation potential of the perovskite film. As it is used in SC energy generation, the PSC is exposed to long periods of UV-exposure from the sun. The engineering of UV-resistant PSC layers is a significant step towards the SC's efficiency longevity. Lately, self-assembled monolayers (SAMs) have started to be commonly used for this purpose and will be described below.

1.3.4.1 SAM layer

SAMs are self-constructing monolayers usually of a particular molecule that create a specific functional group surface. The layer is formed/attached to the substrate either by utilising physical or chemical bonds. The molecular structure of SAMs can be tailored by manipulating the surface functional groups to achieve a higher affinity towards the subsequent layer. Additionally, further modification of layer alignment and intermolecular interactions can be easily accomplished to increase the charge mobility.[136]

The surface of the CTLs in PSC is covered mainly by hydroxyl groups. These hydroxyl groups readily interact with carboxyl, sulfonic, phosphonic or silane groups to build up the SAM molecule and form a dipole moment inside the contact volume. The newly formed structures can affect charge collection as formed dipoles influence the energy level of both layers.

Singh et al. used para-substituted phenylphosphonic acid SAMs to engineer the NiOx (HTL)/perovskite interface.[137] Phenylphosphonic acid (PPA), 4-cyanophenylphosphonic acid (CNPPA) and 4-methoxyphenylphosphonic acid (MPPA) were assessed as possibly active SAM materials. Their results showed that the use of PPA decreased the WF slightly while MPPA decreased it further due to the methoxy group's distinct electron-donating characteristics. A reference device with no SAM layer exhibited a PCE of 17.02%, while PSC modified with PPA and MPPA displayed lower PCE, 15.35% and 12.08%,

indicating unfavourable energy band alignment. On the other hand, CNPPA, used as a SAM, improved the PCE to 18.45%, with concurrent increase in V_{oc} and J_{sc} via advantageous level shifting via favourable dipole direction.

SAMs are able to influence the energy level alignment on both CTL/perovskite and ITO/CTL interfaces. Arkan et al. proposed a novel SAM based on carboxylic acid anchoring groups, specifically intended for ITO, due to its self-organisation on oxide surfaces via chemical adsorption.[138] Lower delocalisation energy of thiophene, compared to benzene, prompted its use as a spacer group as it leads to a pronounced bonding effect. Bare-ITO surface WF (4.62 eV) was amplified (4.80 eV) to better align with PEDOT: PSS's (5.3 eV), which served as HTL, achieving more favourable energy level alignment. Moreover, the photo carrier gathering efficiency was improved by the introduction of the interfacial layer whose WF was aligned close to that of innate ITO, resulting in PCE improvement from 9.57% to 13.71%. Additionally, SAMs promote the formation of large grain-sized perovskite films by passivating the halide vacancy and crystal defects, which leads to improved efficiency and stability of PSCs. The conclusion is based on a study comparing the grain sizes of perovskite films dependent on the dip coating time in 3 mercaptopropyltrimethoxysilane (MPTMS) on a SnO_2 film.[139] It is the sulfhydryl group in the MPTMS structure that coordinates the PbI_2, consequently reducing crystal growth and increasing the crystallite size.

Moreover, CTLs with an added SAM layer remain transparent, display negligible optical losses and raise the J_{sc}.[140] HTLs and ETLs commonly used in p–i–n and n–i–p PSCs (NiOx, PTAA, SnO_2 and TiO_2) have strong absorption in the blue region of the spectrum and thus decrease the J_{sc} of PSCs. Contrarily, a MeO-2PACz ((2-(3,6-dimethoxy-9H-carbazol-9-yl)ethyl) phosphonic acid) SAM acts as HTL, increasing the J_{sc} of p–i–n structure by ~0.8 mA cm^{-2} when compared to the more common PTAA.[141]

Additionally, SAM molecules offer almost full surface coverage of a metal-oxide, as a monolayer, with effective binding to the surface with a defect passivating effect. For

example, PCBA ([6,6]-phenyl-C61-butyric acid) fullerene SAM[142] was successful in mitigating SnO_2 ETL surface defects, delivering enhanced device performance and reproducibility. C60-SAM (4-(1′,5′-dihydro-1′-methyl-2′H-[5,6]fullereno-C60-Ih-[1,9-c]pyrrol-2′-yl) benzoic acid) was also successfully used[143] in creating an electron-selective contact for the fabrication of n–i–p PSCs via modification and passivation of the ITO surface. Beside fullerene-based SAMs, other SAMs, including 4-chlorobenzoic acid,[144] dopamine[145] and 3,4,5-trimethoxybenzoic acid,[146] were probed as passivating agents for metal-oxide ETLs.

The modification of electronic properties at the surface of a TCO is also possible with hole-selective SAMs. The surface of the ITO electrode was modified with 2PACz SAM,[141] which, in addition to passivating the surface defects of ITO, provided a hole-selective ITO-SAM interface. The result was an efficient hole transfer incoming from the perovskite layer, with SAMs surface dipole repelling electrons from the interface, which lowers the charge recombination rate near the interface.

This thesis deals with the use of a SAM as an interface passivation layer for hole transport, described in Chapter 8.

1.4 The Differences between OPV and PSC in Terms of their Working Principle

The underlying mechanism responsible for energy conversion in a PV device is charge separation after photon absorption and followed by CT to the electrodes where it is collected. OPVs and PSCs, however, differ considerably in their principles' processes, primarily due to the inherent physical properties of their photoactive materials (hybrid organic-inorganic perovskite versus organic semiconductor). The major difference between perovskite materials and organic semiconductors comes from the relatively low exciton binding energy of perovskites (relative to organic semiconductors), which is

around a few milli-electron volts, as illustrated in Table 1-2. Therefore, the absorption of a photon in PSCs almost always causes the formation of free charge carriers, as shown in Figure 1-10, which differs significantly from OPVs' working principle.[147] Generation of charge carries in one step is the key advantageous characteristic of PSCs, over OPVs, where a significant amount of energy is lost due to exciton dissociation.

Table 1-2

The Parameters of Active Layers in PSCs and OPVs

Parameter	OPVs ($P3HT/PC_{60}BM$)	References	PSCS ($CH_3NH_3PbI_3$)	References
Bandgap	1.8 eV	[148]	1.55 eV	[149]
Exciton binding energy	~0.3–0.5 eV	[148]	< 0.05 eV	[114]
Electron mobility	~$2x10^{-3}$ $cm^2V^{-1}S^{-1}$	[150]	2–10 $cm^2V^{-1}S^{-1}$	[114]
Hole mobility	10^{-4} $cm^2V^{-1}S^{-1}$	[150]	5–12 $cm^2V^{-1}S^{-1}$	[114]

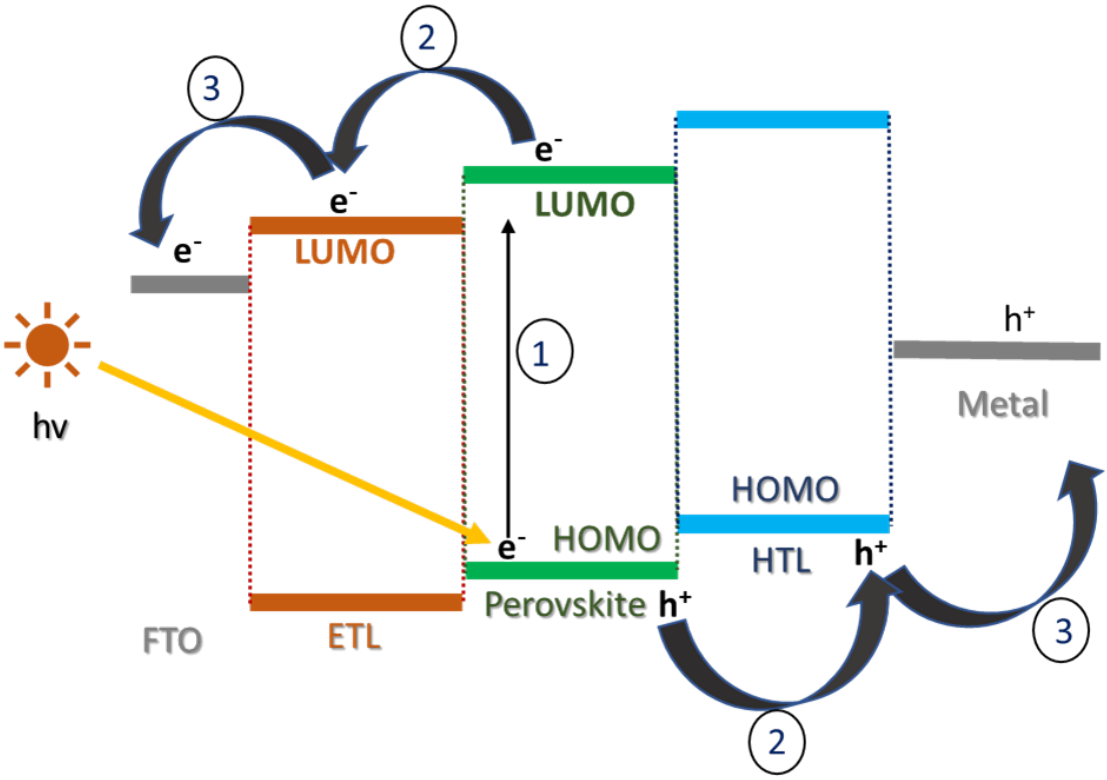

Figure 1-10. Energy level and working principle of PSC. 1) Photon absorption and generation of free charge carriers, 2) transport of free charge carriers and 3) collection of free charge carriers at particular electrodes. Adapted from.[153]

The production of free carriers is efficiently separated through the transport of holes into the HTL and electrons into the ETL. Thus, the electrons formed close to the HTL need to move over the thickness of the absorbent layer to reach the ETL and vice versa in the case of holes, which may increase the possibility of recombination. Yet, reports suggest that absorbers film in PSCs have limited recombination due to a large photo-induced dielectric constant, making electrostatic interaction among generated charge carriers insignificant, which is not the case for OPVs.[151] Perovskites, therefore, inherently provide ambipolar CT, with large diffusion lengths (over 1 micrometre) for both carriers. This was confirmed by measuring injection times for both electrons and holes, which appear to happen on a comparable timescale.[152]

1.5 References

(1) International Energy Agency. *World Energy Outlook*. International Energy Agency, 2017. https://iea.blob.core.windows.net/assets/4a50d774-5e8c-457e-bcc9-513357f9b2fb/World_Energy_Outlook_2017.pdf

(2) World Energy Council. *World Energy Issues Monitor: Exposing The New Energy Realities*. World Energy Council, 2017. https://www.worldenergy.org/assets/downloads/1.-World-Energy-Issues-Monitor-2017-Full-Report.pdf

(3) Epp, B. IEA's Renewables Outlook 2017-2022. *Solarthermalworld.org*. 31 October, 2017. https://solarthermalworld.org/news/ieas-renewables-outlook-2017-2022/ (accessed 20 October 2022).

(4) BP Energy Economics. *BP Energy Outlook*. British Petroleum Company, 2018. https://www.bp.com/content/dam/bp/business-sites/en/global/corporate/pdfs/energy-economics/energy-outlook/bp-energy-outlook-2018.pdf

(5) National Renewable Energy Laboratory (NREL). *Best Research-Cell Efficiency Chart*. https://www.nrel.gov/pv/cell-efficiency.html (accessed 20 October 2022).

(6) Becquerel, A.-E. Recherches sur les Effets de la Radiation Chimique de la Lumiere Solaire au Moyen des Courants Electriques. *CR Acad. Sci.* **1839**, *9* (145), 1.

(7) Fritts, C. E. On a New Form of Selenium Cell, and Some Electrical Discoveries Made by Its Use. *American Journal of Science* **1883**, *3* (156), 465–472.

(8) Chapin, D. M.; Fuller, C. S.; Pearson, G. L. A New Silicon P-N Junction Photocell For Converting Solar Radiation Into Electrical Power. *Journal of Applied Physics* **1954**, *25* (5), 676–677.

(9) Green, M. A. Silicon Photovoltaic Modules: A Brief History of the First 50 Years. *Progress in Photovoltaics: Research and Applications* **2005**, *13* (5), 447–455.

(10) Sariciftci, N. S.; Sun, S.-S. *Organic Photovoltaics: Mechanism, Materials, and Devices*; Taylor and Francis New York, 2005.

(11) Seitkhan, A. Interface Engineering of High Performance Organic and Perovskite Solar Cells. Ph.D. Dissertation, King Abdullah University of Science and Technology, 2021. http://hdl.handle.net/10754/669675

(12) Hecht, J. Perovskites: The Hottest Material in Solar Cells. *Laser Focus World*. 16 December 2021. https://www.laserfocusworld.com/optics/article/14213544/perovskites-the-hottest-material-in-solar-cells/ (accessed 20 November 2022).

(13) Al-Ashouri, A.; Köhnen, E.; Li, B.; Magomedov, A.; Hempel, H.; Caprioglio, P.; Márquez, J. A.; Vilches, A. B. M.; Kasparavicius, E.; Smith, J. A. Monolithic Perovskite/Silicon Tandem Solar Cell With> 29% Efficiency by Enhanced Hole Extraction. *Science* **2020**, *370* (6522), 1300–1309.

(14) Guo, Y.; Li, Y.; Awartani, O.; Han, H.; Zhao, J.; Ade, H.; Yan, H.; Zhao, D. Improved Performance of All-Polymer Solar Cells Enabled by Naphthodiperylenetetraimide-Based Polymer Acceptor. *Advanced Materials* **2017**, *29* (26), 1700309.

(15) Sharma, A.; Watkins, S. E.; Andersson, G.; Lewis, D. A. Effect of Annealing Temperature of ZnO on the Energy Level Alignment in Inverted Organic Photovoltaics (OPVs). *Energy Technology* **2014**, *2* (5), 462–468.

(16) Chambon, S.; Derue, L.; Lahaye, M.; Pavageau, B.; Hirsch, L.; Wantz, G. MoO3 Thickness, Thermal Annealing and Solvent Annealing Effects on Inverted and Direct Polymer Photovoltaic Solar Cells. *Materials* **2012**, *5* (12), 2521–2536.

(17) Bessette, A.; Hanan, G. S. Design, Synthesis and Photophysical Studies of Dipyrromethene-Based Materials: Insights Into Their Applications in Organic Photovoltaic Devices. *Chemical Society Reviews* **2014**, *43* (10), 3342–3405.

(18) Spanggaard, H.; Krebs, F. C. A Brief History of the Development of Organic and Polymeric Photovoltaics. *Solar Energy Materials and Solar Cells* **2004**, *83* (2–3), 125–146.

(19) Kumar, P.; Chand, S. Recent Progress and Future Aspects of Organic Solar Cells. *Progress in Photovoltaics: Research and Applications* **2012**, *20* (4), 377–415.

(20) Liu, Y.; Li, B.; Ma, C.-Q.; Huang, F.; Feng, G.; Chen, H.; Hou, J.; Yan, L.; Wei, Q.; Luo, Q. Recent Progress in Organic Solar Cells (Part I Material Science). *Science China Chemistry* **2021**, 1–45.

(21) Zhu, L.; Zhang, M.; Zhong, W.; Leng, S.; Zhou, G.; Zou, Y.; Su, X.; Ding, H.; Gu, P.; Liu, F. Progress and Prospects of the Morphology of Non-Fullerene Acceptor Based High-Efficiency Organic Solar Cells. *Energy & Environmental Science* **2021**, *14* (8), 4341–4357.

(22) Scharber, M. C.; Sariciftci, N. S. Low Band Gap Conjugated Semiconducting Polymers. *Advanced Materials Technologies* **2021**, *6* (4), 2000857.

(23) Jia, H.; Lei, T. Emerging Research Directions for N-Type Conjugated Polymers. *Journal of Materials Chemistry C* **2019**, *7* (41), 12809–12821.

(24) Rafique, S.; Abdullah, S. M.; Sulaiman, K.; Iwamoto, M. Fundamentals of Bulk Heterojunction Organic Solar Cells: An Overview of Stability/Degradation Issues and Strategies for Improvement. *Renewable and Sustainable Energy Reviews* **2018**, *84*, 43–53.

(25) Pochettino, A. The Development of Organic Conductors, Including Semiconductors, Metals and Superconductors Cont. *Academy Lincei Rendus* **1906**, *15*, 355.

(26) Volmer, M. Die Verschiedenen Lichtelektrischen Erscheinungen am Anthracen, Ihre Beziehungen Zueinander, zur Fluoreszenz und Dianthracenbildung. *Annalen der Physik* **1913**, *345* (4), 775–796.

(27) Okamoto, Y.; Kundu, S. K. Synthesis and Properties of N-ethynylcarbazole and Poly-N-ethynylcarbozole. *The Journal of Organic Chemistry* **1970**, *35* (12), 4250–4252.

(28) Akamatu, H.; Inokuchi, H.; Matsunaga, Y. Electrical Conductivity of the Perylene–Bromine Complex. *Nature* **1954**, *173* (4395), 168–169.

(29) Shirakawa, H.; Louis, E. J.; MacDiarmid, A. G.; Chiang, C. K.; Heeger, A. J. Synthesis of Electrically Conducting Organic Polymers: Halogen Derivatives of Polyacetylene, (CH) x. *Journal of the Chemical Society, Chemical Communications* **1977**, (16), 578–580.

(30) Chamberlain, G. Organic Solar Cells: A Review. *Solar cells* **1983**, *8* (1), 47–83.

(31) Tang, C. W. Two-layer Organic Photovoltaic Cell. *Applied Physics Letters* **1986**, *48* (2), 183–185.

(32) Hiramoto, M.; Fujiwara, H.; Yokoyama, M. Three-layered Organic Solar Cell With a Photoactive Interlayer of Codeposited Pigments. *Applied Physics Letters* **1991**, *58* (10), 1062–1064.

(33) Yu, G.; Gao, J.; Hummelen, J. C.; Wudl, F.; Heeger, A. J. Polymer Photovoltaic Cells: Enhanced Efficiencies via a Network of Internal Donor-Acceptor Heterojunctions. *Science* **1995**, *270* (5243), 1789–1791.

(34) Liu, Q.; Jiang, Y.; Jin, K.; Qin, J.; Xu, J.; Li, W.; Xiong, J.; Liu, J.; Xiao, Z.; Sun, K. 18% Efficiency Organic Solar Cells. *Science Bulletin* **2020**, *65* (4), 272–275.

(35) Meng, L.; Zhang, Y.; Wan, X.; Li, C.; Zhang, X.; Wang, Y.; Ke, X.; Xiao, Z.; Ding, L.; Xia, R. Organic and Solution-Processed Tandem Solar Cells with 17.3% Efficiency. *Science* **2018**, *361* (6407), 1094–1098.

(36) Choy, W. C. Organic Solar Cells: Materials and Device Physics. Springer: 2012.

(37) Collins, B. A.; Li, Z.; Tumbleston, J. R.; Gann, E.; McNeill, C. R.; Ade, H. Absolute Measurement of Domain Composition and Nanoscale Size Distribution Explains Performance in PTB7: $PC_{71}BM$ Solar Cells. *Advanced Energy Materials* **2013**, *3* (1), 65–74.

(38) Brütting, W. Physics of Organic Semiconductors. *Physica Status Solidi (a)* **2004**, *201* (6), 1031–1031.

(39) Nunzi, J.-M. Organic Photovoltaic Materials and Devices. *Comptes Rendus Physique* **2002**, *3* (4), 523–542.

(40) Mikhnenko, O. V.; Azimi, H.; Scharber, M.; Morana, M.; Blom, P. W.; Loi, M. A. Exciton Diffusion Length in Narrow Bandgap Polymers. *Energy & Environmental Science* **2012**, *5* (5), 6960–6965.

(41) Michl, B.; Benick, J.; Richter, A.; Bivour, M.; Yong, J.; Steeman, R.; Schubert, M. C.; Glunz, S. W. Excellent Average Diffusion Lengths of 600 μm of n-type Multicrystalline Silicon Wafers After the Full Solar Cell Process Including Boron Diffusion. *Energy Procedia* **2013**, *33*, 41–49.

(42) Günes, S.; Neugebauer, H.; Sariciftci, N. S. Conjugated Polymer-Based Organic Solar Cells. *Chemical Reviews* **2007**, *107* (4), 1324–1338.

(43) McCulloch, I.; Heeney, M.; Bailey, C.; Genevicius, K.; MacDonald, I.; Shkunov, M.; Sparrowe, D.; Tierney, S.; Wagner, R.; Zhang, W. Liquid-Crystalline Semiconducting Polymers With High Charge-Carrier Mobility. *Nature Materials* **2006**, *5* (4), 328–333.

(44) Kietzke, T. Recent Advances in Organic Solar Cells. *Advances in OptoElectronics* **2007**, *Article ID 40285*.

(45) Mihailetchi, V.; Wildeman, J.; Blom, P. Space-Charge Limited Photocurrent. *Physical Review Letters* **2005**, *94* (12), 126602.

(46) Chen, D.; Nakahara, A.; Wei, D.; Nordlund, D.; Russell, T. P. P3HT/PCBM Bulk Heterojunction Organic Photovoltaics: Correlating Efficiency and Morphology. *Nano Letters* **2011**, *11* (2), 561–567.

(47) Karuthedath, S.; Melianas, A.; Kan, Z.; Pranculis, V.; Wohlfahrt, M.; Khan, J. I.; Gorenflot, J.; Xia, Y.; Inganäs, O.; Gulbinas, V. Thermal Annealing Reduces Geminate Recombination in TQ1: N2200 All-Polymer Solar Cells. *Journal of Materials Chemistry A* **2018**, *6* (17), 7428–7438.

(48) Schwarze, M.; Tress, W.; Beyer, B.; Gao, F.; Scholz, R.; Poelking, C.; Ortstein, K.; Günther, A. A.; Kasemann, D.; Andrienko, D. Band Structure Engineering in Organic Semiconductors. *Science* **2016**, *352* (6292), 1446–1449.

(49) Zhang, Q.; Liu, X.; Jiao, F.; Braun, S.; Jafari, M. J.; Crispin, X.; Ederth, T.; Fahlman, M. Ground-State Charge Transfer for NIR Absorption With Donor/Acceptor Molecules: Interactions Mediated via Energetics and Orbital Symmetries. *Journal of Materials Chemistry C* **2017**, *5* (2), 275–281.

(50) Ru, Y.; Shi, Z.; Zhang, J.; Wang, J.; Chen, B.; Huang, R.; Liu, G.; Yu, T. Recent Progress Of Photochromic Materials Towards Photocontrollable Devices. *Materials Chemistry Frontiers* **2021**, *5* (21), 7737–7758.

(51) Chen, L.-M.; Xu, Z.; Hong, Z.; Yang, Y. Interface Investigation and Engineering–Achieving High Performance Polymer Photovoltaic Devices. *J. Mater. Chem.* **2010**, *20* (13), 2575–2598.

(52) Li, Y.; Li, P.; Lu, Z. H. Molecular Orientation and Energy Levels at Organic Interfaces. *Advanced Electronic Materials* **2016**, *2* (11), 1600306.

(53) Hudhomme, P. An Overview of Molecular Acceptors for Organic Solar Cells. *EPJ Photovoltaics* **2013**, *4*, 40401.

(54) Wang, C.; Ouyang, L.; Xu, X.; Braun, S.; Liu, X.; Fahlman, M. Relationship of Ionization Potential and Oxidation Potential of Organic Semiconductor Films Used in Photovoltaics. *Solar RRL* **2018**, *2* (9), 1800122.

(55) Ito, E.; Oji, H.; Ishii, H.; Oichi, K.; Ouchi, Y.; Seki, K. Interfacial Electronic Structure of Long-Chain Alkane/Metal Systems Studied by UV-Photoelectron and Metastable Atom Electron Spectroscopies. *Chemical Physics Letters* **1998**, *287* (1-2), 137–142.

(56) Braun, S.; Salaneck, W. R.; Fahlman, M. Energy-level Alignment At Organic/Metal and Organic/Organic Interfaces. *Advanced Materials* **2009**, *21* (14-15), 1450–1472.

(57) Lee, S.; Lee, J.-H.; Kim, K. H.; Yoo, S.-J.; Kim, T. G.; Kim, J. W.; Kim, J.-J. Determination of the Interface Energy Level Alignment of a Doped Organic Hetero-Junction Using Capacitance–Voltage Measurements. *Organic Electronics* **2012**, *13* (11), 2346–2351.

(58) Ma, H.; Yip, H. L.; Huang, F.; Jen, A. K. Y. Interface Engineering for Organic Electronics. *Advanced Functional Materials* **2010**, *20* (9), 1371–1388.

(59) Verhoeven, J. Glossary of Terms Used in Photochemistry (IUPAC Recommendations 1996). *Pure and Applied Chemistry* **1996**, *68* (12), 2223–2286.

(60) Goldsmid, J. *The Physics of Thermoelectric Energy Conversion*; Morgan and Claypool Publishers, 2017.

(61) Ozawa, R.; Yamane, A.; Morikawa, K.; Ohwada, M.; Suzuki, K.; Fukutani, H. Angle-Resolved UPS Study of the Oxygen-Induced 2× 1 Surface of Cu (110). *Surface Science* **1996**, *346* (1-3), 237–242.

(62) Hayashi, N.; Ishii, H.; Ouchi, Y.; Seki, K. Examination of Band Bending at C60/Metal Interfaces by the Kelvin Probe Method. *Synthetic Metals* **2003**, *137* (1–3), 1377–1378.

(63) Benramache, S.; Belahssen, O.; Temam, H. B. Effect of Band Gap Energy on the Electrical Conductivity in Doped ZnO Thin Film. *Journal of Semiconductors* **2014**, *35* (7), 073001.

(64) Augusto, A.; Herasimenka, S. Y.; King, R. R.; Bowden, S. G.; Honsberg, C. Analysis of the Recombination Mechanisms of a Silicon Solar Cell With Low Bandgap-Voltage Offset. *Journal of Applied Physics* **2017**, *121* (20), 205704.

(65) Cho, C.-P.; Chu, C.-C.; Chen, W.-T.; Huang, T.-C.; Tao, Y.-T. Molecular Modification on Dye-Sensitized Solar Cells by Phosphonate Self-Assembled Monolayers. *J. Mater. Chem.* **2012**, *22* (7), 2915–2921.

(66) Kahn, A.; Zhao, W.; Gao, W.; Vázquez, H.; Flores, F. Doping-Induced Realignment of Molecular Levels at Organic–Organic Heterojunctions. *Chemical Physics* **2006**, *325* (1), 129–137.

(67) Park, S.; Jeong, J.; Hyun, G.; Kim, M.; Lee, H.; Yi, Y. The Origin of High PCE in PTB7 Based Photovoltaics: Proper Charge Neutrality Level and Free Energy of Charge Separation at PTB7/$PC_{71}BM$ Interface. *Scientific Reports* **2016**, *6* (1), 1–11.

(68) Hu, Z.; Zhong, Z.; Zhang, K.; Hu, Z.; Song, C.; Huang, F.; Peng, J.; Wang, J.; Cao, Y. Dipole Formation at Organic/Metal Interfaces with Pre-Deposited and Post-Deposited Metal. *NPG Asia Materials* **2017**, *9* (5), e379–e379.

(69) Chen, Y.; Liu, X.; Braun, S.; Wang, Y.; Fahlman, M. Image-Force Effects on Energy Level Alignment at Electron Transport Material/Cathode Interfaces. *Journal of Materials Chemistry C* **2020**, *8* (1), 173–179.

(70) Sharma, A.; Berger, R.; Lewis, D. A.; Andersson, G. G. Invisible High Workfunction Materials on Heterogeneous Surfaces. *Applied Surface Science* **2015**, *327*, 22–26.

(71) Berlich, A.; Liu, Y.-C.; Morgner, H. Growth of Nickel Nanoparticles on NiO/Ni (0 0 1): Evidence of Adsorbed Oxygen on Metal Particles by Metastable Induced Electron Spectroscopy (MIES). *Surface Science* **2008**, *602* (24), 3737–3744.

(72) Sachs-Quintana, I.; Heumüller, T.; Mateker, W. R.; Orozco, D. E.; Cheacharoen, R.; Sweetnam, S.; Brabec, C. J.; McGehee, M. D. Electron Barrier Formation at the Organic-Back Contact Interface is the First Step in Thermal Degradation of Polymer Solar Cells. *Advanced Functional Materials* **2014**, *24* (25), 3978–3985.

(73) Bao, Q.; Liu, X.; Braun, S.; Yang, J.; Li, Y.; Tang, J.; Duan, C.; Fahlman, M. The Effect of Oxygen Uptake on Charge Injection Barriers in Conjugated Polymer Films. *ACS Applied Materials & Interfaces* **2018**, *10* (7), 6491–6497.

(74) Cieplechowicz, E.; Munir, R.; Anderson, M. A.; Ratcliff, E. L.; Welch, G. C. Zinc Oxide-Perylene Diimide Hybrid Electron Transport Layers for Air-Processed Inverted Organic Photovoltaic Devices. *ACS Applied Materials & Interfaces* **2021**, *13* (41), 49096–49103.

(75) Jørgensen, M.; Norrman, K.; Gevorgyan, S. A.; Tromholt, T.; Andreasen, B.; Krebs, F. C. Stability of Polymer Solar Cells. *Advanced Materials* **2012**, *24* (5), 580–612.

(76) Lin, Y.; Wang, J. Z. G.; Zhang, H.; Bai Y.; Li, D.; Zhu, X.; Zhan. An Electron Acceptor Challenging Fullerenes for Efficient Polymer Solar Cells. *Adv. Mater.* **2015**, *27*, 1170.

(77) Zhao, W.; Qian, D.; Zhang, S.; Li, S.; Inganäs, O.; Gao, F.; Hou, J. Fullerene-free Polymer Solar Cells With Over 11% Efficiency And Excellent Thermal Stability. *Advanced Materials* **2016**, *28* (23), 4734–4739.

(78) Lattante, S. Electron and Hole Transport Layers: Their Use in Inverted Bulk Heterojunction Polymer Solar Cells. *Electronics* **2014**, *3* (1), 132–164.

(79) Soultati, A.; Verykios, A.; Panagiotakis, S.; Armadorou, K.-K.; Haider, M. I.; Kaltzoglou, A.; Drivas, C.; Fakharuddin, A.; Bao, X.; Yang, C. Suppressing the Photocatalytic Activity of Zinc Oxide Electron-Transport Layer in Nonfullerene Organic Solar Cells with a Pyrene-Bodipy Interlayer. *ACS Applied Materials & Interfaces* **2020**, *12* (19), 21961–21973.

(80) Waldauf, C.; Morana, M.; Denk, P.; Schilinsky, P.; Coakley, K.; Choulis, S.; Brabec, C. Highly Efficient Inverted Organic Photovoltaics Using Solution Based Titanium Oxide as Electron Selective Contact. *Applied Physics Letters* **2006**, *89* (23), 233517.

(81) Xin, Y.; Wang, Z.; Xu, L.; Xu, X.; Liu, Y.; Zhang, F. UV-Ozone Treatment on Cs2CO3 Interfacial Layer for the Improvement of Inverted Polymer Solar Cells. *Journal of Nanomaterials* **2013**, *2013*.

(82) Kondakov, D. Voltammetric Study of Bphen Electron-Transport Layer in Contact With Li F/ Al Cathode in Organic Light-Emitting Diodes. *Journal of Applied Physics* **2006**, *99* (2), 024901.

(83) Yang, Z.; Zhang, T.; Li, J.; Xue, W.; Han, C.; Cheng, Y.; Qian, L.; Cao, W.; Yang, Y.; Chen, S. Multiple Electron Transporting Layers and Their Excellent Properties Based on Organic Solar Cell. *Scientific Reports* **2017**, *7* (1), 1–9.

(84) Chen, Y.; Chu, S.; Li, R.; Qin, Y.; Xu, Y.; Zhang, X.; Wang, J.; Liu, M.; Lai, W.-Y.; Huang, W. Highly Efficient Inverted Organic Light-Emitting Devices Adopting Solution-Processed Double Electron-Injection Layers. *Organic Electronics* **2019**, *66*, 1–6.

(85) Pandi, K.; Naveen Kumar, T. R.; Lakhera, S. K.; Neppolian, B. Simultaneous Passivation of Surface Vacancies And Enhancement in Charge Transfer Property of ZnO Electron Transport Layer for Inverted Organic Solar Cells. *Energy Technology* **2020**, *8* (11), 2000481.

(86) Salim, M. B.; Nekovei, R.; Jeyakumar, R. Organic Tandem Solar Cells With 18.6% Efficiency. *Solar Energy* **2020**, *198*, 160–166.

(87) Liu, L.; Kan, Y.; Gao, K.; Wang, J.; Zhao, M.; Chen, H.; Zhao, C.; Jiu, T.; Jen, A. K. Y.; Li, Y. Graphdiyne Derivative as Multifunctional Solid Additive in Binary Organic Solar Cells with 17.3% Efficiency and High Reproductivity. *Advanced Materials* **2020**, *32* (11), 1907604.

(88) Cai, Y.; Chang, L.; You, L.; Fan, B.; Liu, H.; Sun, Y. Novel Nonconjugated Polymer as Cathode Buffer Layer for Efficient Organic Solar Cells. *ACS Applied Materials & Interfaces* **2018**, *10* (28), 24082–24089.

(89) Jeong, M.; Moon, D. K.; Kim, H. S.; Kim, J. H. Small-Molecule Electrolytes with Different Ionic Functionalities as a Cathode Buffer Layer for Polymer Solar Cells. *Journal of Materials Chemistry C* **2020**, *8* (43), 15183–15188.

(90) Sharma, A.; Kroon, R.; Lewis, D. A.; Andersson, G. G.; Andersson, M. R. Poly (4-vinylpyridine): A New Interface Layer for Organic Solar Cells. *ACS Applied Materials & Interfaces* **2017**, *9* (12), 10929–10936.

(91) Hu, L.; Liu, Y.; Mao, L.; Xiong, S.; Sun, L.; Zhao, N.; Qin, F.; Jiang, Y.; Zhou, Y. Chemical Reaction Between an ITIC Electron Acceptor and an Amine-Containing Interfacial Layer in Non-Fullerene Solar Cells. *Journal of Materials Chemistry A* **2018**, *6* (5), 2273–2278.

(92) Huang, F.; Wu, H.; Wang, D.; Yang, W.; Cao, Y. Novel Electroluminescent Conjugated Polyelectrolytes Based on Polyfluorene. *Chemistry of Materials* **2004**, *16* (4), 708–716.

(93) Wu, Z.; Sun, C.; Dong, S.; Jiang, X.-F.; Wu, S.; Wu, H.; Yip, H.-L.; Huang, F.; Cao, Y. n-Type Water/Alcohol-Soluble Naphthalene Diimide-Based Conjugated Polymers for High-Performance Polymer Solar Cells. *Journal of the American Chemical Society* **2016**, *138* (6), 2004–2013.

(94) Nian, L.; Zhang, W.; Zhu, N.; Liu, L.; Xie, Z.; Wu, H.; Würthner, F.; Ma, Y. Photoconductive Cathode Interlayer for Highly Efficient Inverted Polymer Solar Cells. *Journal of the American Chemical Society* **2015**, *137* (22), 6995–6998.

(95) Zhang, Z.-G.; Qi, B.; Jin, Z.; Chi, D.; Qi, Z.; Li, Y.; Wang, J. Perylene Diimides: A Thickness-Insensitive Cathode Interlayer for High Performance Polymer Solar Cells. *Energy & Environmental Science* **2014**, *7* (6), 1966–1973.

(96) Zhao, K.; Ye, L.; Zhao, W.; Zhang, S.; Yao, H.; Xu, B.; Sun, M.; Hou, J. Enhanced Efficiency of Polymer Photovoltaic Cells via the Incorporation of a Water-Soluble Naphthalene Diimide Derivative as a Cathode Interlayer. *Journal of Materials Chemistry C* **2015**, *3* (37), 9565–9571.

(97) Yao, J.; Qiu, B.; Zhang, Z.-G.; Xue, L.; Wang, R.; Zhang, C.; Chen, S.; Zhou, Q.; Sun, C.; Yang, C. Cathode Engineering with Perylene-Diimide Interlayer Enabling Over 17% Efficiency Single-Junction Organic Solar Cells. *Nature Communications* **2020**, *11* (1), 1–10.

(98) Xu, B.; Zheng, Z.; Zhao, K.; Hou, J. A Bifunctional Interlayer Material for Modifying Both the Anode and Cathode in Highly Efficient Polymer Solar Cells. *Advanced Materials* **2016**, *28* (3), 434–439.

(99) Kang, Q.; Ye, L.; Xu, B.; An, C.; Stuard, S. J.; Zhang, S.; Yao, H.; Ade, H.; Hou, J. A Printable Organic Cathode Interlayer Enables Over 13% Efficiency For 1-cm2 Organic Solar Cells. *Joule* **2019**, *3* (1), 227–239.

(100) 1Ibn-Mohammed, T.; Koh, S.; Reaney, I.; Acquaye, A.; Schileo, G.; Mustapha, K.; Greenough, R. Perovskite Solar Cells: An Integrated Hybrid Lifecycle Assessment and Review in Comparison With Other Photovoltaic Technologies. *Renewable and Sustainable Energy Reviews* **2017**, *80*, 1321–1344.

(101) Eames, C.; Frost, J. M.; Barnes, P. R.; O'Regan, B. C.; Walsh, A.; Islam, M. S. Ionic Transport in Hybrid Lead Iodide Perovskite Solar Cells. *Nature Communications* **2015**, *6* (1), 1–8.

(102) Santomauro, F. G.; Grilj, J.; Mewes, L.; Nedelcu, G.; Yakunin, S.; Rossi, T.; Capano, G.; Al Haddad, A.; Budarz, J.; Kinschel, D. Localized Holes and Delocalized Electrons in Photoexcited Inorganic Perovskites: Watching Each Atomic Actor by Picosecond X-Ray Absorption Spectroscopy. *Structural Dynamics* **2017**, *4* (4), 044002.

(103) Pang, S.; Hu, H.; Zhang, J.; Lv, S.; Yu, Y.; Wei, F.; Qin, T.; Xu, H.; Liu, Z.; Cui, G. NH2CH=NH2PbI3: An Alternative Organolead Iodide Perovskite Sensitizer for Mesoscopic Solar Cells. *Chemistry of Materials* **2014**, *26* (3), 1485–1491.

(104) Im, J.-H.; Chung, J.; Kim, S.-J.; Park, N.-G. Synthesis, Structure, and Photovoltaic Property of a Nanocrystalline 2H Perovskite-Type Novel Sensitizer (CH3CH2NH3) PbI3. *Nanoscale Research Letters* **2012**, *7* (1), 1–7.

(105) Liu, F.; Zhang, Y.; Ding, C.; Kobayashi, S.; Izuishi, T.; Nakazawa, N.; Toyoda, T.; Ohta, T.; Hayase, S.; Minemoto, T. Highly Luminescent Phase-Stable CsPbI3 Perovskite Quantum Dots Achieving Near 100% Absolute Photoluminescence Quantum Yield. *ACS Nano* **2017**, *11* (10), 10373–10383.

(106) Park, N.-G. Perovskite Solar Cells: An Emerging Photovoltaic Technology. *Materials Today* **2015**, *18* (2), 65–72.

(107) Ng, A.; Ren, Z.; Hu, H.; Fong, P. W.; Shen, Q.; Cheung, S. H.; Qin, P.; Lee, J. W.; Djurišić, A. B.; So, S. K. A Cryogenic Process for Antisolvent-Free High-Performance Perovskite Solar Cells. *Advanced Materials* **2018**, *30* (44), 1804402.

(108) Chen, Z.; Dong, Q.; Liu, Y.; Bao, C.; Fang, Y.; Lin, Y.; Tang, S.; Wang, Q.; Xiao, X.; Bai, Y. Thin Single Crystal Perovskite Solar Cells to Harvest Below-Bandgap Light Absorption. *Nature Communications* **2017**, *8* (1), 1–7.

(109) Kulkarni, S. A.; Baikie, T.; Boix, P. P.; Yantara, N.; Mathews, N.; Mhaisalkar, S. Band-Gap Tuning of Lead Halide Perovskites Using a Sequential Deposition Process. *Journal of Materials Chemistry A* **2014**, *2* (24), 9221–9225.

(110) Eperon, G. E.; Stranks, S. D.; Menelaou, C.; Johnston, M. B.; Herz, L. M.; Snaith, H. J. Formamidinium Lead Trihalide: A Broadly Tunable Perovskite for Efficient Planar Heterojunction Solar Cells. *Energy & Environmental Science* **2014**, *7* (3), 982–988.

(111) Dong, Q.; Fang, Y.; Shao, Y.; Mulligan, P.; Qiu, J.; Cao, L.; Huang, J. Electron-Hole Diffusion Lengths > 175 μm in Solution-Grown CH3NH3PbI3 Single Crystals. *Science* **2015**, *347* (6225), 967–970.

(112) Stranks, S. D.; Eperon, G. E.; Grancini, G.; Menelaou, C.; Alcocer, M. J.; Leijtens, T.; Herz, L. M.; Petrozza, A.; Snaith, H. J. Electron-Hole Diffusion Lengths Exceeding 1 Micrometer in an Organometal Trihalide Perovskite Absorber. *Science* **2013**, *342* (6156), 341–344.

(113) D'innocenzo, V.; Grancini, G.; Alcocer, M. J.; Kandada, A. R. S.; Stranks, S. D.; Lee, M. M.; Lanzani, G.; Snaith, H. J.; Petrozza, A. Excitons Versus Free Charges in Organo-Lead Tri-Halide Perovskites. *Nature Communications* **2014**, *5* (1), 1–6.

(114) Wehrenfennig, C.; Eperon, G. E.; Johnston, M. B.; Snaith, H. J.; Herz, L. M. High Charge Carrier Mobilities and Lifetimes in Organolead Trihalide Perovskites. *Advanced Materials* **2014**, *26* (10), 1584–1589.

(115) Seitkhan, A.; Neophytou, M.; Hallani, R. K.; Troughton, J.; Gasparini, N.; Faber, H.; Abou-Hamad, E.; Hedhili, M. N.; Harrison, G. T.; Baran, D. A Multilayered Electron Extracting System for Efficient Perovskite Solar Cells. *Advanced Functional Materials* **2020**, *30* (43), 2004273.

(116) Kojima, A.; Teshima, K.; Shirai, Y.; Miyasaka, T. Organometal Halide Perovskites as Visible-Light Sensitizers for Photovoltaic Cells. *Journal of the American Chemical Society* **2009**, *131* (17), 6050–6051.

(117) Im, J.-H.; Lee, C.-R.; Lee, J.-W.; Park, S.-W.; Park, N.-G. 6.5% Efficient Perovskite Quantum-Dot-Sensitized Solar Cell. *Nanoscale* **2011**, *3* (10), 4088–4093.

(118) Lee, M. M.; Teuscher, J.; Miyasaka, T.; Murakami, T. N.; Snaith, H. J. Efficient Hybrid Solar Cells Based on Meso-Superstructured Organometal Halide Perovskites. *Science* **2012**, *338* (6107), 643–647.

(119) Burschka, J.; Dualeh, A.; Kessler, F.; Baranoff, E.; Cevey-Ha, N.-L.; Yi, C.; Nazeeruddin, M. K.; Grätzel, M. Tris (2-(1 H-pyrazol-1-yl) pyridine) Cobalt (III) as p-Type Dopant for Organic Semiconductors and its Application in Highly Efficient Solid-State Dye-Sensitized Solar Cells. *Journal of the American Chemical Society* **2011**, *133* (45), 18042–18045.

(120) Ball, J. M.; Lee, M. M.; Hey, A.; Snaith, H. J. Low-Temperature Processed Meso-Superstructured to Thin-Film Perovskite Solar Cells. *Energy & Environmental Science* **2013**, *6* (6), 1739–1743.

(121) Eperon, G. E.; Burlakov, V. M.; Docampo, P.; Goriely, A.; Snaith, H. J. Morphological Control for High Performance, Solution-Processed Planar Heterojunction Perovskite Solar Cells. *Advanced Functional Materials* **2014**, *24* (1), 151–157.

(122) Liu, M.; Johnston, M. B.; Snaith, H. J. Efficient Planar Heterojunction Perovskite Solar Cells by Vapour Deposition. *Nature* **2013**, *501* (7467), 395–398.

(123) Jeon, N. J.; Noh, J. H.; Kim, Y. C.; Yang, W. S.; Ryu, S.; Seok, S. I. Solvent Engineering for High-Performance Inorganic–Organic Hybrid Perovskite Solar Cells. *Nature Materials* **2014**, *13* (9), 897–903.

(124) Yang, W. S.; Noh, J. H.; Jeon, N. J.; Kim, Y. C.; Ryu, S.; Seo, J.; Seok, S. I. High-Performance Photovoltaic Perovskite Layers Fabricated Through Intramolecular Exchange. *Science* **2015**, *348* (6240), 1234–1237.

(125) Li, W.; Fan, J.; Li, J.; Mai, Y.; Wang, L. Controllable Grain Morphology of Perovskite Absorber Film by Molecular Self-Assembly Toward Efficient Solar Cell Exceeding 17%. *Journal of the American Chemical Society* **2015**, *137* (32), 10399–10405.

(126) Burschka, J.; Pellet, N.; Moon, S.-J.; Humphry-Baker, R.; Gao, P.; Nazeeruddin, M. K.; Grätzel, M. Sequential Deposition as a Route to High-Performance Perovskite-Sensitized Solar Cells. *Nature* **2013**, *499* (7458), 316–319.

(127) Deng, Y.; Dong, Q.; Bi, C.; Yuan, Y.; Huang, J. Air-Stable, Efficient Mixed-Cation Perovskite Solar Cells with Cu Electrode by Scalable Fabrication of Active Layer. *Advanced Energy Materials* **2016**, *6* (11), 1600372.

(128) Bi, D.; Yi, C.; Luo, J.; Décoppet, J.-D.; Zhang, F.; Zakeeruddin, S. M.; Li, X.; Hagfeldt, A.; Grätzel, M. Polymer-Templated Nucleation and Crystal Growth of Perovskite Films for Solar Cells with Efficiency Greater Than 21%. *Nature Energy* **2016**, *1* (10), 1–5.

(129) Al-Ashouri, A.; Köhnen, E.; Li, B.; Magomedov, A.; Hempel, H.; Caprioglio, P.; Márquez, J. A.; Morales Vilches, A. B.; Kasparavicius, E.; Smith, J. A. Monolithic Perovskite/Silicon Tandem Solar Cell With > 29% Efficiency by Enhanced Hole Extraction. *Science* **2020**, *370* (6522), 1300–1309.

(130) Jeng, J. Y.; Chiang, Y. F.; Lee, M. H.; Peng, S. R.; Guo, T. F.; Chen, P.; Wen, T. C. CH3NH3PbI3 Perovskite/Fullerene Planar-Heterojunction Hybrid Solar Cells. *Advanced Materials* **2013**, *25* (27), 3727–3732.

(131) Hu, L.; Sun, K.; Wang, M.; Chen, W.; Yang, B.; Fu, J.; Xiong, Z.; Li, X.; Tang, X.; Zang, Z. Inverted Planar Perovskite Solar Cells With a High Fill Factor and Negligible Hysteresis by the Dual Effect of NaCl-Doped PEDOT: PSS. *ACS Applied Materials & Interfaces* **2017**, *9* (50), 43902–43909.

(132) Du, Y.; Cai, H.; Wu, Y.; Xing, Z.; Li, Z.; Xu, J.; Huang, L.; Ni, J.; Li, J.; Zhang, J. Enhanced Planar Perovskite Solar Cells With Efficiency Exceeding 16% via Reducing the Oxygen Vacancy Defect State in Titanium Oxide Electrode. *Physical Chemistry Chemical Physics* **2017**, *19* (21), 13679–13686.

(133) Sherkar, T. S.; Momblona, C.; Gil-Escrig, L.; Bolink, H. J.; Koster, L. J. A. Improving Perovskite Solar Cells: Insights From a Validated Device Model. *Advanced Energy Materials* **2017**, *7* (13), 1602432.

(134) Yokoyama, T.; Nishitani, Y.; Miyamoto, Y.; Kusumoto, S.; Uchida, R.; Matsui, T.; Kawano, K.; Sekiguchi, T.; Kaneko, Y. Improving the Open-Circuit Voltage of Sn-Based Perovskite Solar Cells by Band Alignment at the Electron Transport Layer/Perovskite Layer Interface. *ACS Applied Materials & Interfaces* **2020**, *12* (24), 27131–27139.

(135) Wang, T.; Xie, M.; Abbasi, S.; Cheng, Z.; Liu, H.; Shen, W. High Efficiency Perovskite Solar Cells with Tailorable Surface Wettability by Surfactant. *Journal of Power Sources* **2020**, *448*, 227584.

(136) Ali, F.; Roldán-Carmona, C.; Sohail, M.; Nazeeruddin, M. K. Applications of Self-Assembled Monolayers for Perovskite Solar Cells Interface Engineering to Address Efficiency and Stability. *Advanced Energy Materials* **2020**, *10* (48), 2002989.

(137) Singh, N.; Tao, Y. T. Effect of Surface Modification of Nickel Oxide Hole-Transport Layer via Self-Assembled Monolayers In Perovskite Solar Cells. *Nano Select* **2021**, *2* (12), 2390–2399.

(138) Arkan, E.; Unal, M.; Yalcin, E.; Arkan, M. Z. Y.; Yurtdas, S.; Can, M.; Tozlu, C.; Demic, S. Influence of End Groups Variation of Self Assembled Monolayers on Performance of Planar Perovskite Solar Cells by Interface Regulation. *Materials Science in Semiconductor Processing* **2021**, *123*, 105514.

(139) Shi, Y.; Zhang, H.; Tong, X.; Hou, X.; Li, F.; Du, Y.; Wang, S.; Zhang, Q.; Liu, P.; Zhao, X. Interfacial Engineering via Self-Assembled Thiol Silane for High Efficiency and Stability Perovskite Solar Cells. *Solar RRL* **2021**, *5* (7), 2100128.

(140) Lin, Y.; Firdaus, Y.; Isikgor, F. H.; Nugraha, M. I.; Yengel, E.; Harrison, G. T.; Hallani, R.; El-Labban, A.; Faber, H.; Ma, C. Self-Assembled Monolayer Enables Hole Transport Layer-Free Organic Solar Cells With 18% Efficiency and Improved Operational Stability. *ACS Energy Letters* **2020**, *5* (9), 2935–2944.

(141) Al-Ashouri, A.; Magomedov, A.; Roß, M.; Jošt, M.; Talaikis, M.; Chistiakova, G.; Bertram, T.; Márquez, J. A.; Köhnen, E.; Kasparavičius, E. Conformal Monolayer Contacts with Lossless Interfaces for Perovskite Single Junction and Monolithic Tandem Solar Cells. *Energy & Environmental Science* **2019**, *12* (11), 3356–3369.

(142) Wang, J.; Datta, K.; Weijtens, C. H.; Wienk, M. M.; Janssen, R. A. Insights into Fullerene Passivation of SnO2 Electron Transport Layers in Perovskite Solar Cells. *Advanced Functional Materials* **2019**, *29* (46), 1905883.

(143) Hou, Y.; Du, X.; Scheiner, S.; McMeekin, D. P.; Wang, Z.; Li, N.; Killian, M. S.; Chen, H.; Richter, M.; Levchuk, I. A Generic Interface to Reduce the Efficiency-Stability-Cost Gap of Perovskite Solar Cells. *Science* **2017**, *358* (6367), 1192–1197.

(144) Zhu, T.; Su, J.; Labat, F.; Ciofini, I.; Pauporte, T. Interfacial Engineering through Chloride-Functionalized Self-Assembled Monolayers for High-Performance Perovskite Solar Cells. *ACS Applied Materials & Interfaces* **2019**, *12* (1), 744–752.

(145) Hou, M.; Zhang, H.; Wang, Z.; Xia, Y.; Chen, Y.; Huang, W. Enhancing Efficiency and Stability of Perovskite Solar Cells via a Self-Assembled Dopamine Interfacial Layer. *ACS Applied Materials & Interfaces* **2018**, *10* (36), 30607–30613.

(146) Han, J.; Kwon, H.; Kim, E.; Kim, D.-W.; Son, H. J.; Kim, D. H. Interfacial Engineering of a ZnO Electron Transporting Layer Using Self-Assembled Monolayers for High Performance and Stable Perovskite Solar Cells. *Journal of Materials Chemistry A* **2020**, *8* (4), 2105–2113.

(147) Galkowski, K.; Mitioglu, A.; Miyata, A.; Plochocka, P.; Portugall, O.; Eperon, G. E.; Wang, J. T.-W.; Stergiopoulos, T.; Stranks, S. D.; Snaith, H. J. Determination of the Exciton Binding Energy and Effective Masses for Methylammonium and Formamidinium Lead Tri-Halide Perovskite Semiconductors. *Energy & Environmental Science* **2016**, *9* (3), 962–970.

(148) Cook, S.; Katoh, R.; Furube, A. Ultrafast Studies of Charge Generation in PCBM: P3HT Blend Films Following Excitation of the Fullerene PCBM. *The Journal of Physical Chemistry C* **2009**, *113* (6), 2547–2552.

(149) De Wolf, S.; Holovsky, J.; Moon, S.-J.; Loper, P.; Niesen, B.; Ledinsky, M.; Haug, F.-J.; Yum, J.-H.; Ballif, C. Organometallic Halide Perovskites: Sharp Optical Absorption Edge and its Relation to Photovoltaic Performance. *The Journal of Physical Chemistry Letters* **2014**, *5* (6), 1035–1039.

(150) Foster, S.; Deledalle, F.; Mitani, A.; Kimura, T.; Kim, K. B.; Okachi, T.; Kirchartz, T.; Oguma, J.; Miyake, K.; Durrant, J. R. Electron Collection as a Limit to Polymer: PCBM Solar Cell Efficiency: Effect of Blend Microstructure on Carrier Mobility and Device Performance in PTB7: PCBM. *Advanced Energy Materials* **2014**, *4* (14), 1400311.

(151) Juarez-Perez, E. J.; Sanchez, R. S.; Badia, L.; Garcia-Belmonte, G.; Kang, Y. S.; Mora-Sero, I.; Bisquert, J. Photoinduced Giant Dielectric Constant in Lead Halide Perovskite Solar Cells. *The Journal of Physical Chemistry Letters* **2014**, *5* (13), 2390–2394.

(152) Gonzalez-Pedro, V.; Juarez-Perez, E. J.; Arsyad, W.-S.; Barea, E. M.; Fabregat-Santiago, F.; Mora-Sero, I.; Bisquert, J. General Working Principles of CH3NH3PbX3 Perovskite Solar Cells. *Nano Letters* **2014**, 14 (2), 888–893.

(153) Hussain, I.; Tran, H. P.; Jaksik, J.; Moore, J.; Islam, N.; & Uddin, M. J. Functional Materials, Device Architecture, and Flexibility of Perovskite Solar Cell. *Emergent Materials* **2018**, *1* (3), 133–154.

Chapter 2: Research Aim and Contribution

The valance electron structure of interfaces significantly affects the efficiency of SCs; thus, these interfaces were studied in this thesis on two types of SCs: OPVs and PSCs. The main goal of the thesis is to examine the chemical and electronic properties of the interfacial layers and their significance to the performance of the OPVs and PSCs. The organic interfaces in OPVs and the SAM layer in PSCs have been previously studied. The chemical and electronic properties for these interfaces, however, have yet to be thoroughly studied. Various active materials have been chosen in this thesis that can provide a comprehensive understanding of the OPV and PSC devices' performance. The presented studies consisted of a systematic analysis of the electronic structure of the interfaces using photoelectron spectroscopy (PES) and ion scattering spectroscopy.

In terms of the OPV devices, a new potential of organic CIL layers was used with a range of active materials as replacement of inorganic interface layer due to its advantages; for example, they are flexible and easily fabricated, and can potentially be cheaper to design than their inorganic interfaces. These systems consisted of a buried layer of organic CIL in an inverted structure. Then, different thin layers of active materials will be deposited on top by using a spin coater to enable the energy levels at the interface, which will be studied. Understanding the energy level between the interface layer and active layer is crucial to improving device performance. Thus, adding an interface layer between the active layer and the electrode will help to align the energy levels between the individual layers. This could be achieved by determining the electronic structures of the interface layer integrated into the overall structure and to what extent that can influence the performance of the PC cell. The dipole formation at the interface and its effect on charge mobility was also investigated. Further, the valence electron spectra, obtained via UPS, was studied in detail by applying a deconvolution algorithm. The study can help to find

evidence of energy shifts in the active layer, which can provide a proof for the formation of dipole at the interface.

In this thesis, the structure of the energy levels at the interfaces is investigated to describe the probable mechanism of CT. Additionally, the degree of intermixing layers at the interface was investigated, which plays a critical role in identifying the interface between two layers. This was achieved by utilising the depth profiling method—neutral impact collision ion scattering spectroscopy (NICISS). The distribution of the components of active layers also influences the SC performance; thus, further studies were conducted in this thesis that studied the modification of the BHJ layer, with a focus on the outermost layer and subsurface area of the film.

Considering the PSCs, the most challenging issue in the PSCs faced in recent years was the defects and their detrimental effect on the absorption of energy and on storage devices overall. The concentration of the defect in polycrystalline films mainly comes from surface defects. Numerous studies confirmed the increase in the number of surface defects (trap), resulting in charge recombination, which hampers the development of PSCs. In this thesis, the interest is not on the characterisation of the layers in one particular PSC but is geared towards understanding the defect level at the HTL/perovskite interface and how that could affect the energy level structure.

The main contributions presented in this thesis regarding OPVs and PSC are described below.

2.1 Organic Cathode Interfaces in Invert OPVs

a) Investigation of the electronic properties and the dipole formation in organic CILs and active materials. CILs can function to block the holes from the donor layer and could form a dipole at the interface layers, subsequently influencing the CT over the interface. Two new organic CILs were investigated with active materials to study their viability in

blocking the hole and transferring the electrons to the respective electrode. In Chapter 4, the P(NDI3N-T-Br) organic cathode interface was investigated in combination with different thicknesses of a conventional active layer of (TQ1: N2200). The interfaces formed by TQ1 and N2200 with P(NDI3N-T-Br) were investigated separately to investigate the fundamental properties and the CT over the interface of the (TQ1: N2200)/P(NDI3N-T-Br) system, as shown in Figure 2-1. The degree of intermixing at the interface was also examined.

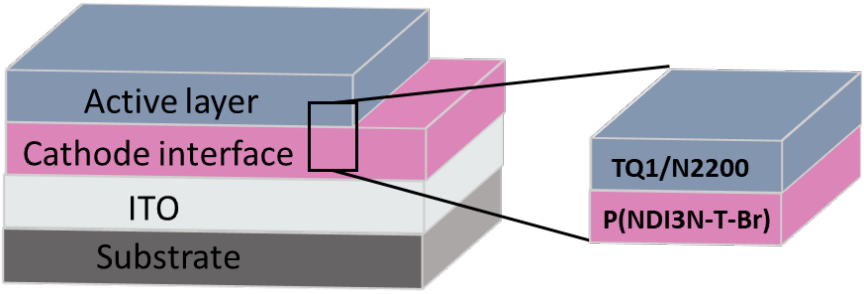

Figure 2-1. Schematic of an inverted device structure of OPV using P(NDI3N-T-Br) as organic CIL with active layers of TQ1 and N2200.

Another organic CIL was used with other active layers to further investigate the impact on CT and device performance. In Chapter 5, the organic CIL P(NDI3N-F8-Br) was studied with the non-fullerene system (NF) of PTB7-Th: ITIC on P(NDI3N-F8-Br), as shown in Figure 2-2. The chemical and electronic properties of different thicknesses of active layers on P(NDI3N-F8-Br) interfaces were studied to understand their effect on the CT.

The possible differences in energy level distribution between the organic and inorganic CIL are investigated in Chapter 6 as a control device.

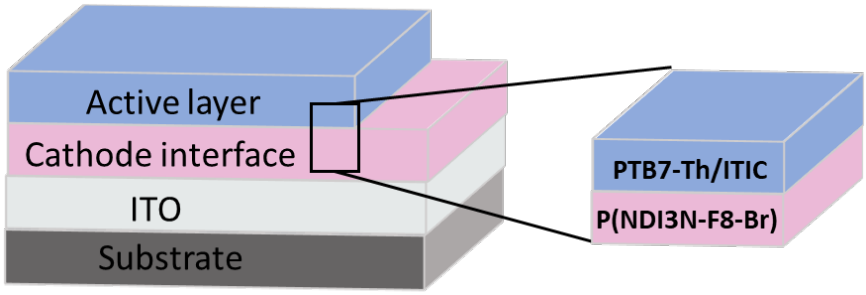

Figure 2-2. Schematic of an inverted device structure of OPV using P(NDI3N-F8-Br) as organic CIL with active layers of PTB7-Th and ITIC.

b) Investigation of the energy level of inorganic CIL and active materials. To achieve a better understanding of energy level, the interface of the NF system of (PTB7-Th: ITIC) was studied on the common inorganic cathode interface material ZnO, as shown in Figure 2-3. The energy level of the NF system of PTB7-Th: ITIC with ZnO has not previously been investigated. Thus, Chapter 6 reports the investigation of the energy level alignment of ZnO with different layers of PTB7-Th and ITIC interfaces on top. The positions of the electronic structures of ZnO were determined and integrated into the overall structure of the active layers. This acted as a control device and was then compared with another organic interface layer presented in Chapter 5.

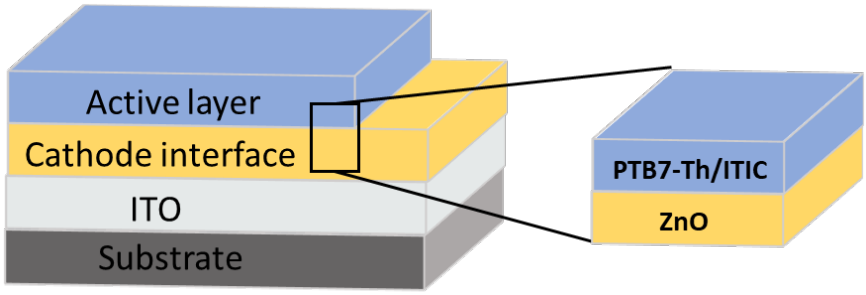

Figure 2-3. Schematic of an inverted device structure of OPV using ZnO as inorganic CIL with active layers of PTB7-Th and ITIC.

c) The influence of the additive on the distribution of the components in the BHJ. The structure of the energy levels across the interface is not the only indicator of overall device performance. The distribution of different molecular species throughout the film also affects the interface properties to a certain degree. However, investigation with a

measured spectrum of the components' distribution at the interface's surface has not previously been reported. Chapter 7 presented an understanding of the addition's effect on p-anisaldehyde (AA) additive on the BHJ components of the PTB7-TH: ITIC at the outermost and subsurface area (see Figure 2-4). Information on molecular distribution is crucial, as it provides information on how to modify the structure of the BHJ layer, which enables us to optimise both electrodes/polymer interfaces and improve the efficiency of the polymer-based OPVs. In the inverted structure, the electrode with the larger WF requires a significant amount of the electron donors. With the energy levels of the donor (PTB7-Th) and MoO_x being close, the enrichment of the interface layer with donor species is advantageous for enabling the CT to MoO_x. NICISS depth profiling technique was used to determine the concentration depth profile at the interface, with a depth resolution of a few angstroms. Additionally, we investigated the contribution of the additive (AA) to the morphology and, more importantly, to the elemental composition at the surface.

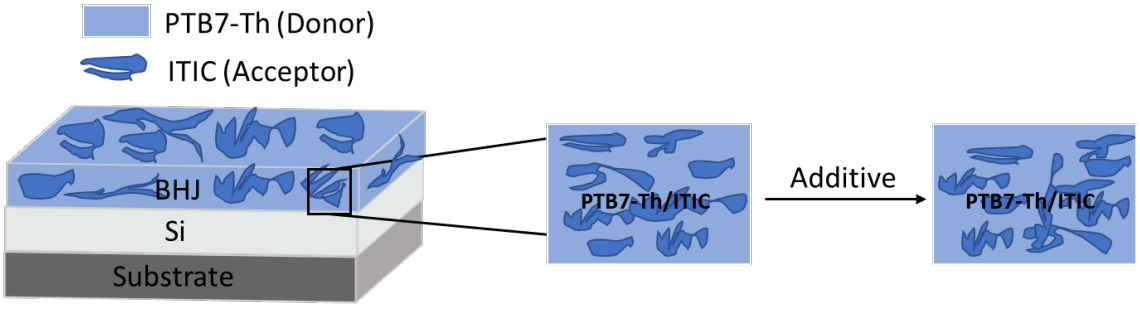

Figure 2-4. Schematic of an inverted device structure of OPV using an additive to modify the donor and acceptor in BHJ.

2.2 SAM in Invert PSCs

a) The influence of a SAM layer on the surface passivation of sputtered NiOx in PSCs.

In recent PSC cell research, NiO_x has been used as a promising, economical hole transport material (HTM) and as a replacement for poly (triaryl amine) (PTAA).[1] Still, its low intrinsic conductivity (~ 10^{-4} S/cm) and the existence of many surfaces' defect sites,

especially pin holes and island formations, are still not completely explored or understood. Moreover, an unfavourable energy gap between the E_f and the VB could potentially induce a large energy level offset at the interface between NiO_x and perovskite. Poor morphology of the material, which is common and severe in solution-processed thin films, also presents a challenge. In planar p–i–n architecture, the properties of HTM, as the under layer, can have a profound effect on the quality of the subsequently formed perovskite layer. To resolve the issue, a SAM layer was deposited on top of the NiO_x film to mitigate the defects at the interface, as shown in Figure 2-5. Chapter 8 will discuss the effects the SAM has on the defect passivation performance, its morphology and how it impacts overall device performance.

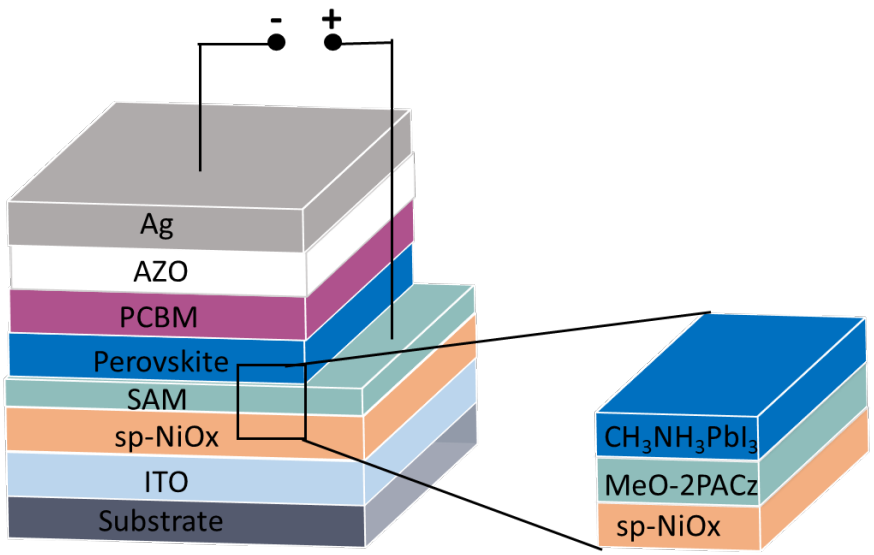

Figure 2-5. Schematic of an inverted device structure of PSC using SAM to passivate the surface of NiOx.

2.3 References

(1) Khadka, D. B.; Shirai, Y.; Yanagida, M.; Tadano, T.; Miyano, K. Interfacial Embedding for High-Efficiency and Stable Methylammonium-Free Perovskite Solar Cells with Fluoroarene Hydrazine. *Advanced Energy Materials* **2022**, 2202029.

Chapter 3: Methodology and Sample Preparation

3.1 Introduction

PES is a technique that imparts detailed analysis of the surface bombardment using X-rays or UV light for electron emission excitation. It quantifies the relative energies of electrons in atoms and molecules and is used to determine their elemental constituents and bonding features. The photoelectric effect involves the emission of an electron (photoelectron) from the sample upon absorbance of incident photons., while metal energy targets such as gold (Au) or silver (Ag) are used for calibrating the Fermi edge. The electron is ejected from the solid when the binding energy is less than the photon energy (hv); hence, kinetic energy occurs as the difference in these powers.[1]

The difference between the generated photoelectron's binding energy and photon energy is determined through electron using a hemispherical analyser. The association between the released photoelectron's photon energy and the kinetic energy is designated using the formula below:

$$E_{Kinetic} = h\nu - \Phi_{Spec} - E_{Binding} \tag{3.1}$$

Where Φ_{Spec} is the spectrometer WF, which is achieved by measuring well-defined features of a highly conductive metal sample such as Au or Ag.

PES is a surface-sensitive analytical approach that can reveal the chemical state information from sample elements. Photons infiltrate the sample through the different orbitals and are absorbed by the electrons. The outermost layer and near-surface region can then be examined.

The multiple-PES of non-monochromatic radiations follows the exact mechanism involving photon absorption and electron emission. First, photon absorption occurs from the radiation, then the photons get absorbed and lead to the emission of electrons. This is followed by the movement of electrons inside and at the outermost layer of the sample. Subsequently, emitted electrons are passing through a lens system and an energy analyser, and recorded by a detector.

PES's surface sensitivity depends on how deep an electron can be produced and escape without inelastically diverging. It is determined by the mean free path of electrons, representing the average distance that an electron can travel without scattering, interacting with the adjacent atoms/electrons and necessitates the use of ultra-high vacuum (UHV) to prevent electron collision, deflection and de-excitation with gas environments. Use of the UHV chamber is essential, as it enables an uninterrupted passage of photoelectrons to the analyser and minimises the re-contamination rate of a newly prepared sample. Proper vacuum level is a critical step, as its use also prevents adsorption of residual gas, eliminates adsorption of contaminants on the sample and prevents arcing and high voltage breakdown.

The photoelectrons can be derived from either core orbitals in the sample's depth or valence orbital in the outermost layer. Consequently, PES is of various types depending on the photoelectron source. The core electrons contain strong bonds that necessitate high photon energy to break and release electrons, while valence electrons contain delocalised molecular features that require reduced energy. Therefore, since the X-ray examines core levels while the UV light investigates valence levels, the former exhibits higher excitation energy than the latter. The schematic of the in situ- spectroscopy apparatus is shown in Figure 3-1. Figure 3-2 shows the UHV instrument used to run the experiment at Flinders University.

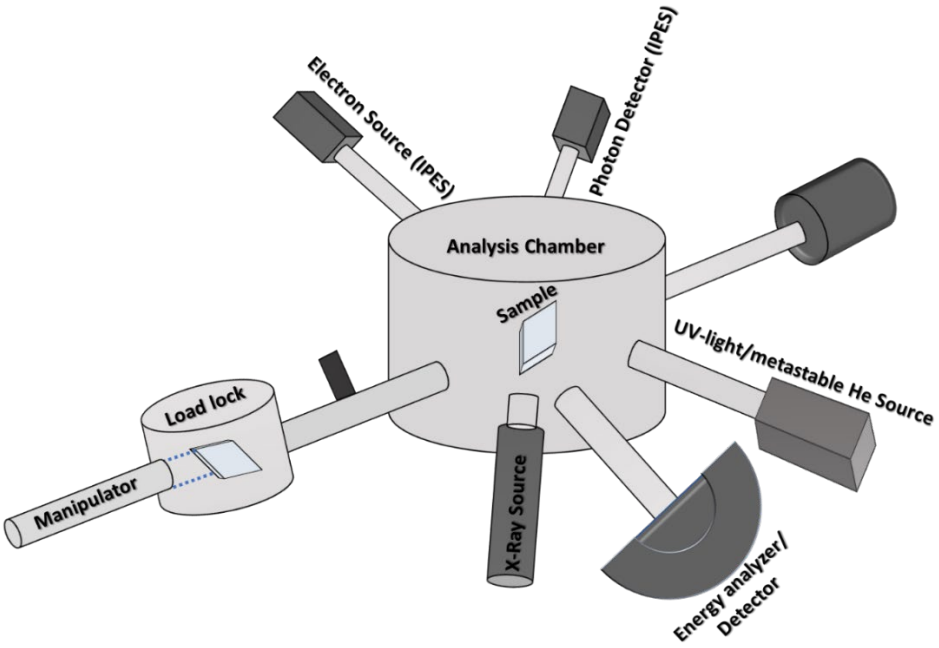

Figure 3-1. Schematic of UHV instrument of the multi-spectroscopy.

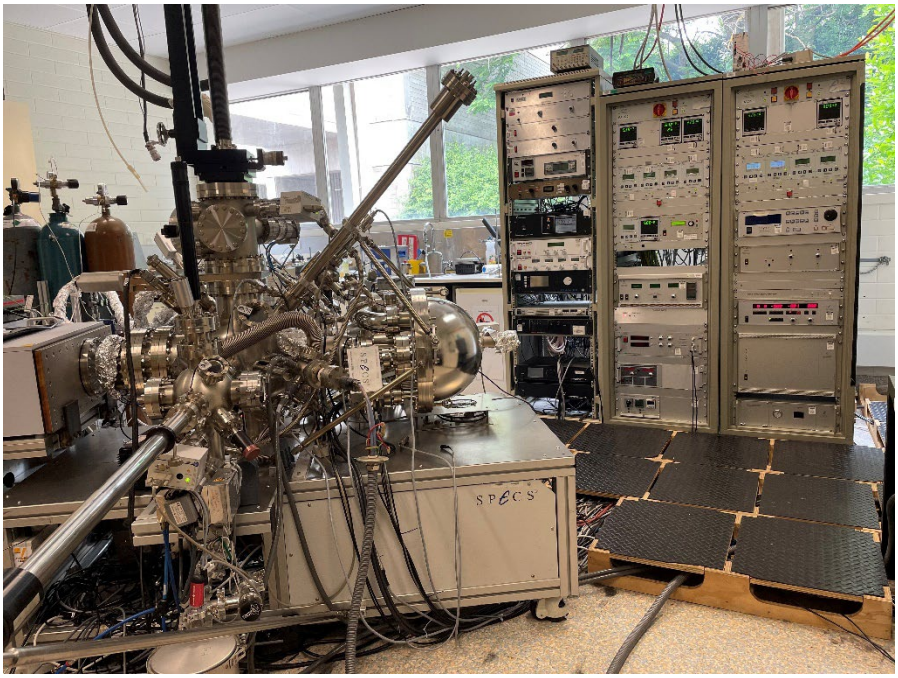

Figure 3-2. The instrument of UHV at Flinders University for XPS, MIES/UPS and IPES. The instrument was manufactured by SPECS (Berlin, Germany).

3.1.1 X-ray photoelectron spectroscopy

The XPS spectra are derived by irradiating a sample with a beam of X-rays and concurrently quantifying the kinetic energy and number of escaping electrons. The XPS spectra are measured using UHV non-monochromated X-ray source (12 kV–200 W) with Mg anode in the current experiment. Heated Thoria-coated Tungsten filaments are used to produce an accelerated electron source to the high voltage Mg anode, producing X-ray emission that enter a vacuum tube and project on the sample surface. The high-energy photon of X-ray excites the core level electrons of samples due to the Mg's excitation energy (1,253.6 eV), causing a photoelectron transition across the entire energy bands. Subsequently, the sequence of electron excitation energy can be employed to recognise the sample constituents and binding method. The elemental composition per orbital depth can also be determined. The intensity (I) of electrons released from a material at a particular depth can be obtained using the equation below:

$$I\ (E, \alpha, d) = Io\ exp(-d/cos(\Theta).\lambda(E)) \tag{3.2}$$

Where d, I_o, $\lambda(E)$ and Θ represent the measuring depth, maximum intensity (at outmost layer), mean free path of electrons and angle between the orientation to the detector and the surface normal. Notably, the X-ray irradiation and analyser angle was 54°, high pass energy of 40 eV will be applied for survey scans, and low pass energy of 10 eV for high-resolution scans will be documented. Composition information for the top 3–5 nm of the sample was obtained by using Mg Kα source with a photon energy of 1,253.6 eV.[2–4]

The removal of the XPS core electron results in a core hole that leaves the atom in the excited ionised state. The atom can be relaxed by filling the hole with an electron from a valence level. Energy is released during the relaxation process through either X-ray fluorescence or the production of an Auger electron. In X-ray fluorescence, the hole is filled through an electronic transition from a higher energy orbital, and generates excess energy by emitting an X-ray photon. Conversely, relaxation by Auger electrons involves

passing the extra energy from shift to another electron in higher orbitals.[5,6] Figure 3-3 shows the excitation of X-ray photoelectron from the elemental core level.

The XPS spectrum provides different information, including the peak intensity, the full width at half maximum (FWHM) and the peak position. Every element contains a unique spectrum depending on its energy levels. Modifications in the peak position of a particular element represent an alteration in its chemical nature through processes such as reduction or oxidation. Additionally, XPS can be applied in identifying and quantifying surface elemental composition by comparing the measured values to the data base for individual elements.

The main components of an XPS instruments include X-ray source/s, sample holders, focusing lenses, hemispherical analysers and electron detectors kept under UHV. These devices function properly when operated in an UHV chamber at specified conditions (SPECS, Berlin, Germany). The working pressure of the instrument is in the order of few 10^{-10} mbar for our SPECS PHOIBOS-HSA3500 analyser. The spectra are documented at high-resolution scans, particularly low passed energy of 10 eV and bias of –10 eV. Further, MgKα radiation is used as the X-ray source, under working conditions of 200 W, 12 kV and 1,253.6 eV excitation power. Before performing peak fitting and quantification, the high-resolution and survey spectrum peaks were corrected for electron scattering background by using Shirley background. Then, peaks were fitted using the Gaussian-Lorentzian functions to fit the peaks.[5,7] Finally, from the quality of the fitting,

the uncertainty of the peak location has been evaluated by estimating how well the position can be determined and taking that into consideration.

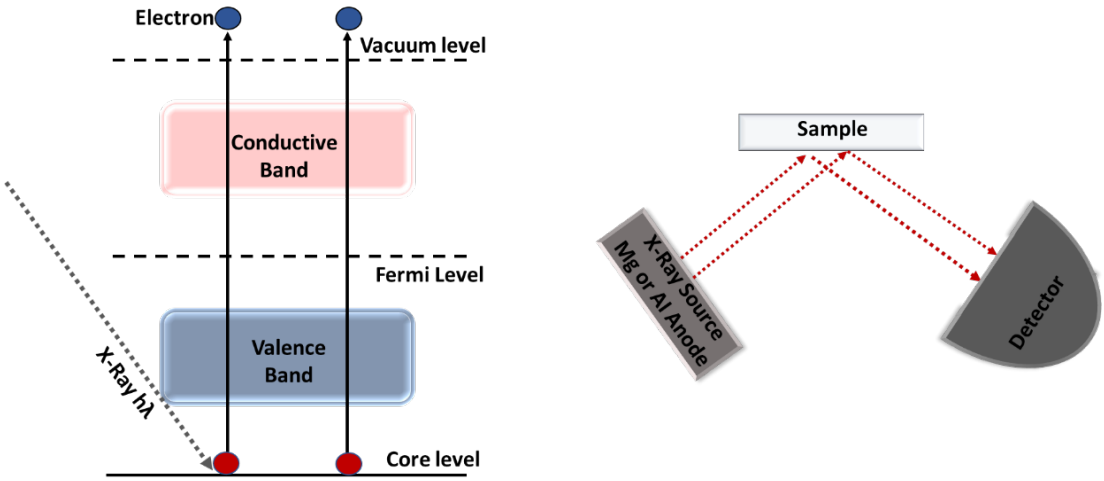

Figure 3-3. Excitation of X-ray photoelectron from elemental core level.

3.1.2 Ultraviolet photoelectron spectroscopy

In UPS, a helium discharge lamp is used to generate UV radiation at 21.2 eV (He 1) for electron excitation. Since it is a surface-sensitive method, UPS uses UV rays' energy to interact with the VB electrons and eject them from the top 3 nm surface layer and provide information about valence states orbitals and secondary electron densities. The WF of a sample is determined by secondary electrons distribution, where WF is the minimum energy required for sample surface electron removal.[8]

The emitted electrons entering the analyser are detected. The emitted electron's kinetic energy is supplemented with 10 eV to remove all secondary electrons and accelerate them into the semicircular analyser. The electron's binding energy in the UPS system is determined using the following formula. A –10 eV bias is applied in the work to allow a full emission of the electron, thus increasing the intensity of the spectrum.

$$E_{Binding} = 21.2\ eV - (E_{Kinetic} - (-10\ eV)) - \Phi_{Spec} \tag{3.4}$$

In this thesis, we used UPS to determine the valance electron spectra as an indication of the dipole at the surface of a sample.

Figure 3-4 depicts the UP spectrum of the VB and secondary electron cut-off by plotting a line across the x-axis; therefore, WF is determined and minimised by 21.218 eV (excitation energy).

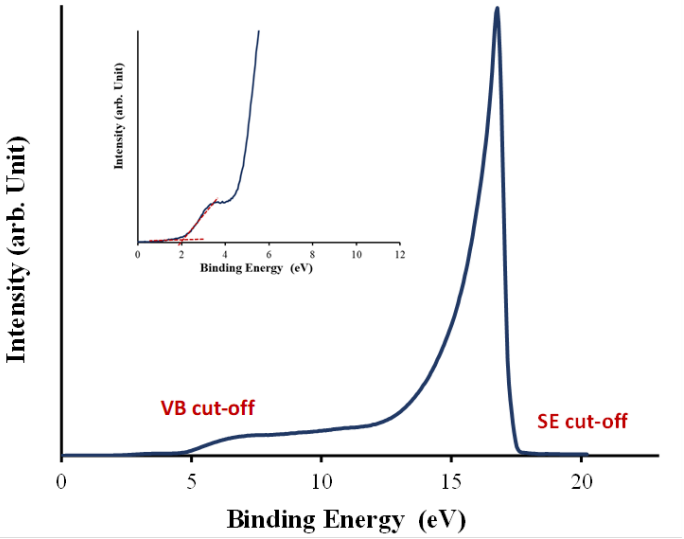

Figure 3-4. Typical UP spectrum with marked VB and secondary electron cut-off.

3.1.3 Metastable induced electron spectroscopy

Similar to UPS, the core of the metastable induced electron spectroscopy (MIES) method revolves around the use of metastable helium atoms to bombard the intended surface where helium atoms get excited, with the excitation energy of 19.8 eV, to a metastable state (He* 2s1s), which enables the determination of the VB structure for the outermost atoms.

There are two mechanisms at play when He* atoms interact with the surface atoms. The essential process is resonant ionisation (RI), which is accompanied by either Auger neutralisation (AN) or Auger de-excitation (AD). RI accompanied by AN is predominant on metal surfaces, with RI occurring on free sample surface when 2s He* orbital electrons excite and induce electron emission.[9] Equation 3.5 provides the energy of the electron.

$$E_{electron} = E(He^{+}) - 2(\Phi + \varepsilon) \tag{3.5}$$

Where Φ represents the WF at the surface and ε represents the mean binding energy of electrons taking part in the Auger process. In the AN mechanism, He^+ is neutralised when an electron from the atoms at the surface emits its electron. Conversely, the AD pathway is predominant in organic materials and semiconductors. In the latter's case, an electron leaving the atoms at the surface fills the He 1s level. Due to its energy, He* is stabilised by emitting an electron from the He 2s level. During these events, an energy difference is formed between the electron occupying He 1s and those at the sample surface (where the He 1s is transferred). What follows is the electron emission for ionisation and neutralisation. The nature of MIES is in the characterisation of energy shifts in the valence region within roughly 2 Å depth, which is especially useful in characterising organic species and their state at the surface. Spectrum obtained where AD is the dominant process has distinct features.

Cross-section for de-excitation is considerable; however, He* has sufficient energy to probe the surface atoms up to few angstroms in depth. This is also the reason that MIES only characterises the electronic structure of the outmost layer and we use the AD process throughout this work.

UPS and MIES processes are carried out in UHV. Concurrently, 21.2 eV UV light energy and metastable helium atoms He^* (S_1, 19.8 eV) are produced using MFS's (Clausthal-Zellerfeld, Germany) dual-phase cathode discharge. The signal derived from the UV photons and He^* are then separated using a 2 kHz frequency chopper.

3.1.4 Inverse photoemission spectroscopy

IPES uses the mechanism of electron-in and photon-out to perform photoemission in a reverse mode. The processes were executed using well-defined energy that was directed onto the sample. Our set-up was structured so the electrons were generated in an electron gun equipped with a BaO filament. The electrons are absorbed by the sample and make a transition to the unoccupied states via emission of a photon. The energy of the photon is measured and allows determination of the energy of the unoccupied state.. The

observation of the intensity of induced photon was done using the isochromatic detector of Geiger-Mueller tube. . Argon gas was used for filling the GM tube. Acetone was mixed with Argon to form an ionising gas with a mixed ionising energy of around 7.88 eV, there is a window on the GM tube with a transmission function that matches the ionisation energy of the gas mixture.

The states below the Fermi level are in accessible for IPES (no emission of photons). Thus, by combining the in situ-UPS and IPES, a complete energy band structure of the samples containing WF, VB/HOMO and CB/LUMO is illustrated.[10] Moreover, it should be noted that the duration of radiation on the electron gun towards a sample surface has to be limited. That is because of the flux of low kinetic energy electrons from the source, which can easily cause the molecular resonance of a sample surface, especially on organics. Thus, the sample composition can be destroyed. The energy resolution of IPES and UPS is 0.5 eV and 0.1 eV respectively.

3.1.5 Singular value decomposition

The samples investigated in this research were composed of materials derived from the recorded spectra. The UP and MIE spectra can be considered as a linear combination of the measured spectra of the individual components. The UP and MIE spectra were analysed with the singular value decomposition (SVD) method, which is described in detail in prior works;[11,12] however, we provided a brief explanation in this section.

The series of UP and MIE spectra of the samples can be considered as a matrix. The initial steps of the SVD involved the analysis of the matrix under consideration. Moreover, the stage involved the determination of the number of base spectra required to reconstruct the measured series spectra. It resulted in the determination of the number of base spectra needed for the reconstruction and the yields from each of the base spectra. It is worth noting that the base spectra are not required in the reconstruction processes. However, it has physical meaning in the measurement of the electron spectra. While the operation is not mathematically rigorous, it yields an ambiguous set of reference spectra. This second

operation required the application of boundary conditions to determine the individual spectra from the measured spectra by applying the following equation:

$$S^i_{meas} = \sum_j a^i_j \times S_{ref,j} \qquad \text{with} \qquad \sum_j a^i_j = 1 \tag{3.6}$$

S^i_{meas}: the measured spectrum i

$S_{ref,j}$: the reference spectrum

a^i_j : the weighting factors used in the fitting procedure

The sum of the weighting factors must have unity within experimental uncertainty. The acceptable error is approximately 0.1 for the sum of the weighting factor, as shown below:

$$\sum_j a^i_j$$

The data obtained from the experimental data required fitting using the parameters in the spectra. If there was the formation of a dipole at the interface between the layer adsorbed onto the surface of the sample and the substrate beneath, then it required a shift from the original spectra on the energy scale of the spectral component to be done.

3.1.6 Neutral impact collision ion scattering spectroscopy

NICISS is a spectroscopic method of quantifying the concentration depth profile of an element within a few angstroms below the surface of interest with the aim of providing vital information on structure, especially that of soft matter surfaces. Initially, this technique was designed to investigate the structure of a crystal surface. In the years that followed, it was employed to quantify the concentration depth profile of soft surface samples. The spectroscopic instrument features the following parts: a detector that quantifies the time of flight (TOF) of backscattered He^+; a source of ion gun, preferably, helium (He), which generates the beam of ions, deflecting units that use electrostatic forces to produce ion beam pulses; and vacuum chamber. The experiment is conducted

by first placing the sample in the vacuum chamber. Second, a pulsed beam of He ions bombard the sample in the chamber at low kinetic energies in the range of 1–5 keV.

The incoming He ions are backscattered as neutral ions and lose energy during this process. Due to kinetic energy loss, their velocity is also decreased correlatedly. Decrease in the velocity can be specified by the TOF detector, which measures the time needed for species to reach the detector after scattering event. The loss in velocity is proportional to the loss in energy of the ion and can be used to determine it. From collision theory, measured energy loss of a He species can be used to determine the mass of the scattering atom. Precision measurement of TOF of backscattered helium is, therefore, of utmost importance in characterising the target.

Energy loss during backscattering occurs through two types of processes. The first process involves significant energy losses based on the backscattering atom's mass and manifesting once on a single trajectory. This process is applied to identify an atom's mass. Conversely, the second process involves small energy losses occurring in large quantities on a single circuit through electronic excitations (stopping power) and low angle scattering.[13] Therefore, the second process entails continuous energy loss correlated to the trajectory's length and provides information about the depth at which backscattering occurred. TOF from the target to the detector is directly proportional to particle's energy. The illustration of NICISS and the typical conversion spectrum of NICISS from energy loss spectrum are shown in Figure 3-5. The instrument used to run the experiment at Flinders University is shown in Figure 3-6.

The TOF path dimension of the instrument is 1.34 m, and the scattering angle is 168°. Integration of the two energy loss processes is employed to quantify an element's concentration depth profile. The NICISS results are outlined as a spectrum encompassing individual peaks and phases for recognising different atoms included that constitute the sample. It is documented as intensity vs TOF. Since hydrogen is a lighter element, thus being represented as background of the spectra.[14]

The following equation is used to convert TOF spectrum to energy spectrum:

$$\mathrm{I(E)} = \mathrm{I(t)}\frac{\mathrm{dt}}{\mathrm{dE}}\frac{1}{\mathrm{d}\sigma/\mathrm{d}\Omega(E)}\frac{1}{\det(E)} \tag{3.7}$$

Where II, I(t), $\mathrm{d}\sigma/\mathrm{d}\Omega(E)$ and $\det(E)$ denote the energy loss spectrum, the element's involvement in TOF spectrum, differential cross-section and detector sensitivity. Particularly, the factor dt/dE is essential in describing the non-linear correlation between TOF and energy.

In this thesis, NICISS was used to identify the concentration depth profiles, the thickness of the layers and the regions of chemical phase mixing.

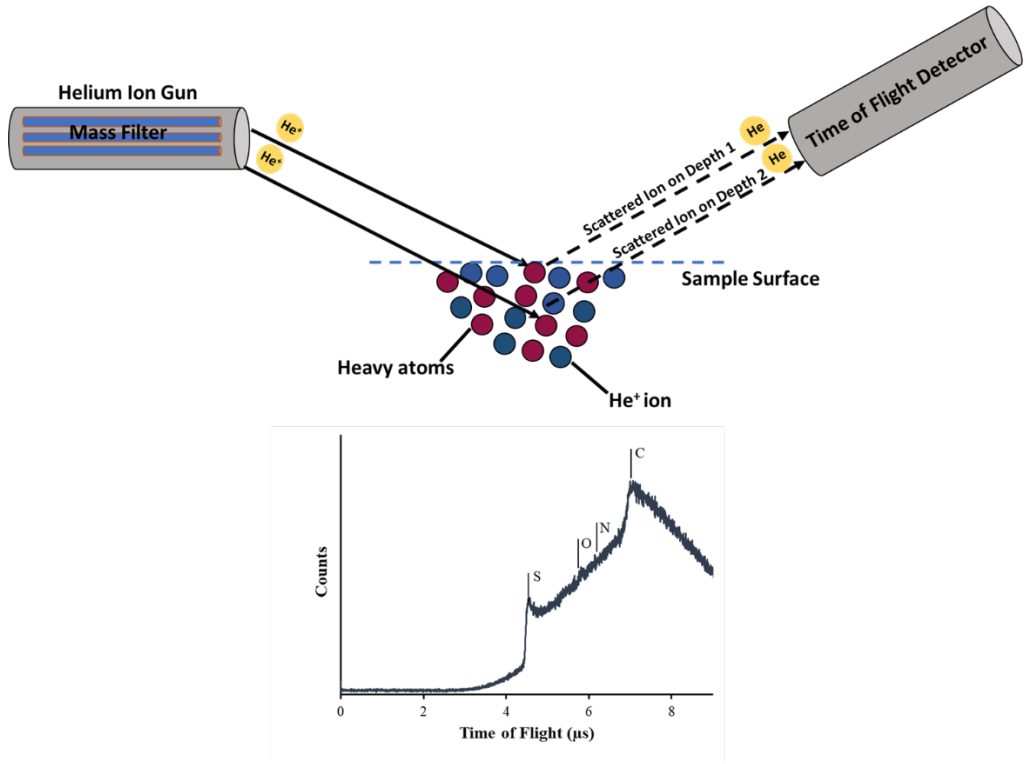

Figure 3-5. Diagram of NICISS operation and the raw NICISS spectrum.

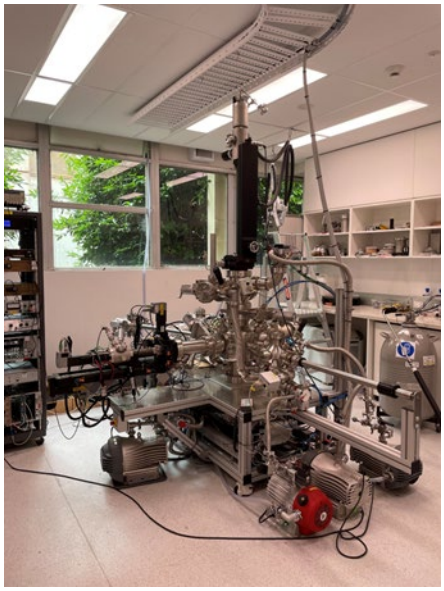

Figure 3-6. The NICISS instrument at Flinders University. The instrument was manufactured by SPECS (Berlin, Germany).

3.1.7 X-ray diffraction

X-ray diffraction (XRD) is the process of illuminating a sample with X-rays to obtain a diffraction pattern. This pattern is recorded by detectors where it can be analysed to determine the orientation of molecules in a material.[15]

In more detail, the X-ray can only be diffracted from the atomic plane when the distance between adjacent lattice planes follows the law of Bragg, as illustrated in equation 2.8.[16] As shown in Figure 3-7, Bragg's law can be used to express the relationship between X-ray wavelength, incidence angle and lattice spacing between crystal lattice planes of atoms.

$$n\lambda = 2d\ sin(\theta) \tag{3.8}$$

Where:

1. n (integer) is the order of interference
2. λ is the wavelength of the incident X-rays

3. d is the lattice spacing in nm
4. θ is the angle of 50 incidence in degrees.

The XRD method is used to study the perovskite films and to determine the crystal structure of the perovskite materials. By examining the size of the nanocrystallites, the orientation of the molecules can be defined in the sample.

The XRD patterns were obtained by employing an advanced X-ray diffractometer, the Bruker D8 with Cu K* radiation λ=1.54050 Å and the scan rate set at 3°min^{-1}. The morphological image of the films was collected using a field emission scanning electron microscope (SEM) (Hitachi S-4800) with an accelerating voltage of 5 kV. To measure the transmission and absorption spectra, an ultraviolet-visible-near-infrared spectrometer (7200, V-JASCO) was used.

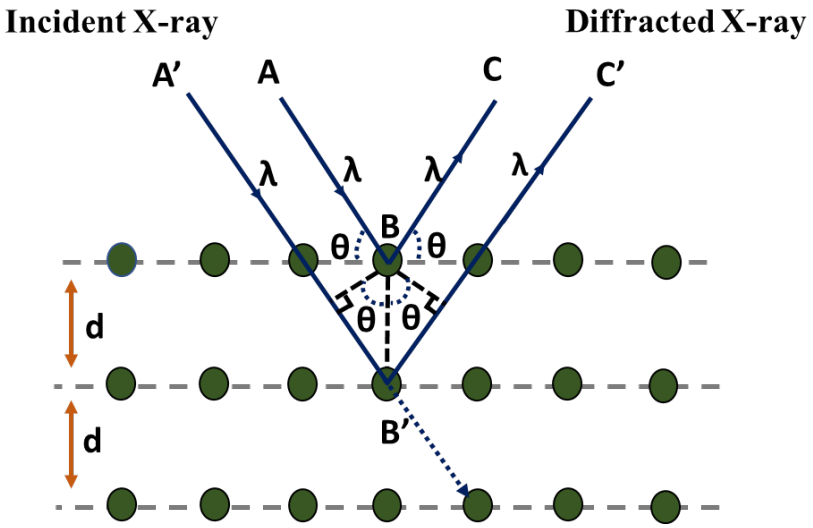

Figure 3-7. Schematic illustration of diffraction process in XRD measurement.

3.1.8 Scanning electron microscopy

An SEM is an imaging technique and is used to determine the nanoparticle shape, size, arrangement and degree of agglomeration.[16] In the SEM (see Figure 3-8), an electron beam is generated by multiple condenser lenses and an electron gun. By varying the angle of inclination of the optic axis, the electromagnetic coils deflect the rays of the beam[17]

and an objective lens is used to focus the beam onto the sample (note: beam spots of size 1–5 nm).

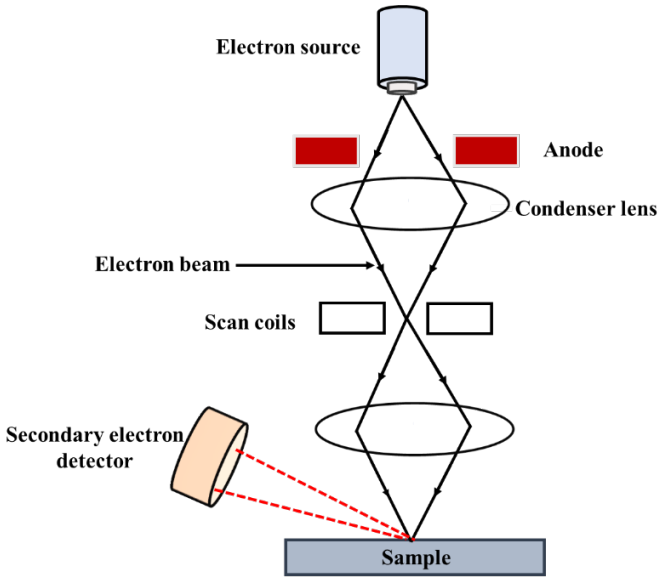

Figure 3-8. Schematic illustration of SEM set-up.

To produce an SEM image, secondary electrons are emitted from the surface of the sample when the primary electron beam is scanned over the sample.[17] It also produces backscattered electrons that are subsequently detected. Using the backscattered electron image, different sample regions can be contrasted and an image is formed. The SEM technique has the advantage of a superior lateral resolution and is capable of analysing a wide range of scales, from the nanometre to the millimetre.[18]

In this thesis, SEM technique was used to observe the surface and the cross-section of the perovskite films on HTL (JSM-5600LV, JEOL and SU-8020, Hitach High-technologies). For cross-sectional analysis, sample pieces were cut with a diamond cutter into two pieces and the fractures surfaces were observed.

3.1.9 Atomic force microscopy

Atomic force microscopy (AFM) is a high-resolution scanning probe microscopy (SPM) method that provides a detailed assessment of atomic-level surface morphology. It uses a sharp tip or probe (usually made of hard material like silicon nitride) attached to the end

of the cantilever that scans the surface. The force on its sharp tip that is created by its proximity to the surface of a sample is measured based on Hooke's law:

$$F = -Kx \tag{3.9}$$

Where:

F is the force exerted on the cantilever in the displacement position.

K is the spring constant.

X is the displacement of the cantilever form its equilibrium position.

With a laser applied to the cantilever's top surface, the interaction between the tip and surface can be observed through a reflection of the laser onto the array of photodiodes. Forces, such as van der Waals force and dipole attraction, act on the cantilever when the tip approaches the surface. By mounting the sample on a piezoelectric scanner and employing a feedback loop, it is possible to manipulate the sample in x and y directions for surface scanning and to adjust the z direction of the sample so as to minimise these forces of attraction and to maintain a constant oscillation.[19,20] The resolution is determined by the radius of curvature of the AFM tip, which can range from a few nanometres to several tens of nanometres.

AFM can be operated in three modes, namely contact mode, non-contact mode and intermediately or tapping mode. In this thesis, AFM tapping mode analysis was run to study the topography of BHJ in OPV devices. Using tapping mode, an oscillating cantilever scans the surface of a sample by attaching a tip to it. The oscillating pattern of the cantilever is deviated by the interactions between the tip and the surface. Lasers are used to scan the surface and collect these deviations in a three-dimensional topography map, which is then used to monitor these deviations (see Figure 3-9).

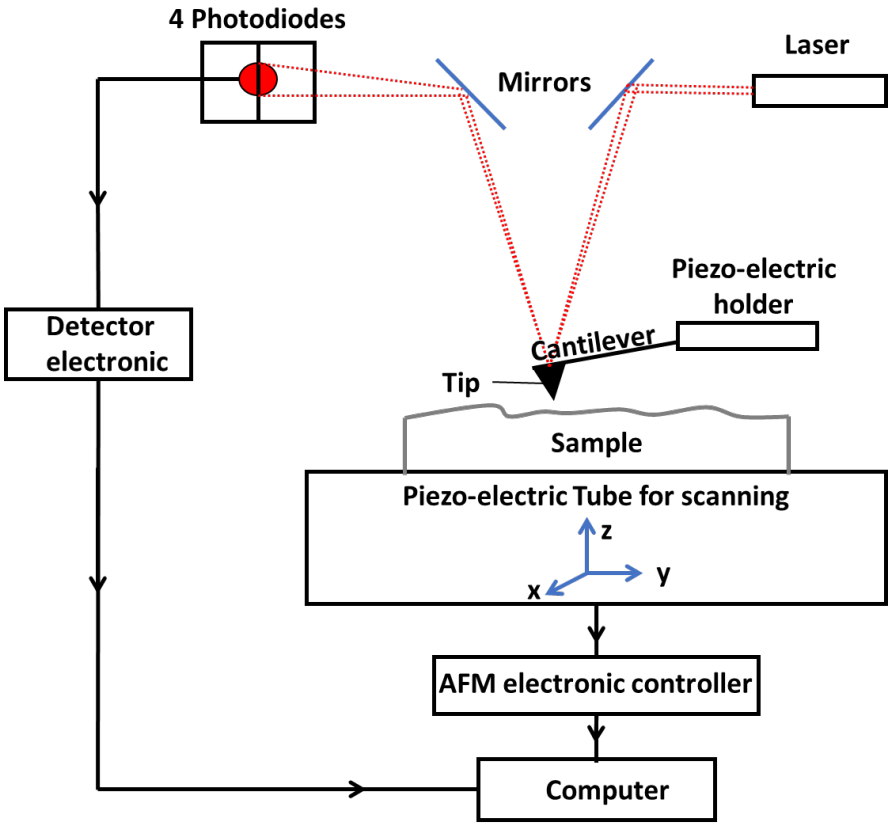

Figure 3-9. Basic schematic of the AFM.

3.1.10 Photothermal deflection spectroscopy

Photothermal deflection spectroscopy (PDS) detects the charge states in accordance with the absorption coefficient.[21–23]

Monochromatic light was used to irradiate the sample surface at a normal angle created by a halogen lamp (700 nm to 1,200 nm) with a chopping frequency of 11 Hz. The light was concentrated using a cylindrical lens. The dimensions of the lens were 1×10 mm^2. A semiconductor laser (660 nm) was then used to probe the sample surface in parallel with the light. During probing, the laser was deflected based on the thermal energy produced by the combination of the electrons activated by the light. During the process, there was a need to enhance the deflection of the laser probe. This was achieved by conventionally dipping the sample into a fluorinert (FCI) solution characterised by a high coefficient-of-temperature dependence of the refractive index, $\delta n = \delta T$, where T and n represent the

temperature and refractive index, respectively. Figure 3-10 shows the process of the PDS set-up. In this research, we used PDS to determine the defect level of the perovskite films.

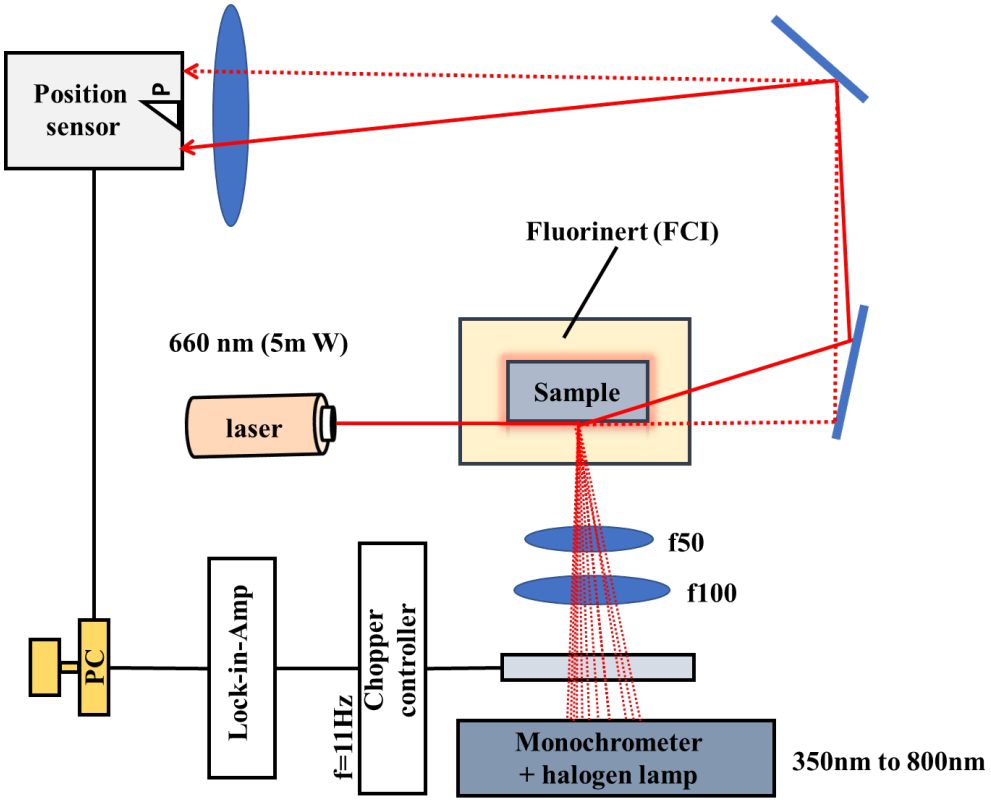

Figure 3-10. Schematic illustration of PDS set-up.

3.1.11 Ultraviolet-Visible Absorption Spectroscopy

Ultraviolet-visible (UV-vis) absorption spectroscopy is a technique that can be employed for characterising the electronic structure and composition of semiconductors based on their absorption characteristics.[16]

In semiconductor materials, UV-vis light passes through molecules or atoms, and electrons are excited from a lower level of energy to a higher level of energy.[24] It is noteworthy that absorption's probability is strongly influenced by the material, wavelength, and the distance of light travelling through the material. The formula below can be used to express Beer's Lambert law as an expression for the absorbance of a material:

$$A' = \varepsilon lc \tag{3.10}$$

Where A is the absorbance, ε is molar absorptivity, $l=$ is the length of the light path and c is concentration.

In this thesis, we used UV-vis to examine the transmittance of NiOx film and MeO-2PACz on NiOx film.

3.1.12 Photoluminescence spectroscopy

Photoluminescence (PL) spectroscopy is used to study and characterise the electronic structure of materials and understand their dynamic processes. It is used to measure the distribution of energy of photons produced after optical excitation.

By analysing the resulting spectra, it is possible to identify the material's properties, including possible stimulated emission, defect species, defect concentration, recombination mechanisms and E_g. Particularly, steady-state PL measurements have been widely used in the study of charge-hole recombination at the perovskite/ETL or HTL interfaces, trap state, and the passivation effect.[25] In this thesis, PL spectra were obtained using a spectrometer (FP8500, JASCO) to determine the properties of the materials.

3.1.13 Time-resolved photoluminescence

Time-resolved PL (TRPL) is used to determine the dynamics of semiconductor charge carriers. Hence, an accurate assessment of charge carrier lifetime can only be made after the device systems have been characterised. Depending on the materials and interface used in some semiconductors, the carrier can have a different lifetime. There are some factors that affect the measured results, include the surface effects of the sensitiser, the passivation effect, the energy transfer property and the impurities and defects.

In this thesis, the TRPL measurements were carried out to understand the recombination lifetime in perovskites films with a fluorescence lifetime spectrometer (Quantaurus-τ

from Hamamatsu-Photonics K.K.) equipped with ~ 405 nm laser diode (ttyp. Peak power of 400 mW) at 200 kHz repetition rate.

3.1.14 PV characterisation

The PV cell efficiency, a cell's ability to transform the input energy from the sunlight to an output electrical power, was determined by establishing the ratio between the energy that the cell produces (P_{output}) and the energy provided by the light (P_{input}). This determines the PCE η expressed as a percentage (as illustrated in equation 3.11).

$$\eta = \frac{P_{output}}{P_{input}} \tag{3.11}$$

Within equation 3.11, P_{input} relates to the solar spectrum. However, as the solar spectrum that hits the Earth's surface varies with location and time of day, a well-established reference solar spectrum with air mass (AM) coefficient was used. The AM has a constant value of 1.5 G, which represents the sea level spectral distribution of averaged solar radiation across the planet's surface after atmosphere's permeation 1.5 times with a radiation intensity of 100 mW/cm^2.[26]

The cell's P_{output} is experimentally determined from the current voltage (I-V) analysis. The I-V characteristics enable the determination of measures, such as V_{oc}, short-circuit current (I_{sc}) and the fill factor (FF). V_{oc} represents the cell's maximum voltage when the current is not transmitted through the external circuit. Conversely, the I_{sc} represents the maximum current produced at zero voltage. The cell's P_{output} is determined when the voltage and current reach their maximum values (I_{max} and V_{max}) and is calculated using the following equation:

$$Poutput = Imax\,Vmax \tag{3.12}$$

The FF is the ratio of the P_{output} to that of the product of I_{sc} and V_{oc}. It can be evaluated using the following equation:

$$FF = \frac{P_{output}}{I_{sc}V_{oc}} \tag{3.13}$$

Since the cell's general performance depends on its efficiency, the following equation can be used to determine the efficiency:

$$\eta = \frac{I_{SC}V_{OC}\,FF}{P_{input}}\ X\ 100 \tag{3.14}$$

A solar simulator with a 1,000 W Xeon lamp, adjusted to produce a 100 mW/cm^2 output, at 1.5 G AM, was used throughout the work for cell testing. An Si cell was used for the lamp calibration and using Keithley 2400 SourceMeter run by Labview software to measure the overall efficiencies of the cell.

3.1.15 Quantum efficiency measurements

Quantum efficiency (QE) of an external SC is given as the portion of incoming photons converted into electrons in the external circuit, as a function of wavelength. Two types were established: 1) the external QE (EQE) and 2) the internal QE (IQE).

EQE can be viewed as incident photon-to-electron conversion efficiency (IPCE), which considers the number of photons emanating from the solar simulator that reach the photosensitised area of the SC. After the photon absorption and subsequent electron (e^-) and hole (h^+) generation, separation and collection of charge carriers at the interface is required. If charge recombination occurs, it will result in a drop in the IPCE. Via equation 3.15, the IPCE value can be obtained by knowing the photon flux J_0 of the solar simulator, with J_{sc} representing the short-circuit current density and e the elementary charge.

$$IPCE\ = Jsc\ /\ eJ_0 \tag{3.15}$$

In this thesis, we used QE measurements to study the efficiency of photocurrent conversion.

3.2 Sample Preparations

This section will describe the sample preparation of the organic SC and PSC.

3.2.1 Cleaning of ITO substrate

The ITO-coated glass substrates were immersed to a 5% Pyroneg solution for 20 minutes at 90 °C. Subsequently, the substrates were rinsed with MilliQ water and sonicated for 10 minutes in MilliQ water, which was repeated with acetone then 2-propanol. The cleaned substrates were dried under a stream of nitrogen, followed by 20 minutes of UV/ozone treatment.

3.2.2 Polymer layers

In Chapters 4, 5, 6 and 7, the polymer interface was studied. The sample preparation for these chapters is as follows.

A) Cathode Interface Layer (CIL)

i. P(NDI3N-T-Br) and P(NDI3N-F8-Br) layers

The polymer SC project focuses on an n-type CIL polymer—poly[(*N,N'*-bis(3-(*N,N*-dimethyl)-*N*-ethylammonium)propyl)naphthalene-1,4,5,8-bis(dicarboximide)-2,6-diyl)-alt-2,5-thiophene)]dibromide P(NDI3N-T-Br) and poly[(*N,N'*-bis(3-(*N,N*-dimethyl)-*N*-ethylammonium)propyl)naphthalene-1,4,5,8-bis(dicarboximide)-2,6-diyl)-alt-2,7-(9,9'-dihexylfluorene))]dibromide P(NDI3N-F8-Br)—with pendant side groups containing quaternary amines.

This is an A-D copolymer consisting of an NDI acceptor unit and a thiophene linker as the donor unit. The design of the polymer with the pendant side groups positioned on the NDI unit allows for ease of modification by the switching of the donor linker unit. Moreover, the preparation of the new cathode interface material focused on green processing, which means they can be solution processed from green solvent. The pendant

side groups contributed to the increased solubility in polar and green solvent, such as alcohol. The synthesis procedure of P(NDI3N-T-Br) can be found in the supplementary section (Appendix A). The chemical structures of P(NDI3N-T-Br) and P(NDI3N-F8-Br) are shown in Figure 3-11.

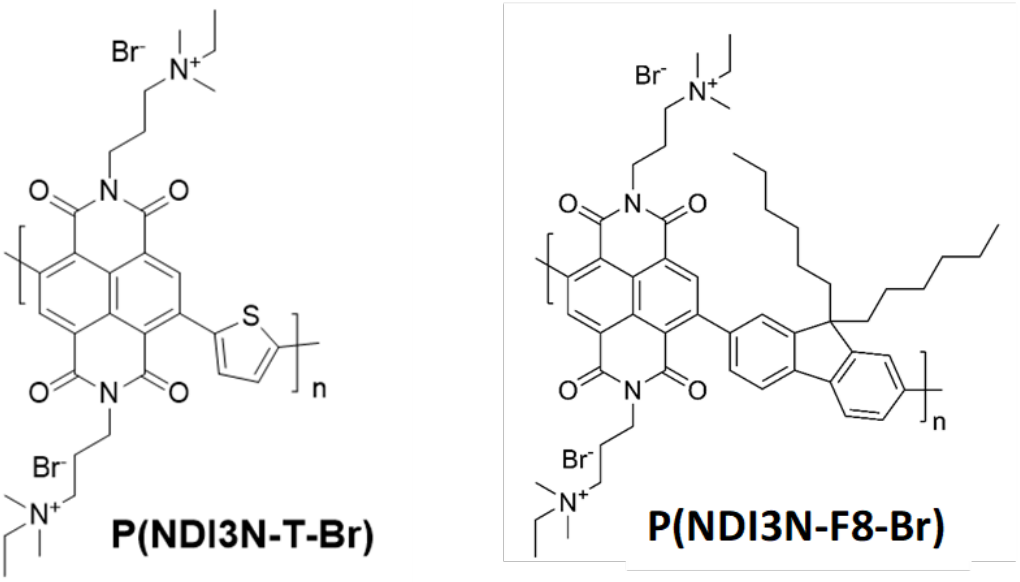

Figure 3-11. Chemical structures of the n-type cathode interface materials P(NDI3N-T-Br) and P(NDI3N-F8-Br).

For preparing an interface layer, MeOH was used as the solvent for the P(NDI3N-T-Br) and the thin film was spin-coated from a 15 mg/mL methanol solution on ITO-coated glass at a 2,000 rpm. P(NDI3N-F8-Br) was spin-coated from a 12 mg/mL MeOH solution on ITO at a speed of 2,000 rpm. These were the optimal concentrations and solvent to make a thin layer of CIL and allow for measuring the interface structure after depositing different active layers on the top.

ii. Zinc oxide (ZnO)

Zinc acetate dihydrate (500 mg) was dissolved overnight in a mixture of ethanolamine (150 μL) and 2-methoxyethanol (Sigma-Aldrich, 99.8%, 5 mL). The resulting solution was filtered with a PTFE syringe filter (0.45 μm) to remove any undissolved particulates

prior to being spun on cleaned ITO-coated glass substrates at 3,000 rpm for 60 seconds. The formed film was annealed in a 280 °C preheated furnace in air for 10 minutes.

B) Active Layer Formation

i. TQ1 (donor)

Poly[2,3-bis(3-octyloxyphenyl) quinoxaline-5,8-diyl-alt-thiophene-2,5-diyl] (TQ1) was spin-coated from tetrahydrofuran (THF) solution at 2,000 rpm onto the previously formed P(NDI3N-T-Br) layer. THF solution concentrations of 0.05, 0.08, 0.1, 0.15 and 0.2 mg/mL were used to generate TQ1 layers of various thicknesses on top of the P(NDI3N-T-Br). A reference sample was also prepared by spin coating TQ1 directly onto ITO. The chemical structures of donors and acceptors materials used in this thesis are shown in Figure 3-12.

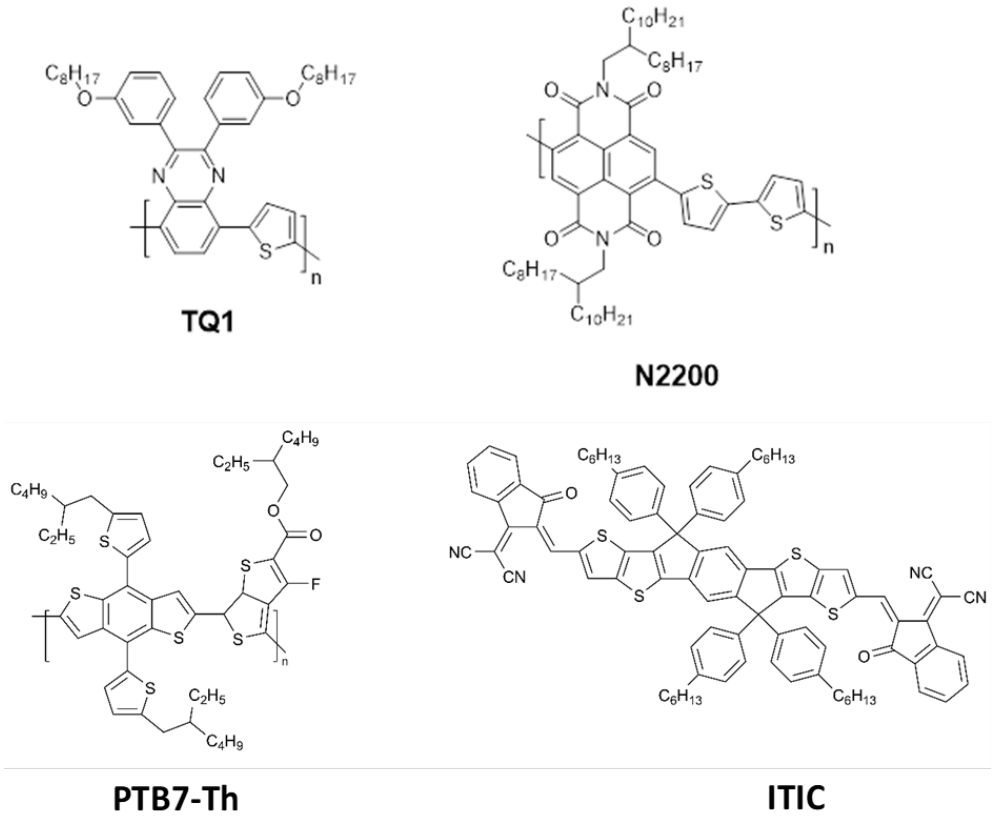

Figure 3-12. Chemical structure of donor material (TQ1 and PTB7-Th) and acceptor materials (N2200 and ITIC).

ii. N2200 (acceptor)

Poly[[N,N′-bis(2-octyldodecyl)-naphthalene-1,4,5,8-bis(dicarboximide)-2,6-diyl]-alt-5,5′-(2,2′-bithiophene)] (N2200) (Mn = 43 kg/mol, Mw = 120 kg/mol) was spin-coated at 2,000 rpm from *o*-xylene solutions with different concentrations of 0.3, 1.0, 1.5, 2.0 and 2.5 mg/mL on top of P(NDI3N-T-Br) as the acceptor active layer. A reference sample was also prepared by spin coating N2200 directly onto ITO.

iii. PTB7-Th (donor)

The o-xylene was used as the solvent for the poly[[2,60 -4,8-di(5-ethylhexylthienyl)benzo[1,2-b:3,3-b]dithiophene][3-fluoro-2 [(2-ethylhexyl)carbonyl]thieno[3,4-b]thiophenediyl]] (PTB7-Th). This donor layer was spin-coated on a pre-formed P(NDI3N-F8-Br) layer, which was prepared at a speed of 2,000 rpm with different concentrations of 0.3, 0.6, 1.0, 1.5, 2.0 and 2.5 mg/mL.

iv. ITIC (acceptor)

Chloroform was used for 3,9-bis(2-methylene-(3-(1,1-dicyanomethylene)-indanone))-5,5,11,11-tetrakis(4-hexylphenyl)-dithieno[2,3-d:20,30-d0]-s-indaceno[1,2-b:5,6-b0]-dithiophene (ITIC), and was spin-coated at 2,000 rpm onto the P(NDI3N-F8). The concentration was varied as 0.05, 0.1, 0.2, 0.3, 0.6 and 1.0 mg/mL.

3.2.3 Perovskite layers

In Chapter 8, we studied the PSC. The material preparation for that study is as follows.

i. Hole transport layer deposition

A radio frequency (RF) sputtering method was applied to deposit the 20 nm NiO_x hole-transporting layer onto ITO glass (10 ± 2 ohm/square, Ra < 2.6 nm) at room temperature. The RF sputter equipment was obtained from Sanyu Electron Co., Ltd., Tokyo, Japan, SVC-700 RF II NA. Commercially available 99.9% pure NiO (Kojundo Chemical Lab.

Co., Ltd., Saitama, Japan) was used as the target, and the sputtering was done at 3.5 Pa argon pressure. The sputtering chamber was evacuated to reach less than $2x10^{-3}$ Pa before the deposition.

ii. Self-assembled monolayer (SAM) deposition

The glass substrate with sputtered NiO_x (sp-NiOx) was brought inside a glovebox under inert atmosphere. SAM preparation utilised [2-(3,6-dimethoxy-9H-carbazol-9-yl) ethyl]phosphonic acid, (MeO-2PACz) (TCI, >98.0%), which was prepared by dissolving 6 mg of MeO-2PACz in 18 mL of ethanol. Extra care was taken to prevent particle formation, where all solutions were prepared inside a glovebox and filtration was carried out using 0.22 μm syringe filters. The next step was to spin coat the MeO-2PACz over sp-NiO_x HTL at 3,000 rpm for approximately 30 seconds. Annealing was performed for 10 minutes on a hot plate (100 °C) inside the glovebox. The chemical structure of SAM is shown in Figure 3-13.

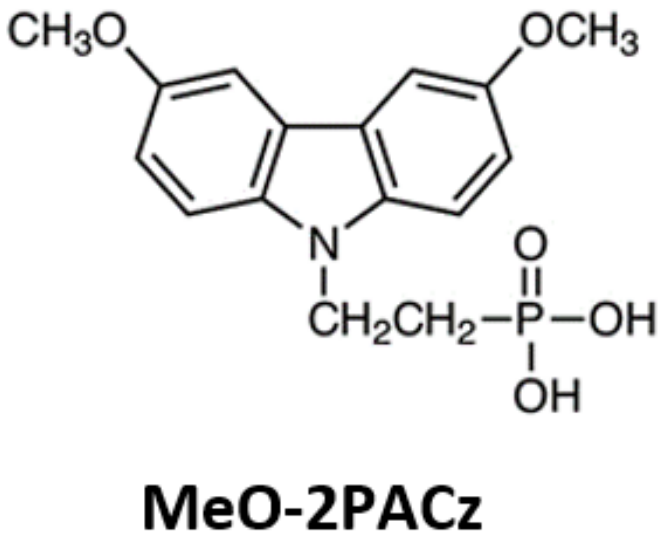

Figure 3-13. Chemical structure of SAM (MeO-2PACz).

iii. Perovskite solution preparation and layer deposition

Perovskite layer deposition began with the preparation of the perovskite precursor solutions inside the gloves box, where 5-AVAI (5-aminovaleric acid hydroiodide) (6.3 mg) and PbI_2 (Kanto Chemical, 98% purity) (1,260 mg) were dissolved in DMF−DMSO (2.85–0.15 mL). Methylammonium chloride (MACl) (Wako Chemicals, battery grade]) (5 mg) and methylammonium iodide (MAI) (Wako Chemicals) (95 mg) were dissolved in 2 mL ethanol and then stirred overnight at 300 rpm/70 °C in a closed vessel. Subsequently, spin coating was performed by preparing perovskite using a two-step interdiffusion method; more detail can be found in our previous work.[27]

The perovskite films were deposited in two steps, starting with spin coating PbI_2 solution onto MeO-2PACz (3,000 rpm, 30 seconds), annealing for three minutes on a hot plate (100 °C) and spin coating the MAI solution (4,000 rpm, 30 seconds) as a second step. The films obtained were then annealed under a MACl vapour environment to improve the perovskite film.[28]

iv. Electron transport layer and metal electrode deposition

Preparation of the metal electrode and ETL inside the gloves box began by dissolving phenyl-C_{61}-butyric acid methyl ester ($PC_{61}BM$) in 20 mg/mL chlorobenzene, which was followed by spin coating over the previously prepared perovskite films (1,000 rpm, seven seconds, then 3,000 rpm for 30 seconds). After this, the samples were annealed at 100 °C for 15 minutes.

For spin coating aluminium-doped zinc oxide (AZO) from Avantama AG (N-21X), the AZO solution was placed onto the $PC_{61}BM$ layer (1,500 rpm for 5.5 seconds, then 4,000 rpm for 20 seconds), which was followed by annealing on a hot plate (100 °C for 10 minutes). The cells were completed by thermally evaporating 150 nm thick Ag electrodes. The final step of the process involved encapsulation with cavity glasses, which

were sealed using UV curable resins, such as UVRESIN XNR5516Z, Nagase ChemteX, Japan.

3.3 References

(1) Reinert, F.; Hüfner, S. Photoemission Spectroscopy—From Early Days to Recent Applications. *New Journal of Physics* **2005**, *7*, 97–97.

(2) Kovalev, A.; Wainstein, D. Surface Analysis Techniques for Investigations of Modified Surfaces, Nanocomposites, Chemical, and Structure Transformations. In *Self-Organization During Friction*, CRC Press, 2006; pp 81–120.

(3) Tougaard, S. Surface Analysis | X-ray Photoelectron Spectroscopy. In *Encyclopedia of Analytical Science*, 3rd ed.; Elsevier, 2013; pp 400–409. DOI: https://doi.org/10.1016/B978-0-12-409547-2.00527-8

(4) Moulder, J. F. *Handbook of X-ray Photoelectron Spectroscopy*; Physical Electronics, 1995.

(5) Oswald, S. X-Ray Photoelectron Spectroscopy in Analysis of Surfaces. Update based on the original article by Steffen Oswald, *Encyclopedia of Analytical Chemistry*, © 2000, John Wiley and Sons, Ltd. 2013. DOI: https://doi.org/10.1002/9780470027318.a2517

(6) O'Connor, D. J.; Sexton, B. A.; Smart, R. St. C., Eds. *Surface Analysis Methods in Materials Science*; Springer, 2003.

(7) Hüfner, S. *Photoelectron Spectroscopy: Principles and Applications*; Springer Science and Business Media, 2013.

(8) Hofft, O.; Bahr, S.; Himmerlich, M.; Krischok, S.; Schaefer, J. A.; Kempter, V. Electronic Structure of the Surface of the Ionic Liquid [EMIM][Tf2N] Studied by Metastable Impact Electron Spectroscopy (MIES), UPS, and XPS. *Langmuir* **2006**, *22* (17), 7120–7123.

(9) Morgner, H. The Quantitative Characterization of Liquid and Solid Surfaces with Metastable Helium Atoms. *AIP Conference Proceedings* **2000**, *500*, 687–698.

(10) Scudiero, L.; Shen, Y.; Gupta, M. C. Effect of Light Illumination and Temperature on P3HT Films, n-type Si, and ITO. *Applied Surface Science* **2014**, *292*, 100–106.

(11) Berlich, A.; Liu, Y. C.; Morgner, H. Evaporation of Ni and Carbon Containing Species onto NiO/Ni as Case Study for Metal Support Catalysts Investigated by Metastable Induced Electron Spectroscopy (MIES). *Radiation Physics and Chemistry* **2005**, *74* (3–4), 201–209.

(12) Berlich, A.; Liu, Y.-C.; Morgner, H. Growth of Nickel Nanoparticles on NiO/Ni (0 0 1): Evidence of Adsorbed Oxygen on Metal Particles by Metastable Induced Electron Spectroscopy (MIES). *Surface Science* **2008**, *602* (24), 3737–3744.

(13) Andersson, G.; Morgner, H. Determining the Stopping Power of Low Energy Helium in Alkanethiolates with Neutral Impact Collision Ion Scattering Spectroscopy (NICISS). *Nuclear Instruments & Methods in Physics Research Section B-Beam Interactions with Materials and Atoms* **1999**, *155* (4), 357–368.

(14) Andersson, G.; Morgner, H. Impact Collision Ion Scattering Spectroscopy (ICISS) and neutral Impact Collision Ion Scattering Spectroscopy (NICISS) at Surfaces of Organic Liquids. *Surface Science* **1998**, *405* (1), 138–151.

(15) Krebs, F. C. *Polymer Photovoltaics: A Practical Approach*; SPIE-International Society for Optical Engineering, 2008.

(16) Lu, K. *Nanoparticulate Materials: Synthesis, Characterization, and Processing*; John Wiley and Sons, 2012.

(17) Bowles, J. G.; Rochow, E. G. *An Introduction to Microscopy by Means of Light, Electrons, X-rays or Ultrasound*; Plenum Press, 1978.

(18) Krebs, F. C. Fabrication and Processing of Polymer Solar Cells: A Review of Printing and Coating Techniques. *Solar Energy Materials and Solar Cells* **2009**, *93* (4), 394–412.

(19) Butt, H.-J.; Cappella, B.; Kappl, M. Force Measurements with the Atomic Force Microscope: Technique, Interpretation and Applications. *Surface Science Reports* **2005**, *59* (1–6), 1–152.

(20) Melitz, W.; Shen, J.; Kummel, A. C.; Lee, S. Kelvin Probe Force Microscopy and its Application. *Surface Science Reports* **2011**, *66* (1), 1–27.

(21) Upama, M. B.; Wright, M.; Puthen-Veettil, B.; Elumalai, N. K.; Mahmud, M. A.; Wang, D.; Chan, K. H.; Xu, C.; Haque, F.; Uddin, A. Analysis of burn-in Photo Degradation in Low Bandgap Polymer PTB7 Using Photothermal Deflection Spectroscopy. *RSC Advances* **2016**, *6* (106), 103899–103904.

(22) Sumiya, M.; Ueda, S.; Fukuda, K.; Asai, Y.; Cho, Y.; Sang, L.; Uedono, A.; Sekiguchi, T.; Onuma, T.; Honda, T. Valence Band Edge Tail States and Band Gap Defect Levels of GaN Bulk and In x Ga1− x N Films Detected by Hard X-ray Photoemission and Photothermal Deflection Spectroscopy. *Applied Physics Express* **2018**, *11* (2), 021002.

(23) Sumiya, M.; Fukuda, K.; Yasiro, S.; Honda, T. Influence of Thin MOCVD-Grown GaN Layer on Underlying AlN Template. *Journal of Crystal Growth* **2020**, *532*, 125376.

(24) Borchert, H. *Solar Cells Based on Colloidal Nanocrystals*; Springer, 2014.

(25) Shao, Y.; Xiao, Z.; Bi, C.; Yuan, Y.; Huang, J. Origin and Elimination of Photocurrent Hysteresis by Fullerene Passivation in CH3NH3PbI3 Planar Heterojunction Solar Cells. *Nature Communications* **2014**, *5* (1), 1–7.

(26) Gueymard, C. A.; Myers, D.; Emery, K. Proposed reference Irradiance Spectra for Solar Energy Systems Testing. *Solar Energy* **2002**, *73* (6), 443–467.

(27) Tripathi, N.; Yanagida, M.; Shirai, Y.; Miyano, K. Improved Performance of Planar Perovskite Devices via Inclusion of Ammonium Acid Iodide (AAI) Derivatives Using a Two Step Inter-Diffusion Process. *Journal of Materials Chemistry C* **2019**, *7* (12), 3447–3451.

(28) Khadka, D. B.; Shirai, Y.; Yanagida, M.; Masuda, T.; Miyano, K. Enhancement in Efficiency and Optoelectronic Quality of Perovskite Thin Films Annealed in MACl Vapor. *Sustainable Energy & Fuels* **2017**, *1* (4), 755–766.

Chapter 4: Dipole Formation at Active Materials/P(NDI3N-T-Br) Interface in OPVs

Amira R Alghamdi,[1,2] Jonas M Bjuggren,[1] Xun Pan,[1,2] Mats R. Andersson[1,2] and Gunther G. Andersson[1,2*]

[1] Flinders Institute for Nanoscale Science and Technology, Flinders University, GPO Box 2100 Adelaide SA 5001, Australia.

[2] Flinders Microscopy and Microanalysis, College of Science and Engineering, Flinders University, Adelaide, South Australia 5042, Australia.

This work has been published in *Macromolecular Materials and Engineering*, 2022. The only alterations are that any experimental methods and analysis procedures previously described in Chapter 3 have been removed from this chapter, and supplementary information from the publication has been shown in the supplementary section (Appendix A).

Author contributions:

Amira Alghamdi: Designed and performed experiments, data analysis and interpretation of the data and prepared the manuscript for publication. **Jonas M Bjuggren:** Synthesised the new polymer to use it an interface layer and revision of manuscript. **Xun Pan:** revision of manuscript. **Gunther Andersson:** Intellectual contribution in conceptualising experiments, data interpretation and revision of manuscript. **Mats Andersson:** Intellectual contribution and revision of manuscript.

4.1 Abstract

In this work, a new potential electron transport material, poly[(*N,N′*-bis(3-(*N,N*-dimethyl)-*N*-ethylammonium)propyl)naphthalene-1,4,5,8-bis(dicarboximide)-2,6-diyl)-alt-2,5-thiophene)]dibromide P(NDI3N-T-Br), was studied in conjunction with active layers formed by poly[2,3-bis(3-octyloxyphenyl)quinoxaline-5,8-diyl-alt-thiophene-2,5-diyl] (TQ1) and poly[[N,N′-bis(2-octyldodecyl)-naphthalene-1,4,5,8-bis(dicarboximide)-2,6-diyl]-alt-5,5′-(2,2′-bithiophene)] (N2200). The energy levels of the active layer TQ1 and N2200 in contact with P(NDI3N-T-Br) have been determined by PES. The dipole formed at the interface of the active layer and P(NDI3N-T-Br) is significantly different to the dipole formed at the respective interface with ITO. The dipole between the active layer and P(NDI3N-T-Br) blocks the transfer of holes from TQ1 to P(NDI3N-T-Br), which is desired, but the electrons still transfer from the N2200 to P(NDI3N-T-Br) due to N2200 being an electron acceptor. This energy level alignment meets the expectation of using P(NDI3N-T-Br) as an interface layer in blocking the hole transfer to the interface layer when TQ1:N2200 is used in the active layer. This work provides an understanding of P(NDI3N-T-Br) as a charge extraction layer and indicates its potential to be used in organic PVs.

4.2 Introduction

OPV devices have now reached power conversion efficiencies of over 18%.[1–4,5] Their advantages are potential low fabrication costs, upscaling through roll-to-roll printing and flexibility. However, further improvements in their efficiency and stability are required for the active layer and the interfaces between the active layer and the electrodes.

Interfacial engineering using different interface layers is known as an essential approach for improving PCE of polymer SC by optimising the charge transport (CT) between the active layer and the electrodes through aligning the energy levels between the layers in a

device, leading to an improvement of the device efficiency. The properties of an interface layer have to allow for the transport of one type of charge carrier and the simultaneous blocking of the other. As an example, the interface layer helping to extract the electrons from the active layer should simultaneously block the transport of the holes in the same direction and, in this way, minimise undesired charge recombination, leading to improved device performance.

ZnO,[6–8] Ca and LiF have been shown to be effective electron extracting materials. The use of Ca,[9,10] LiF[11–14] and $CsCO_3$[15,16] is limited by these materials evaporating under vacuum. Ca and LiF are chemically unstable, which could lead to deterioration of the interface properties.[17] An advantage of ZnO over other materials is that it can be deposited from sol-gel solution or as nanoparticles from dispersions in device fabrication.[8,18–20,21–23] Organic-based materials have also been used as interface layers.[20,23–30]

The electronic energy levels of the component forming a real device are, among other factors, key for the device's performance and need to be determined. As an example, HOMO and LUMO levels are required to match between layers for achieving high-performing devices such that, in the direction of the desired transition, a small downhill gradient in energy of the energy levels between layers exists. The electronic structure at the electron extracting/active layer interface is influenced by the formation of dipoles. Such dipoles can support or block CT over interfaces. Examples are interface layers formed by LiF,[31] NaF,[32] Al[33,34] and ZnO,[35] which are well studied. The same can be expected when using organic materials as interface layers.[17,22,23,36–38] Presently, the formation of dipoles has to be investigated experimentally because they cannot yet be predicted from the chemical and electronic structure of the individual materials involved in the interface formation. In contrast to inorganic/organic interface layers, the formation of dipoles at organic/organic interfaces has been less studied.

The use of polymer-based CIL could improve the device's flexibility compared to using inorganic materials during the fabrication of the OPVs. Currently, reported polymer CIL

materials include poly[9,9-bis(1-sulfopropane-3-yl)-fl uorene-2,7-diyl-alt-(2,2′-bithiophene-5,5′)-diyl] (PFS),[26] water/alcohol soluble conjugated polymers (WSCPs),[39] PEI[25]and solution-processed CIL.[27] The material used in the present work have quaternary amines for WF modification of the electrodes and could form a dipole at the interface to the BHJ layer. The valence electron structure of the CIL improves its performance as electron transport materials because of the free electron pair, the counter ion and the amine group.[24]

Herein, poly[(*N,N′*-bis(3-(*N,N*-dimethyl)-*N*-ethylammonium)propyl)naphthalene-1,4,5,8-bis(dicarboximide)-2,6-diyl)-alt-2,5-thiophene)]dibromide P(NDI3N-T-Br) is investigated as an electron extraction interfacial layer. The aim of the work is to determine the position of the energy levels of P(NDI3N-T-Br) relative to the two active layer materials poly[2,3-bis(3-octyloxyphenyl)quinoxaline-5,8-diyl-alt-thiophene-2,5-diyl] (TQ1) and poly[[N,N′-bis(2-octyldodecyl)-naphthalene-1,4,5,8-bis(dicarboximide)-2,6-diyl]-alt-5,5′-(2,2′-bithiophene)] (N2200), and the potential formation of dipoles at these interfaces. The investigation shows that a dipole is formed at the interface between TQ1 (donor) and P(NDI3N-T-Br) blocks the transfer of holes from the active layer to the P(NDI3N-T-Br) interfacial layer while facilitating the transfer of electrons from N2200 (acceptor) to the electrode.

4.3 Experimental

4.3.1 Material and sample preparation

The materials and sample preparation used in this chapter are described in Chapter 3, Section 3.2.2.

The chemical structures of polymers studied in this work are illustrated in Figure 4-1. Two different batches of P(NDI3N-T-Br) were used for the present work, with minor differences in material properties.

In this study, the interfaces formed by TQ1 and N2200 with P(NDI3N-T-Br) were investigated separately, even though TQ1 and N2200 would form in a device a BHJ. However, even at the BHJ/P(NDI3N-T-Br) interface, TQ1 and N2200 would be individually in contact with the P(NDI3N-T-Br).

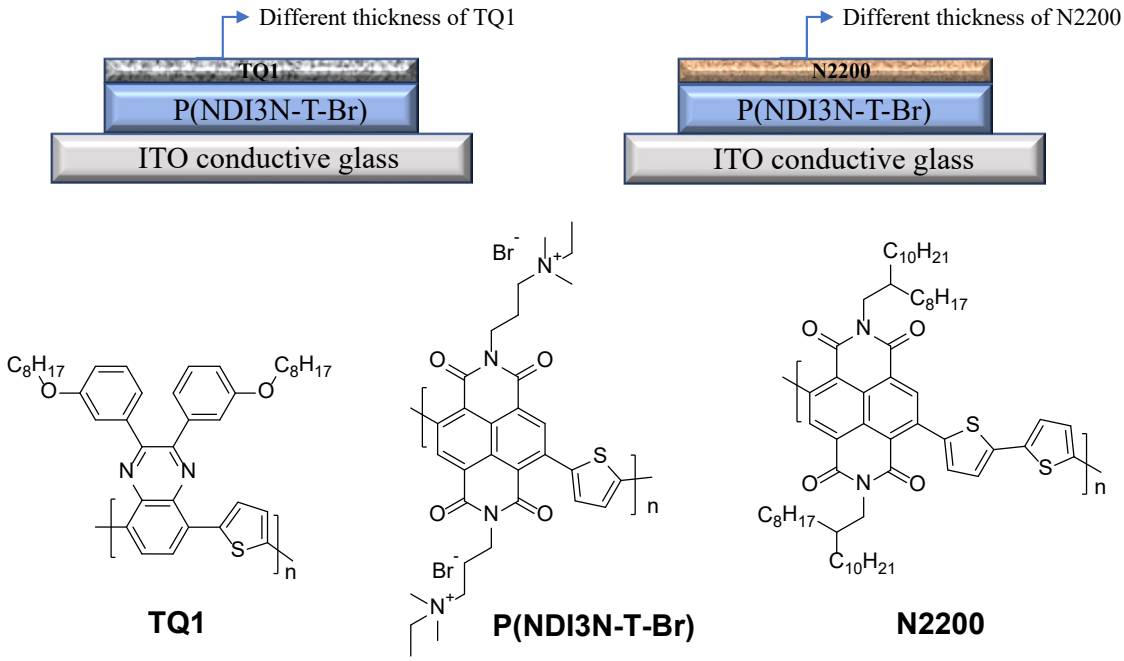

Figure 4-1. (Top) FA device structure using P(NDI3N-T-Br) as a CIL with the active layers TQ1 and N2200, and (Bottom) the chemical structure of the materials used in this work.

4.3.2 Methods: electron and ion spectroscopy methods

Experimental details for electron spectroscopy (XPS, UPS, IPES and MIES) and ion spectroscopy (NICISS) are described in Chapter 3. The analysis of UP and MIE spectra, including SVD analysis, are also described in Chapter 3.

4.4 Results

4.4.1 Depth distribution - NICISS results

Concentration depth profiles of all Br samples were extracted from the measured NICISS as described in Zhao et al.[40] and Andersson et al.[41] Br is only present in P(NDI3N-T-Br) and thus represents the concentration depth profile of this component. Figures 4-2 and S4-1 show the concentration depth profiles of Br derived from the NICIS spectra of the TQ1/P(NDI3N-T-Br) and N2200/P(NDI3N-T-Br) samples with different thicknesses of TQ1 and N2200. The depth profiles of the pristine P(NDI3N-T-Br) were used as reference. The concentration depth profiles of Br show a shift of the onset of the profiles towards larger depth and a decrease in gradient when TQ1 or N2200 are deposited onto P(NDI3N-T-Br). The average thickness of both TQ1 and N2200 layers are determined from the shift of the half onset of the Br concentration depth profile between that of the pristine P(NDI3N-T-Br) sample and samples with TQ1 or N2200 deposited onto P(NDI3N-T-Br).[42–44] Based on the working principle of NICISS, the increasing shift has to be interpreted as an increase in the TQ1 layer thickness.[41,45] In Table 4-1, the thickness of the TQ1 and N2200 layers deposited onto the P(NDI3N-T-Br) are shown for various solution concentrations of TQ1 and N2200. It is found that the TQ1 thickness is not proportional to the concentration of the TQ1 solution spin-coated on top of P(NDI3N-T-Br), as shown in Figure 4-2. The probable reason is that the conditions for the spin coating were slightly changing between samples. For the purpose of the present work, this variation of the TQ1 thickness is not relevant because the purpose for preparing the set of the TQ1/P(NDI3N-T-Br) samples is fabricating samples with a variation in TQ1 thickness. The change in gradient of the onset of the step means that either the TQ1 layer is not homogeneous in thickness or intermixes with the P(NDI3N-T-Br).[46] The gradient of the onset of the Br step is determined by two factors. First, the actual concentration depth profiles of Br, including the influence of inhomogeneity of the TQ1 layer or intermixing at the TQ1 and P(NDI3N-T-Br) interface.

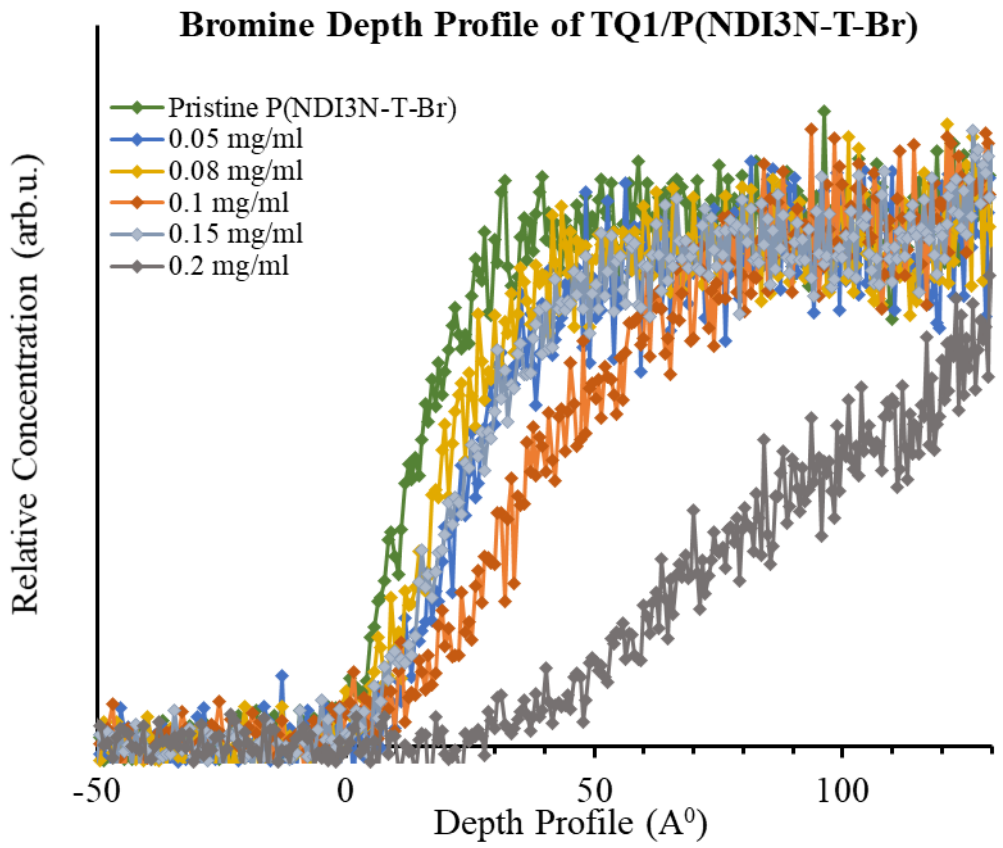

Figure 4-2. The distribution of Br at the TQ1/P(NDI3N-T-BR) interface layer, with the zero mark indicating the very surface of the samples.

Table 4-1

The Thicknesses of the TQ1 and N2200 Layers Deposited on P(NDI3N-T-BR), Evaluated from NICISS

Concentration of TQ1 TQ1/P(NDI3N-T-Br) interface	Thickness (nm)	Concentration of N2200 N2200/P(NDI3N-T-Br) interface	Thickness (nm)
0.20 mg/mL	7.7	2.5 mg/mL	10.0
0.15 mg/mL	1.2	2.0 mg/mL	8.0
0.10 mg/mL	2.2	1.5 mg/mL	5.0
0.08 mg/mL	0.8	1.0 mg/mL	3.0
0.05 mg/mL	1.3	0.3 mg/mL	1.0

Second, energy loss straggling of the He projectiles on their trajectory through the organic materials as investigated by Andersson[46] and Andersson et al.[47] It also causes an increase

in the broadening of the onset of the Br part of the spectrum. This second contribution to the gradient, however, is small compared to the first contribution for all samples but the plain P(NDI3N-T-Br). Thus, the gradient of the onset of the Br concentration depth profile reflects the inhomogeneity of the TQ1 thickness or the degree of intermixing. These two causes cannot be separated. However, this does not affect the interpretation of the results.

For the present work, it is not relevant whether the materials intermix or layers with inhomogeneous thickness are formed. The important aspect is that an interface is formed between TQ1 and P(NDI3N-T-Br) and between N2200 and P(NDI3N-T-Br), which can be analysed with electron spectroscopy.

4.4.2 Interface chemical composition - XPS results

TQ1/P(NDI3N-T-Br) interface

High-resolution XPS of TQ1/P(NDI3N-T-Br) for C, N, S, Br are shown in Figure 4-3 and for O in Figure S4-2A for the electron donor TQ1. The C1s spectra were fitted with four peaks for the TQ1/P(NDI3N-T-Br).

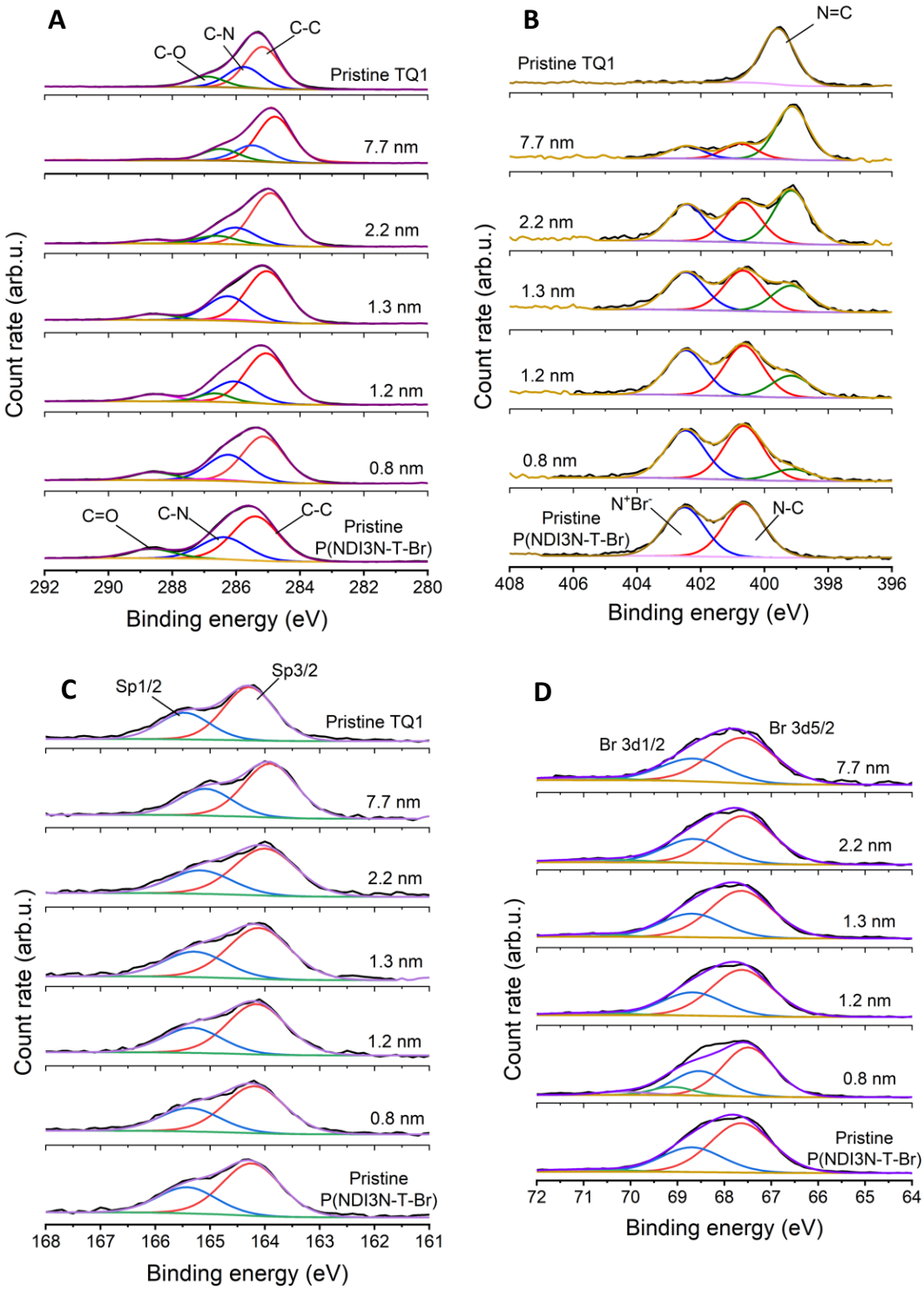

Figure 4-3. High-resolution XPS of (A) C1s, (B) N1s, (C) S 2p and (D) Br 3d of pristine P(NDI3N-T-Br), pristine TQ1 and samples with layers of 0.8 to 7.7 nm of TQ1 on P(NDI3N-T-Br).

Pristine TQ1 is required to be fitted with three peaks. The first C1s peak in the spectrum of pure TQ1 is found at 285.2 ± 0.3 eV and can be assigned to C-C bonds.[48] The second peak is at 285.7 ± 0.3 eV and can be identified as representing the C-N bond.[49] A third peak is found at 286.9 ± 0.3 eV, which is related to C-O.[50] Additionally, P(NDI3N-T-Br) has three C1s peaks, at 285.4 ± 0.3, 286.4 ± 0.3 and 288.7 ± 0.3 eV, related to C-C, C-N and C=O respectively.[48]

The position of the low binding energy C1s peak shifts with increasing thickness of TQ1, as shown in Figures 4-3A and 4-4A and in Table S4-1. The C-C peak shifts gradually, by a total of –0.6 ± 0.3 eV, which is discussed further below.

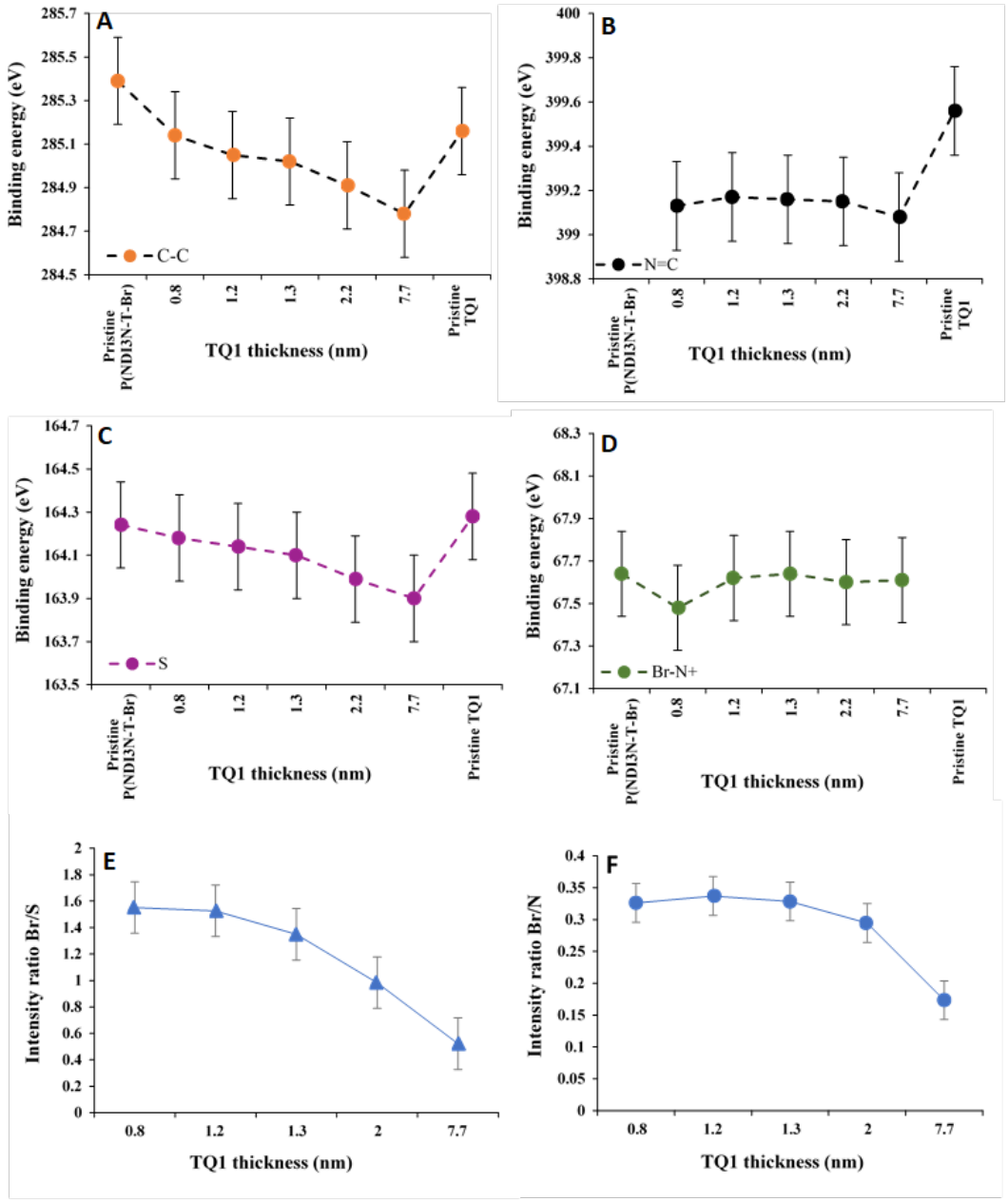

Figure 4-4. (A), (B) and (C) show the shift in the C, N and S peak positions towards lower binding energy with increasing TQ1 thickness. However, the $N^{+}Br^{-}$ and N-C stay constant without shift, as shown in Figure S4-3. (D) shows the Br peak position without any obvious shift. (E) shows the intensity ratios of Br/S and (F) Br/N for various deposition thickness of TQ1.

The N1s spectrum of the pristine TQ1 polymer were fitted with one peak at 399.5 ± 0.2 eV and the pristine P(NDI3N-T-Br) polymer were fitted with two peaks at 400.6 ± 0.2 eV and 402.5 ± 0.2 eV. The TQ1/P(NDI3N-T-Br) layered sample thus had to be fitted with three peaks, as shown in Figure 4-3B. The position of the first component

N=C at around 399.1 ± 0.2 is related to TQ1,[51,52] as shown in Figure 4-3B. The position of this peak is 0.4 eV lower than that of the pristine TQ1 sample, which is also shown in Figure 4-4B. This shift in binding energy will be attributed to the formation of a dipole at the TQ1/P(NDI3N-T-Br) interface in conjunction with the valance electron spectra. The dipole formation will be discussed below in more detail after more evidence for the dipole formation is provided via UPS and MIES.

In the layered system, the N peaks at 400.7 ± 0.2 and 402.4 ± 0.2 eV are related to N-C and N^+Br^- from P(NDI3N-T-Br),[53] and are at the same position as those of the pristine P(NDI3N-T-Br) sample. With increasing TQ1 thickness, the N peaks of P(NDI3N-T-Br) decrease in intensity and that of TQ1 increases, reflecting the increasing TQ1 thickness. The ratio of the two N peaks of P(NDI3N-T-Br) is close to 1:1 within the uncertainties of the experiments and the fitting procedure and does not change (see Table S4-2).

In Figure 4-3C, the S $2p_{3/2}$ peak is found at 164.0 ± 0.2 eV[54] and shows a gradual shift towards lower binding energy (see Figure 4-4C) with increasing thickness of TQ1. The largest shift is found for the 7.7 nm TQ1 sample of 0.4 ± 0.3 eV. There also might be a non-shifted S component of P(NDI3N-T-Br) that is difficult to separate from the shifting component of TQ1 because the first would be decreasing in intensity with increasing TQ1 thickness.

The Br $3d_{5/2}$ peak in Figure 4-3D was found at 67.6 ± 0.3 eV for all TQ1/P(NDI3N-T-Br) samples at a range of TQ1 thicknesses, including the pristine P(NDI3N-T-Br) sample interfaces layer with different thicknesses of TQ1, and corresponds to Br^-N^+[55]. The Br peak does not shift with increasing TQ1 thickness, as can be seen in Figure 4-4D, which shows that all the TQ1/P(NDI3N-T-Br) samples are not charging. The reason for the above-described shift of the C-C peak must therefore have another origin than the charging of the samples.

Figures 4-4E and 4-4F indicate the ratio of Br/S and Br/N as a function of different thicknesses of TQ1. The intensities of Br/S and Br/N show a significant decrease with increasing TQ1 layer thickness as Br is only a part of P(NDI3N-T-Br).

N2200/P(NDI3N-T-Br) interface

High-resolution XPS of C, N, S and Br for N2200/P(NDI3N-T-Br) are shown in Figure 4-5 and for O in Figure S4-2B for the electron acceptor N2200. The C1s spectra were fitted with three peaks. For pristine N2200, the first peak is located at 285 ± 0.2 eV and can be assigned to a C-C bond. The second peak is at 286.2 ± 0.2 and can be assigned to C-O. The third peak is at 288.6 ± 0.3 eV and related to C=O.[56] P(NDI3N-T-Br) is fitted with three peaks—at 285.4 ± 0.3, 286.6 ± 0.3 and 288.8 ± 0.3 eV—related to C-C, C-N and C=O, respectively.

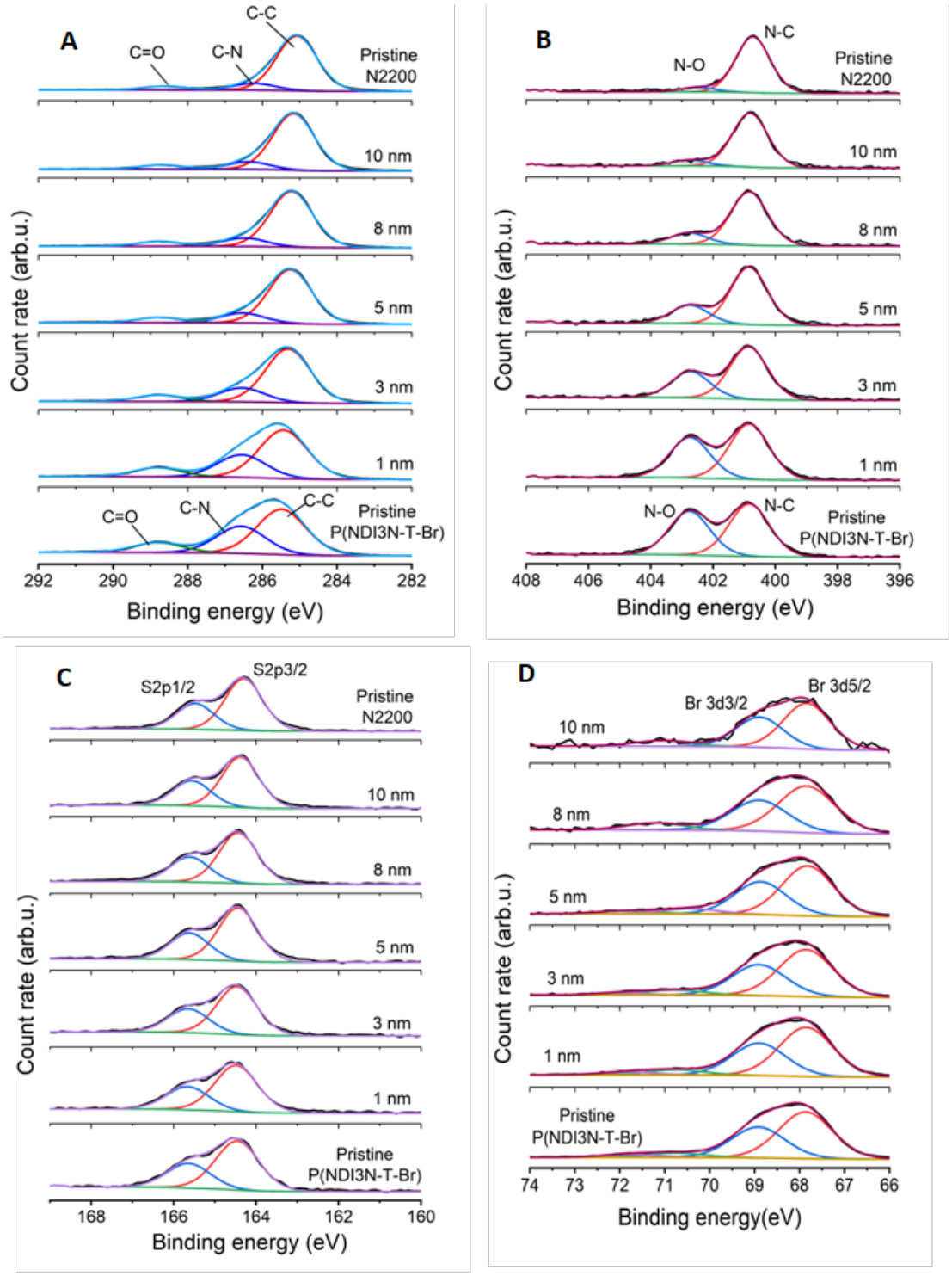

Figure 4-5. High-resolution XPS of (A) C1s, (B) N1s, (C) S 2p and (D) Br 3d of pristine P(NDI3N-T-Br), pristine N2200 and samples with layers of 1 to 10 nm of N2200 on P(NDI3N-T-Br).

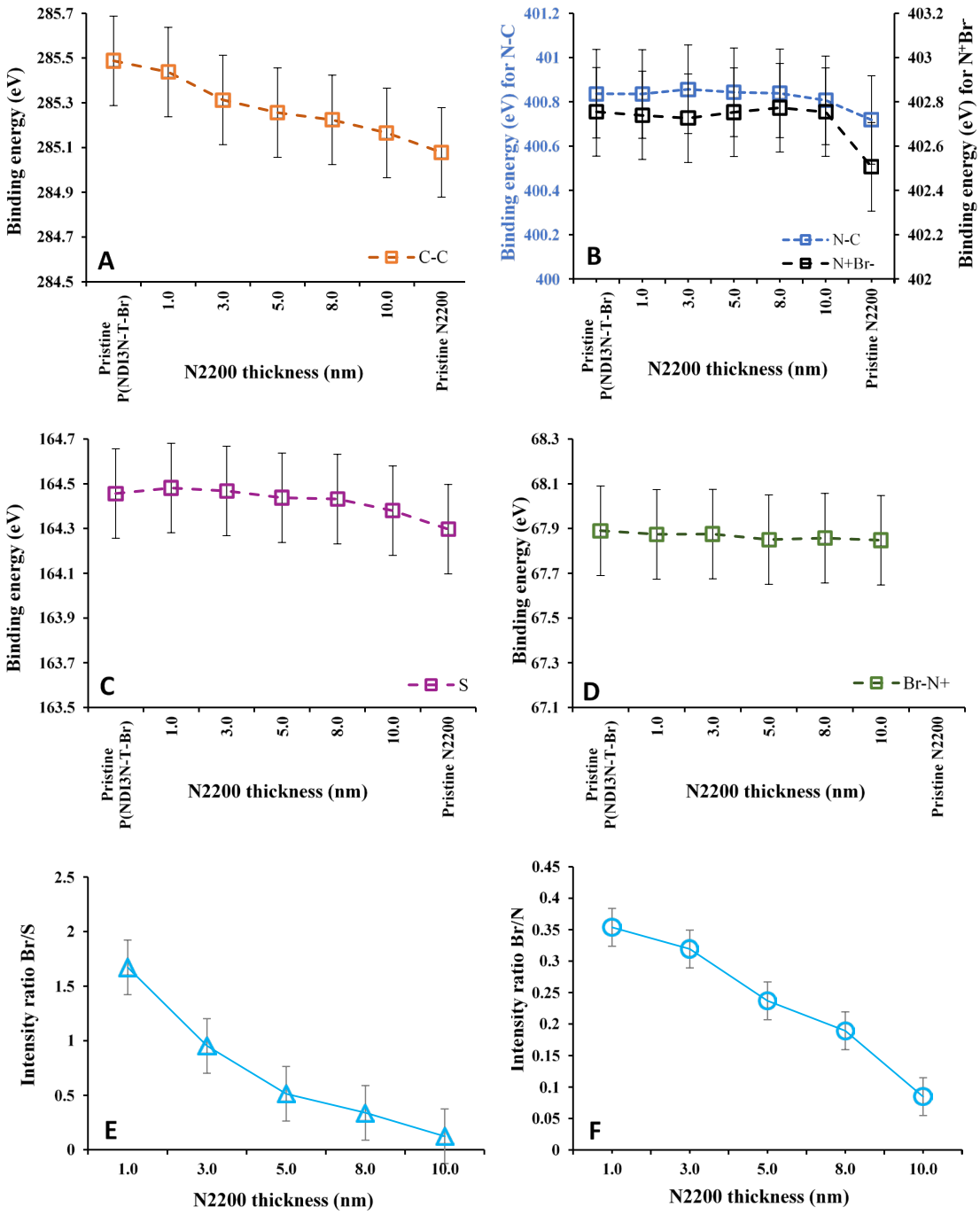

Figure 4-6. (A), (B), (C) and (D) show the position peaks of the C, N, S and Br and the change after increasing N2200 thickness. (E) shows the intensity ratios of Br/S and (F) Br/N for various deposition thickness of N2200.

The position of C-C peaks shows a small transition between the position of N2200 and P(NDI3N-T-Br), but there is no obvious shift due to a dipole formation, as shown in Figures 4-5A and 4-6A.

For all N2200/P(NDI3N-T-Br) samples, two N1s peaks were found: at 400.8 ± 0.2 eV, related to N-C, and at 402.7 ± 0.2 eV, assigned to N-O (see Figure 4-5B). The S $2p_{3/2}$ peak was found at 164.3 ± 0.2 eV, as shown in Figure 4-5C. The Br $3d_{5/2}$ peak was found at 67.8 ± 0.2eV, as shown in Figure 4-5D. Notably, the N1s, S $2p_{3/2}$ and Br $3d_{5/2}$ peaks do not shift with increasing N2200 thickness, as can be seen in Figures 4-6B, 4-6C and 4-6D, which will be discussed below.

As seen in Figures 4-6E and 4-6F, the intensity ratios of Br/S and Br/N decrease with an increasing the amount of N2200 deposited onto P(NDI3N-T-Br) as Br is only a part of P(NDI3N-T-Br).

4.4.3 Analysis of MIES, UPS and IPES results

First, we consider the sample with pristine TQ1, with TQ1 being the electron donor. In Figure 4-7A, the valence electron region as measured with UPS is shown together with the regions of the conduction electrons as measured with IPES. The procedure for obtaining the VB cut-off/E_{HOMO} and CB cut-off/E_{LUMO} can be determined by approximating the base line and the onset of the UP and IPE spectra with a linear curve and determining their intersections as illustrated for the pristine P(NDI3N-T-Br) sample in Figure 4-7A. The VB cut-off/E_{HOMO} and the CB cut-off/E_{LUMO} for pristine TQ1 are 1.4 ± 0.1 eV and –0.9 ± 0.1 eV, respectively. The VB cut-off/E_{HOMO} of pristine P(NDI3N-T-Br) is 2.2 ± 0.1 eV, and the CB cut-off/E_{LUMO} is –0.4 ± 0.1 eV, as listed in Table 4-2. The spectra of UPS, IPES and MIES for all TQ1/P(NDI3N-T-Br) samples are shown in Figure S4-4, and the values for VB, CB and WF are listed in Table S4-4.

Second, we consider the sample with pristine N2200, with N2200 being the electron accepter. In Figure 4-7B, the valence electron region as measured with UPS and the

regions of the conduction electron as measured with IPES of pristine N2200 are shown. The procedure for determining the VB cut-off/HOMO and CB cut-off/LUMO is the same as explained above and these are listed for all samples in Table 4-2. P(NDI3N-T-Br) is shown in Figures 4-8A and 4-8B. The reason is that these were two different batches with differences in the structure of the occupied and unoccupied energy levels but with the same HOMO and LUMO. The N2200/P(NDI3N-T-Br) interfaces of UPS, IPES and MIES are shown in Figure S4-5, and the values are listed in Table S4-5. The full spectra of UPS and MIES of TQ1 and N2200 are shown in Figures S4-6 and S4-7.

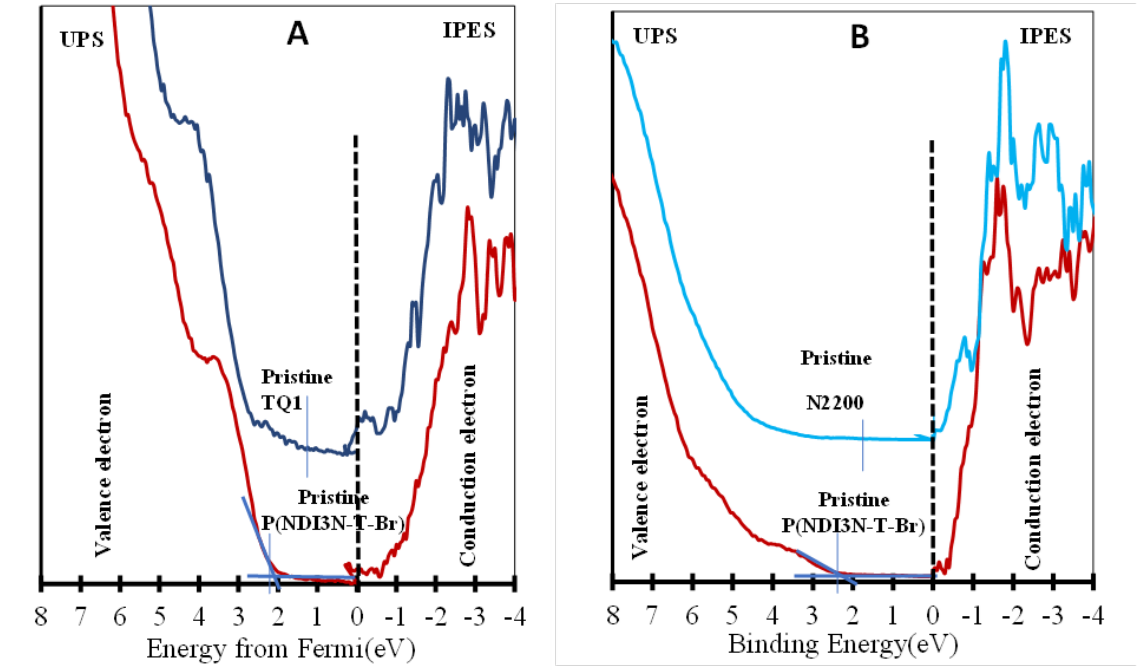

Figure 4-7. (A) The plot of the CB/E_{LUMO} and VB/E_{HOMO} region of TQ1 and P(NDI3N-T-Br) as measured via UPS and IPES. (B) The plot of the CB/E_{LUMO} and VB/E_{HOMO} region of N2200 and P(NDI3N-T-Br) as measured via UPS and IPES. For determining the cut-off for VB and CB, the level of noise in the UP and IPE spectra must be considered, with the IPE spectra showing a higher level of noise.

Table 4-2

The Values of VB/E_{HOMO}, CB/E_{LUMO} and Energy gap (Eg) of the TQ1, N2200 and P(NDI3N-T-Br) Samples

Polymer	VB/E_{HOMO} (eV) ± 0.1	CB/E_{LUMO} (eV) ± 0.1	Eg (eV) ± 0.2
Pristine TQ1	1.4	–0.9	2.3
Pristine N2200	1.7	–0.8	2.5
Pristine P(NDI3N-T-Br)	2.2	–0.4	2.6

Note. All energies are indicated with a zero point at E_F.

The P(NDI3N-T-Br) spectra for UPS, IPES and MIES are slightly different for the investigation of the TQ1/P(NDI3N-T-Br) and N2200/P(NDI3N-T-Br) interfaces due to using two different batches of P(NDI3N-T-Br). The features of P(NDI3N-T-Br) in the spectra are the same, but their relative intensities differ. The reason is most likely some difference in the ratio of the tertiary amine pendant groups to the quaternary amine pendant groups, which affects only slightly the function of the polymer. The cut-offs for UPS, IPES and MIES are the same for both batches, showing that the overall results are not affected by the differences between the batches.

4.4.4 Decomposition of valance electron of MIES and UPS

TQ1/P(NDI3N-T-Br) interface

The UP and MIE spectra are shown in Figure 4-8. The SVD algorithm was applied for component analysis of the UP and MIE spectra, with the results of the analysis shown in Figure 4-8 for the TQ1/P(NDI3N-T-Br) interface. The SVD analysis shows that two components were required to fit the entire series of spectra for both UPS (see Figure 4-8A) and MIES (see Figure 4-8B). The first component, reference A, can be identified as the TQ1 spectrum, but shifted on the energy scale by around –0.7 ± 0.1 eV; thus, towards lower binding energy compared to the pristine TQ1 spectrum. MIES shows a similar finding where reference A has the same shape as the spectrum of pristine TQ1 but shifted by –0.5 ± 0.1 eV towards lower binding energy compared to the spectrum of pristine TQ1. The reference spectrum B in both UPS and MIES analysis is that of P(NDI3N-T-Br) and

does not show any shift, as shown in Figure S4-8 (A and B). The shift of the UP and MIE spectra corresponds approximately to the shift as found via XPS in the position of the C1s peak between the pristine TQ1 sample and the TQ1 deposited onto P(NDI3N-T-Br) at the largest thickness of TQ1 (7.7 nm), as can be seen in Figure 4-4A.

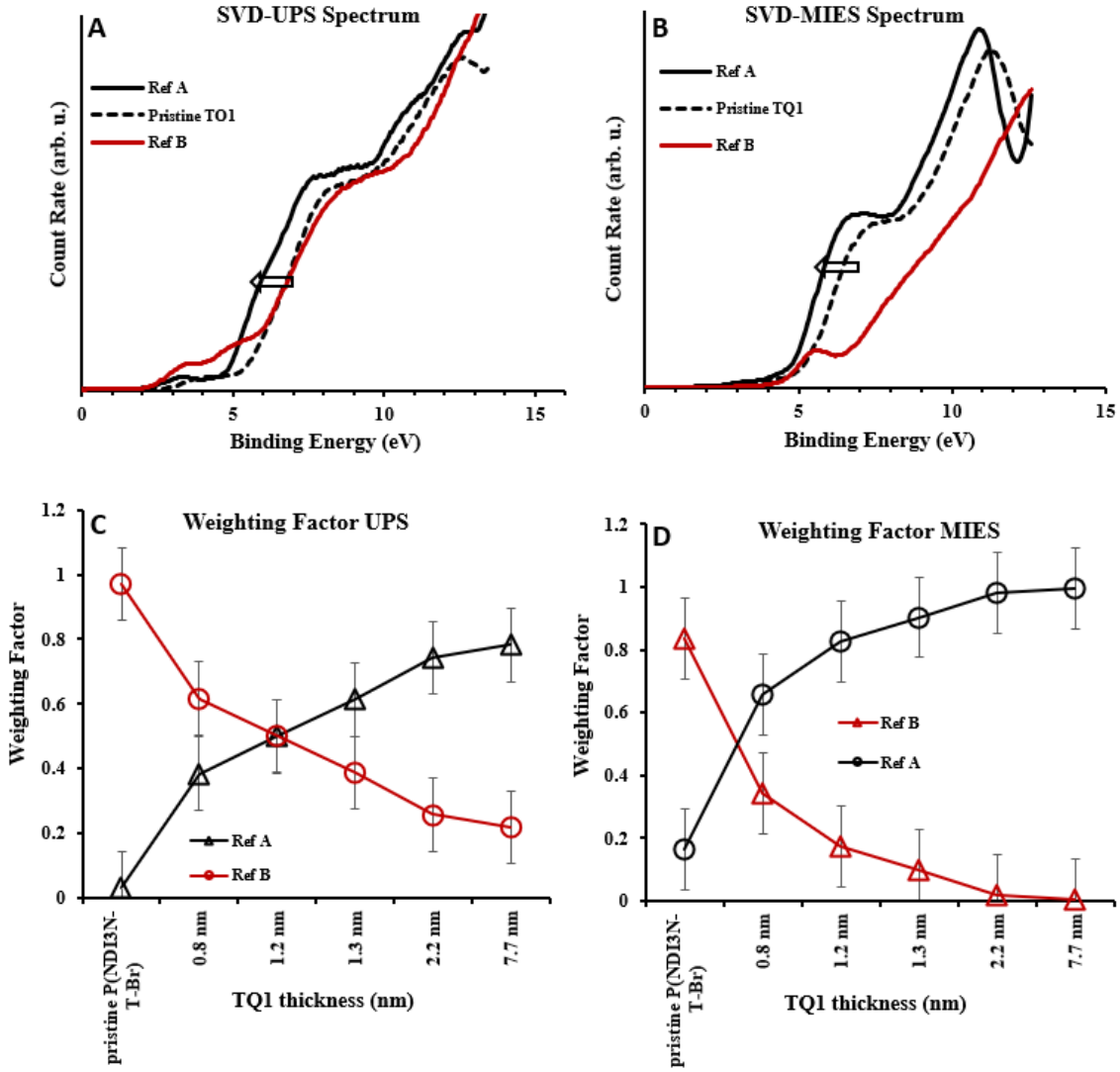

Figure 4-8. (A) and (B) show the reference spectra of UPS and MIES for TQ1/P(NDI3N-T-Br). TQ1 shifts towards lower binding energy. (C) and (D) show the weighting factors for TQ1 and P(NDI3N-T-Br) of the UP and MIES spectra.

The UPS weighting factors for the P(NDI3N-T-Br) show a decrease with increasing thickness of TQ1, as indicated in Figure 4-8C. A similar observation was found for the MIES weighting factors, as shown in Figure 4-8D. The findings in Figures 4-8C and 4-

8D demonstrate that TQ1 and P(NDI3N-T-Br) could be intermixing when the first is spin-coated on top of the second or island formation where the islands have a range of thickness. This conclusion is based on the MIES sensitive exclusively for the outermost layer. Thus, finding a MIES weighting factor being larger than zero (see Figure 4-8D) indicates that the specific substance forms part of the outermost layer. The same argument holds in a similar way also for UPS, which is sensitive for the outermost few nm only. The MIES weighting factor for TQ1 and for the pristine P(NDI3N-T-Br) sample in Figure 4-8D is 0.1. This seems to show a presence of TQ1 in the pristine P(NDI3N-T-Br) sample. However, the uncertainty of the weighting factors is 0.1; thus, within the accuracy of the SVD analysis, the contribution of TQ1 can still be considered as zero. This is in agreement with the NICISS results. At 7.7 nm thickness of TQ1, an almost close TQ1 layer is achieved. The weighting factor of the shifted TQ1 UP spectrum increases with increasing thickness of TQ1 on P(NDI3N-T-Br). It should be noted that the weighting factors for the reference spectra for UPS and MIES are different because the probing depth of both techniques is different. Figures 4-8C and 4-8D show that the intermixing of TQ1 and P(NDI3N-T-Br) is similar in the outermost layer and the subsurface region.

N2200/P(NDI3N-T-Br) interface

For the N2200/P(NDI3N-T-Br) interface, two components were found for both UPS and MIES, as shown in Figures 4-9A and 4-9B. The reference A from the UPS analysis can be identified as the N2200 spectrum and shifted on the energy scale by around -0.2 ± 0.1 eV towards lower binding energy. Reference spectrum B is identical to P(NDI3N-T-Br) and does not show any shift, as shown in Figure S4-9A. MIES finding shows two references. Reference A has the same shape as the spectrum of pristine N2200, and reference B is the same as P(NDI3N-T-Br). However, MIES spectra do not show any shift, as shown in Figures 4-9B and S4-8B. The minor shift of the UP and MIE spectra corresponds approximately to the absence of a shift in XPS in the position of the C1s peak between the pristine N2200 sample and the N2200 deposited onto P(NDI3N-T-Br) at the largest thickness of N2200 (10 nm), as can be seen in Figure 4-6A.

The weighting factors for both UPS and MIES are shown in Figures 4-9C and 4-9D. The same holds here for the uncertainty of the weighting factors as described above. It can be seen in Figures 4-9C and 4-9D that the intermixing of N2200 and P(NDI3N-T-Br) is lesser in the outermost layer compared to the subsurface region. This contrasts with the finding for TQ1 and is also reflected in the concentration depth profiles measured with NICISS.

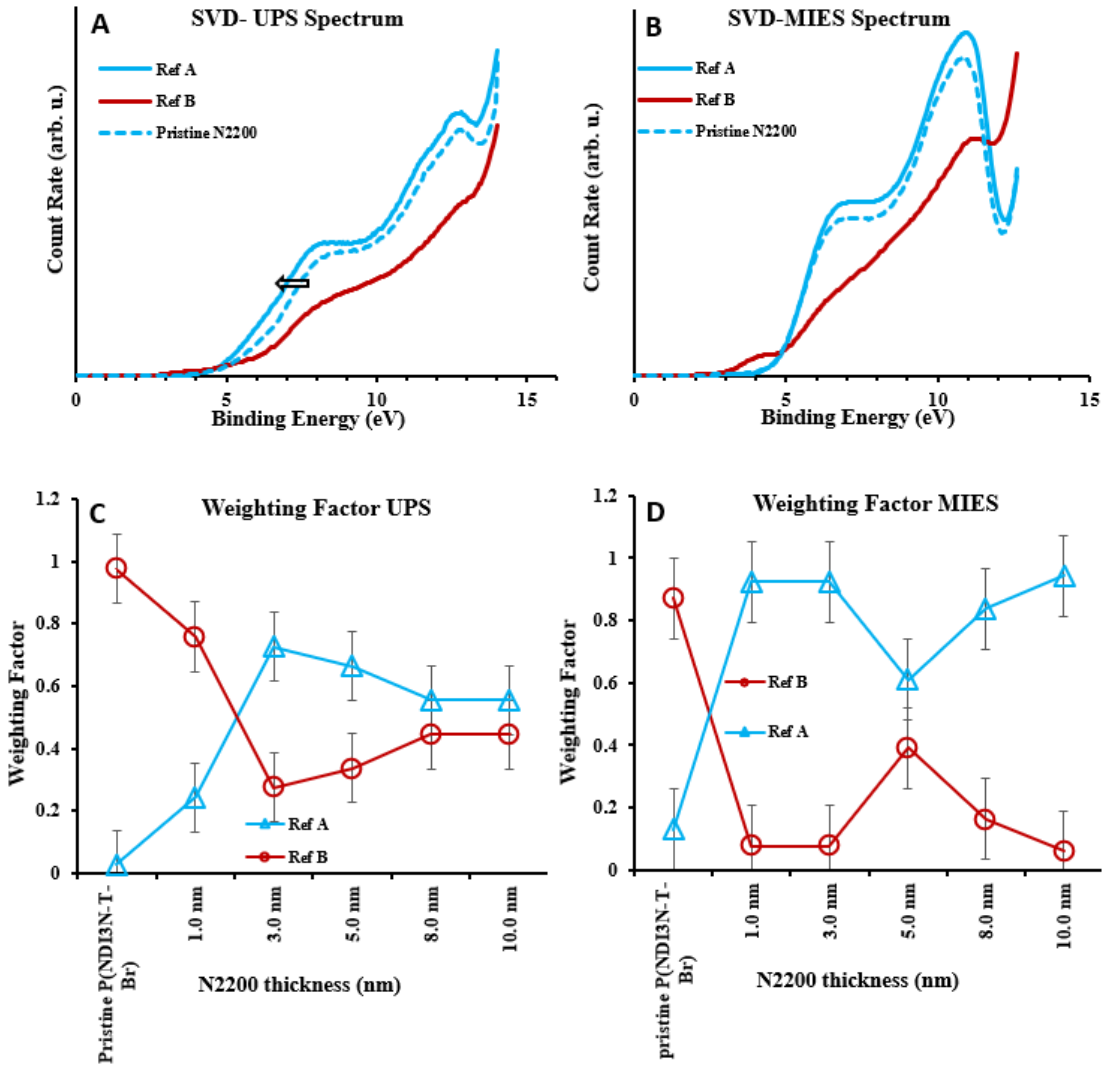

Figure 4-9. (A) and (B) show the reference spectra of N2200/P(NDI3N-T-Br) obtained from UPS and MIES, where N2200 shifts towards lower binding energy. (C) and (D) show the weighting factors of N2200 and P(NDI3N-T-Br) from UP and MIES spectra.

It should be noted that the intermixing of both combinations of substances (N2200/P(NDI3N-T-Br) and TQ1/P(NDI3N-T-Br)) could be either a mixing on the molecular scale or by the formation of domains. Intermixing of substances is based on their physical properties, including their solvation in the respective solvents. The specific reason for the difference in intermixing is not clear and not a subject of the present work.

4.5 Discussion

Samples with a range of TQ1 and N2200 thickness deposited onto P(NDI3N-T-Br) were prepared for analysing the structure of the TQ1/P(NDI3N-T-Br) and N2200/P(NDI3N-T-Br) interfaces. A combination of methods has been used to determine the intermixing and electronic structure of the TQ1/P(NDI3N-T-Br) and N2200/P(NDI3N-T-Br) interfaces. NICISS was used to determine the concentration depth profiles across the interface of TQ1 and N2200 on P(NDI3N-T-Br). The thickness can be obtained from the shift of the half onset of the Br peak with respect to the Br of pristine P(NDI3N-T-Br), as Br is a component of the P(NDI3N-T-Br) layer.

Through UPS and MIES, it was found that the spectra of TQ1 and N2200 experience a shift in binding energy for UPS by –0.7 eV for TQ1 and –0.2 eV for N2200. The shift is to a lower binding energy, demonstrating that the negative end of the dipole is directed towards TQ1 and N2200, while the positive end moves towards the buried layer of P(NDI3N-T-Br).

The physical meaning of the spectrum shift of the TQ1 and N2200 can be explained with the formation of a dipole at the TQ1/P(NDI3N-T-Br) and N2200/P(NDI3N-T-Br) interface. The component of TQ1 and N2200 shifted due to the dipole at the interface being subject to a bias on the electron energy scale of the UP spectra. The formation of a dipole at the interface also increases the WF of TQ1 when deposited onto P(NDI3N-T-Br). However, for N2200, the WF did not show a significant change after the deposition onto P(NDI3N-T-Br). The change in dipole at the TQ1/P(NDI3N-T-Br) and

N2200/P(NDI3N-T-Br) interface is not necessarily reflected in a change in the WF of the samples. The reason is that the WF is a measure for the dipole at the sample surface and not the buried interface between TQ1/P(NDI3N-T-Br) and N2200/P(NDI3N-T-Br). Further, the samples investigated here show a mixture of TQ1 and P(NDI3N-T-Br) and N2200 and P(NDI3N-T-Br), and the WF of the samples is thus determined by the presence of both components. In such a mixture, the component with the higher WF defines the overall WF of the surface unless the two components are not well mixed but separate, as shown by Sharma et al.[57] It also should be noted that ITO is a reference sample here and noting the formation of a dipole is referring to a change of the dipole existing at the interface with the reference sample. The formation of a dipole at a buried interface will influence the electronic properties of the components in the same way as an electronic bias will shift the electric potential of a sample, thus shifting the UP spectra as observed here but also influencing the WF through a shift as well. The reference to the XPS core levels, however, provides a reference for which component is subject to a dipole or bias, which shows that the TQ1/P(NDI3N-T-Br) interface is subject to the formation of a dipole.

The formation of a dipole is supported by the XPS result. For TQ1, the C1s, N1s (N=C) and S components of TQ1 show a shift towards lower binding energy and can be linked to the functional groups of TQ1 deposited onto P(NDI3N-T-Br), which are located in the interface dipole. Previously, we showed that the shifts observed via XPS were not caused by charging of the samples.

In Figures 4-4A, 4-4B and 4-4C, the shift of the C, N and S peaks related to TQ1 are around 0.4 eV towards lower binding energy. For the analysis of C1s, the C-C peak at the TQ1/P(NDI3N-T-Br) interface within the dipole layer shifted with the increasing thickness of TQ1 relative to the pristine TQ1, indicating that the TQ1 layer is affected by the dipole formation. The absolute position of the C1s peak in XPS allows for determining which interface the dipole formed at. The C1s peak for P(NDI3N-T-Br) on ITO and TQ1

on ITO are the same in binding energy within 0.2 eV. The binding energy of C1s for 7 nm TQ1 on P(NDI3N-T-Br) is 0.4 eV, lower than that for TQ1 on ITO. Thus, the dipole is formed at the TQ1/P(NDI3N-T-Br) interface.

It can be noted that the C and S components show a gradual shift, while the N component (N=C) of TQ1 shows an instant shift. The reason for this difference is that C and S are a part of both substances, while N is only a part of TQ1. Thus, the XPS C1s and S 2p spectra are a superposition of the spectra of TQ1 and P(NDI3N-T-Br), and the contribution of C and S coming from each of the substances are difficult to separate. The shift is seen instantly for N because it is only a part of TQ1 and thus does not overlap with another N contribution coming from P(NDI3N-T-Br).

For N2200, it was found via UPS that the shift in binding energy of N2200 is –0.2 eV. This shift is caused by the formation of a small dipole between N2200 and P(NDI3N-T-Br). The formation of a small dipole between N2200 and P(NDI3N-T-Br) is also reflected in the XPS of C, S and N, as shown in Figure 4-6.

The shift in UPS of TQ1 (–0.7 ± 0.1 eV) is larger than the shift of N2200 (–0.2 ± 0.1 eV), which indicates that TQ1 has a stronger dipole formed at the interface with P(NDI3N-T-Br) than N2200. The TQ1/P(NDI3N-T-Br) interface XPS allows also to determine the location of the dipole for the N2200/P(NDI3N-T-Br) interface. The C1s peak for N2200 on ITO and N2200 on P(NDI3N-T-Br) are the same in binding energy within 0.1 eV. The binding energy of C1s for 10 nm N2200 on ITO is 0.4 eV lower than for P(NDI3N-T-Br) on ITO. Thus, there is no dipole formed at the N2200/P(NDI3N-T-Br) interface.

Energy levels and implication for CT over the interface

Figure 4-10 illustrates the energy level diagram of electron donor TQ1 and electron acceptor N2200 with the values for the energy levels taken from the electron spectroscopy measurements. The energy shift found via UPS is interpreted as formation of a dipole at the respective interface and allows for estimating the strength of the dipole between TQ1 and P(NDI3N-T-Br) and between N2200 and P(NDI3N-T-Br). In the top row of Figure

4-10A, the energy level diagrams at the interface between each of the three substances TQ1, N2200 and P(NDI3N-T-Br) on ITO are shown. In the bottom row of Figures 4-10B and 4-10C, the energy level diagrams for TQ1/P(NDI3N-T-Br)/ITO and N2200/P(NDI3N-T-Br)/ITO are shown. In the bottom row, the possible and not possible CT processes for holes (from the donor TQ1) and electrons (from the acceptor N2200) are also indicated. The desired CT processes are the transfer of electrons from TQ1/N2200 to P(NDI3N-T-Br) and blocking the transfer of holes in the same direction. Electrons would be transferred only from N2200 as the acceptor and holes from TQ1 as the donor.

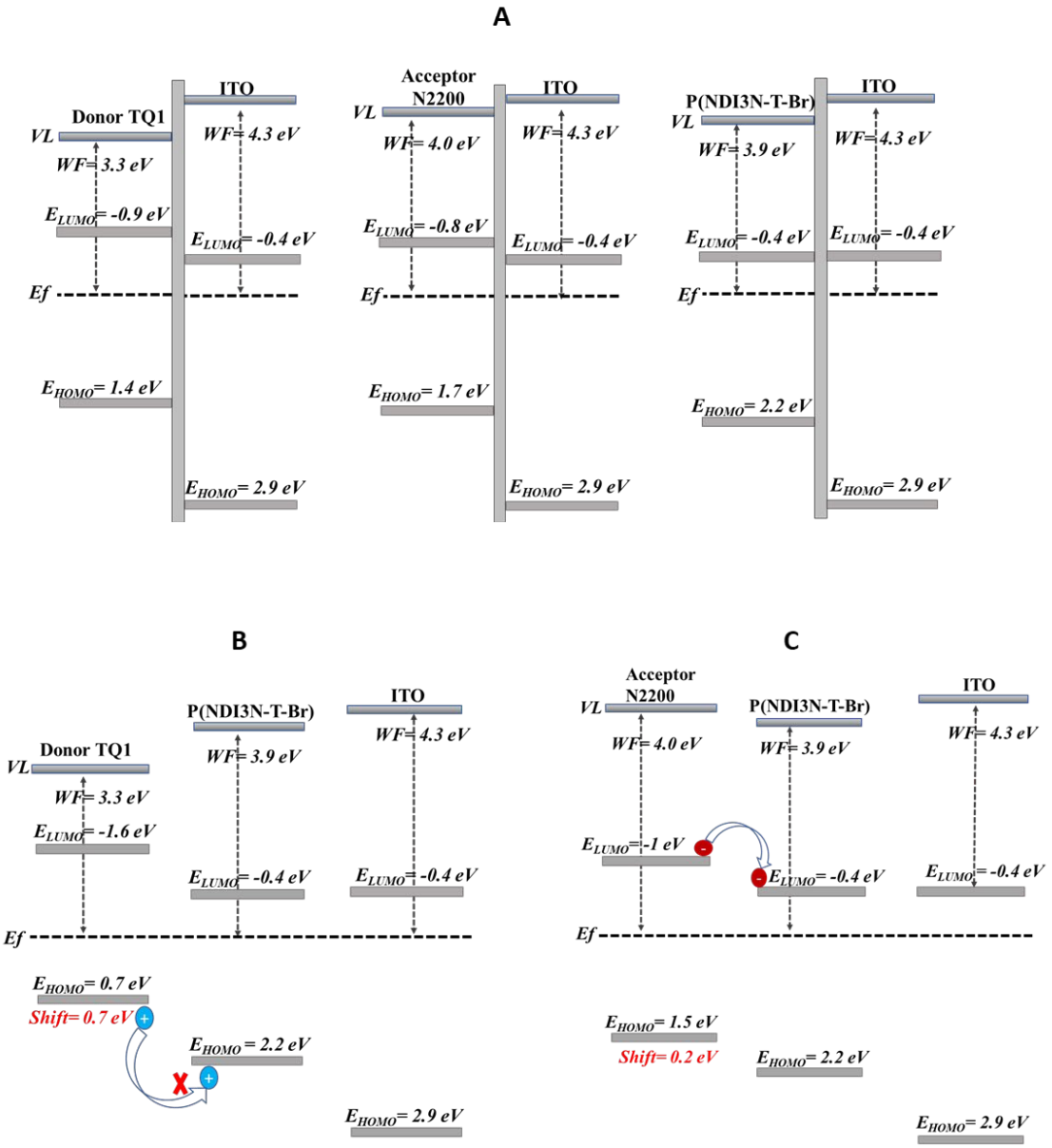

Figure 4-10. (A) the energy level of TQ1/ITO, P(NDI3N-T-Br)/ITO and N2200/ITO. (B) the energy level of TQ1/P(NDI3N-T-Br)/ITO. (C) the energy level of N2200/P(NDI3N-T-Br)/ITO, the energy level of TQ1/P(NDI3N-T-Br)/ITO and N2200/P(NDI3N-T-Br)/ITO and the CT over the interface layers with the interface dipole that shifted the VB/E_{HOMO} and CB/E_{LUMO} level. VL, vacuum level.

As illustrated in Figure 4-10, the E_{HOMO} and E_{LOMO} show that the TQ1 and N2200 layers shifted upwards on the energy scale as a result of the dipole formation at the interface layer. This shift moves the VB/E_{HOMO} of TQ1 (see Figure 4-10B) far above that of P(NDI3N-T-Br), blocking the hole transfer from TQ1 to P(NDI3N-T-Br). Being affected

only slightly by a shift, the CB/E_{LUMO} of N2200 is now above that of P(NDI3N-T-Br). This energy level alignment meets the expectation of using P(NDI3N-T-Br) as an interface layer in blocking the hole transfer and facilitating the electron transfer to the interface layer when TQ1:N2200 is used in the active layer.

In the present work, the TQ1/P(NDI3N-T-Br) and N2200/P(NDI3N-T-Br) interfaces are investigated individually. In a functioning device, TQ1 and N2200 would form a joint BHJ layer forming an interface with P(NDI3N-T-Br). At the TQ1/N2200 BHJ and P(NDI3N-T-Br) interfaces, TQ1 and N2200 would be in contact with P(NDI3N-T-Br). The present study then represents these individual interfaces.

The interpretation of the shift between the spectra as dipole is based on the referencing of the dipole to the interface between all three substances (TQ1, N2200 and P(NDI3N-T-Br)) and ITO. The reason is that the spectra of the reference samples are from the respective substance deposited onto ITO. In case there is a dipole between each of TQ1, N2200, P(NDI3N-T-Br) and ITO, the dipole is different. However, the interpretation of the energy transfer of electrons and holes is not affected by such changes.

4.6 Conclusion

The energy levels of the active layer (TQ1 and N2200) in contact with P(NDI3N-T-Br) were determined with electron spectroscopy. It was found that the spectra of TQ1 experience a significant shift in binding energy while those of N2200 experience only a minor shift. The shifts observed are interpreted as dipole formation at the respective interface. The strong dipole was found at the TQ1/(NDI3N-T-Br) through valence electron spectroscopy (UPS and MIES) and was supported by XPS results. The C1s, N1s (N=C) and S components of TQ1 show a shift towards lower binding energy and can be linked to the functional groups of TQ1 deposited onto P(NDI3N-T-Br), which are located in the region of the interface dipole. Given the existence of the shift, the E_{HOMO} of TQ1

moved above that of P(NDI3N-T-Br) when the materials made contact, thus blocking the hole from the E_{HOMO} of TQ1 to E_{HOMO} of P(NDI3N-T-Br). However, the electron still transfers from the E_{LUMO} of N2200 to P(NDI3N-T-Br). It is concluded that the energy level alignment of TQ1, N2200 and P(NDI3N-T-Br) meets the expectation of using P(NDI3N-T-Br) as an interface layer in blocking the hole transfer and allowing for the electron transfer to the interface layer when TQ1:N2200 is used in the active layer.

4.7 Acknowledgement

The authors would like to acknowledge the support of the Australian National Fabrication Facility (ANFF) and Australian Microscopy & Microanalysis Research Facility (AMMRF) regarding using experimental equipment. The authors acknowledge Flinders Microscopy and Microanalysis and their expertise.

4.8 References

(1) Zhang, T.; An, C.; Bi, P.; Lv, Q.; Qin, J.; Hong, L.; Cui, Y.; Zhang, S.; Hou, J. A Thiadiazole-Based Conjugated Polymer with Ultradeep HOMO Level and Strong Electroluminescence Enables 18.6% Efficiency in Organic Solar Cell. *Advanced Energy Materials* **2021**, *11* (35), 2101705.

(2) Zhang, M.; Zhu, L.; Zhou, G.; Hao, T.; Qiu, C.; Zhao, Z.; Hu, Q.; Larson, B. W.; Zhu, H.; Ma, Z. Single-Layered Organic Photovoltaics with Double Cascading Charge Transport Pathways: 18% Efficiencies. *Nature Communications* **2021**, *12* (1), 1–10.

(3) Peng, W.; Lin, Y.; Jeong, S. Y.; Genene, Z.; Magomedov, A.; Woo, H. Y.; Chen, C.; Wahyudi, W.; Tao, Q.; Deng, J. Over 18% Ternary Polymer Solar Cells Enabled by a Terpolymer as the Third Component. *Nano Energy* **2022**, *92*, 106681.

(4) Bi, P.; Zhang, S.; Chen, Z.; Xu, Y.; Cui, Y.; Zhang, T.; Ren, J.; Qin, J.; Hong, L.; Hao, X. Reduced Non-Radiative Charge Recombination Enables Organic Photovoltaic Cell Approaching 19% Efficiency. *Joule* **2021**, *5* (9), 2408–2419.

(5) Liu, Q.; Jiang, Y.; Jin, K.; Qin, J.; Xu, J.; Li, W.; Xiong, J.; Liu, J.; Xiao, Z.; Sun, K.; Yang, S.; Zhang, X.; Ding, L. 18% Efficiency Organic Solar Cells. *Science Bulletin* **2020**, *65* (4), 272–275.

(6) Cheng, Y.-S.; Liao, S.-H.; Li, Y.-L.; Chen, S.-A. Physically Adsorbed Fullerene Layer on Positively Charged Sites on Zinc Oxide Cathode Affords Efficiency Enhancement in Inverted Polymer Solar Cell. *ACS Applied Materials & Interfaces* **2013**, *5* (14), 6665–6671.

(7) Gilot, J.; Barbu, I.; Wienk, M. M.; Janssen, R. A. The Use of ZnO as Optical Spacer in Polymer Solar Cells: Theoretical and Experimental Study. *Applied Physics Letters* **2007**, *91* (11), 113520.

(8) White, M.-S.; Olson, D.; Shaheen, S.; Kopidakis, N.; Ginley, D. S. Inverted Bulk-Heterojunction Organic Photovoltaic Device Using a Solution-Derived ZnO Underlayer. *Applied Physics Letters* **2006**, *89* (14), 143517.

(9) Guo, X.; Zhang, M.; Ma, W.; Ye, L.; Zhang, S.; Liu, S.; Ade, H.; Huang, F.; Hou, J. Enhanced Photovoltaic Performance by Modulating Surface Composition in Bulk Heterojunction Polymer Solar Cells Based on PBDTTT-C-T/$PC_{71}BM$. *Advanced Materials* **2014**, *26* (24), 4043–4049.

(10) Braun, D.; Heeger, A. Erratum: Visible light emission from semiconducting polymer diodes [Appl. Phys. Lett. 58, 1982 (1991)]. *Applied Physics Letters* **1991**, *59* (7), 878–878.

(11) Jönsson, S.; Carlegrim, E.; Zhang, F.; Salaneck, W. R.; Fahlman, M. Photoelectron Spectroscopy of the Contact Between the Cathode and the Active Layers in Plastic Solar Cells: The Role of LiF. *Japanese Journal of Applied Physics* **2005**, *44* (6R), 3695.

(12) Zhao, S.-H.; Chang, J.-K.; Fang, J.-J.; Tsai, H.-W.; Liu, I.-H.; Tseng, W.-H.; Pi, T.-W.; Chen, M.-H. Efficiency Enhancement Caused by Using LiF to Change Electronic Structures in Polymer Photovoltaics. *Thin Solid Films* **2013**, *545*, 361–364.

(13) Turak, A.; Zgierski, M. Z.; Dharma-Wardana, M. C. LiF Doping of C60 Studied with X-ray Photoemission Shake-Up Analysis. *ECS Journal of Solid State Science and Technology* **2017**, *6* (6), M3116.

(14) Gao, Y. Surface Analytical Studies of Interfaces in Organic Semiconductor Devices. *Materials Science and Engineering: R: Reports* **2010**, *68* (3), 39–87.

(15) Huang, J.; Li, G.; Yang, Y. A Semi-Transparent Plastic Solar Cell Fabricated by a Lamination Process. *Advanced Materials* **2008**, *20* (3), 415–419.

(16) Liao, H.-H.; Chen, L.-M.; Xu, Z.; Li, G.; Yang, Y. Highly Efficient Inverted Polymer Solar Cell by Low Temperature Annealing of Cs 2 CO 3 Interlayer. *Applied Physics Letters* **2008**, *92* (17), 156.

(17) Zhou, Y.; Fuentes-Hernandez, C.; Shim, J.; Meyer, J.; Giordano, A. J.; Li, H.; Winget, P.; Papadopoulos, T.; Cheun, H.; Kim, J. A Universal Method to Produce Low–Work Function Electrodes for Organic Electronics. *Science* **2012**, *336* (6079), 327–332.

(18) Gilot, J.; Wienk, M. M.; Janssen, R. A. Double and Triple Junction Polymer Solar Cells Processed From Solution. *Applied Physics Letters* **2007**, *90* (14), 143512.

(19) Hau, S. K.; Yip, H.-L.; Baek, N. S.; Zou, J.; O'Malley, K.; Jen, A. K.-Y. Air-Stable Inverted Flexible Polymer Solar Cells Using Zinc Oxide Nanoparticles as an Electron Selective Layer. *Applied Physics Letters* **2008**, *92* (25), 225.

(20) Yang, Z.; Zhang, T.; Li, J.; Xue, W.; Han, C.; Cheng, Y.; Qian, L.; Cao, W.; Yang, Y.; Chen, S. Multiple Electron Transporting Layers and Their Excellent Properties Based on Organic Solar Cell. *Scientific Reports* **2017**, *7* (1), 1–9.

(21) He, Z.; Zhang, C.; Xu, X.; Zhang, L.; Huang, L.; Chen, J.; Wu, H.; Cao, Y. Largely Enhanced Efficiency with a PFN/Al bilayer Cathode in High Efficiency Bulk Heterojunction Photovoltaic Cells with a Low Bandgap Polycarbazole Donor. *Advanced Materials* **2011**, *23* (27), 3086–3089.

(22) Zhang, Z.-G.; Qi, B.; Jin, Z.; Chi, D.; Qi, Z.; Li, Y.; Wang, J. Perylene Diimides: A Thickness-Insensitive Cathode Interlayer for High Performance Polymer Solar Cells. *Energy & Environmental Science* **2014**, *7* (6), 1966–1973.

(23) Yao, J.; Qiu, B.; Zhang, Z.-G.; Xue, L.; Wang, R.; Zhang, C.; Chen, S.; Zhou, Q.; Sun, C.; Yang, C. Cathode Engineering with Perylene-Diimide Interlayer Enabling Over 17% Efficiency Single-Junction Organic Solar Cells. *Nature Communications* **2020**, *11* (1), 1–10.

(24) Wu, Z.; Sun, C.; Dong, S.; Jiang, X.-F.; Wu, S.; Wu, H.; Yip, H.-L.; Huang, F.; Cao, Y. n-Type Water/Alcohol-Soluble Naphthalene Diimide-Based Conjugated Polymers for High-Performance Polymer Solar Cells. *Journal of the American Chemical Society* **2016**, *138* (6), 2004–2013.

(25) Yan, L.; Song, Y.; Zhou, Y.; Song, B.; Li, Y. Effect of PEI Cathode Interlayer on Work Function and Interface Resistance of ITO Electrode in the Inverted Polymer Solar Cells. *Organic Electronics* **2015**, *17*, 94–101.

(26) Xu, B.; Zheng, Z.; Zhao, K.; Hou, J. A Bifunctional Interlayer Material for Modifying Both the Anode and Cathode in Highly Efficient Polymer Solar Cells. *Advanced Materials* **2016**, *28* (3), 434–439.

(27) Xiao, B.; Wu, H.; Cao, Y. Solution-Processed Cathode Interfacial Layer Materials for High-Efficiency Polymer Solar Cells. *Materials Today* **2015**, *18* (7), 385–394.

(28) Liao, Q.; Kang, Q.; Yang, Y.; An, C.; Xu, B.; Hou, J. Tailoring and Modifying an Organic Electron Acceptor Toward the Cathode Interlayer for Highly Efficient Organic Solar Cells. *Advanced Materials* **2020**, *32* (7), 1906557.

(29) Cui, M.; Li, D.; Du, X.; Li, N.; Rong, Q.; Li, N.; Shui, L.; Zhou, G.; Wang, X.; Brabec, C. J. A Cost-Effective, Aqueous-Solution-Processed Cathode Interlayer Based on Organosilica Nanodots for Highly Efficient and Stable Organic Solar Cells. *Advanced Materials* **2020**, *32* (38), 2002973.

(30) Zhao, C.; Zhang, Z.; Han, F.; Xia, D.; Xiao, C.; Fang, J.; Zhang, Y.; Wu, B.; You, S.; Wu, Y. An Organic–Inorganic Hybrid Electrolyte as a Cathode Interlayer for Efficient Organic Solar Cells. *Angewandte Chemie International Edition* **2021**, *60* (15), 8526–8531.

(31) Schmerl, N. M.; Quinton, J. S.; Andersson, G. G. On the Growth of Evaporated LiF on P3HT and PCBM. *J. Phys. Chem. C* **2018**, *122* (41), 23420–23431.

(32) Schmerl, N. M.; Andersson, G. G. On the Growth of Evaporated NaF on Phenyl-C61-Butyric Acid Methyl Ester and Poly(3-Hexylthiophene). *J. Phys. Chem. C* **2020**, *124* (28), 15140–15151.

(33) Zhao, X.; Xu, C.; Wang, H.; Chen, F.; Zhang, W.; Zhao, Z.; Chen, L.; Yang, S. Application of Biuret, Dicyandiamide, or Urea as a Cathode Buffer Layer Toward the Efficiency Enhancement of Polymer Solar Cells. *ACS Applied Materials & Interfaces* **2014**, *6* (6), 4329–4337.

(34) Li, S.; Lei, M.; Lv, M.; Watkins, S. E.; Tan, Z. a.; Zhu, J.; Hou, J.; Chen, X.; Li, Y. [6, 6]-Phenyl-C61-Butyric Acid Dimethylamino Ester as a Cathode Buffer Layer for High-Performance Polymer Solar Cells. *Advanced Energy Materials* **2013**, *3* (12), 1569–1574.

(35) Yu, W.; Huang, L.; Yang, D.; Fu, P.; Zhou, L.; Zhang, J.; Li, C. Efficiency Exceeding 10% for Inverted Polymer Solar Cells with a ZnO/Ionic Liquid Combined Cathode Interfacial Layer. *Journal of Materials Chemistry A* **2015**, *3* (20), 10660–10665.

(36) Huang, K.-T.; Shih, C.-C.; Liu, H.-Y.; Murakami, D.; Kanto, R.; Lo, C.-T.; Mori, H.; Chueh, C.-C.; Chen, W.-C. Alcohol-Soluble Cross-Linked Poly (n BA) n-b-Poly (NVTri) m Block Copolymer and Its Applications in Organic Photovoltaic Cells for Improved Stability. *ACS Applied Materials & Interfaces* **2018**, *10* (51), 44741–44750.

(37) Sun, C.; Wu, Z.; Hu, Z.; Xiao, J.; Zhao, W.; Li, H.-W.; Li, Q.-Y.; Tsang, S.-W.; Xu, Y.-X.; Zhang, K. Interface Design for High-Efficiency Non-Fullerene Polymer Solar Cells. *Energy & Environmental Science* **2017**, *10* (8), 1784–1791.

(38) Su, L. Y.; Huang, H. H.; Lin, Y. C.; Chen, G. L.; Chen, W. C.; Chen, W.; Wang, L.; Chueh, C. C. Enhancing Long-Term Thermal Stability of Non-Fullerene Organic Solar Cells Using Self-Assembly Amphiphilic Dendritic Block Copolymer Interlayers. *Advanced Functional Materials* **2021**, *31* (4), 2005753.

(39) Hu, Z.; Zhang, K.; Huang, F.; Cao, Y. Water/Alcohol Soluble Conjugated Polymers for the Interface Engineering of Highly Efficient Polymer Light-Emitting Diodes and Polymer Solar Cells. *Chemical Communications* **2015**, *51* (26), 5572–5585.

(40) Zhao, X.; Nathanson, G. M.; Andersson, G. G. Experimental Depth Profiles of Surfactants, Ions, and Solvent at the Angstrom Scale: Studies of Cationic and Anionic Surfactants and Their Salting Out. *J. Phys. Chem. B* **2020**, *124* (11), 2218–2229.

(41) Andersson, G.; Morgner, H. Impact Collision Ion Scattering Spectroscopy (ICISS) and Neutral Impact Collision Ion Scattering Spectroscopy (NICISS) at Surfaces Of Organic Liquids. *Surface Science* **1998**, *405* (1), 138–151.

(42) Andersson, G.; Morgner, H. Determining the Stopping Power of Low Energy Helium in Alkanethiolates with Neutral Impact Collision Ion Scattering Spectroscopy (NICISS). *Nuclear Instruments and Methods in Physics Research Section B: Beam Interactions with Materials and Atoms* **1999**, *155* (4), 357–368.

(43) Andersson, G.; Krebs, T.; Morgner, H. Activity of Surface Active Substances Determined From Their Surface Excess. *Physical Chemistry Chemical Physics* **2005**, *7* (1), 136–142.

(44) Tan, H. L.; Krebs, T.; Andersson, G.; Neff, D.; Norton, M.; Morgner, H.; Van Patten, P. G. Internal Structure of Polyelectrolyte Multilayers Probed via Neutral Impact Collision Ion Scattering Spectroscopy. *Langmuir* **2005**, *21* (6), 2598–2604.

(45) Andersson, G.; Morgner, H. Thermodynamics and Structure of Liquid Surfaces Investigated Directly with Surface Analytical Tools. *Annalen der Physik* **2017**, *529* (6), 1600230.

(46) Andersson, G. Energy-loss Straggling of Helium Projectiles at Low Kinetic Energies. *Physical Review A* **2007**, *75* (3), 032901.

(47) Andersson, G.; Morgner, H.; Pohl, H. Energy-Loss Straggling of Helium Projectiles at Low Kinetic Energies: Deconvolution of Concentration Depth Profiles of Inorganic Salt Solutes in Aqueous Solutions. *Phys. Rev. A* **2008**, *78* (3), 032904.

(48) Yin, Y.; Lewis, D. A.; Andersson, G. G. Influence of Moisture on the Energy-Level Alignment at the MoO3/Organic Interfaces. *ACS Applied Materials & Interfaces* **2018**, *10* (50), 44163–44172.

(49) Rocks, C.; Svrcek, V.; Maguire, P.; Mariotti, D. Understanding Surface Chemistry During MAPbI 3 Spray Deposition and its Effect on Photovoltaic Performance. *Journal of Materials Chemistry C* **2017**, *5* (4), 902–916.

(50) Shrestha, A.; Batmunkh, M.; Shearer, C. J.; Yin, Y.; Andersson, G. G.; Shapter, J. G.; Qiao, S.; Dai, S. Nitrogen-Doped CNx/CNTs Heteroelectrocatalysts for Highly Efficient Dye-Sensitized Solar Cells. *Advanced Energy Materials* **2017**, *7* (8), 1602276.

(51) Stevens, J. S.; Byard, S. J.; Seaton, C. C.; Sadiq, G.; Davey, R. J.; Schroeder, S. L. Proton Transfer and Hydrogen Bonding in the Organic Solid State: A Combined XRD/XPS/ssNMR Study of 17 Organic Acid–Base Complexes. *Physical Chemistry Chemical Physics* **2014**, *16* (3), 1150–1160.

(52) Mao, M.; Luo, C.; Pollard, T. P.; Hou, S.; Gao, T.; Fan, X.; Cui, C.; Yue, J.; Tong, Y.; Yang, G. A Pyrazine-Based Polymer for Fast-Charge Batteries. *Angewandte Chemie International Edition* **2019**, *58* (49), 17820–17826.

(53) Wen, X.; Wu, J.; Gao, D.; Lin, C. Interfacial Engineering with Amino-Functionalized Graphene for Efficient Perovskite Solar Cells. *Journal of Materials Chemistry A* **2016**, *4* (35), 13482–13487.

(54) Scudiero, L.; Shen, Y.; Gupta, M. C. Effect of Light Illumination and Temperature on P3HT Films, n-Type Si, and ITO. *Applied Surface Science* **2014**, *292*, 100–106.

(55) Greczynski, G.; Hultman, L. X-ray Photoelectron Spectroscopy: Towards Reliable Binding Energy Referencing. *Progress in Materials Science* **2019**, 100591.

(56) Zhang, D.; Xiao, J.; Guo, Q.; Yang, J. 3D-Printed Highly Porous and Reusable Chitosan Monoliths for Cu (II) Removal. *Journal of Materials Science* **2019**, *54* (8), 6728–6741.

(57) Sharma, A.; Berger, R.; Lewis, D. A.; Andersson, G. G. Invisible High Workfunction Materials on Heterogeneous Surfaces. *Appl. Surf. Sci.* **2015**, *327* (0), 22–26.

Chapter 5: Energy Level of PTB7-Th and ITIC with New P(NDI3N-F8-Br) CIL in OPVs

Amira R. Alghamdi[1,2], Bradley Kirk[1,2], Jonas M. Bjuggren[1], Mats R. Andersson[1,2] and Gunther G. Andersson[1,2*]

[1] Flinders Institute for Nanoscale Science and Technology, Flinders University, GPO Box 2100 Adelaide SA 5001, Australia.

[2] Flinders Microscopy and Microanalysis, College of Science and Engineering, Flinders University, Adelaide, South Australia 5042, Australia.

This work has been finalised and is ready to submit. The only alterations are that any experimental methods and analysis procedures previously described in Chapter 3 have been removed from this chapter, and additional information from this chapter is shown in the supplementary section (Appendix B).

Author contributions:

Amira Alghamdi: Designed and performed experiments, data analysis and interpretation of the data and prepared the manuscript for publication. **Bradley Kirk:** Fabricated and characterised the devices and revised the manuscript. **Jonas M. Bjuggren:** Synthesised the new polymer to use it an interface layer and revised the manuscript. **Gunther Andersson:** Intellectual contribution in conceptualising experiments, data interpretation and revision of manuscript. **Mats Andersson:** Intellectual contribution and revision of manuscript.

5.1 Abstract

In this work, poly[(*N,N'*-bis(3-(*N,N*-dimethyl)-*N*-ethylammonium)propyl)naphthalene-1,4,5,8-bis(dicarboximide)-2,6-diyl)-alt-2,7-(9,9'-dihexylfluorene))]dibromide P(NDI3N-F8-Br), an alcohol-soluble, novel, NDI-thiophene-based polymer, was studied as a CIL in OPVs. P(NDI3N-F8-Br) was found to have good solubility in green solvents and effectively reduce the WF of the electrodes, making it suitable for use as a CIL. The respective interfaces between the donor polymer PTB7-Th and acceptor molecule ITIC with the P(NDI3N-F8-Br) CIL were investigated using PES. Both poly[[2,60 -4,8-di(5-ethylhexylthienyl)benzo[1,2-b:3,3-b]dithiophene][3-fluoro-2 [(2-ethylhexyl)carbonyl]thieno[3,4-b]thiophenediyl]] (PTB7-Th) and 3,9-bis(2-methylene-(3-(1,1-dicyanomethylene)-indanone))- 5,5,11,11-tetrakis(4-hexylphenyl)-dithieno[2,3-d:20 ,30 -d0]-s-indaceno[1,2-b:5,6-b0]-dithiophene (ITIC) were deposited onto P(NDI3N-F8-Br), as in the case of inverted devices. The results indicate that P(NDI3N-F8-Br) functions as a hole-blocking layer, which is desirable. Simultaneously, the electrons were blocked from transferring from ITIC to P(NDI3N-F8-Br) due to the latter's high LUMO level. This could be a possible reason for the lower PCE. Further, energy shifts of the components of PTB7-Th and ITIC were investigated via XPS for different layer thicknesses. The results indicate that two dipoles formed at the interfaces of active layers and P(NDI3N-F8-Br). The first dipole was formed at the active layers/P(NDI3N-F8-Br) interface, while a dipole with opposite polarity was formed across thicker layers further away from the interface. This study highlights the importance of understanding energy level—a significant factor in designing a device.

5.2 Introduction

In inverted devices, ITO cannot directly be used as a cathode because of its high WF. Thus, a CIL is needed to reduce the WF of ITO, facilitate an optimum charge transport

(CT) across the interfaces and act as a barrier to block the holes. Therefore, the use of an interfacial layer in OPVs can be considered an important approach for improving PCE.[1–5]

A CIL helps to match the LUMO energy level of the acceptor in the active layer and forms a good Ohmic contact,[6] which is appropriate for electron collection. Therefore, studying the energy level alignment at each interface is an essential factor in understanding the CT over the interfaces. Efficient CT across an interface is dependent on the relative positions and alignments of the energy levels of the interface materials.[7–9] Thus, studies in this area can aid understanding of the mechanism of CT using CILs.

Many studies have focused on using organic materials as CILs and applied them to optimise device efficiency and stability due to their advantages over inorganic CIL with a cost-effective processing method. For instance, solution processing can be applied and moderate heat treatment used (if necessary) to fabricate a variety of CIL materials, thus permitting low-cost fabrication of large-area OPVs. However, efforts are still ongoing to develop an efficient organic CIL using orthogonal solvents such as water and alcohol to prepare solution-processable CIL materials.[10]

Various organic interface layers based on solution processing have been used in OPVs, such as 1,4,5,8-naphthalenediimide (NDI)-[11], perylenediimide (PDI)-[12], pyrrolo[3,4-c]-pyrrole-1,4-dione (DPP)[13]-, isoindigo (IID)-[14], 2,1,3-benzothiadiazole (BT)-[15] and [2,2′-bipyridine-3,3′-diaminato]tetrafluorodiboron adduct (BNBP)-based[16] materials and their derivatives. NDI-based[11,17,18] interface polymers have exhibited promising features in OPVs. NDI-based interface polymers have some unique advantages, such as greater synthetic simplicity and chemical tunability, enhanced mechanical flexibility, and excellent device stability, that make them a promising candidate to replace ZnO derivatives.

In this work, a new n-type polymeric CIL—poly[(N,N'-bis(3-(N,N-dimethyl)-N-ethylammonium)propyl)naphthalene-1,4,5,8-bis(dicarboximide)-2,6-diyl)-alt-2,7-(9,9'-dihexylfluorene))]dibromide P(NDI3N-F8-Br)—was orthogonally solution processed from alcohol and used with poly[[2,60 -4,8-di(5-ethylhexylthienyl)benzo[1,2-b:3,3-b]dithiophene][3-fluoro-2 [(2-ethylhexyl)carbonyl]thieno[3,4-b]thiophenediyl]] (PTB7-Th) and 3,9-bis(2-methylene-(3-(1,1-dicyanomethylene)-indanone))- 5,5,11,11-tetrakis(4-hexylphenyl)-dithieno[2,3-d:20 ,30 -d0]-s-indaceno[1,2-b:5,6-b0]-dithiophene (ITIC)system. This new CIL polymer is based on a NDI core and pendant side groups containing quaternary amines. The energy level of the active layers of PTB7-Th and ITIC with P(NDI3N-F8-Br) were determined. Subsequently, a quantitative analysis of the electronic structure of the interfaces using PES and NICISS was performed. The implication of the energy level for CT over interfaces is discussed.

5.3 Experimental

5.3.1 Material and sample preparation

The materials and sample preparation used in this chapter are described in Chapter 3, Section 3.2.2. The structures of PTB7-Th, ITIC and P(NDI3N-F8-Br) are illustrated in Figure 5-1. More details about the device fabrication are provided in the supplementary section (Appendix B). A reference sample was prepared by spin coating PTB7-Th and ITIC directly onto ITO.

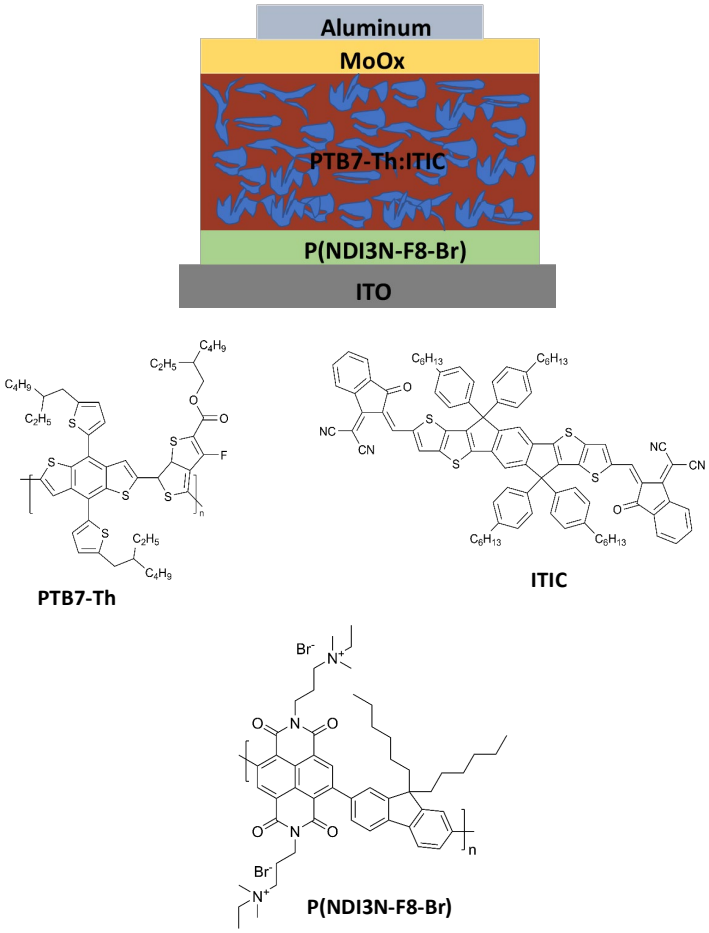

Figure 5-1. (Top) The inverted device architecture using P(NDI3N-F8-Br) as a CIL with a PTB7-Th: ITIC system and (Bottom) the chemical structures of PTB7-Th, ITIC and P(NDI3N-F8-Br) CIL.

5.3.2 Methods: electron and ion spectroscopy methods

Experimental details for electron spectroscopy (XPS, UPS and IPES) and NICISS are described in Chapter 3. The analysis of UP spectra, including SVD analysis, are also described in Chapter 3.

5.4 Results and Discussion

5.4.1 Device performance using P(NDI3N-F8-Br) interface with PTB7-Th: ITIC BHJ

OPVs were fabricated with an inverted device structure of ITO/P(NDI3N-F8-Br)/PTB7-Th: ITIC/MoO3/Ag and a conventional structure of ITO/PEDOT: PSS/PTB7-Th: ITIC/P(NDI3N-F8-Br)/Ag. The fabrication is described in the supplementary section (Appendix B).

The current density-voltage (J-V) characteristics of the devices with the cathode interface of P(NDI3N-F8-Br) are shown in Table 5-1. The inverted structures exhibited 3.2% PCE, mainly due to poor V_{oc} and FF, compared to the conventional structure, which achieved a PCE of 6.8%. This improvement was attributed to facilitating the charge extraction.

The reduced PCE of inverted devices was due to a reduction in J_{sc}, possibly due to the transparency of the P(NDI3N-F8-Br) layer deposited onto ITO, which absorbs visible light and reduces electron extraction. The inverted and conventional structures are discussed below. A systematic analysis of PES and ion scattering spectroscopy results was performed to understand the electronic properties and CT at the active layer/CIL interface when the active layer is deposited onto P(NDI3N-F8-Br).

Table 5-1

Device Characteristics of Inverted and Conventional Devices Based on PTB7-Th: ITIC Fabricated with New Cathode Interface of P(NDI3N-F8-Br)

Device	J_{SC} (mA cm^{-2})	V_{OC} (V)	FF	PCE (%)
PTB7-Th: ITIC/P(NDI3N-F8-Br) [inverted]	13.18 ± 0.19	0.61 ± 0.03	0.40 ± 0.01	3.21 ± 0.19
P(NDI3N-F8-Br)/PTB7-Th: ITIC [conventional]	15.35 ± 0.19	0.8 ± 0.00	0.55 ± 0.01	6.83 ± 0.15

Note. Averages were based on six devices with a defined device area of 0.1 cm^2.

5.4.2 Film thickness - NICISS results

Before studying the electronic properties, NICISS was used to investigate the layer thicknesses of PTB7-Th and ITIC on P(NDI3N-F8-Br). When a projectile travels through a material, it loses energy. This is due to the interaction between the projectile and the molecules within the layer resulting in the helium ions slowing down. The ability to slow down projectiles within a given material is known as stopping power and has previously been measured in monolayers of self-assembled alkanethiolates—representing organic molecules—of known thickness.[13] The energy loss (ΔE) can be approximated with the following equation:

$$\Delta E = Sp \times d/(1 + 1/\cos(165°)) \qquad (5.1)$$

Equation 5.1 relates the energy loss (ΔE) to the stopping power (Sp) of the material and the depth (d) that the projectile reaches within the layer. The applied procedure is detailed by Zhao et al.[15] The thickness of the layers is determined from the shift of the half onset of the Br spectra, as shown in Figure 5-2. The NICISS results are similar to those in our prior work.[19] The different thicknesses of the PTB7-Th and ITIC layers are shown in Table 5-2.

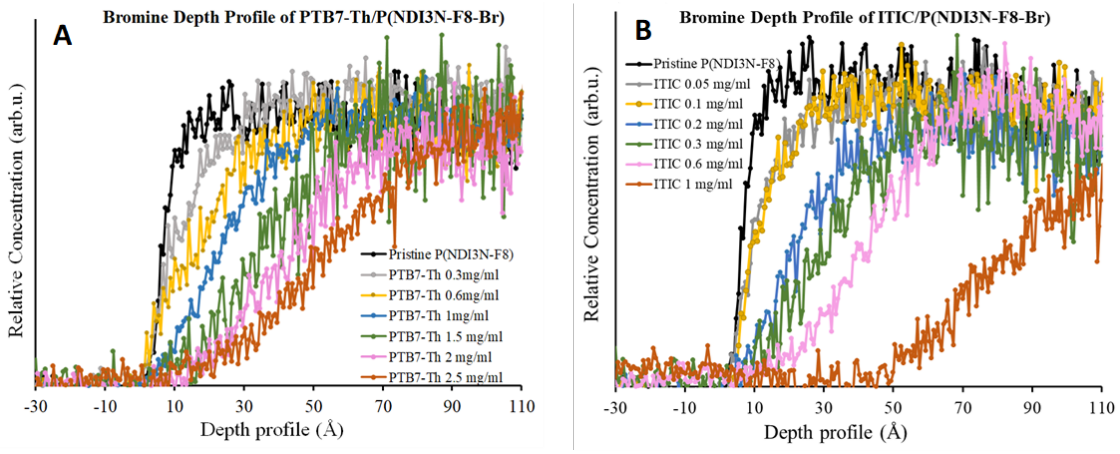

(A) The concentration depth profile of Br in the PTB7-Th/P(NDI3N-F8-Br) interface layers, with the zero mark indicating the very surface of the samples. (B) The distribution of Br in the ITIC/P(NDI3N-F8-Br) interface layers.

Table 5-2
Thicknesses of the ITIC and PTB7-Th Layers Deposited on P(NDI3N-F8-Br), Evaluated from NICISS

Accepter (ITIC) concentrations (mg mL^{-1})	ITIC thickness (nm) ± 0.2 eV	Donor (PTB7-Th) concentrations (mg mL^{-1})	PTB7-Th thickness (nm) ± 0.2 eV
0.05	1.0	0.3	1.0
0.1	1.0	0.6	2.0
0.2	2.0	1.0	2.5
0.3	3.0	1.5	3.6
0.6	4.0	2.0	4.2
1.0	8.0	2.5	5.4

5.4.3 Characterisation of chemical compositions - XPS results

To characterise the chemical changes of active materials deposited on P(NDI3N-F8-Br) with different concentrations, XPS was used to investigate the samples. A pristine sample was also prepared as a reference by spin coating PTB7-Th and ITIC directly onto ITO.

The chemical composition of PTB7-Th on P(NDI3N-F8-Br) interfaces
High-resolution XPS of PTB7-Th/P(NDI3N-F8-Br) for C, F, S and Br are shown in Figure S5-1. The C1s spectra for pristine PTB7-Th were fitted with three peaks: 284.9 ± 0.2 eV, assigned to a C-C bond[20]; 287.0 ± 0.2, identified as C-S; and 289.2 ± 0.2 eV, related to C=O.[21] The pristine P(NDI3N-F8-Br) was fitted with four peaks—285.2 ± 0.2 eV, 285.9 ± 0.2 eV, 286.9 ± 0.2 eV and 289.0 ± 0.2 eV—related to C-C[22], C-N[21], C* and C=O[21], respectively, as shown in Table S5-1. It should be noted that the C* peak of P(NDI3N-F8-Br) is assigning the 10 C atoms between the O=C-N-C=O in NDI as a separate species at 285.9 eV.

For the PTB7-Th/P(NDI3N-F8-Br) interfaces, the C1s spectra were required to be fitted with three peaks, which are C-C, C-O and C=O. The C-C peak for all the samples has the

same positions as the pristine PTB7-Th but shifted slightly towards higher binding energy after decreasing the layer thickness of PTB7-Th on P(NDI3N-F8-Br), as shown in Figure 5-3A. The C-C peak shifts by a total of +0.3 ± 0.2 eV, which is discussed below.

One F1s peak was found at 687.7 ± 0.2 eV for pristine PTB7-Th. The PTB7-Th/P(NDI3N-F8-Br) interfaces had one peak, as shown in Figure S5-1B. The S $2p_{3/2}$ peak for pristine PTB7-Th was at 164.1 ± 0.2 eV, as shown in Figure S5-1C.

The F and S peaks show a shift towards higher binding energy of 0.3 ± 0.2 eV and 0.5 ± 0.2 eV, respectively, after decreasing the thickness of the PTB7-Th layers on P(NDI3N-F8-Br), as shown in Figures 5-3B and 5-3C. These shifts are likely an indication of a dipole formation (electrical bias) at the PTB7-Th/P(NDI3N-F8-Br) interface. This is investigated further via UPS analysis in Section 5.4.4.

The Br $3d_{5/2}$ peak, which is a part of the P(NDI3N-F8-Br) layer, was found at 67.9 ± 0.2eV for pristine P(NDI3N-F8-Br) and all PTB7-Th/P(NDI3N-F8-Br) interfaces, as shown in Figure S5-1D. The positions of the Br peaks did not change after depositing PTB7-Th layers on P(NDI3N-F8-Br) (see Figure 5-3D), suggesting the samples are not charging after depositing PTB7-Th on P(NDI3N-F8-Br). Therefore, the shifts in the C-C, F and S peaks have a physical meaning. All the peak positions of the PTB7-Th/P(NDI3N-F8-Br) samples, including the pristine samples, are shown in Table S5-1.

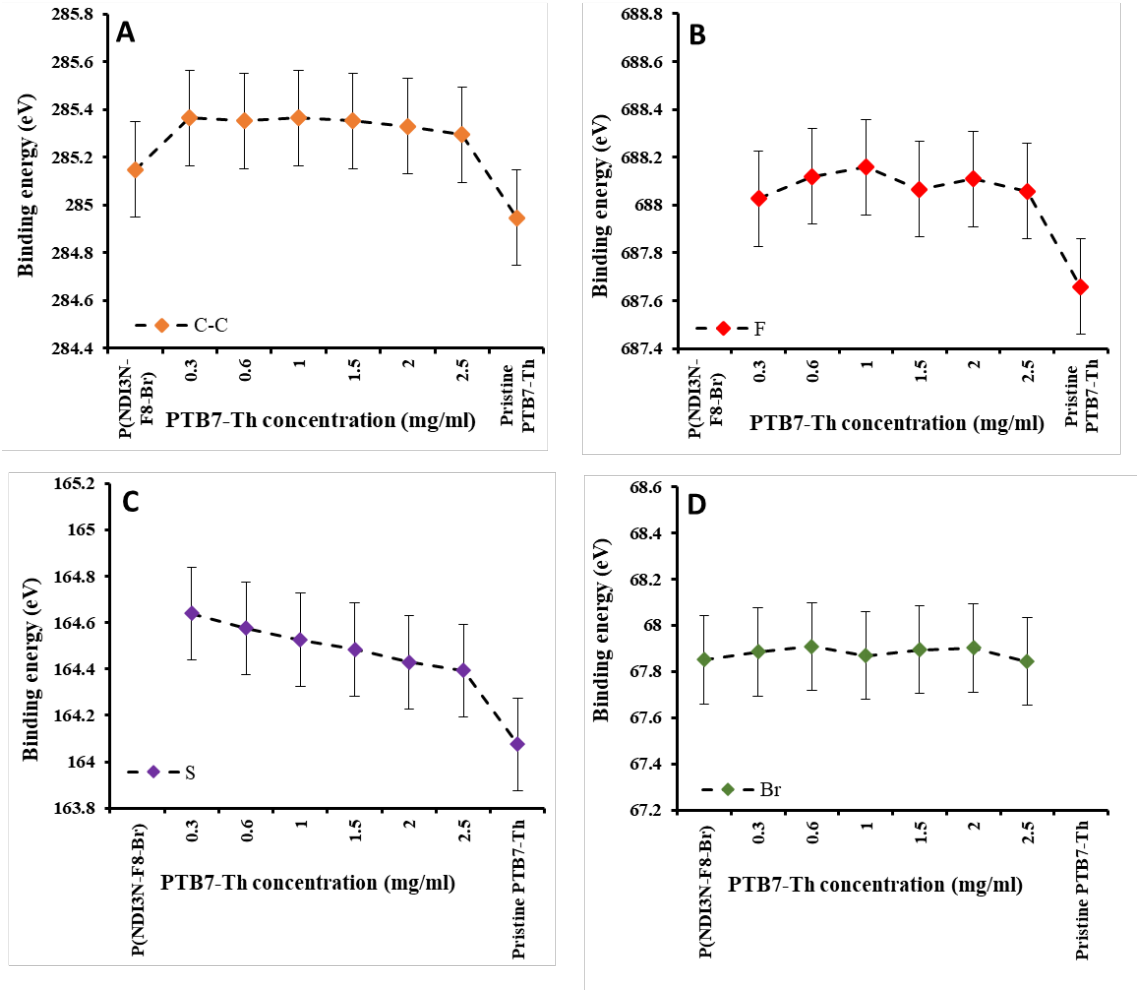

Figure 5-3. XPS results showing the change in (A) C1s, (B) F1s, (C) S 2p and (D) Br 3d for PTB7-Th layers deposited on P(NDI3N-F8-Br).

The chemical composition of ITIC on P(NDI3N-F8-Br) interfaces

The NF electron acceptor of ITIC/P(NDI3N-F8-Br), high-resolution XPS for C, S, N, and Br with different layer thicknesses of ITIC are shown in Figure S5-2. The C1s spectra for pristine ITIC were fitted with four peaks: 284.8 ± 0.2 eV, related to a C-C bond; 285.7 ± 0.2 eV, a C-N bond; 286.6 ± 0.2, assigned to C-S; and 287.6 ± 0.2[21], a C=O bond (see Table S5-2). The pristine P(NDI3N-F8-Br) has four peaks of C1s, as stated above.

The C1s for ITIC/P(NDI3N-F8-Br) interfaces were fitted with four peaks. The position of the C-C peak for all ITIC/P(NDI3N-F8-Br) samples shifted towards higher binding energy after decreasing the thickness of the ITIC layers on P(NDI3N-F8-Br), as shown in Figure 5-4A.

The N1s spectrum of the pristine ITIC were fitted with three peaks—399.2 ± 0.2 eV, 400.6 ± 0.2 eV and 402.5 ± 0.2 eV—corresponding to N=C, N-C and N-O[23,24], respectively. The pristine P(NDI3N-F8-Br) polymer was fitted with two peaks—400.9 ± 0.2 eV and 403.0 ± 0.2 eV—related to N-C and N-O, respectively[24] (see Table S5-2).

The ITIC/P(NDI3N-F8-Br) layered samples had to be fitted with three peaks, and the position of the N=C, which is a part of the ITIC layer, shifted towards higher binding energy by 0.2 ± 0.2 eV after depositing different thicknesses of ITIC on P(NDI3N-F8-Br), as shown in Figure 5-4B.

The S $2p_{3/2}$ peak for pristine ITIC is found at 164.3 ± 0.2 eV, showing a liner shift towards higher binding energy by 0.3 eV after decreasing the thickness of the ITIC layers on P(NDI3N-F8-Br), as shown in Figure 5-4C. The shift in N and S is most likely an indication of a dipole formation at the interface, as suggested by the relationship between the layer thickness and the shift. This is discussed further below.

The Br $3d_{5/2}$ peak was found at 67.9 ± 0.2 eV for all ITIC/P(NDI3N-F8-Br) samples. In the same manner as previously discussed, the Br peak does not shift after decreasing the thickness of the ITIC layers, as shown in Figure 5-4D. All the peak positions are shown in Table S5-2.

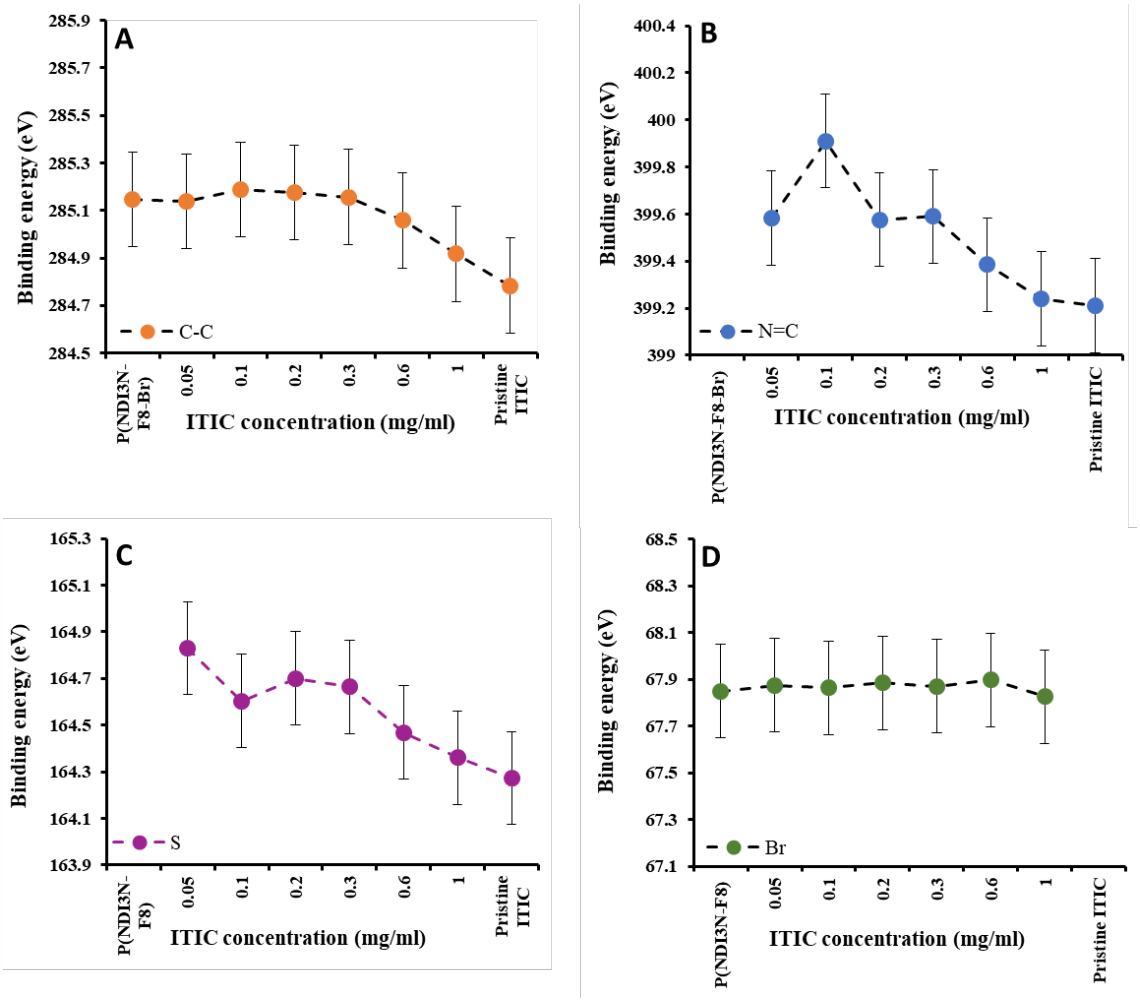

Figure 5-4. XPS results showing the change in (A) C1s, (B) N1s, (C) S 2p and (D) Br 3d for ITIC layers deposited on P(NDI3N-F8-Br). The changes of two other N peaks of ITIC/P(NDI3N-F8-Br) interfaces are shown in Figure S5-3.

The XPS results show a change of the chemical state of the compounds of PTB7-Th and ITIC after changing their thickness on P(NDI3N-F8-Br), which is an indication of a dipole formation at the PTB7-Th/P(NDI3N-F8-Br) and ITIC/P(NDI3N-F8-Br) interfaces. To confirm the suspected dipole formation at the interfaces, the samples were analysed via UPS.

5.4.4 Evaluation of electronic properties of active materials deposited onto P(NDI3N-F8-Br): UPS and IPES results

The electronic structure of the PTB7Th/P(NDI3N-F8-Br) and ITIC/P(NDI3N-F8-Br) interfaces were analysed via UPS and IPES. UPS and IPES were individually used to examine pristine PTB7-Th, ITIC and P(NDI3N-F8-Br) on ITO.

The VB/highest occupied molecular orbital electron (E_{HOMO}) of the UP spectra and CB/lowest unoccupied molecular orbital electron (E_{LUMO}) of the IPE spectra are combined and shown in Figure 5-5. The low binding energy cut-off and the background are both fitted with a linear function. The cross-section of both linear functions then represents the VB cut-off/E_{HOMO}. The same procedure was applied to the low kinetic energy region in IPE spectra, from which the CB/$_{LUMO}$ energy are identified, as shown in Figure 5-5. The level of noise in the UP and IPE spectra should be considered when determining the cut-off for VB and CB, with the IPE spectra showing a higher level of noise. The values are listed in Table 5-3. Our analyses of the UP spectra are discussed further below. The E_{HOMO} and E_{LUMO} values of all PTB7-Th/P(NDI3N-F8-Br) and ITIC/P(NDI3N-F8-Br) interfaces are provided in Tables S5-3 and S5-4. The plots of the UP and IPE spectra for all the interfaces are shown in Figure S5-4.

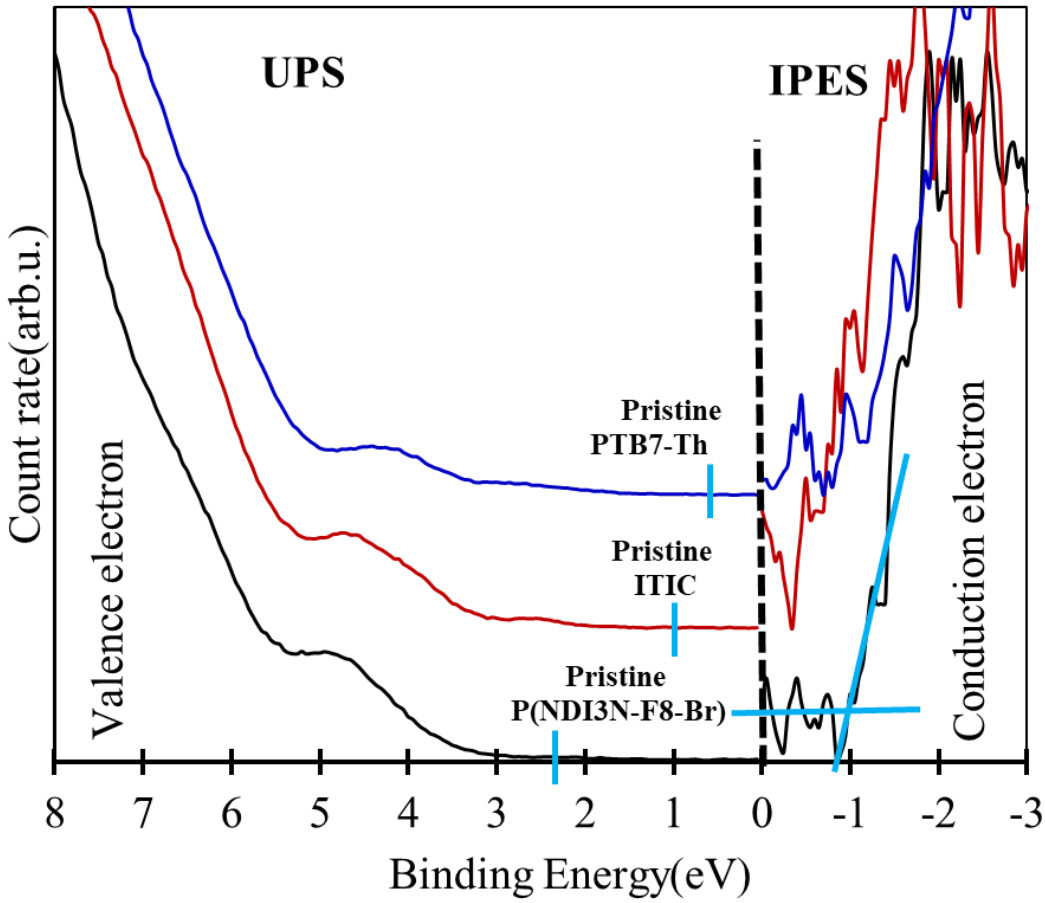

Figure 5-5. The plot of the VB/E_{HOMO} and CB/E_{LUMO} region as measured via UPS and IPES of PTB7-Th, ITIC and P(NDI3N-F8-Br) samples. For determining the cut-off for VB and CB, the level of noise in the UP and IPE spectra must be considered, with the IPE spectra showing a higher level of noise.

Table 5-3

The Values of WF, VB/E_{HOMO}, CB/E_{LUMO} and Energy gap (Eg) of the PTB7-Th, ITIC and P(NDI3N-F8-Br) Samples

Sample	VB/E_{HOMO} (eV) ± 0.1	CB/E_{LUMO} (eV) ± 0.1	Eg (eV) ± 0.1
Pristine PTB7-Th	0.6	–1.0	1.6
Pristine ITIC	1.0	–0.4	1.4
Pristine P(NDI3N-F8-Br)	2.3	–0.9	3.2

Note. All energies are indicated with a zero point at Fermi Level (E_f). The VB/E_{HOMO} is higher than the Fermi level and noted as positive, while the CB/E_{LUMO} is lower and noted as negative.

Decomposition of valence electron spectra of UPS to identify the individual components

To understand the features of the UP spectra, the SVD algorithm was applied for component analysis. This allows us to identify the composing compounds and their contribution to the spectra.

The analysis results for PTB7-Th/P(NDI3N-F8-Br) and ITIC/P(NDI3N-F8-Br) are shown in Figure 5-6. SVD analysis identified two components, which allows the fitting of the entire series of spectra in all PTB7-Th/P(NDI3N-F8-Br) interfaces and ITIC/P(NDI3N-F8-Br) interfaces, as shown in Figures 5-6A and 5-6B, respectively. Reference A in the three interfaces can be assigned to the P(NDI3N-F8-Br) spectrum because they have similar features across the valence electron region.

For PTB7-Th/P(NDI3N-F8-Br), reference B in Figure 5-6A has a similar shape of valence electron distribution to the spectrum of PTB7-Th. For ITIC/P(NDI3N-F8-Br), reference B in Figure 5-6B can be identified as the ITIC spectra.

The SVD components for all interfaces demonstrated that there is no shift in the energy scale after depositing the active layers on P(NDI3N-F8-Br). Thus, our UPS results show no dipole formation at the PTB7-Th/P(NDI3N-F8-Br) or ITIC/P(NDI3N-F8-Br) interfaces.

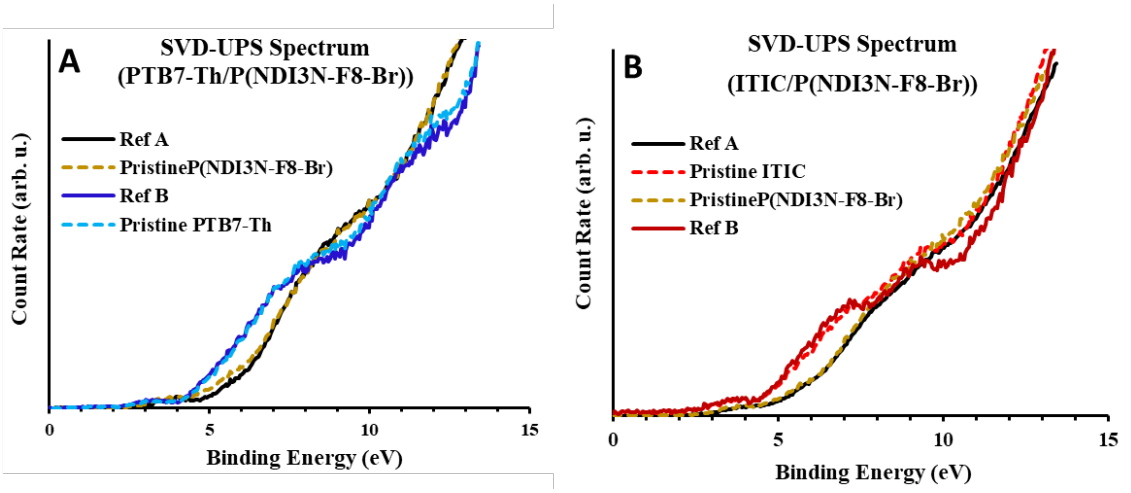

Figure 5-6. The reference spectra of UPS (obtained from SVD analysis) for (A) PTB7-Th/P(NDI3N-F8-Br) interfaces and (B) ITIC/P(NDI3N-F8-Br) interfaces.

The UPS weighting factors for the two references of PTB7-Th/P(NDI3N-F8-Br) and ITIC/P(NDI3N-F8-Br) layers are shown in Figure 5-7. The weighting factors for P(NDI3N-F8-Br) in Figures 5-7A and 5-7B show a decrease with increasing thickness of PTB7-Th and ITIC, respectively. This finding indicates that at the surface of P(NDI3N-F8-Br), there could be an intermix of the active layers when the first is spin-coated on top of the second.

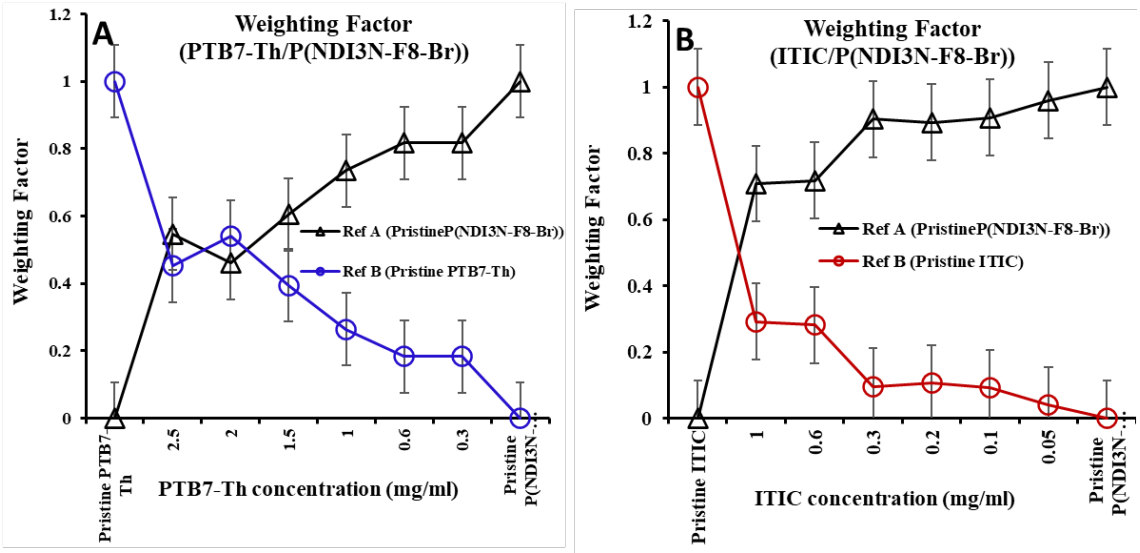

Figure 5-7. Weighting factors of UPS for (A) PTB7-Th/P(NDI3N-F8-Br) layers and (B) ITIC/P(NDI3N-F8-Br) layers.

Interpretation of the PES findings

The chemical and electronic properties of the interface samples of PTB7-Th/P(NDI3N-F8-Br) and ITIC/P(NDI3N-F8-Br) were analysed via XPS and UPS. XPS results show a shift in C, S, N and F towards higher binding energy after reducing the thickness of the PTB7-Th and ITIC layers on P(NDI3N-F8-Br) by a total of +0.5 eV for PTB7-Th interface and +0.3 eV for ITIC interface. The shift of the components was caused by the net dipole across the layer thickness, which was probed with XPS. We found that the dipole direction will be from the PTB7-Th and ITIC layers to P(NDI3N-F8-Br). Thus, the positive end of the dipole is directed towards the active layers while the negative end moves towards the buried layer of P(NDI3N-F8-Br). Conversely, UPS results showed no shift in the energy scale in the valance region when depositing different thicknesses of PTB7-Th and ITIC on P(NDI3N-F8-Br); this indicates that there is no net dipole across the layer thickness that can be probed with UPS. A possible reason for this difference in observations between XPS and UPS of the dipole formation is the different probing depths of the techniques. X-ray (XPS) examines core levels, estimated from the electron mean free path resulting in the peaks of the elements, while UV light (UPS) investigates valence electron region; the former exhibits higher excitation energy than the latter. A second possible reason is the opposing orientation of the molecules further away from the PTB7-Th/P(NDI3N-F8-Br) and ITIC/P(NDI3N-F8-Br) interfaces. Therefore, two dipoles can be identified. The first dipole is located at the boundary of the interface (as determined via XPS), and the second dipole is formed with opposite polarity across thicker layers (as determined from the shift of the core-level elements via XPS). This double dipole is illustrated in Figure 5-8. The second dipole has an opposite orientation to that at the interface and does not contribute to a shift of the PTB7-Th or ITIC valance spectra, as the dipoles decrease in overall strength when they oppose each other. UPS would not identify the shift as UPS is sensitive for the outermost nm only.

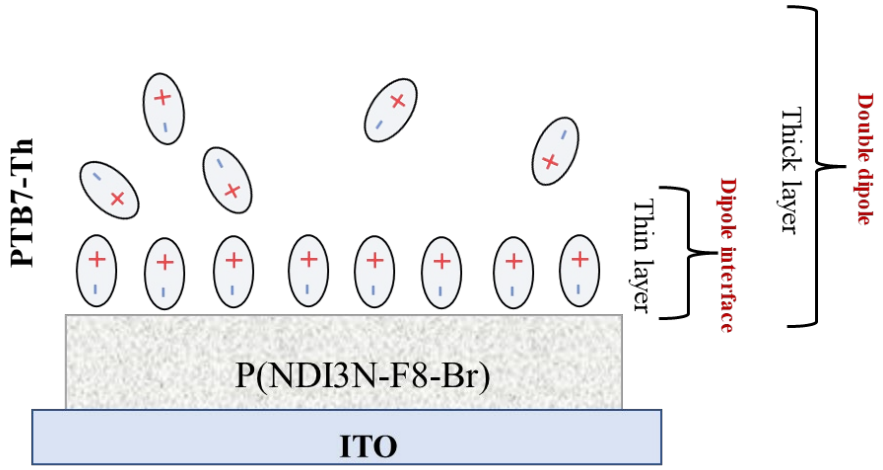

Figure 5-8. Schematic of an interface dipole formed with the thin layer. An opposite dipole is also formed across thicker layers.

The findings from UPS and IPES analyses help us to draw conclusions about the energy level alignment between the active layers and P(NDI3N-F8-Br) and the implication for CT over the interfaces. Therefore, all the quantities and values for full consideration of the energy levels at PTB7-Th/P(NDI3N-F8-Br) and ITIC/P(NDI3N-F8-Br) interfaces were determined.

As seen in Figure 5-9A, the E_{HOMO} of the P(NDI3N-F8-Br) layer (located deep from the fermi level) allows for blocking the hole transport from PTB7-Th to P(NDI3N-F8-Br), which is favourable as the P(NDI3N-F8-Br) functions as a hole-blocking layer. However, the E_{LUMO} of P(NDI3N-F8-Br) is higher than that of ITIC; this mismatch will have an effect on the electrons transferring from ITIC to P(NDI3N-F8-Br). This mismatch is a possible reason for the inverted device's reduced performance. Thus, P(NDI3N-F8-Br) does not seem to be an efficient interface for inverted devices. However, in conventional device configuration, the electrons transfer from ITIC to P(NDI3N-F8-Br) appears to be more efficient (based on the device data in Table 5-1). However, the CT in the materials is the next factor to be considered, but it can be assumed that it will not change between conventional and inverted structures. Therefore, investigating the interface of P(NDI3N-F8-Br) on top of ITIC under the conditions as generated in inverted devices should be considered. It is possible that the solubility of P(NDI3N-F8-Br) in the active layer's

solvent could affect the electronic structure of the interface. The only way to probe that is by measuring the ion and electron spectroscopy of the P(NDI3N-F8-Br)/ITIC interface.

Considering the 0.5 eV and 0.3 eV shift towards higher binding energy for PTB7-Th and ITIC, respectively, which was observed from XPS results due to the dipole formation at the PTB7-Th/P(NDI3N-F8-Br) and ITIC/P(NDI3N-F8-Br) interfaces, the E_{HOMO} and E_{LOMO} of the PTB7-Th and ITIC layers shifted downwards (as illustrated in Figures 5-9A and 5-9B). The shift of the E_{HOMO} and E_{LOMO} levels (which sees the E_{LOMO} of ITIC reduced to near zero) and the mismatch gap between ITIC and P(NDI3N-F8-Br) are not improved by the dipole formation. Meanwhile, the E_{HOMO} of P(NDI3N-F8-Br) is still deeper than that of PTB7-Th, and so blocks the hole transport from PTB7-Th.

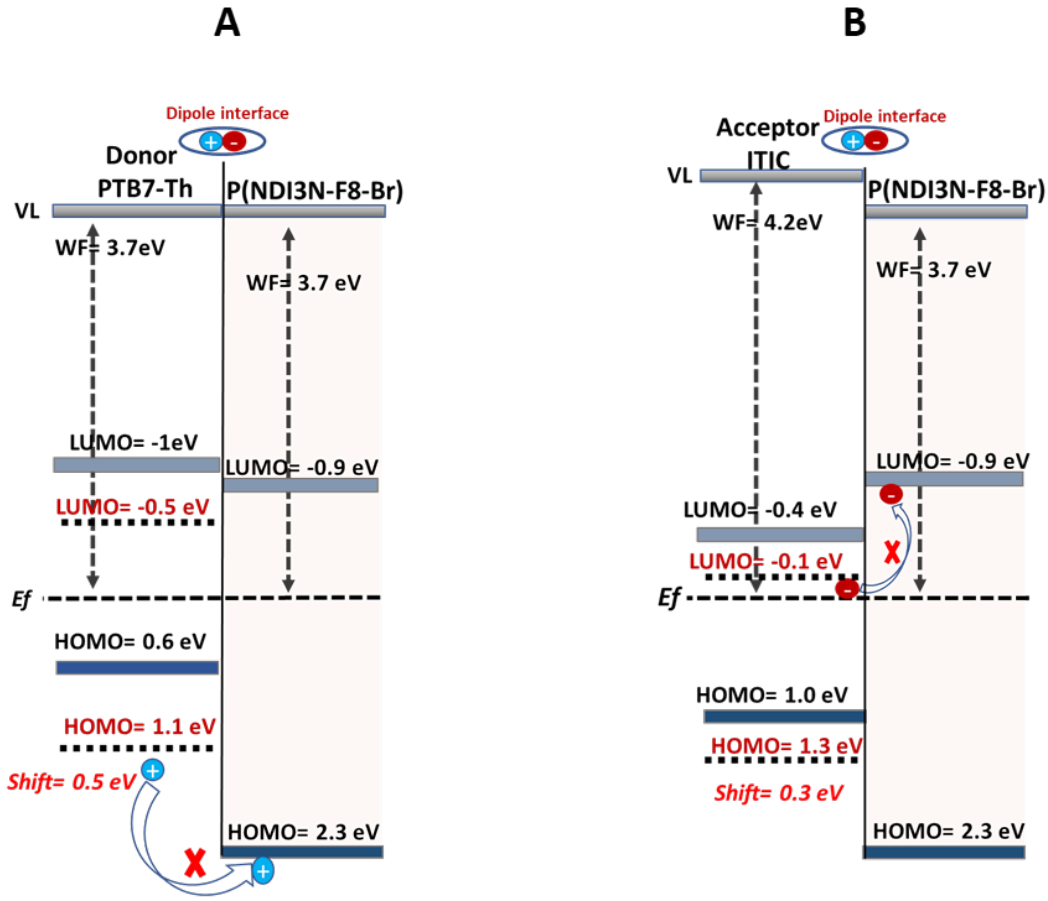

Figure 5-9. The energy level of (A) PTB7-Th/P(NDI3N-F8-Br) and (B) ITIC/P(NDI3N-F8-Br) and the CT over the interface layers. VL, vacuum level.

5.5 Conclusion

A new CIL, P(NDI3N-F8-Br), was investigated in conjunction with a photoactive layer of PTB7-Th and ITIC. XPS results show a shift in the energy scale of the components of PTB7-Th and ITIC towards higher binding energy with decreased layer thickness. This shift is subject to two dipole formations: one at the interface with P(NDI3N-F8-Br), and a second (with opposite polarity) across the layer. The inverted structure device showed reduced PCE compared to the conventional device. The complete energy level structure of the inverted interfaces was modelled, and the mechanism of CT showed that P(NDI3N-F8) functions as a hole-blocking layer. Simultaneously, P(NDI3N-F8) cannot extract the electrons transferring from ITIC due to the mismatched energy level. The PCE of OPVs fabricated in an inverted configuration was found to be 3.2%, compared to a significantly higher PCE of 6.8% for OPVs fabricated with the conventional structure. Nevertheless, P(NDI3N-F8-Br) appeared to improve the PCE of the conventional devices, thus making the conventional structure promising for OPV applications. This study's findings should inspire a new research interest in PVs regarding determining the energy level and CT for conventional devices using P(NDI3N-F8-Br) on top of BHJ.

5.6 Acknowledgement

The authors would like to acknowledge the support of the Australian National Fabrication Facility (ANFF) and Australian Microscopy & Microanalysis Research Facility (AMMRF) regarding using experimental equipment. The authors acknowledge Flinders Microscopy and Microanalysis and their expertise. The authors would like to thank Dr Anirudh Sharma and Dr Yanting Yin for their help and support in this project.

5.7 References

(1) Hoven, C. V.; Garcia, A.; Bazan, G. C.; Nguyen, T. Q. Recent Applications of Conjugated Polyelectrolytes in Optoelectronic Devices. *Advanced Materials* **2008**, *20* (20), 3793–3810.

(2) Duarte, A.; Pu, K.-Y.; Liu, B.; Bazan, G. C. Recent Advances in Conjugated Polyelectrolytes for Emerging Optoelectronic Applications. *Chemistry of Materials* **2011**, *23* (3), 501–515.

(3) Chen, L.-M.; Xu, Z.; Hong, Z.; Yang, Y. Interface Investigation and Engineering–Achieving High Performance Polymer Photovoltaic Devices. *J. Mater. Chem.* **2010**, *20* (13), 2575–2598.

(4) Ma, H.; Yip, H. L.; Huang, F.; Jen, A. K. Y. Interface Engineering for Organic Electronics. *Advanced Functional Materials* **2010**, *20* (9), 1371–1388.

(5) Po, R.; Carbonera, C.; Bernardi, A.; Camaioni, N. The Role of Buffer Layers in Polymer Solar Cells. *Energy & Environmental Science* **2011**, *4* (2), 285–310.

(6) Chueh, C.-C.; Li, C.-Z.; Jen, A. K.-Y. Recent Progress and Perspective in Solution-Processed Interfacial Materials for Efficient and Stable Polymer and Organometal Perovskite Solar Cells. *Energy & Environmental Science* **2015**, *8* (4), 1160–1189.

(7) Liu, Y.; Duzhko, V. V.; Page, Z. A.; Emrick, T.; Russell, T. P. Conjugated Polymer Zwitterions: Efficient Interlayer Materials in Organic Electronics. *Accounts of Chemical Research* **2016**, *49* (11), 2478–2488.

(8) Tan, Y.; Chen, L.; Wu, F.; Huang, B.; Liao, Z.; Yu, Z.; Hu, L.; Zhou, Y.; Chen, Y. Regulation of the Polar Groups in n-Type Conjugated Polyelectrolytes as Electron Transfer Layer for Inverted Polymer Solar Cells. *Macromolecules* **2018**, *51* (20), 8197–8204.

(9) Lim, K.-G.; Ahn, S.; Lee, T.-W. Energy Level Alignment of Dipolar Interface Layer in Organic and Hybrid Perovskite Solar Cells. *Journal of Materials Chemistry C* **2018**, *6* (12), 2915–2924.

(10) Hu, Z.; Zhang, K.; Huang, F.; Cao, Y. Water/Alcohol Soluble Conjugated Polymers for the Interface Engineering of Highly Efficient Polymer Light-Emitting Diodes and Polymer Solar Cells. *Chemical Communications* **2015**, *51* (26), 5572–5585.

(11) Gao, L.; Zhang, Z. G.; Xue, L.; Min, J.; Zhang, J.; Wei, Z.; Li, Y. All-Polymer Solar Cells Based on Absorption-Complementary Polymer Donor and Acceptor with High Power Conversion Efficiency of 8.27%. *Advanced Materials* **2016**, *28* (9), 1884–1890.

(12) Guo, Y.; Li, Y.; Awartani, O.; Han, H.; Zhao, J.; Ade, H.; Yan, H.; Zhao, D. Improved Performance of All-Polymer Solar Cells Enabled by Naphthodiperylenetetraimide-Based Polymer Acceptor. *Advanced Materials* **2017**, *29* (26), 1700309.

(13) Li, Y.; Yang, Y.; Bao, X.; Qiu, M.; Liu, Z.; Wang, N.; Zhang, G.; Yang, R.; Zhang, D. New π-Conjugated Polymers as Acceptors Designed for All Polymer Solar Cells Based on Imide/Amide-Derivatives. *Journal of Materials Chemistry C* **2016**, *4* (1), 185–192.

(14) Li, Z.; Xu, X.; Zhang, W.; Genene, Z.; Mammo, W.; Yartsev, A.; Andersson, M. R.; Janssen, R. A.; Wang, E. High-Photovoltage All-Polymer Solar Cells Based on a Diketopyrrolopyrrole–Isoindigo Acceptor Polymer. *Journal of Materials Chemistry A* **2017**, *5* (23), 11693–11700.

(15) Zhao, J.; Li, Y.; Yang, G.; Jiang, K.; Lin, H.; Ade, H.; Ma, W.; Yan, H. Efficient Organic Solar Cells Processed from Hydrocarbon Solvents. *Nature Energy* **2016**, *1* (2), 1–7.

(16) Dou, C.; Long, X.; Ding, Z.; Xie, Z.; Liu, J.; Wang, L. An Electron-Deficient Building Block Based on the B← N Unit: An Electron Acceptor for All-Polymer Solar Cells. *Angewandte Chemie International Edition* **2016**, *55* (4), 1436–1440.

(17) Wu, Z.; Sun, C.; Dong, S.; Jiang, X.-F.; Wu, S.; Wu, H.; Yip, H.-L.; Huang, F.; Cao, Y. n-Type Water/Alcohol-Soluble Naphthalene Diimide-Based Conjugated Polymers for High-Performance Polymer Solar Cells. *Journal of the American Chemical Society* **2016**, *138* (6), 2004–2013.

(18) Sharma, A.; Singh, S.; Song, X.; Rosas Villalva, D.; Troughton, J.; Corzo, D.; Toppare, L.; Gunbas, G.; Schroeder, B. C.; Baran, D. A Nonionic Alcohol Soluble Polymer Cathode Interlayer Enables Efficient Organic and Perovskite Solar Cells. *Chemistry of Materials* **2021**, *33* (22), 8602–8611.

(19) Alghamdi, A. R.; Bjuggren, J. M.; Pan, X.; Andersson, M. R.; Andersson, G. G. Dipole Formation at Active Materials/P (NDI3N-T-Br) Interface in Organic-Based Photovoltaic. *Macromolecular Materials and Engineering* **2022**, 2200303.

(20) Du, F.-P.; Cao, N.-N.; Zhang, Y.-F.; Fu, P.; Wu, Y.-G.; Lin, Z.-D.; Shi, R.; Amini, A.; Cheng, C. PEDOT: PSS/Graphene Quantum Dots Films with Enhanced Thermoelectric Properties via Strong Interfacial Interaction and Phase Separation. *Scientific Reports* **2018**, *8* (1), 1–12.

(21) Yin, F.; Ren, J.; Zhang, Y.; Tan, T.; Chen, Z. A PPy/ZnO Functional Interlayer to Enhance Electrochemical Performance of Lithium/Sulfur Batteries. *Nanoscale Research Letters* **2018**, *13* (1), 1–7.

(22) Yin, Y.; Pan, X.; Andersson, M. R.; Lewis, D. A.; Andersson, G. G. Correlation of Changes in Electronic and Device Properties in Organic Photovoltaic with Exposure to Air. *Advanced Materials Interfaces* **2021**, 2101657.

(23) Mao, M.; Luo, C.; Pollard, T. P.; Hou, S.; Gao, T.; Fan, X.; Cui, C.; Yue, J.; Tong, Y.; Yang, G. A Pyrazine-Based Polymer for Fast-Charge Batteries. *Angewandte Chemie International Edition* **2019**, *58* (49), 17820–17826.

(24) Osadchii, D. Y.; Olivos-Suarez, A. I.; Bavykina, A. V.; Gascon, J. Revisiting Nitrogen Species in Covalent Triazine Frameworks. *Langmuir* **2017**, *33* (50), 14278–14285.

Chapter 6: Chemical and Electronic Properties of PTB7-Th and ITIC on ZnO Interfaces in OPVs

Amira R. Alghamdi,[1,2,3] Bradley P. Kirk,[1,2] Mats R. Andersson[1,2] and Gunther G. Andersson[1,2*]

[1] Flinders Institute for Nanoscale Science and Technology, Flinders University, GPO Box 2100 Adelaide SA 5001, Australia.

[2] Flinders Microscopy and Microanalysis, College of Science and Engineering, Flinders University, Adelaide, South Australia 5042, Australia.

This work has been finalised and is ready to submit. The only alterations are that any experimental methods and analysis procedures previously described in Chapter 3 have been removed from this chapter, and supplementary information from the publication has been shown in the supplementary section (Appendix C).

Author contributions:

Amira Alghamdi: Designed and performed experiments, data analysis and interpretation of the data and prepared the manuscript for publication. **Bradley Kirk:** Revised the manuscript. **Gunther Andersson:** Intellectual contribution in conceptualising experiments, data interpretation and revision of manuscript. **Mats Andersson:** Intellectual contribution and revision of manuscript.

6.1 Abstract

ZnO is commonly used as a CIL in OPVs due to its capability to extract electrons from the active layer. In this work, we focus on the electronic structuring of the interface between ZnO and an active layer containing PTB7-Th and ITIC. A broad range of techniques was implemented to determine the energy levels of these materials at their interface. The investigations show that the energy levels of PTB7-Th and ITIC are well aligned with ZnO. It was also found that two dipoles formed between PTB7-Th and ZnO. The first dipole was formed at the PTB7-Th/ZnO interface with thin layers, while a dipole with opposite polarity was formed within thicker PTB7-Th layers further away from the interface. The findings contribute to understanding the transport of charges over the interfaces.

6.2 Introduction

NFAs have recently been developed with highly tenable photoelectronic properties (such as light absorption and electron mobilities) and diverse structural variations for use in OPV devices.[1] A well-known example is ITIC, which is based on small-molecule fused rings, such as indacenodithiophene (IDT). ITIC has been shown to be a very promising acceptor, especially when paired with PTB7-Th as the polymer donor, while ZnO has commonly been used as a hole-blocking layer.[2–4] Whether a given configuration of a PV device can be efficient depends to a large degree on the relative position of the energy levels (i.e., electronic structure) across the interfaces in the device. The energy levels facilitating the transport of the electrons need to show a gradient or transition across an interface towards higher positive values, while the energy levels facilitating the transport of the holes should change towards higher negative values.

The interfacial electronic structures of the configuration considered here, ZnO and NFA-based organic materials, have not previously been studied in sufficient detail. For example,

some studies have attempted to explain the electronic structures of bulk electronics,[5–7] yet it is well known that the individual active layer could have quite different properties at the interface with the CTL. The present work investigates the interfacial electronic structure between ZnO and ITIC (an NFA material), the results of which will help to inform the selection and synthesis of NFA materials for future generations of high-performance organic semiconductor devices.[6]

A combination of in situ UPS and IPES in conjunction with XPS was used to directly probe the energy levels of the occupied and unoccupied states at the interface of the BHJ formed by PTB7-Th and ITIC with ZnO. The study showed a good alignment of the energy levels between PTB7-Th/ITIC and ZnO, thus blocking the transfer of holes from the active layer to the ZnO interfacial layer while facilitating the transfer of electrons from ITIC (acceptor) to the electrode. The results also showed the formation of two dipoles between PTB7-Th and ZnO. The first dipole was formed at the PTB7-Th/ZnO interface, and the second dipole, with an opposite polarity to the first, was formed within the PTB7-Th in the bulk of the BHJ, further away from the PTB7-Th/ZnO interface.

6.3 Experimental

6.3.1 Material and sample preparation

The materials and sample preparation used in this chapter are described in Chapter 3, Section 3.2.2. The structures of PTB7-Th and ITIC are illustrated in Figure 6-1.

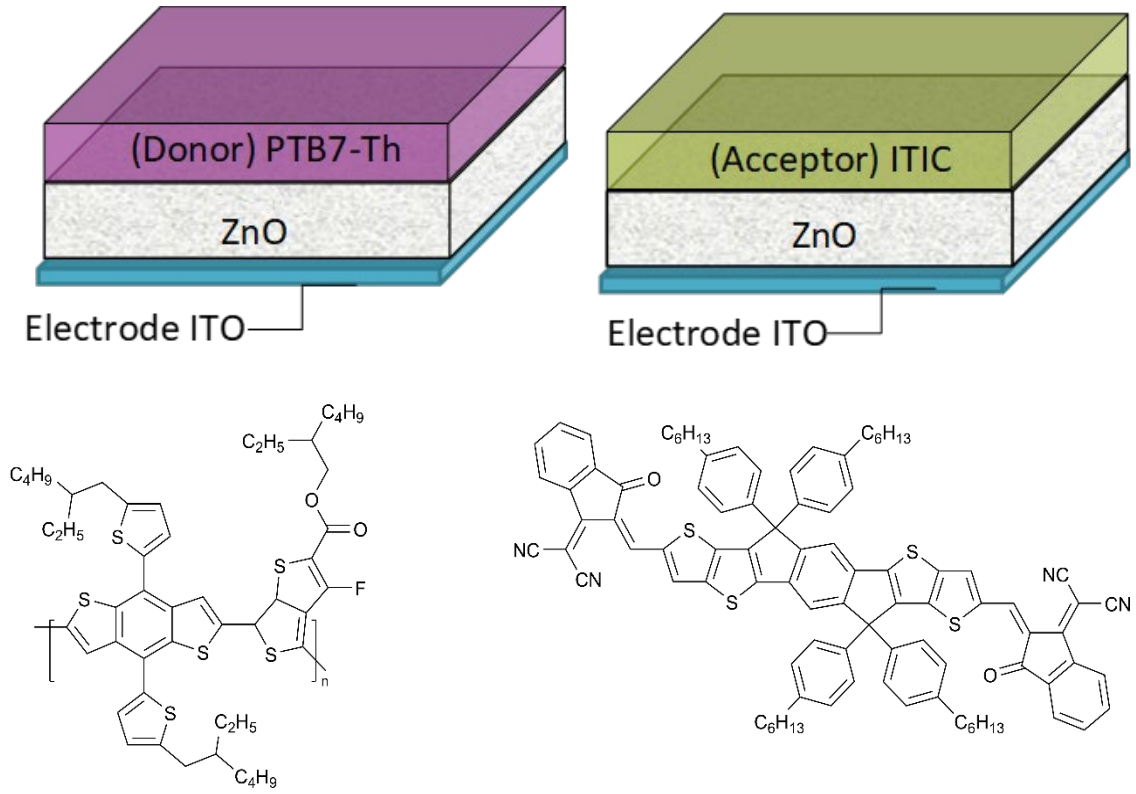

Figure 6-1. (Top) Device structure using ZnO as the interface layer, and (Bottom) the chemical structure of the polymer base PTB7-Th and ITIC.

6.3.2 Methods: electron and ion spectroscopy methods

Experimental details for electron spectroscopy (XPS, UPS and IPES) and NICISS are described in Chapter 3. The analysis of UP spectra, including SVD analysis, are also described in Chapter 3.

6.4 Results and Discussion

6.4.1 Film thickness - NICISS results

NICISS was used to determine the thickness of the PTB7-Th and ITIC layers deposited on the ZnO film. The thickness of the layers was determined from the energy loss in the overlayer (PTB7-Th and ITIC) attached to ZnO.[16] The energy loss of the He projectiles was determined from the shift of the half onset of the Zn contribution in the NICIS spectra

of the PTB7-Th and ITIC layers formed on ZnO. The energy backscattered spectra are shown in Figure 6-2, and the layer thicknesses are shown in Table 6-1.

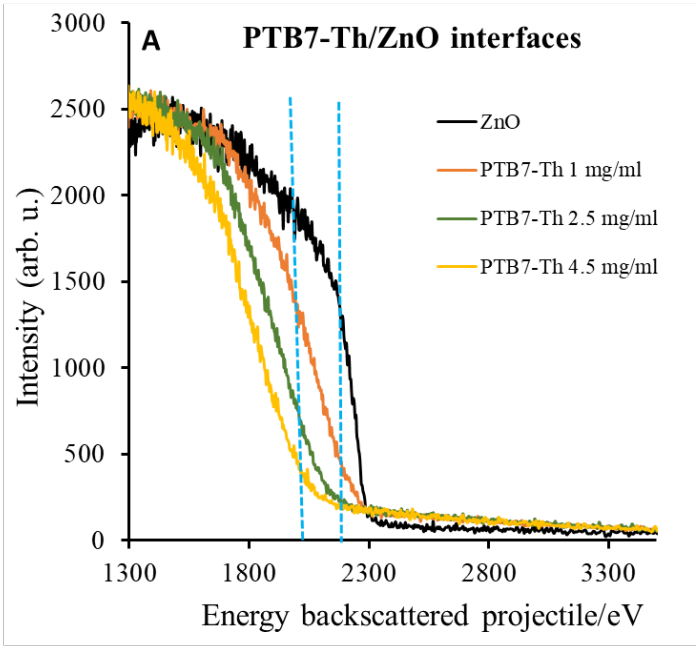

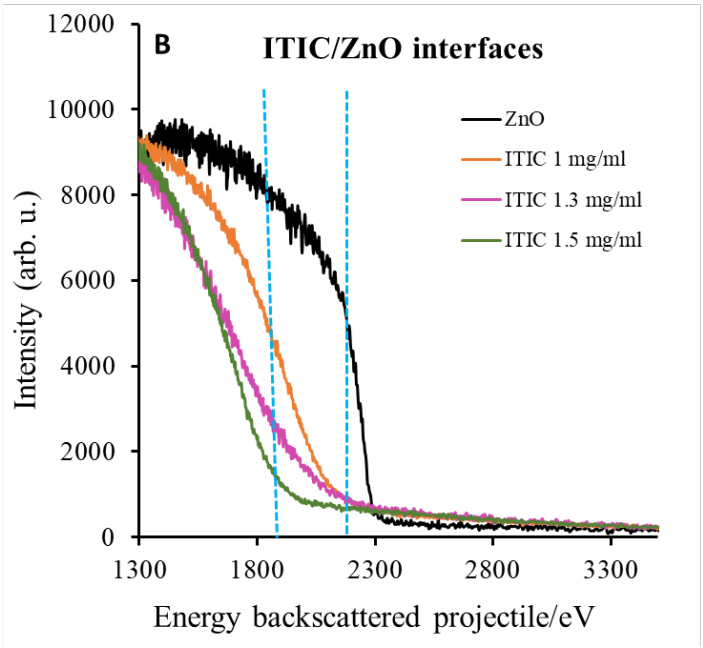

Figure 6-2. (A) NICIS spectra of pristine ZnO and PTB7-Th layers deposited on ZnO with different concentrations. (B) NICIS spectra of pristine ZnO and ITIC layers deposited on ZnO with different concentrations.

It must be noted that the layer thicknesses determined from the NICIS spectra are average thicknesses. As can be seen in Figure 6-2, the depth profiles of Zn of the ITIC/ZnO samples have a much shallower onset, demonstrating that the ITIC layer is inhomogeneous in thickness.

Table 6-1
Thicknesses of the ITIC and PTB7-Th Layers Deposited on ZnO, Evaluated from NICISS

Accepter (ITIC) concentrations (mg mL^{-1})	ITIC thickness (nm) ± 0.4 nm	Donor (PTB7-Th) concentrations (mg mL^{-1})	PTB7-Th thickness (nm) ± 0.4 nm
1	5.1	1	3.1
1.3	7.8	2.5	4.9
1.5	8.6	4.5	6.8

6.4.2 Characterisation of chemical changes - XPS results

To understand the composition and chemical structure of the active layers/ZnO interfaces, each material of PTB7-Th and ITIC deposited onto ZnO were studied separately with XPS for different concentrations of the spin coating solutions of PTB7-Th and ITIC, respectively. A pristine sample as a reference was also prepared by spin coating PTB7-Th and ITIC directly onto ITO.

The chemical composition of PTB7-Th/ZnO interfaces

High-resolution XPS was used for the C, S, F, O and Zn for PTB7-Th/ZnO samples, and all peck positions can be seen in Table S6-1. The C1s spectra in pristine PTB7-Th were fitted with three peaks—C-C, C-S and C=O—at 284.9 ± 0.2 eV[17], 287.0 ± 0.2 eV and 289.2 ± 0.2 eV,[18] respectively (see Table S6-1). The C-S bond is likely at a similar position to the C-N bond.

The C1s spectra for PTB7-Th/ZnO layers were fitted with three peaks—C-C, C-N[16] and C=O.[19] The positions of the C-C peaks for all PTB7-Th/ZnO samples show a significant

(~0.6 eV) shift towards higher binding energy after decreasing the thickness of the PTB7-Th spin-coated on top of ZnO, as shown in Figure 6-3A.

The same finding was observed for the S $2p_{3/2}$ peak, located at 164.1 ± 0.2 eV for pristine PTB7-Th, and the F1s peak, located at 687.7 ± 0.2 eV for pristine PTB7-Th. Both S and F peaks show a significant (~0.6 eV) shift towards higher binding energy after depositing PTB7-Th layers on top of ZnO, as shown in Figures 6-3B and 6-3C, respectively. This shift is likely an indication of a dipole forming at the PTB7-Th/ZnO interface and will be discussed below.

However, the positions of Zn were 1,022.6 ± 0.2 eV for the pristine ZnO sample and did not change after depositing different thicknesses of PTB7-Th. This demonstrates that these samples are not charging after depositing PTB7-Th on ZnO as shown in Figures 6-3D. The peak positions of all the species are provided in Table S6-1.

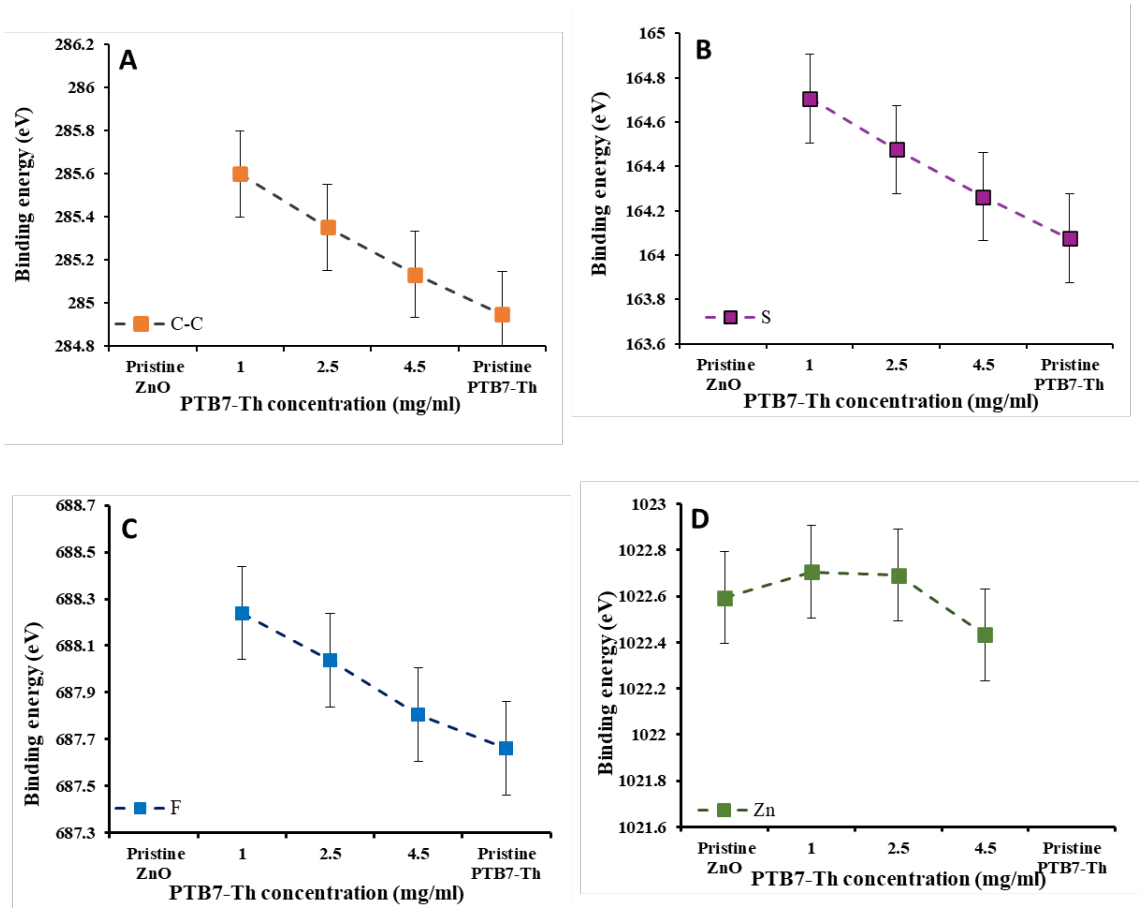

Figure 6-3. XPS results for PTB7-Th/ZnO interface. (A) shows the change in C-C, (B) shows the change in S, (C) shows the change in F and (D) shows the peak positions of Zn without any obvious shift.

The chemical composition of ITIC/ZnO interfaces

For the electron acceptor (ITIC), high-resolution XPS for Zn, S, N, C and O were applied for the ITIC/ZnO interface, as shown in Table S6-2. The C1s spectra for pristine ITIC were fitted with four peaks: 284.8 ± 0.2 eV,[17] related to a C-C bond; 285.7 ± 0.2 eV, identified as a C-N bond[20]; 286.6 ± 0.2, assigned to a C-S and 287.6 eV, identified as a C=O bond (see Table S6-2).

The C1s spectra for ITIC/ZnO interfaces were fitted with two peaks, which are C-C and C-N. The C1s peak position for ITIC/ZnO interfaces did not show any change after depositing different ITIC layer thicknesses on ZnO, as shown in Figure 6-4A.

Similarly, the S $2p_{3/2}$ peak for pristine ITIC and the ITIC/ZnO layer is found at 164.3 ± 0.2 eV[21] and does not show any shift after decreasing the ITIC layer thicknesses, as shown in Figure 6-4B.

The N1s spectra of the pristine ITIC were fitted with three peaks—399.2 ± 0.2 eV, 400.6 ± 0.2 eV and 402.5 ± 0.2 eV—corresponding to N=C, N-C and N-O[22,23]. The N1s spectra of the ITIC/ZnO layered sample were fitted with one peak, 399.2 ± 0.2, related to N=C. This peak does not show any shift on the energy scale after decreasing the ITIC layer thicknesses on ZnO, as shown in Figure 6-4C. This suggests that there is no electric bias and dipole formation at the ITIC/ZnO interfaces.

It should be noted that the Zn peak shows a small but noticeable shift towards higher binding energy after increasing the ITIC layer thickness on ZnO, as shown in Figure 6-4D. In previous investigations, the surface of the interface layer did not show a shift in binding energy, reflecting that it is connected to the underlying ITO. The reason could be that either ZnO is chemically affected by ITIC, or that with an increasing amount of ITIC at the interface, some of the ITIC is penetrating between ITO and ZnO. In either case, the effect is small. All the peak positions of all the ITIC/ZnO interfaces are shown in Table S6-2.

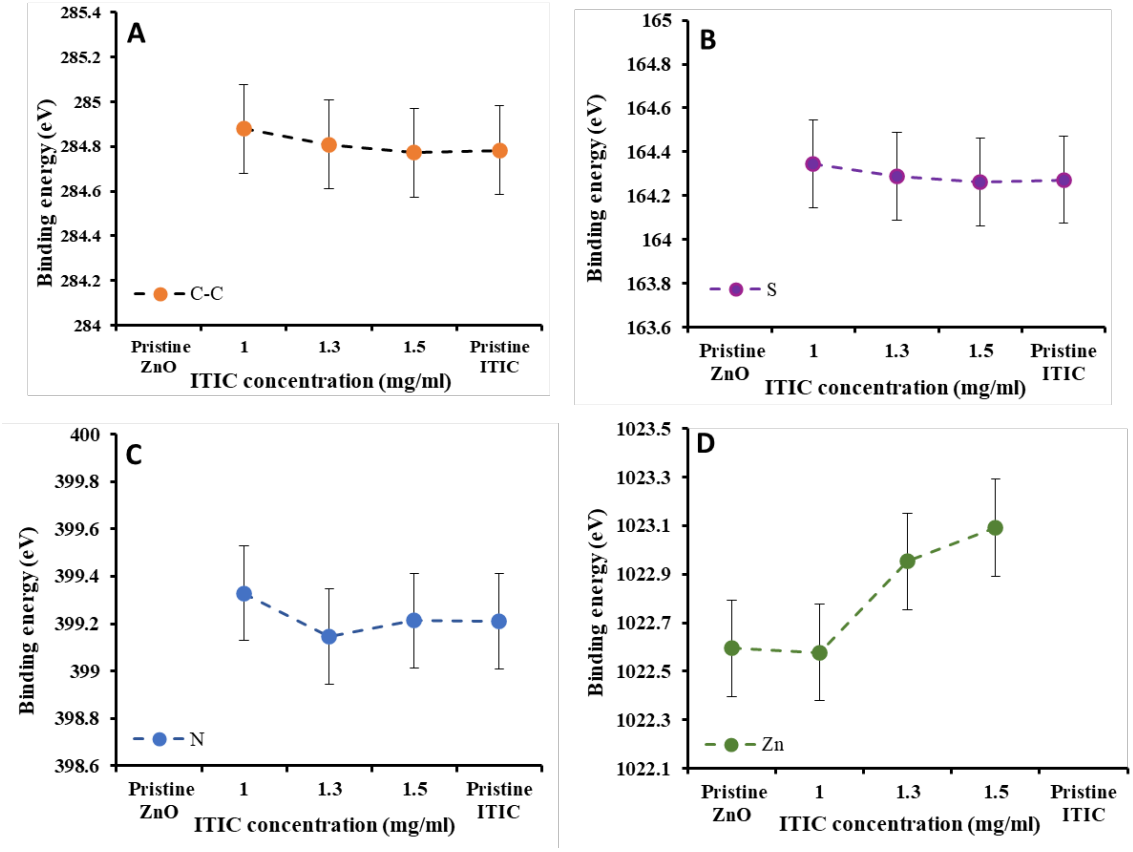

Figure 6-4. XPS results for ITIC/ZnO interfaces layers. (A) shows the peak position of C-C, (B) shows S peak positions, (C) shows N peak positions and (D) shows the peak positions of Zn with transition shift.

6.4.3 Analysis of UP and IPE Spectra

Data evaluation of UPS and IPES

The electronic properties of PTB7-Th and ITIC on ZnO interfaces were analysed via UPS and IPES. UPS and IPES were also individually applied to pristine ITIC, PTB7-Th and ZnO to identify the position of the VB/E_{HOMO} from the UP spectra, and the CB/E_{LUMO} from the IPE spectra. The procedure for determining the cut-off of VB and CB is explained in Chapter 4, Section 4.4.3. The UPS and IPE spectra of each sample were combined in one graph each and are shown in Figure 6-5. Table 6-2 shows the values of VB/E_{HOMO} and CB/E_{LUMO} obtained from UPS and IPES of pristine PTB7-Th, pristine ITIC and pristine ZnO on ITO. All UPS and IPE spectra of the PTB7-Th/ZnO and ITIC/ZnO interfaces with varying layer thickness are shown in Figure S6-1. The cut-offs

of the VB regions are shown in Figures S6-2 and S6-3. All values are shown in Tables S6-3 and S6-4.

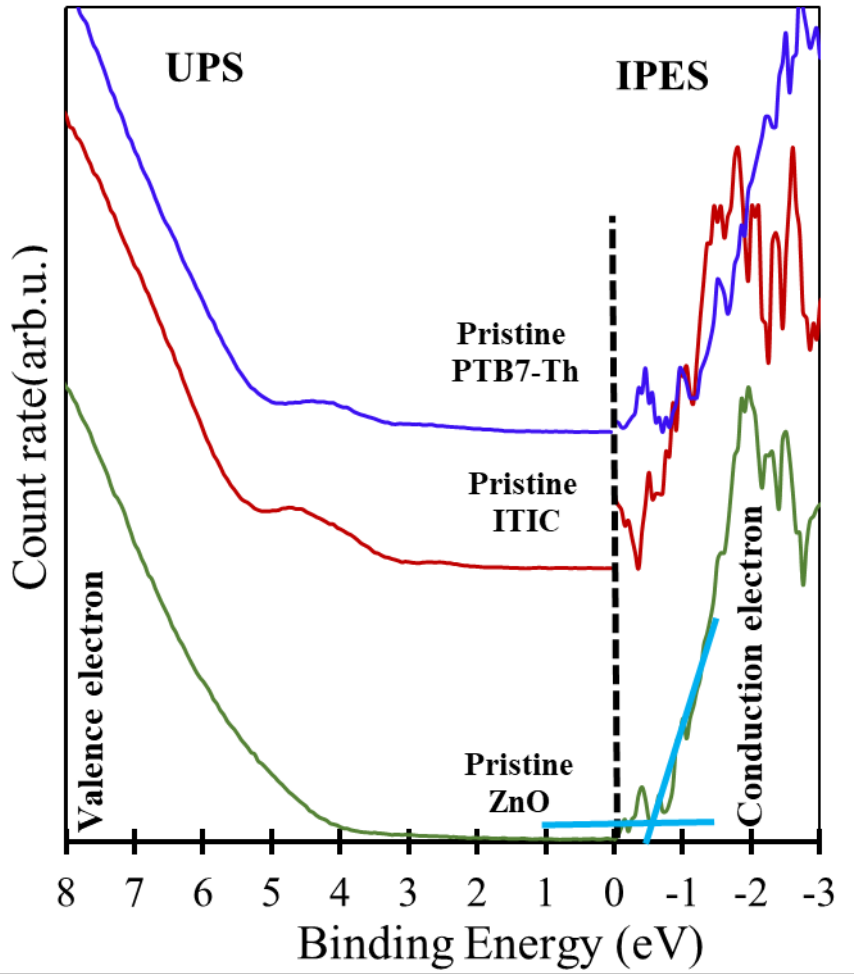

Figure 6-5. The plot of the CB/E_{LUMO} and VB/E_{HOMO} region as measured via UPS and IPES of the PTB7-Th, ITIC and ZnO samples. For determining the cut-off for VB and CB, the level of noise in the UP and IPE spectra must be considered, with the IPE spectra showing a higher level of noise.

Table 6-2

The Values of VB/E_{HOMO}, CB/E_{LUMO} and the Energy gap (Eg) of the PTB7-Th, ITIC and ZnO Samples

Sample	VB/E_{HOMO} (eV) ± 0.1	CB/E_{LUMO} (eV) ± 0.1	Eg (eV) ± 0.1
Pristine PTB7-Th	0.6	–1.0	1.6
Pristine ITIC	1.0	–0.4	1.4
Pristine ZnO	3.1	–0.4	3.5

Note. All energies are indicated with a zero point at Fermi Level (E_f). The VB/E_{HOMO} is higher than the Fermi level and noted as positive, while the CB/E_{LUMO} is lower and noted as negative.

Decomposition of valence electron spectra of UPS

The valence electron region of the UP spectra was analysed using the SVD method to identify the components that constitute the measured spectra. Reference spectra representing each constituting component and the corresponding weighting factors are shown in Figure 6-6. The aim was to analyse the electronic structure of the PTB7-Th/ZnO and ITIC/ZnO interfaces.

Figure 6-6A shows three reference spectra required to fit the whole set of measured spectra of the PTB7-Th/ZnO interface. Reference A has features very similar to the pristine ZnO spectrum and is thus considered as representing the same. Reference B and reference C can be assigned to pristine PTB7-Th, as those references are similar in shape to PTB7-Th spectra, as shown in Figure 6-6A. However, reference C is subject to an ~0.2 eV shift towards higher binding energy, as shown in Figure 6-6C. Such a reference spectrum has been identified in our earlier work[16] and represents the pristine polymer being subject to a shift on the energy scale due to the formation of a dipole between the polymer and the interface layer. Thus, the minor shift of PTB7-Th can be attributed to the formation of a dipole between PTB7-Th and ZnO.

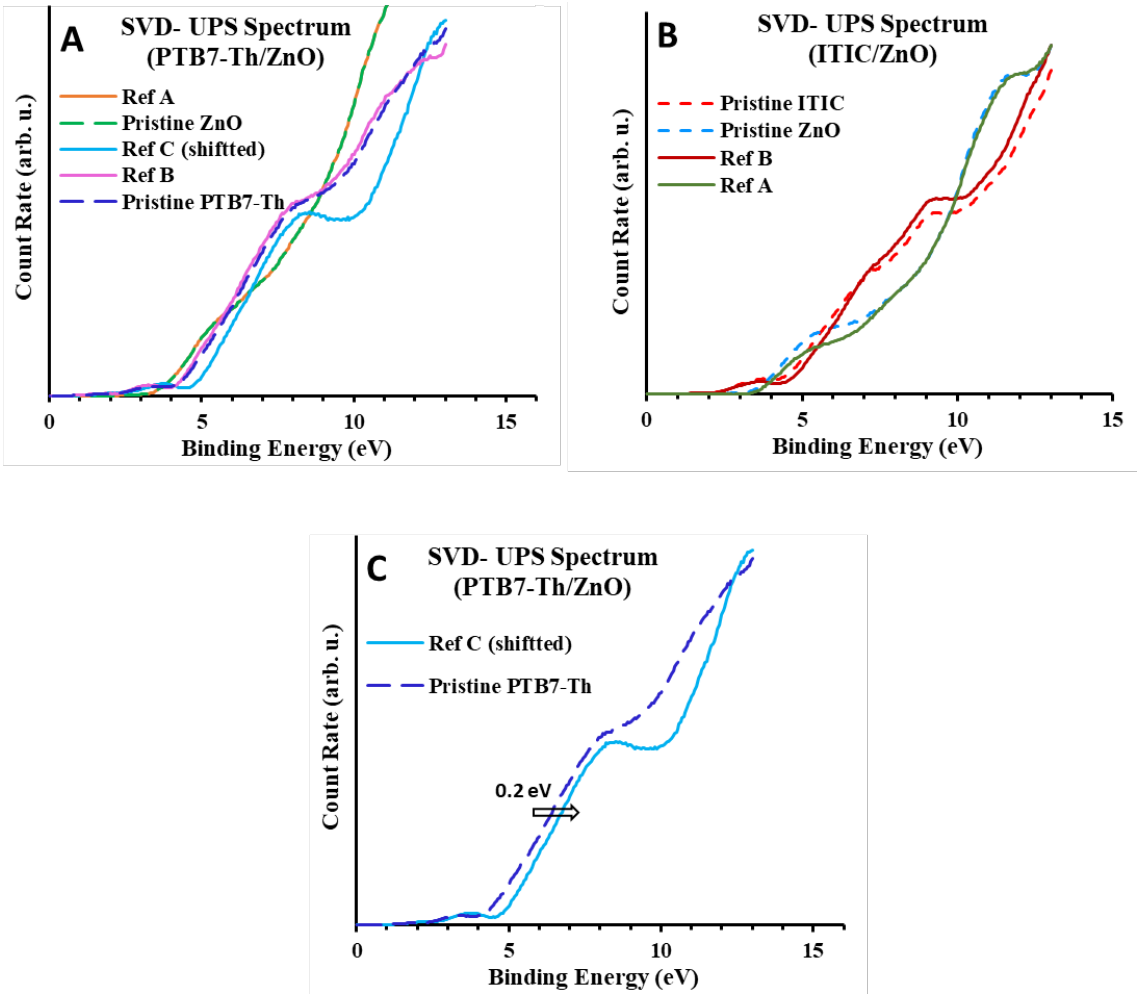

Figure 6-6. The reference spectra of UPS (obtained from SVD analysis) for (A) PTB7-Th/ZnO interfaces and (B) ITIC/ZnO interfaces. (C) The third reference of PTB7-Th/ZnO interfaces, shifted towards higher binding energy by 0.2 eV. Note that Ref A and Pristine ZnO overlap.

The weighting factors of the three reference spectra of the PTB7-Th/ZnO interface are shown in Figure 6-7A. The weighting factors for ZnO (Ref A) show a decrease as PTB7-Th (Ref B) increases in thickness concentration, as shown in Figure 6-7A. PTB7-Th (Ref C) mainly shows the contributions of ZnO at 1 mg/mL and 2.5 mg/mL.

It must be noted that the weighting factors in this SVD analysis had to be normalised, as the set of spectra was acquired over a longer period and the intensity of the UV source might have changed over this period.

The UP spectra of ITIC/ZnO were analysed using SVD to investigate the change upon the deposition of ITIC on ZnO. Two references were found in the ITIC/ZnO interface, as shown in Figure 6-7B. Based on the shape of the spectra, reference A can be identified as the ZnO spectrum, and reference B is assigned as ITIC. There is no notable shift for the ITIC spectrum, meaning no dipole forms at the interface of TIC and ZnO. The weighting factors for UPS for the two references can be seen in Figure 6-7B. Similar to the above, the weighting factors can be applied here for the ITIC/ZnO interface.

It should be noted that the average layer thicknesses of ITIC and PTB7-Th exceed three times the electron mean free path of the conditions for UPS. However, the ITIC and PTB7-Th layers are inhomogeneous in thickness and so can be seen in UPS of the ITIC/ZnO and PTB7-Th/ZnO samples.

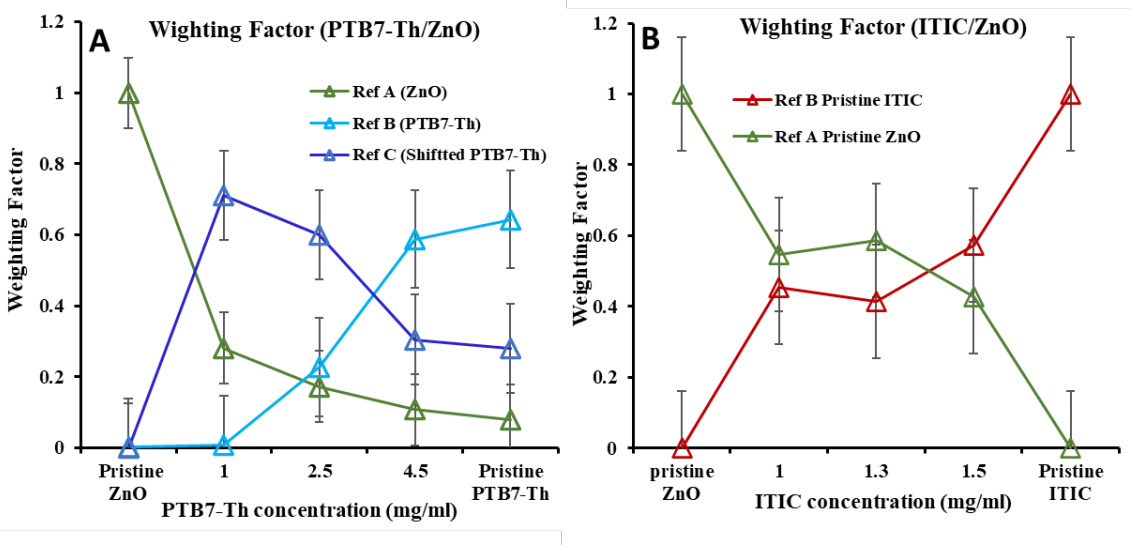

Figure 6-7. Weighting factors of UPS for (A) PTB7-Th/ZnO interfaces and (B) ITIC/ZnO interfaces.

Interpretation of the electron spectra

The samples of PTB7-Th and ITIC, with a range of layer thicknesses, deposited onto ZnO were used to analyse the structure of the PTB7-Th/ZnO and ITIC/ZnO interfaces. From UPS results, it was found that the ITIC spectra show no shift on the energy scale after deposition onto ZnO, indicating that there is no dipole formed at the ITIC/ZnO interface.

Conversely, the PTB7-Th spectra show a shift of +0.2 eV on the energy scale after deposition onto ZnO, caused by the formation of a weak dipole between PTB7-Th and ZnO. This shift is towards higher binding energy, indicating that the dipole direction is from PTB7-Th to ZnO; that is, the positive end of the dipole is directed towards PTB7-Th, while the negative end moves towards the buried layer of ZnO. XPS results confirmed the formation of a dipole between PTB7-Th and ZnO; S and F, which are linked to the functional groups of PTB7-Th, exhibited a ~0.6 eV ± 0.1 shift towards higher binding energy with increasing thickness of PTB7-Th on ZnO.

The differences in the dipole strength identified via XPS and UPS mean two dipoles are formed between PTB7-Th and ZnO. The first dipole is formed directly at the PTB7-Th/ZnO interface, and the second dipole, with an opposite polarity to the first, is formed within the PTB7-Th layer. The second dipole adds to the dipole at the PTB7-Th/ZnO interface and, due to its opposite orientation, diminishes the overall dipole between PTB7-Th and ZnO. This conclusion is supported by the observed shift in the peak positions of S and F as a function of PTB7-Th layer thickness. Similar results were found by Chen et al., who investigated the dipole at the interface between the electron transport material BPhen (at different thicknesses) and a range of different conducting substrates.[24] Their results showed two types of interface dipoles were formed: one at the interface and a second—named the 'double dipole step'—induced by the positive and negative charged species of BPhen when they are close to the surface of substrates.[24]

The differences in the dipole strength found via XPS and UPS in our work are due to differences in the probing depth. UPS, with the comparatively smaller probing depth, probes the region where the two dipoles have diminished the overall dipole due to their opposite polarity. XPS probes deeper, thus detecting a stronger contribution from the PTB7-Th/ZnO interface and showing a different dipole. For the ITIC/ZnO interface, the positions of S and N (being a part of ITIC) are consistent with the UPS results that show

no shift when increasing the thickness of ITIC on ZnO. This demonstrates that there is no molecular orientation at the ITIC/ZnO interface.

Energy levels modelling and implications for charge transport (CT) over the interface

The XPS, UPS and IPES results can be combined in an energy level diagram of the PTB7-Th/ZnO and ITIC/ZnO interfaces, as shown in Figure 6-8. In an OPV system, the electrons would be transferred only from the accepter to ZnO and holes from the donor to the high WF materials. The XPS-detected shift in the energy scale towards higher binding energy for PTB7-Th is 0.6 ± 0.1 eV due to the dipole formation at the PTB7-Th/ZnO interface. This shift pushes the E_{HOMO} and E_{LOMO} of PTB7-Th downward. With this shift, the VB/E_{HOMO} of PTB7-Th is still far from the VB/E_{HOMO} of ZnO, which blocks the hole transfer from PTB7-Th to ZnO, as shown in Figure 6-8A.

Figure 6-8B shows the energy level between ITIC and ZnO. There is no dipole formed at the ITIC/ZnO interfaces. In this case, no change in the position of E_{HOMO} and E_{LOMO} of ITIC would apply compared to the reference substrate. The CB/E_{LUMO} of ITIC is aligned with the CB/E_{LUMO} of ZnO; thus, electrons can be transferred to ZnO.

Overall, the desired charge transfer processes using ZnO meet the expectation of blocking the hole and facilitating the electron transfer to ITIC—since the CB/E_{LUMO} of PTB7-Th with the shift is still aligning with the CB/E_{LUMO} of ITIC, which, ultimately, would allow the transport of electrons over the interface.

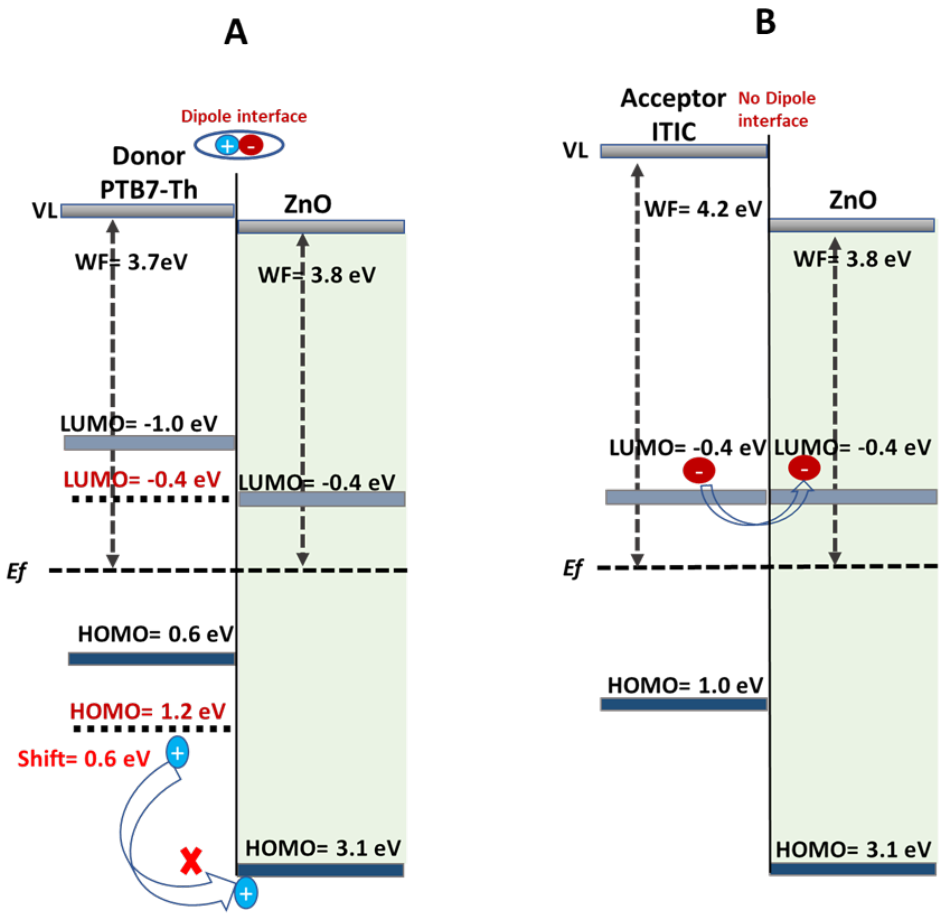

Figure 6-8. The energy level of (A) PTB7-Th/ZnO/ITO and (B) ITIC/ZnO/ITO and the CT over the interface layers. VL, vacuum level.

6.5 Conclusion

The electronic structures at the PTB7-Th/ZnO and ITIC/ZnO interfaces were investigated. XPS and UPS were used to study the chemical and electronic properties at the interfaces upon deposition of different active layers onto ZnO. It was found that two dipoles were formed when PTB7-Th was deposited onto ZnO: one at the PTB7-Th/ZnO interface, and a second (with opposite polarity) within the PTB7-Th layer. The formation of these dipoles was confirmed by analysing the shifts of the PTB7-Th components (via XPS) and VB region (via UPS). In contrast, no dipole was found at the ITIC/ZnO interface. The complete energy level structure at the interfaces was constructed and shows that the energy levels are suitable for CT between ZnO and PTB7-Th/ITIC.

6.6 Acknowledgement

The authors would like to acknowledge the support of the Australian National Fabrication Facility (ANFF) and Australian Microscopy & Microanalysis Research Facility (AMMRF) regarding using experimental equipment. The authors acknowledge Flinders Microscopy and Microanalysis and their expertise. The authors would like to thank Dr Caroline Pan for her help and support in this project.

6.7 References

(1) Wadsworth, A.; Moser, M.; Marks, A.; Little, M. S.; Gasparini, N.; Brabec, C. J.; Baran, D.; McCulloch, I. Critical Review of the Molecular Design Progress in Non-Fullerene Electron Acceptors Towards Commercially Viable Organic Solar Cells. *Chemical Society Reviews* **2019**, *48* (6), 1596–1625.

(2) Lin, Y.; Wang, J.; Zhang, Z. G.; Bai, H.; Li, Y.; Zhu, D.; Zhan, X. An Electron Acceptor Challenging Fullerenes for Efficient Polymer Solar Cells. *Advanced Materials* **2015**, *27* (7), 1170–1174.

(3) Gurney, R. S.; Li, W.; Yan, Y.; Liu, D.; Pearson, A. J.; Wang, T. Morphology and Efficiency Enhancements of PTB7-Th: ITIC Nonfullerene Organic Solar Cells Processed via Solvent Vapor Annealing. *Journal of Energy Chemistry* **2019**, *37*, 148–156.

(4) Alghamdi, A. R.; Kirk, B. P.; Kocak, G.; Andersson, M. R.; Andersson, G. G. Modification of the Surface Composition of PTB7-Th: ITIC Blend Using an Additive. *Molecules* **2022**, *27* (19), 6358.

(5) Bao, Q.; Liu, X.; Braun, S.; Li, Y.; Tang, J.; Duan, C.; Fahlman, M. Intermixing Effect on Electronic Structures of TQ1: $PC_{71}BM$ Bulk Heterojunction in Organic Photovoltaics. *Solar RRL* **2017**, *1* (10), 1700142.

(6) Li, Y.; Li, P.; Lu, Z. H. Molecular Orientation and Energy Levels at Organic Interfaces. *Advanced Electronic Materials* **2016,** *2* (11), 1600306.

(7) Li, X. E.; Zhang, Q.; Yu, J.; Xu, Y.; Zhang, R.; Wang, C.; Zhang, H.; Fabiano, S.; Liu, X.; Hou, J. Mapping the Energy Level Alignment at Donor/Acceptor Interfaces in Non-Fullerene Organic Solar Cells. *Nature Communications* **2022**, *13* (1), 1–9.

(8) Sun, Y.; Seo, J. H.; Takacs, C. J.; Seifter, J.; Heeger, A. J. Inverted Polymer Solar Cells Integrated with a Low-Temperature-Annealed Sol-Gel-Derived ZnO Film as an Electron Transport Layer. *Advanced Materials* **2011**, *23* (14), 1679–1683.

(9) Park, S.; Jeong, J.; Hyun, G.; Kim, M.; Lee, H.; Yi, Y. The Origin of High PCE in PTB7 Based Photovoltaics: Proper Charge Neutrality Level and Free Energy of Charge Separation at PTB7/PC 71 BM Interface. *Scientific Reports* **2016**, *6*, 35262.

(10) Andersson, G. G.; Golovko, V. B.; Alvino, J. F.; Bennett, T.; Wrede, O.; Mejia, S. M.; Al Qahtani, H. S.; Adnan, R.; Gunby, N.; Anderson, D. P. Phosphine-Stabilised Au9 Clusters Interacting with Titania and Silica Surfaces: The First Evidence for the Density of States Signature of the Support-Immobilised Cluster. *The Journal of Chemical Physics* **2014**, *141* (1), 014702.

(11) Oberbrodhage, J. Determination of a Solute Electron Energy Spectrum Not Accessible Experimentally by Means of Singular Value Decomposition. *Journal of Electron Spectroscopy and Related Phenomena* **2000**, *107* (3), 231–238.

(12) Andersson, G.; Morgner, H.; Pohl, H. Energy-Loss Straggling of Helium Projectiles at Low Kinetic Energies: Deconvolution of Concentration Depth Profiles of Inorganic Salt Solutes in Aqueous Solutions. *Physical Review A* **2008**, *78* (3).

(13) Andersson, G.; Morgner, H. Determining the Stopping Power of Low Energy Helium in Alkanethiolates with Neutral Impact Collision Ion Scattering Spectroscopy (NICISS). *Nuclear Instruments and Methods in Physics Research Section B: Beam Interactions with Materials and Atoms* **1999**, *155* (4), 357–368.

(14) Andersson, G.; Morgner, H. Investigations on Solutions of Tetrabutylonium Salts in Formamide with NICISS and ICISS: Concentration Depth Profiles and Composition of the Outermost Layer. *Surface Science* **2000**, *445* (1), 89–99.

(15) Andersson, G.; Morgner, H. Impact Collision Ion Scattering Spectroscopy (ICISS) and Neutral Impact Collision Ion Scattering Spectroscopy (NICISS) at Surfaces of Organic Liquids. *Surface Science* **1998**, *405* (1), 138–151.

(16) Alghamdi, A. R.; Bjuggren, J. M.; Pan, X.; Andersson, M. R.; Andersson, G. G. Dipole Formation at Active Materials/P (NDI3N-T-Br) Interface in Organic Based Photovoltaic. *Macromolecular Materials and Engineering* **2022**, 2200303.

(17) Yin, Y.; Sibley, A.; Quinton, J. S.; Lewis, D. A.; Andersson, G. G. Dipole Formation at the MoO3/Conjugated Polymer Interface. *Advanced Functional Materials* **2018**, *28* (46), 1802825.

(18) Dolgov, A.; Lopaev, D.; Lee, C. J.; Zoethout, E.; Medvedev, V.; Yakushev, O.; Bijkerk, F. Characterization of Carbon Contamination Under Ion and Hot Atom Bombardment in a Tin-Plasma Extreme Ultraviolet Light Source. *Applied Surface Science* **2015**, *353*, 708–713.

(19) Yin, Y.; Lewis, D. A.; Andersson, G. G. Influence of Moisture on the Energy-Level Alignment at the MoO3/Organic Interfaces. *ACS Applied Materials & Interfaces* **2018**, *10* (50), 44163–44172.

(20) Shin, Y.-E.; Sa, Y. J.; Park, S.; Lee, J.; Shin, K.-H.; Joo, S. H.; Ko, H. An Ice-Templated, pH-Tunable Self-Assembly Route to Hierarchically Porous Graphene Nanoscroll Networks. *Nanoscale* **2014**, *6* (16), 9734–9741.

(21) Scudiero, L.; Shen, Y.; Gupta, M. C. Effect of Light Illumination and Temperature on P3HT Films, n-Type Si, and ITO. *Applied Surface Science* **2014**, *292*, 100–106.

(22) Mao, M.; Luo, C.; Pollard, T. P.; Hou, S.; Gao, T.; Fan, X.; Cui, C.; Yue, J.; Tong, Y.; Yang, G. A Pyrazine-Based Polymer for Fast-Charge Batteries. *Angewandte Chemie International Edition* **2019**, *58* (49), 17820–17826.

(23) Osadchii, D. Y.; Olivos-Suarez, A. I.; Bavykina, A. V.; Gascon, J. Revisiting Nitrogen Species in Covalent Triazine Frameworks. *Langmuir* **2017**, *33* (50), 14278–14285.

(24) Chen, Y.; Liu, X.; Braun, S.; Wang, Y.; Fahlman, M. Image-Force Effects on Energy Level Alignment at Electron Transport Material/Cathode Interfaces. *Journal of Materials Chemistry C* **2020**, *8* (1), 173–179.

Chapter 7: Modification of the Surface Composition of PTB7-Th: ITIC Blend Using an Additive

Amira R Alghamdi,[1,2] Bradley Kirk,[1,2] Guler Kocak,[1,2] Mats R. Andersson,[1,2] and Gunther G. Andersson[1,2*]

[1] Flinders Institute for Nanoscale Science and Technology, Flinders University, GPO Box 2100 Adelaide SA 5001, Australia.

[2] Flinders Microscopy and Microanalysis, College of Science and Engineering, Flinders University, Adelaide, South Australia 5042, Australia.

This work has been published in *Molecules Materials*, 2022. The only alterations are that any experimental methods and analysis procedures previously described in Chapter 3 have been removed from this chapter.

Author contributions:

Amira Alghamdi: Designed and performed experiments, data analysis and interpretation of the data and prepared the manuscript for publication. **Bradley Kirk:** Performed AFM measurements and revised the manuscript. **Guler Kocak:** Provided the devices' performance data. **Gunther Andersson:** Intellectual contribution in conceptualising experiments, data interpretation and revision of manuscript. **Mats Andersson:** Intellectual contribution.

7.1 Abstract

The effect of adding *p*-anisaldehyde (AA) solvent to the ink containing PTB7-Th and ITIC on the morphology of the active layer was investigated. The present study focuses on determining the effect of the additive on the compositions at the surface of the PTB7-Th: ITIC composite and its morphology forming one side of the interface of the blend with the MoO_x electrode and the influence of the structural change on the performance of devices.

Studies of the device performance show that the additive AA leads to an improvement in device performance. Upon the addition of AA, the concentration of PTB7-Th at the surface of the BHJ increases, causing an increase in surface roughness of the BHJ surface. This finding contributes to an understanding of the interaction between the donor material and high WF electrode/interface material. The implication for the interface is discussed.

7.2 Introduction

OPV devices consist of organic-based electron donor and acceptor materials that have well-designed molecular structures, appropriate energy levels and wide absorption in the visible spectrum, which has demonstrated a PCE of greater than 19%.[1,2] However, by optimising the morphology of the BHJ, a high-performance OPV can be achieved more readily. With the optimisation of the BHJ structure, a sufficient interfacial contact between the donor and acceptor components of the BHJ allows for adequate exciton dissociation into free charges.[3] The control of the morphology, which influences the domain size and component distribution across the interface, can then be achieved.[4]

Many factors can influence the morphology, including a selection of solvents and additives used in the solution preparation, donor/acceptor ratio and thermal and solvent conditions of annealing the films.[5] It has significantly contributed to an effective charge

transport (CT) that comes from the interconnectivity of the donor and acceptor phases and a proper phase separation between them, which can lead to improved charge separation.[6–8] Further, tuning the crystallinity of the active layer[9] and the domain size could affect the charge carrier mobility. This can be achieved by introducing thiol groups,[10] incorporations of electron-withdrawing groups in thiophene polymers[11] or through the use of different solvent mixtures.[12,13]

To improve the efficiency of the device performance through the manipulation of the BHJ, many studies have focused on additives in the solvents that affect the aggregation of active materials, ultimately influencing the film morphology and device efficiencies.[14] Gurney et al. studied the effect of solvent vapour annealing on the performance of devices based PTB7-Th: ITIC. They found that the annealing process of the solvent impacts on the morphology of the BHJ, which resulted in a better phase separation of BHJ.[15] A similar study was done by Wang, who investigated the influence of the solvents on the crystallinity of the acceptor (ITIC) phase. They found an improvement in the V_{oc} and the film morphology (PTB7-Th: ITIC).[16]

Typically, solvent additives have a higher boiling point than the main solvent. They are able to dissolve at least one of the two blend components.[17] A number of additive studies have been conducted with alkane dithiols and halogenated alkanes.[10] In most polymer fullerene systems, halogenated solvent additives such as 1,8-diiodooctane (DIO) are added to the active layer ink prior to deposition. The addition of DIO has been found to dissolve 6,6-PCBM selectively and achieve better phase separation and domain purity, thus improving device performance.[18–21] The addition of DIO to a system that uses non-fullerene acceptors, such as PTB7-Th: ITIC, resulted in large domains in the BHJ, which increased the probability of charge recombination and thus a reduction in performance.[22,23] This indicated that the processing methods must be tailored to the specific properties of the material. In addition to affecting solution miscibility, the high

boiling point of DIO limits solvent evaporation and drying time, leading to a more ordered and crystalline film.[4,19]

A direct comparison of PTB7-Th devices with either $PC_{71}BM$ or ITIC acceptors resulted in an outcome that indicated that 3 wt.% DIO optimised the domain sizes and purity in the fullerene system, whereas similar conditions yielded stronger separated phases in the non-fullerene system.[23,24] In another study, Zhao et al. discovered the benefits of using DIO as a solvent additive in other non-fullerene systems. The findings showed that adding 0.5 wt.% DIO contributed to the creation of a favourable aggregation, leading to an improvement in CT, low recombination and high performance, which enabled poly[(2,6-(4,8-bis-5-(2-ethylhexyl)thiophen-2-yl)benzo[1,2-b:4,5-b′]dithiophene)-co-(1,3-di(5-thiophene-2-yl)-5,7-bis(2-ethylhexyl)benzo[1,2-c:4,5-c′]dithiophene-4,8-dione)] (PBDB-T): ITIC to outperform its fullerene counterpart.[25] Hence, it is possible that the orientation of the alkyl side chains found on the IDT backbone interacts with the DIO, resulting in better miscibility by lowering steric hindrance between the molecules, thereby enhancing finer phase separation and creating purer crystalline phases.[26] However, according to Zhan et al., different mixing enthalpies renders the control of donor polymers mixing with NFAs difficult.[27] This limitation hinders the realisation of an optimal microstructure for enabling pure and mixed domains in NFA systems with solvent additives.[28–30] Therefore, typical optimisation approaches adopted in fullerene-based procedures may lack validity for NFA SCs.

Despite the advantages of using high boiling-point solvent additives, the slow process of evaporation means slower fabrication times, such as holding the device under vacuum for long periods of time to eliminate residual solvent. Any remaining residual solvent within the active layer could result in the formation of radicals under UV illumination[31] or the creation of a pathway for oxygen penetration, thereby resulting in film degradation.[32,33]

A further factor influencing the device performance is phase segregation and concentration distribution of the donor and acceptor.[34–38] In simple terms, the

transmission of a hole along consecutive donor domains will benefit from interfaces that are donor-rich at the anode and vice versa. As an example, it was proposed that increasing the surface coverage of P3HT at the anode would result in an improved conventional OPV; however, device performances were not strictly based on the measured vertical stratification.[13,39]

In the literature, BHJ are reported to have a high donor concentration at the surface in the inverted OPV. Chen et al. investigated the effects of the fluorinated counterparts on the concentration gradient, and they explored a higher concentration of donor in the BHJ before and after the fluorination. The fluorination of NFAs reduces the number of donors in this donor-rich region, encouraging the mixing of donors and acceptors for the generation of efficient charges.[40] Although the concentration distribution has been well studied, identifying the composition of blends at the surfaces has not been studied with the same rigour. We anticipate that the donor, which facilitates the hole transfer to the high WF electrode, should be enriched at the interface with the high WF electrode, which would significantly expand our understanding of the functions of BHJ-based OPVs. Huang et al. investigated the effect of using *p*-anisaldehyde (AA) on the device performance based on poly[(2,6-(4,8-bis-5- (2-ethylhexyl)thiophen-2-yl)benzo[1,2-b:4,5-b′]dithiophene)-co-(1,3-di(5-thiophene-2-yl)-5,7-bis(2-ethylhexyl)benzo[1,2-c:4,5-c′]dithiophene-4,8-dione)]:poly{[N,N0-bis(2-octyldodecyl) naphthalene 1,4,5,8-bis(dicarboximide)-2,6-diyl]-alt-5,5′-(2,2′-bithiophene)} (PBDB-T: N2200). They found the interfacial contact between PBDB-T and N2200 itself and between the active layer and PEDOT: PSS improved, which led to the promotion of the efficient exciton dissociation.[41]

In this work, we modified the compositions of the active layer by introducing AA as an additive. AA has both an oleophilic methoxy group and a hydrophilic aldehyde group. The purpose of adding AA is to optimise the interfacial compatibility of PTB7-Th and ITIC by increasing the PTB7-Th concentration at the interface. AA is non-toxic and has

a high volatility, allowing for its complete evaporation during the spin coating process of the active layer.[42] The focus of this study is to understand the composition of the surface and near-surface area of the blend based on PTB7-Th: ITIC with the effect of AA additive. In inverted devices, it is required to have a sufficient electron donor concentration at the high WF electrode. Since the energy levels between the donor (PTB7-Th) and MoO_x are rather close, the donor enrichment at the interface is beneficial for CT to MoO_x. For our work, we apply NICISS as a depth profiling technique to quantitatively determine the concentration depth profiles at the surface with a depth resolution of a few Å and thus determine the concentration of materials present at the surface. We report the effect of the additive AA solvent on the composition of the sample at the surface and on the surface morphology. We show that AA has a beneficial effect on phase separation, increasing the donor at the surface and improving device performance.

7.3 Experimental

7.3.1 Material and device fabrication

PTB7-Th (Mn = 80 000) was purchased from 1-Materials Inc. and the acceptor polymer ITIC was purchased from Raynergy Tek Inc. o-Xylene and AA were purchased from Sigma-Aldrich, whereas acetone and 2-propanol were supplied by Chem-Supply. All solvents were used directly without purification.

The procedure for preparing ZnO can be found in Chapter 3, Section 3.2.2.

The BHJ blend films of devices, PTB7-Th: ITIC inverted polymer SC were fabricated using a non-toxic solvent additive AA and host solvent o-xylene. Devices were fabricated in a glass/ITO/ZnO/PTB7-Th: ITIC/MoO_X/Ag device configuration. The active layer ink was prepared by dissolving active layer materials, with a donor:acceptor weight-to-weight ratio of 1:1.3, in o-xylene (total 19.5 mg mL^{-1}), either with or without 2% V/V AA. The AA additive has been tested in the literature for a different system and recorded

the highest efficiency at 2%.[42] Here, we choose the same AA concentration. Active layer ink was mixed overnight at 75 °C under vigorous stirring. With the prepared ink, the solution was spin-coated over the ZnO film at 2,500 rpm for 60 seconds for the controlled and modified devices, respectively. The chemical structure of PTB7-Th, ITIC and AA is illustrated in Figure 7-1.

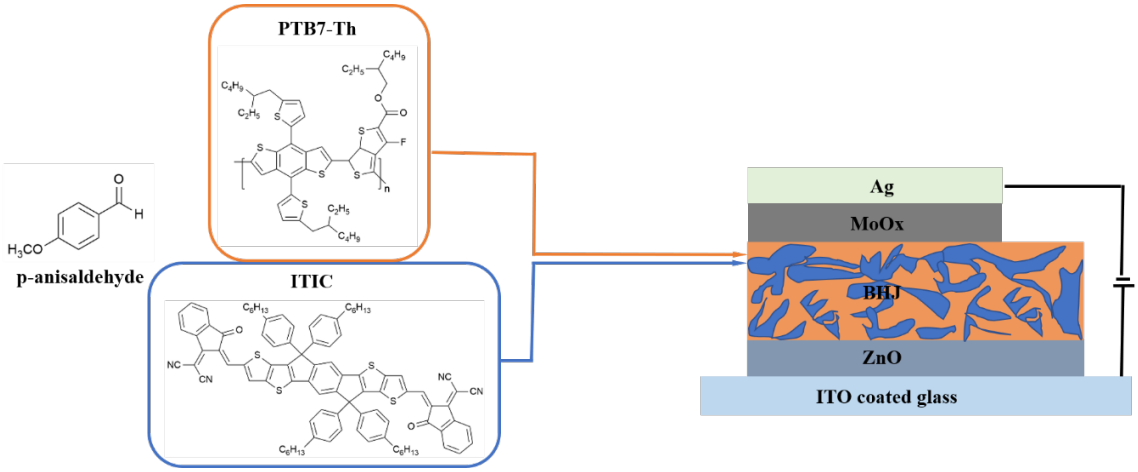

Figure 7-1. (Left) The chemical structures of PTB7-Th, ITIC and AA, and (Right) the device structure.

After the spin coating of the active layer, the devices were vacuum dried in an evaporation chamber at 10^{-6} mbar for a further hour after the chamber pressure had reached 10^{-6} mbar. After vacuum drying, MoO_x and Ag were deposited via the following method. The MoO_x (12 nm) was thermally deposited on the BHJ layer under high vacuum using a Covap thermal evaporation system (Angstrom Engineering). This was followed by the evaporation of the Ag electrode (80 nm) using a shadow mask to define the active area to 0.1 cm^2.

7.3.2 Device performance

The SC devices were measured using an Oriel Solar simulator fitted with a 150 W Xeon lamp (Newport), filtered to give an output of 100 mW cm^{-2} at 1.5 AM standard and calibrated using a silicon reference cell with NIST traceable certification. Device testing

was conducted under ambient conditions. The averages were based on six inverted devices with a defined device area of 0.1 cm^2.

7.3.3 Neutral impact collision ion spectroscopy

The NICISS results are presented as a spectrum consisting of individual peaks and steps representative of the different elements in the sample. The first peak in the NICISS spectra is the photon peak, which corresponds to the first He^+ interactions with the sample surface.

In non-deconvoluted NICISS, concentration depth profile count rate can be found at negative depth. This count rate at negative depth does not have any physical meaning in the sense of concentration at negative depth. The effect is related to the finite energy resolution of the method and explained in detail elsewhere.[43,44] The elements investigated in this work are sulphur, fluorine, oxygen, nitrogen and carbon. A previous investigation by our lab using NICISS determined the composition of the surface and near-surface area of a blend of P3HT: PCBM, identifying a layered structure at the surface.[45] The known bulk concentration of a sample is used to convert the measured count rate into concentration.[46] The description of NICISS can be found in Chapter 3.

7.3.4 Atomic force microscope

The BHJ layer topography is crucial for achieving high PCE SCs. AFM was run in tapping mode to study the topography. In AFM tapping mode, a tip is attached to an oscillating cantilever that scans the surface of a sample. Interactions between the tip and the surface are registered as deviations of the oscillating pattern of the cantilever. These deviations are monitored with a laser as the surface is scanned and then transferred into a three-dimensional topography map. More details about AFM can be found in Chapter 3.

7.4 Results and Discussion

7.4.1 Device performance

Prior to the BHJ investigation, and prior to deposition on the performance of the OPV devices, it was important to determine the influence of the AA addition to the active layer ink prior to deposition on the device performance of the OPVs. Comparing the performance of devices with and without AA additive can be found in Table 7-1. To reduce the potential traces of AA that could still be present in the active layer, we used high vacuum drying (10^{-6} mbar) as a surface/morphology treatment during fabrication. This is an outcome of the work with the PTB7-Th: ITIC system, reaching a higher efficiency using a more environmentally friendly solvent system and a novel drying technique of the thin film. The common procedures for drying the BHJ layer and removing any residual of the additive is by annealing the film at a specific temperature.[40,42]

Table 7-1
Device Characteristics of PTB7-Th: ITIC With and Without AA Additive

Device	J_{sc} (mA cm^{-2})	V_{oc} (V)	FF	PCE (%)
PTB7-Th: ITIC + 0% AA	15.55 ± *0.16*	0.81 ± *0.01*	0.56 ± *0.01*	7.03 ± *0.13*
PTB7-Th: ITIC + 2% AA	16.47 ± *0.18*	0.80 ± *0.01*	0.62 ± *0.01*	8.20 ± *0.21*

Note. The averages were based on six inverted devices with a defined device area of 0.1 cm^2.

The addition of AA to the active layer prior to the deposition of the active layer resulted in an improvement of PCE from 7.03% to 8.20%, without and with AA, respectively. This increase predominately resulted from the increase in J_{sc} and FF, whereas a minimal change was observed for the V_{oc}.

In the literature, adding solvent additives to active layer inks improved morphology and resulted in an improvement in the J_{sc} and FF.[47–49] By achieving a more performance, there is a reduction in the probability of an electron-hole recombination, leading to an increase in J_{sc} and FF.[48] Concerning our results shown in Table 7-1, these findings demonstrate that the use of AA, which has an oleophilic methoxy group and a hydrophilic aldehyde group, is a very effective additive to the chosen BHJ to achieve excellent performance in an OPV. A comparison table of the surface roughness and concentration of BHJ with/without AA will be discussed below.

7.4.2 AFM results

To have a general understanding of the influence of the AA additive on the PTB7-Th: ITIC morphology, AFM was used to investigate the surface morphology of the active layer. It has been speculated that changes observed on the surface of the BHJ can be related to changes to the morphology.[50] AFM images of the surface of spin-coated PTB7-Th: ITIC with and without AA additive are shown in Figure 7-2.

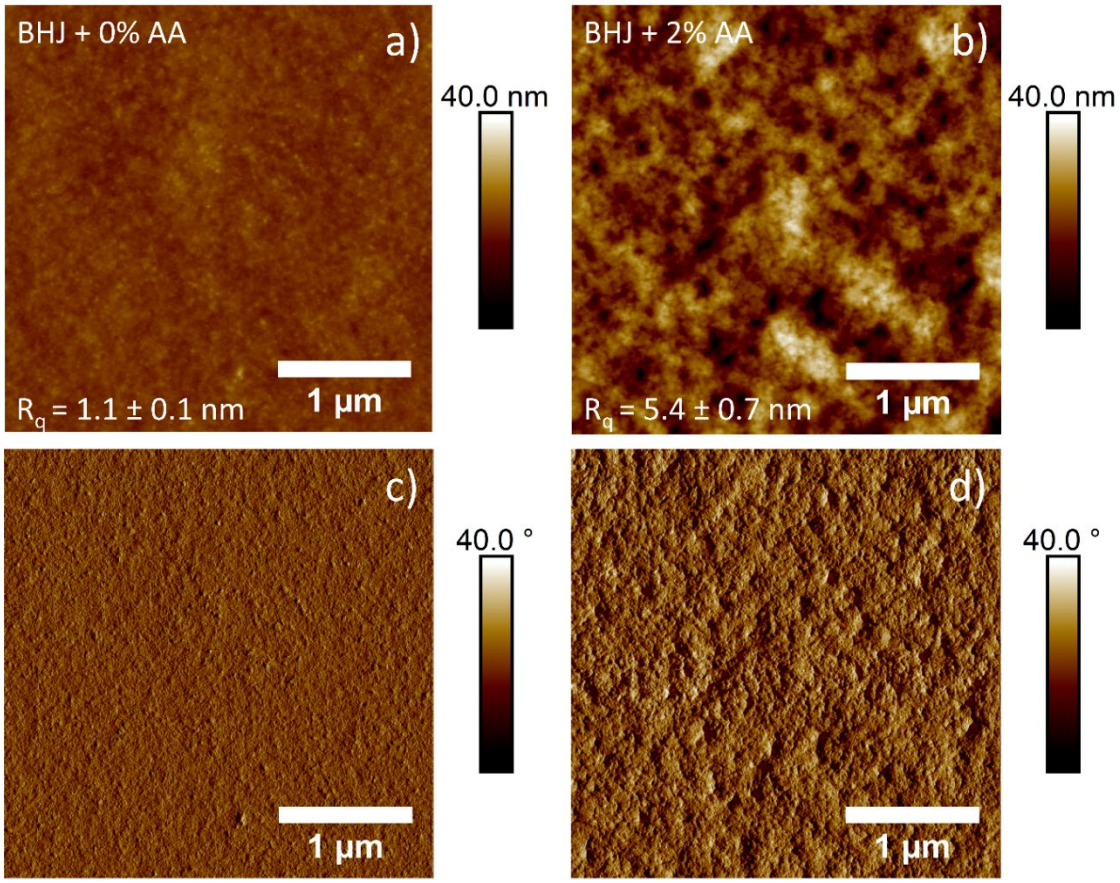

Figure 7-2. AFM topography height (a and b) and phase (c and d) images (5 µm x 5 µm) of the surface morphology of BHJ with 0% AA (a and c) and 2% AA (b and d). Average R_q roughness was calculated from five scan locations per sample.

Based on the AFM images and calculated roughness values, significant changes to the surface of the BHJ were observed when comparing active layers with and without AA prior to deposition. First, the addition of AA resulted in an increase in feature size and in surface roughness, indicating a likely increase in domain size. This increase in roughness would usually result in an increased probability in charge recombination, as seen in previous literature that prepared PTB7-Th: ITIC devices with the addition of DIO.[24] It is possible that the increase in roughness is related to the enhancement of polymer order and crystallinity direction of the PTB7-Th.[51,52] This could lead to improved exciton dissociation and CT in the photoactive film.

7.4.3 NICISS results

Figure 7-3 shows the NICIS TOF spectra of layers of pristine PTB7-Th, pristine ITIC, a blend (PTB7-Th: ITIC) with 2% AA and a blend (PTB7-Th: ITIC) without additive. Vertical lines are an indication of the signal onset of the He projectiles backscattered from the elements, constituting the sample. The heavier elements have higher kinetic energy, thus backscattering

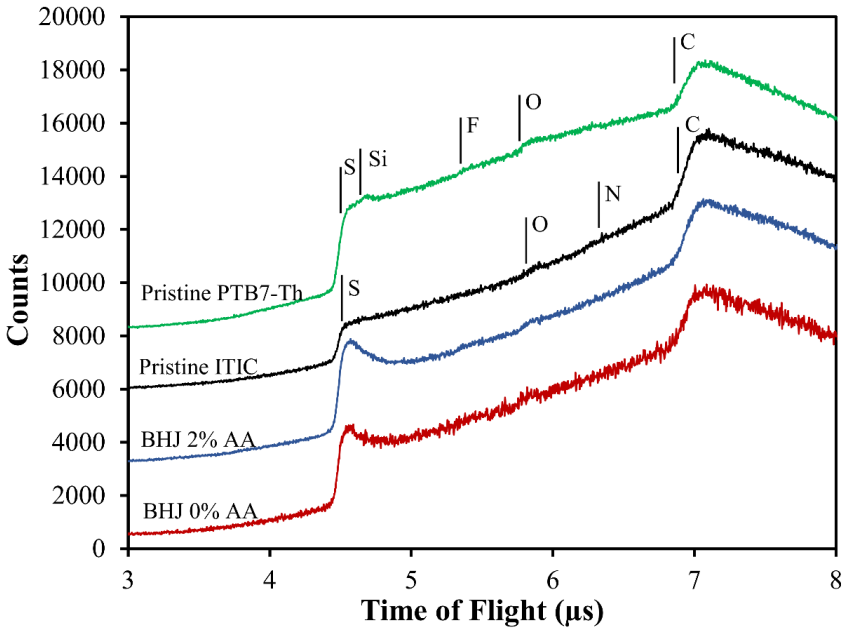

Figure 7-3. NICIS TOF spectra of PTB7-Th, ITIC and a 1:1.3 blend of PTB7-Th and ITIC. Signal onset of helium backscattered from sulphur, silicon, oxygen, nitrogen and carbon is marked by vertical bars. The spectra are offset vertically for clarity.

Projectiles were detected at a lower TOF. The spectrum of PTB7-Th contains contributions from sulphur (S), fluorine (F), oxygen (O) and carbon (C). A small signal of silicon was obtained in PTB7-Th spectra, implying the presence of an impurity, most likely siloxane.[45,53] The spectrum of ITIC contains S, O, N and C. These elements are the main components of ITIC. S, O and C can be identified in the blend spectra with and without an additive. Mainly, the S at the BHJ showed enrichment at the surface, which can be identified through the enhanced count rate at the onset of the step related to S.

However, F and N could not be identified in the NICIS spectra, as their count rates are too low to allow a proper evaluation.

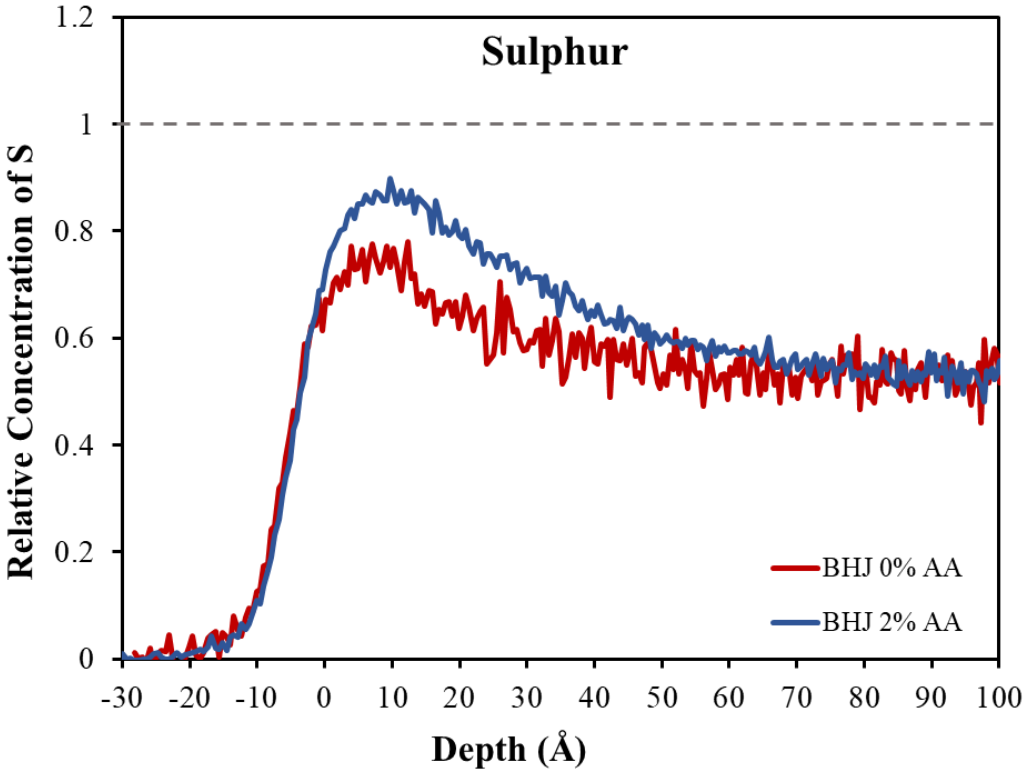

Figure 7-4. Comparison of the concentration profiles of BHJ with 2% AA and without an additive. The dashed line indicates the bulk concentration of S for the ratio of 1:1.3 (the ratio of PTB7-Th: ITIC). The S to C ratio for the bulk in the spectrum of the BHJ can be determined from the elemental composition of the individual components.

For determining the composition of the BHJ at its surface, we evaluated the S concentration depth profiles quantitatively for the BHJ samples with and without the AA additive. As the first step, the TOF spectra for the BHJ were converted into a concentration depth profile as described in reference.[46] Converting count rate into concentration requires to know the bulk concentration of one of the elements. In the present case, the concentration of carbon has been used in combination with the C:S intensity ratio as measured of the pristine PTB7-Th and ITIC. This allows us to determine whether the S count rate in the spectra of the BHJ should be based on the known bulk composition of the BHJ (1:1.3 ratio of PTB7-Th to ITIC). The count rate for the known

bulk concentration was used as reference and set to unity. This relative measure for the concentration is used for the y-axis in Figure 7-4.

To understand the distribution of the species forming the layers at the near-surface region, we determined the concentration depth profile of S in the BHJ with and without additive, as shown in Figure 7-4. In the measured profile, the zero-depth refers to the outermost layer where the increase in the depth indicates the direction towards the bulk. Both depth profiles of the S have the same onset close to 0 Å, and the ratio of the profiles in the subsurface is the same.

Figure 7-4 indicates a higher concentration of the S at the surface compared to the region below the surface (i.e., at depth > 40 Å). This can be noted by an increase of the concentration up to 40 Å. The enhancement of the S is attributed to a greater presence of the PTB7-Th at the surface of the BHJ than in the subsurface region (depth > 40 Å). This analysis of the concentrations is based on the chemical structure of PTB7-Th and ITIC with the S concentration being higher in the PTB7-Th component than in the ITIC. However, the distribution of the compositions throughout the BHJ is more complicated. The concentration of PTB7-Th in the subsurface is depleted compared to the surface (see Table 7-2).

Table 7-2

Surface Roughness and S Relative Concentration of the PTB7-Th: ITIC Device With and Without AA

Device	Surface roughness (nm) (AFM)	Relative concentration (NICISS)
PTB7-Th: ITIC + 0% AA	1.1 ± 0.1	0.78 ± 0.1
PTB7-Th: ITIC + 2% AA	5.4 ± 0.1	0.90 ± 0.1

Note. A relative concentration of 1 would mean that the surface concentration is the same as the bulk concentration.

The presence of the PTB7-Th neither with additive nor without additive reached unity, that is, the related bulk concentration (1:1.3) as shown through the dashed line in Figure

7-4. The values of the surface concentration can be seen in Table 7-2. Hence, PTB7-Th is depleted at the surface of the BHJ in both systems and thus must have segregated more to the substrate/BHJ interface. Therefore, ITIC shows an overall enrichment in the surface region compared with the PTB7-Th. This means that PTB7-Th does not occupy the whole outermost layer. The possible reason for the depletion of PTB7-Th at the surface is attributed to the drying behaviours for the two components. The drying process during the spin-coated films could affect the distribution and lead to poor miscibility or incompatible crystalline structure of PTB7-Th and ITIC and thus also influences the formation of the crystalline structure. The solubility of materials within the active layer ink plays an important role in the control of morphology; thus, it is a key factor when selecting appropriate base solvents and additives.[54,55] In our studies, it is suspected the PTB7-Th would remain in the solution longer than ITIC, giving the appearance of ITIC drying faster than PTB7-Th. This is based on the solubility of ITIC, which is lesser than PTB7-Th. As a result, ITIC will move into the solid phase sooner and precipitate first on the surface. PTB7-Th remains quenched if no additive is used to transform the blend into the equilibrium crystalline phase.

The second phenomenon is related to the difference of the ratio between the surface and the subsurface, which is based on the surface energy of the two components. The depth profile in Figure 7-4 shows a notable difference in the concentration of PTB7-Th at the surface in the first few Å (~0 to 40 Å) and at subsurface (~50 to 100 Å). That indicates more concentration of PTB7-Th at the surface than the subsurface. As reported by Lin et al., ITIC has a higher surface energy than PTB7-Th, which allows moving PTB7-Th towards the surface.[56] A similar result was reported by Wang et al., who found strong segregation of different components of PTB7-Th, $PC_{71}BM$ and m-ITIC in the ternary system. The authors determined the surface energy and the wetting coefficient for the components. PTB7-Th, with the component with lowest surface energy, being located at the surface, and ITIC tended to be segregated between PTB7-Th and $PC_{71}BM$.[57] However,

their finding shows an estimation of the surface enrichment. The authors also did not show a detailed profile distinguishing between the surface and subsurface.

After adding 2% of AA into the BHJ, the surface shows an increase in PTB7-Th concentration. For a schematic showing of this enrichment, see Figure 7-5. The possible reason for this phenomenon can be related to the change in the bulk properties of the BHJ upon adding AA. The AA has an oleophilic methoxy and a hydrophilic aldehyde group and it is a polar molecule with higher surface energy, which could drive the electron donor to the surface.

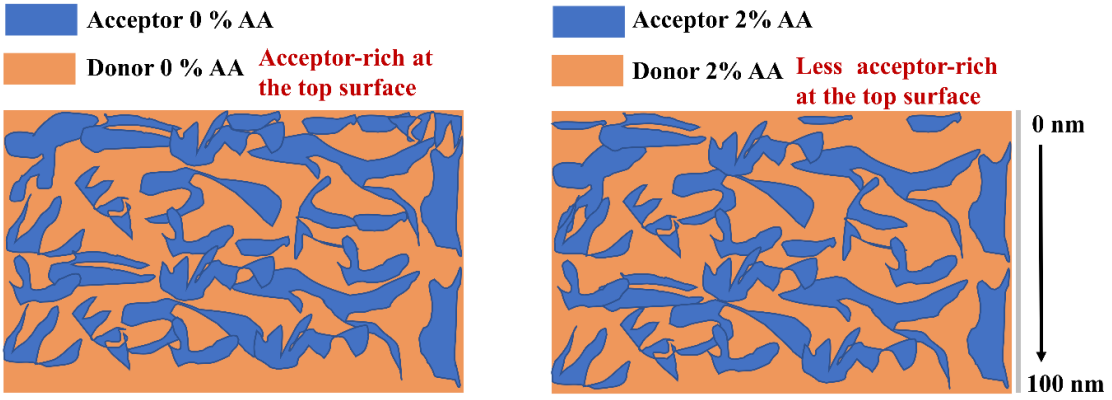

Figure 7-5. Schematic showing the effect of the AA additive on the donor enrichment at the surface.

In the inverted devices, the energy levels between the donor (PTB7-Th) and MoO_x are closer, thus donor enrichment at the surface is beneficial for the CT and collection for an inverted OPV. However, an enrichment of accepter in the surface region would result in lesser intermixing of donors and acceptors and decrease the interfacial area for exciton dissociation, which would result in reduced device performance.

7.5 Conclusion

The influence of AA as an additive on the PTB7-Th: ITIC ratio as the function of the depth was investigated by measuring the concentration depth profile of S. The depth

profiles of S were measured directly to determine the concentration of the compositions at the surface and in the subsurface region. The results showed an overall enrichment of ITIC at the top layer of the BHJ, followed by the PTB7-Th layer, revealing an enriched layer of PTB7-Th at the substrate/BHJ interface. The difference in the PTB7-Th ratio at the surface and subsurface regions is related to the difference of the surface energy of PTB7-Th and ITIC. PTB7-Th has comparatively lower surface energy materials, thus driving PTB7-Th towards the surface. The AA additive increased the concentration of PTB7-Th at the surface and decreased that of ITIC. The enhancement of PTB7-Th at the surface is beneficial for the CT to the MoO_x electrode in the inverted OPV. AFM results also showed that the addition of AA increased the feature size and roughness of the BHJ, which improved exciton dissociation and CT in the photoactive film. Consequently, the enhancement of the donor at the surface (after adding AA) results in improved PCE, from 7.03% to 8.20%.

7.6 Acknowledgement

This work is supported by the Australian Research Council project DP220102900. The authors would like to acknowledge the support of the Australian National Fabrication Facility (ANFF) and Australian Microscopy & Microanalysis Research Facility (AMMRF) regarding using experimental equipment. The authors acknowledge Flinders Microscopy and Microanalysis and their expertise.

7.7 References

(1) Cui, Y.; Xu, Y.; Yao, H.; Bi, P.; Hong, L.; Zhang, J.; Zu, Y.; Zhang, T.; Qin, J.; Ren, J. Single-Junction Organic Photovoltaic Cell with 19% Efficiency. *Advanced Materials* **2021**, *33* (41), 2102420.

(2) Gao, W.; Qi, F.; Peng, Z.; Lin, F. R.; Jiang, K.; Zhong, C.; Kaminsky, W.; Guan, Z.; Lee, C. S.; Marks, T. J. Achieving 19% Power Conversion Efficiency in Planar-Mixed Heterojunction Organic Solar Cells Using a Pseudo-Symmetric Electron Acceptor. *Advanced Materials* **2022**, 2202089.

(3) Nakano, K.; Tajima, K. Organic Planar Heterojunctions: From Models for Interfaces in Bulk Heterojunctions to High-Performance Solar Cells. *Advanced Materials* **2017**, *29* (25), 1603269.

(4) Richter, L. J.; DeLongchamp, D. M.; Amassian, A. Morphology Development in Solution-Processed Functional Organic Blend Films: An In Situ Viewpoint. *Chemical Reviews* **2017**, *117* (9), 6332–6366.

(5) Chen, L. M.; Hong, Z.; Li, G.; Yang, Y. Recent Progress in Polymer Solar Cells: Manipulation of Polymer: Fullerene Morphology and the Formation of Efficient Inverted Polymer Solar Cells. *Advanced Materials* **2009**, *21* (14–15), 1434–1449.

(6) Zhao, J.; Li, Y.; Yang, G.; Jiang, K.; Lin, H.; Ade, H.; Ma, W.; Yan, H. Efficient Organic Solar Cells Processed from Hydrocarbon Solvents. *Nature Energy* **2016**, *1* (2), 1–7.

(7) Ye, L.; Collins, B. A.; Jiao, X.; Zhao, J.; Yan, H.; Ade, H. Miscibility–Function Relations in Organic Solar Cells: Significance of Optimal Miscibility in Relation to Percolation. *Advanced Energy Materials* **2018**, *8* (28), 1703058.

(8) Han, X.; Zhou, S. J.; Tan, Y. Z.; Wu, X.; Gao, F.; Liao, Z. J.; Huang, R. B.; Feng, Y. Q.; Lu, X.; Xie, S. Y. Crystal Structures of Saturn-Like C50Cl10 and Pineapple-Shaped C64Cl4: Geometric Implications of Double-and Triple-Pentagon-Fused Chlorofullerenes. *Angewandte Chemie International Edition* **2008**, *47* (29), 5340–5343.

(9) Li, Z.; Xu, X.; Zhang, W.; Meng, X.; Ma, W.; Yartsev, A.; Inganas, O.; Andersson, M. R.; Janssen, R. A.; Wang, E. High Performance All-Polymer Solar Cells by Synergistic Effects of Fine-Tuned Crystallinity and Solvent Annealing. *Journal of the American Chemical Society* **2016**, *138* (34), 10935–10944.

(10) Peet, J.; Kim, J. Y.; Coates, N. E.; Ma, W. L.; Moses, D.; Heeger, A. J.; Bazan, G. C. Efficiency Enhancement in Low-Bandgap Polymer Solar Cells by Processing with Alkane Dithiols. *Nature Materials* **2007**, *6* (7), 497–500.

(11) Chen, H.-Y.; Hou, J.; Zhang, S.; Liang, Y.; Yang, G.; Yang, Y.; Yu, L.; Wu, Y.; Li, G. Polymer Solar Cells with Enhanced Open-Circuit Voltage and Efficiency. *Nature Photonics* **2009**, *3* (11), 649–653.

(12) Moulé, A. J.; Meerholz, K. Controlling Morphology in Polymer–Fullerene Mixtures. *Advanced Materials* **2008**, *20* (2), 240–245.

(13) Xu, W.; Zhu, X.; Ma, X.; Zhou, H.; Li, X.; Jeong, S. Y.; Woo, H. Y.; Zhou, Z.; Sun, Q.; Zhang, F. Achieving 15.81% and 15.29% Efficiency of all-Polymer Solar Cells Based on Layer-by-Layer and Bulk Heterojunction Structures. *Journal of Materials Chemistry A* **2022**, *10* (25), 13492–13499.

(14) Shi, G.; Yuan, J.; Huang, X.; Lu, Y.; Liu, Z.; Peng, J.; Ding, G.; Shi, S.; Sun, J.; Lu, K. Combinative Effect of Additive and Thermal Annealing Processes Delivers High Efficiency All-Polymer Solar Cells. *The Journal of Physical Chemistry C* **2015**, *119* (45), 25298–25306.

(15) Gurney, R. S.; Li, W.; Yan, Y.; Liu, D.; Pearson, A. J.; Wang, T. Morphology and Efficiency Enhancements of PTB7-Th: ITIC Nonfullerene Organic Solar Cells Processed via Solvent Vapor Annealing. *Journal of Energy Chemistry* **2019**, *37*, 148–156.

(16) Wang, X.; Yang, Y.; He, Z.; Wu, H.; Cao, Y. Influence of the Acceptor Crystallinity on the Open-Circuit Voltage in PTB7-Th: ITIC Organic Solar Cells. *Journal of Materials Chemistry C* **2019**, *7* (47), 14861–14866.

(17) Lee, J. K.; Ma, W. L.; Brabec, C. J.; Yuen, J.; Moon, J. S.; Kim, J. Y.; Lee, K.; Bazan, G. C.; Heeger, A. J. Processing Additives for Improved Efficiency from Bulk Heterojunction Solar Cells. *Journal of the American Chemical Society* **2008**, *130* (11), 3619–3623.

(18) Love, J. A.; Chou, S.-H.; Huang, Y.; Bazan, G. C.; Nguyen, T.-Q. Effects of Solvent Additive on "S-Shaped" Curves in Solution-Processed Small Molecule Solar Cells. *Beilstein Journal of Organic Chemistry* **2016**, *12* (1), 2543–2555.

(19) Collins, B. A.; Li, Z.; Tumbleston, J. R.; Gann, E.; McNeill, C. R.; Ade, H. Absolute Measurement of Domain Composition and Nanoscale Size Distribution Explains Performance in PTB7: $PC_{71}BM$ Solar Cells. *Advanced Energy Materials* **2013**, *3* (1), 65–74.

(20) Van Franeker, J. J.; Turbiez, M.; Li, W.; Wienk, M. M.; Janssen, R. A. A Real-Time Study of the Benefits of Co-Solvents in Polymer Solar Cell Processing. *Nature Communications* **2015**, *6* (1), 1–8.

(21) Mukherjee, S.; Proctor, C. M.; Tumbleston, J. R.; Bazan, G. C.; Nguyen, T. Q.; Ade, H. Importance of Domain Purity and Molecular Packing in Efficient Solution-Processed Small-Molecule Solar Cells. *Advanced Materials* **2015**, *27* (6), 1105–1111.

(22) Song, X.; Gasparini, N.; Ye, L.; Yao, H.; Hou, J.; Ade, H.; Baran, D. Controlling Blend Morphology for Ultrahigh Current Density in Nonfullerene Acceptor-Based Organic Solar Cells. *ACS Energy Letters* **2018**, *3* (3), 669–676.

(23) Jiang, X.; Xu, Y.; Wang, X.; Wu, Y.; Feng, G.; Li, C.; Ma, W.; Li, W. Non-Fullerene Organic Solar Cells Based on Diketopyrrolopyrrole Polymers as Electron Donors and ITIC as an Electron Acceptor. *Physical Chemistry Chemical Physics* **2017**, *19* (11), 8069–8075.

(24) Song, X.; Gasparini, N.; Baran, D. The Influence of Solvent Additive on Polymer Solar Cells Employing Fullerene and Non-Fullerene Acceptors. *Advanced Electronic Materials* **2018**, *4* (10), 1700358.

(25) Zhao, W.; Qian, D.; Zhang, S.; Li, S.; Inganäs, O.; Gao, F.; Hou, J. Fullerene-Free Polymer Solar Cells with Over 11% Efficiency and Excellent Thermal Stability. *Advanced Materials* **2016**, *28* (23), 4734–4739.

(26) Ye, L.; Jiao, X.; Zhao, W.; Zhang, S.; Yao, H.; Li, S.; Ade, H.; Hou, J. Manipulation of Domain Purity and Orientational Ordering in High Performance All-Polymer Solar Cells. *Chemistry of Materials* **2016**, *28* (17), 6178–6185.

(27) Cheng, P.; Lin, Y.; Zawacka, N. K.; Andersen, T. R.; Liu, W.; Bundgaard, E.; Jørgensen, M.; Chen, H.; Krebs, F. C.; Zhan, X. Comparison of Additive Amount Used in Spin-Coated and Roll-Coated Organic Solar Cells. *Journal of Materials Chemistry A* **2014**, *2* (45), 19542–19549.

(28) Zhao, F.; Dai, S.; Wu, Y.; Zhang, Q.; Wang, J.; Jiang, L.; Ling, Q.; Wei, Z.; Ma, W.; You, W. Single-Junction Binary-Blend Nonfullerene Polymer Solar Cells with 12.1% Efficiency. *Advanced Materials* **2017**, *29* (18), 1700144.

(29) Li, Z.; Dai, S.; Xin, J.; Zhang, L.; Wu, Y.; Rech, J.; Zhao, F.; Li, T.; Liu, K.; Liu, Q. Enhancing the Performance of the Electron Acceptor ITIC-Th via Tailoring its End Groups. *Materials Chemistry Frontiers* **2018**, *2* (3), 537–543.

(30) Lin, Y.; Zhao, F.; He, Q.; Huo, L.; Wu, Y.; Parker, T. C.; Ma, W.; Sun, Y.; Wang, C.; Zhu, D. High-Performance Electron Acceptor with Thienyl Side Chains for Organic Photovoltaics. *Journal of the American Chemical Society* **2016**, *138* (14), 4955–4961.

(31) Tremolet de Villers, B. J.; O'Hara, K. A.; Ostrowski, D. P.; Biddle, P. H.; Shaheen, S. E.; Chabinyc, M. L.; Olson, D. C.; Kopidakis, N. Removal of Residual Diiodooctane Improves Photostability of High-Performance Organic Solar Cell Polymers. *Chemistry of Materials* **2016**, *28* (3), 876–884.

(32) Weu, A.; Kress, J. A.; Paulus, F.; Becker-Koch, D.; Lami, V.; Bakulin, A. A.; Vaynzof, Y. Oxygen-Induced Doping as a Degradation Mechanism in Highly Efficient Organic Solar Cells. *ACS Applied Energy Materials* **2019**, *2* (3), 1943–1950.

(33) Holliday, S.; Luscombe, C. K. Low Boiling Point Solvent Additives for Improved Photooxidative Stability in Organic Photovoltaics. *Advanced Electronic Materials* **2018**, *4* (10), 1700416.

(34) Jin, Y.; Chen, Z.; Dong, S.; Zheng, N.; Ying, L.; Jiang, X. F.; Liu, F.; Huang, F.; Cao, Y. A Novel Naphtho [1, 2-c: 5, 6-c′] Bis ([1, 2, 5] Thiadiazole)-Based Narrow-Bandgap π-Conjugated Polymer with Power Conversion Efficiency Over 10%. *Advanced Materials* **2016**, *28* (44), 9811–9818.

(35) Chou, K. W.; Yan, B.; Li, R.; Li, E. Q.; Zhao, K.; Anjum, D. H.; Alvarez, S.; Gassaway, R.; Biocca, A.; Thoroddsen, S. T. Spin-Cast Bulk Heterojunction Solar Cells: A Dynamical Investigation. *Advanced Materials* **2013**, *25* (13), 1923–1929.

(36) Xiao, Z.; Yuan, Y.; Yang, B.; VanDerslice, J.; Chen, J.; Dyck, O.; Duscher, G.; Huang, J. Universal Formation of Compositionally Graded Bulk Heterojunction for Efficiency Enhancement in Organic Photovoltaics. *Advanced Materials* **2014**, *26* (19), 3068–3075.

(37) Yamamoto, S.; Kitazawa, D.; Tsukamoto, J.; Shibamori, T.; Seki, H.; Nakagawa, Y. Composition Depth Profile Analysis of Bulk Heterojunction Layer by Time-of-Flight Secondary Ion Mass Spectrometry with Gradient Shaving Preparation. *Thin Solid Films* **2010**, *518* (8), 2115–2118.

(38) Germack, D. S.; Chan, C. K.; Kline, R. J.; Fischer, D. A.; Gundlach, D. J.; Toney, M. F.; Richter, L. J.; DeLongchamp, D. M. Interfacial Segregation in Polymer/Fullerene Blend Films for Photovoltaic Devices. *Macromolecules* **2010**, *43* (8), 3828–3836.

(39) Jasieniak, J. J.; Treat, N. D.; McNeill, C. R.; de Villers, B. J. T.; Della Gaspera, E.; Chabinyc, M. L. Interfacial Characteristics of Efficient Bulk Heterojunction Solar Cells Fabricated on MoO_x Anode Interlayers. *Advanced Materials* **2016**, *28* (20), 3944–3951.

(40) Chen, M.; Liu, D.; Li, W.; Gurney, R. S.; Li, D.; Cai, J.; Spooner, E. L.; Kilbride, R. C.; McGettrick, J. D.; Watson, T. M. Influences of Non-Fullerene Acceptor Fluorination on Three-Dimensional Morphology and Photovoltaic Properties of Organic Solar Cells. *ACS Applied Materials & Interfaces* **2019**, *11* (29), 26194–26203.

(41) Huang, S.; Huai, Z.; Ren, J.; Sun, Y.; Zhao, X.; Wang, L.; Kong, W.; Fu, G.; Yang, S. Improved Morphology and Interfacial Contact of PBDB-T: N2200-Based All-Polymer Solar Cells by Using the Solvent Additive p-Anisaldehyde. *ACS Applied Energy Materials* **2019**, *3* (1), 358–365.

(42) Sprau, C.; Buss, F.; Wagner, M.; Landerer, D.; Koppitz, M.; Schulz, A.; Bahro, D.; Schabel, W.; Scharfer, P.; Colsmann, A. Highly Efficient Polymer Solar Cells Cast from non-Halogenated Xylene/Anisaldehyde Solution. *Energy & Environmental Science* **2015**, *8* (9), 2744–2752.

(43) Andersson, G.; Morgner, H. Determining the Stopping Power of Low Energy Helium in Alkanethiolates with Neutral Impact Collision Ion Scattering Spectroscopy (NICISS). *Nuclear Instruments and Methods in Physics Research Section B: Beam Interactions with Materials and Atoms* **1999**, *155* (4), 357–368.

(44) Zhao, X.; Nathanson, G. M.; Andersson, G. G. Experimental Depth Profiles of Surfactants, Ions, and Solvent at the Angstrom Scale: Studies of Cationic and Anionic Surfactants and Their Salting Out. *J. Phys. Chem. B* **2020**, *124* (11), 2218–2229.

(45) Schmerl, N.; Andersson, G. A Layered Structure at the Surface of P3HT/PCBM Blends. *Physical Chemistry Chemical Physics* **2011**, *13* (33), 14993–15002.

(46) Andersson, G.; Morgner, H. Investigations on Solutions of Tetrabutylonium Salts in Formamide with NICISS and ICISS: Concentration Depth Profiles and Composition of the Outermost Layer. *Surface Science* **2000**, *445* (1), 89–99.

(47) Ho, C. H. Y.; Dong, Q.; Yin, H.; Leung, W. W. K.; Yang, Q.; Lee, H. K. H.; Tsang, S. W.; So, S. K. Impact of Solvent Additive on Carrier Transport in Polymer: Fullerene Bulk Heterojunction Photovoltaic Cells. *Advanced Materials Interfaces* **2015**, *2* (12), 1500166.

(48) Sharenko, A.; Gehrig, D.; Laquai, F.; Nguyen, T.-Q. The Effect of Solvent Additive on the Charge Generation and Photovoltaic Performance of a Solution-Processed Small Molecule: Perylene Diimide Bulk Heterojunction Solar Cell. *Chemistry of Materials* **2014**, *26* (14), 4109–4118.

(49) Perez, L. A.; Rogers, J. T.; Brady, M. A.; Sun, Y.; Welch, G. C.; Schmidt, K.; Toney, M. F.; Jinnai, H.; Heeger, A. J.; Chabinyc, M. L.; Bazan, G. C.; Kramer, E. J. The Role of Solvent Additive Processing in High Performance Small Molecule Solar Cells. *Chemistry of Materials* **2014**, *26* (22), 6531–6541.

(50) Jang, Y.; Ju Cho, Y.; Kim, M.; Seok, J.; Ahn, H.; Kim, K. Formation of Thermally Stable Bulk Heterojunction by Reducing the Polymer and Fullerene Intermixing. *Scientific Reports* **2017**, *7* (1), 1–9.

(51) Li, P.; Zhang, Y.; Yu, T.; Zhang, Q.; Masse, J.-P.; Yang, Y.; Izquierdo, R.; Sun, B.; Ma, D. Unveiling Photovoltaic Performance Enhancement Mechanism of Polymer Solar Cells via Synergistic Effect of Binary Solvent Additives. *Solar RRL* **2020**, *4* (10), 2000239.

(52) Dehoff, R.; Duty, C.; Peter, W.; Yamamoto, Y.; Chen, W.; Blue, C.; Tallman, C. Case Study: Additive Manufacturing of Aerospace Brackets. *Advanced Materials & Processes* **2013**, *171* (3), 19–23.

(53) Tan, H. L.; Krebs, T.; Andersson, G.; Neff, D.; Norton, M.; Morgner, H.; Van Patten, P. G. Internal Structure of Polyelectrolyte Multilayers Probed via Neutral Impact Collision Ion Scattering Spectroscopy. *Langmuir* **2005**, *21* (6), 2598–2604.

(54) Chen, H.; Hsiao, Y. C.; Hu, B.; Dadmun, M. Tuning the Morphology and Performance of low Bandgap Polymer: Fullerene Heterojunctions via Solvent Annealing in Selective Solvents. *Advanced Functional Materials* **2014**, *24* (32), 5129–5136.

(55) van Franeker, J. J.; Heintges, G. H.; Schaefer, C.; Portale, G.; Li, W.; Wienk, M. M.; van der Schoot, P.; Janssen, R. A. Polymer Solar Cells: Solubility Controls Fiber Network Formation. *Journal of the American Chemical Society* **2015**, *137* (36), 11783–11794.

(56) Lin, Y.; Jin, Y.; Dong, S.; Zheng, W.; Yang, J.; Liu, A.; Liu, F.; Jiang, Y.; Russell, T. P.; Zhang, F. Printed Nonfullerene Organic Solar Cells with the Highest Efficiency of 9.5%. *Advanced Energy Materials* **2018**, *8* (13), 1701942.

(57) Wang, C.; Xu, X.; Zhang, W.; Dkhil, S. B.; Meng, X.; Liu, X.; Margeat, O.; Yartsev, A.; Ma, W.; Ackermann, J. Ternary Organic Solar Cells with Enhanced Open Circuit Voltage. *Nano Energy* **2017**, *37*, 24–31.

Chapter 8: Surface Passivation of Sputtered NiO_x Using a SAM Interface Layer to Enhance the Performance of PSCs

Amira R. M. Alghamdi,[1,2] Masatoshi Yanagida,*[,1] Yasuhiro Shirai,*[,1] Gunther G. Andersson,[2] Kenjiro Miyano[1]

[1] Photovoltaic Materials Group, Center for Green Research on Energy and Environmental Materials (GREEN), National Institute for Materials Science (NIMS), 1-1 Namiki, Tsukuba, Ibaraki 305-0044, Japan.

[2] Flinders Centre for Nanoscale Science and Technology, Flinders University, PO Box 2100, Adelaide SA 5001, Australia.

This work has been published in *ACS omega*, 2022. The only alterations are that any experimental methods and analysis procedures previously described in Chapter 3 have been removed from this chapter, and supplementary information from the publication has been shown in the supplementary section (Appendix D).

Author contributions:

Amira Alghamdi: Designed and performed experiments, data analysis and interpretation of the data and prepared the manuscript for publication. **Masatoshi Yanagida:** Intellectual contribution in conceptualising experiments, data interpretation and revision of manuscript. **Yasuhiro Shirai:** Intellectual contribution in conceptualising experiments, data interpretation and revision of manuscript. **Gunther Andersson:** Intellectual contribution and revision of manuscript. **Kenjiro Miyano:** Intellectual contribution and revision of manuscript.

8.1 Abstract

Sputtered NiO_x (sp-NiO_x) is a preferred hole-transporting material for PSCs because of its hole mobility, ease of manufacturability, good stability and suitable E_F for hole extraction. However, uncontrolled defects in sp-NiO_x can limit the efficiency of SCs fabricated with this hole-transporting layer. An interfacial layer has been proposed to modify the sp-NiO_x/perovskite interface, which can contribute to improving the crystallinity of the perovskite film. A self-assembled monolayer of [2-(3,6-dimethoxy-9H-carbazol-9-yl)ethyl]phosphonic acid (MeO-2PACz) was used to modify a sp-NiO_x surface. We found that the MeO-2PACz interlayer improves the quality of the perovskite film due to an enlarged domain size, reduced charge recombination at the sp-NiO_x/perovskite interface and passivation of the defects in sp-NiO_x surfaces. Additionally, the band tail states are also reduced, as indicated by PDS, which thus indicates a reduction in defect levels. The overall outcome is an improvement in the device efficiency from 11.9% to 17.2% due to the modified sp-NiO_x/perovskite interface, with an active area of 1 cm^2 (certified efficiency of 16.25%). Based on these results, the interfacial engineering of the electronic properties of sp-NiO_x/MeO-2PACz/perovskite is discussed in relation to the improved device performance.

8.2 Introduction

PSCs offer several advantages because of their ease of fabrication, low cost and ability to produce transparent, flexible, good-quality devices with a laminated output.[1,2] The device performance of PSCs with inverted structure is influenced by the HTL. Some semiconductor materials that are used as HTMs in PSCs have attracted the attention of researchers; these materials include PEDOT: PSS, CuO, graphene oxide, V_2O_5, PbS and PTAA.[3–7] The main reasons for preferring these inorganic HTMs over organic HTMs are the higher hole-transporting ability and higher stability.

Notably, NiO_x has been successfully applied as a wide band gap (3.6–4.0 eV) p-type semiconductor material in an inverted structure.[8–10] The preference of NiO_x is based on its intrinsic properties, including suitable WF and adequate charge carrier mobility, which can sufficiently match the energy level of perovskites by adjustment of the O^{2-} or Ni^{2+} concentration.[11–14] Another advantage of NiO_x is that multiple methods are applicable and available for its deposition,[15–17] where sputtering offers suitable control of the composition of NiO_x, allowing for roll-to-roll fabrication.[18,19] Perovskite based on sp-NiO_x can show an operational stability as high as 4,000 h.[20] According to its stoichiometry,[21] NiO_x is a Mott–Hubbard insulator. However, nonstoichiometric composites (such as NiOOH and Ni_2O_3, and Ni^{3+} species) can be induced by the oxidation of NiO_x, which significantly improves the p-type conductivity.[19]

Pristine NiO_x has low conductivity, which may degrade hole extraction by aggravating charge carrier recombination.[22] Consequently, methods to increase the conductivity of NiO_x have emerged for treating NiO_x.[11,23–25] Notably, nickel vacancies dominate the p-type conduction in non-treated NiO_x.[26] Moreover, the internal p-type conductivity is limited because the Ni vacancies in untreated NiO_x have a large IE. Consequently, extrinsic treatments such as dopants, which contain shallow acceptor levels, are preferred,[27] helping to increase the conductivity of NiO_x and yielding enhanced PSCs.[24,28–30]

Additionally, the charge carrier transfer is significantly affected by the interface defects/traps occurring between the NiO_x and perovskite layers because charge extraction takes place at the interface, which suffers from charge recombination.[31] These defects may be minimised by introducing a layer between perovskite and NiO_x. Moreover, the introduced interface layer improves energy level matching; hence, this has become a preferred method for realising further improvement of PSC performance.[32] Further, SAMs form layers by the self-assembly of surfactant molecules at surfaces. SAMs are capable of being physiosorbed or chemisorbed onto a number of surfaces and forming

extremely thin layers when they are applied using solution-processed techniques, such as dip coating, slot-die coating, blade, spraying and spin coating.[33] Surface modification using SAM has been widely applied in PSCs.[34–36] Consequently, SAM-based HTL for inverted PSCs have been used[37–39] and helped in achieving 21% efficiency for single-junction devices.[40]

Bai et al.[41] modified a NiO_x crystal film surface using a small molecule (diethanolamine). As a result, the chemical reaction rate of the conversion of PbI_2 to $MAPbI_3$ ($MA^+ = CH_3NH_3^+$) was slowed down, creating a better interface and film quality. Zhang et al.[42] focused on reducing trap-assisted recombination between NiO_x and perovskite layer through introducing ferrocenedicarboxylic acid to modify NiO_x. Hence, the modifications yielded improved PCEs to 18.2% with improvement of the crystallisation of the perovskite layer, hole transport and collection abilities. Further, the resulting PSCs were stable, which concurs with another modification that was performed using ferrocene dicarboxylic acid and PTAA. This modification attained better perovskite films with efficient hole extraction.[43] To passivate the NiO_x surface, Wang et al.[32] investigated a series of para-substituted benzoic acid (R-BA) SAM layers on NP NiO_x. Consequently, the devices that included SAM had PCEs of 18.4% and were less affected by trap-assisted recombination, minimised energy offset between NiO_x NP and perovskite and changed the surface wettability.

Recently, it has been shown that modify NiO_x is the key challenge to improve the V_{oc} by reducing the defects of NiO_x.[44–46] Additionally, to reduce the surface defect and hydroxyl group presented on NiO_x, Mann et al. used 3-(Triethoxysilyl)propylamine (TSPA) as a SAM between NiOx and perovskite. They found that this SAM passivated the surface of NiO_x and reduced the recombination of the charge.[47]

A new generation of SAMs, known as ([2-(3,6-dimethoxy-9H-carbazol-9-yl)ethyl]phosphonic acid) (MeO-2PACz), were developed for the first time by Al-

Ashouri et al. as hole-selective contacts with intrinsic scalability, ease of processing, low cost and free of dopants. Another improvement entails enabling highly efficient p–i–n PSCs and a record-efficiency monolithic perovskite/CIGSe tandem device.[48] Further, selecting SAMs for application in perovskite devices is an important factor, whereby [2-(9H-carbazol-9-yl) ethyl]phosphonic acid) (2PACz) and MeO-2PACz can create an interface that is energetically well aligned with the perovskite absorber with minimal non-radiative recombination.[48] After this, they further designed a tandem PSC using the same SAM (MeO-2PACz) and found that a fast hole extraction was linked to a low ideality factor.[49] They also investigated the ITO surface coverage using MeO-2PACz on the top surface and introduced NiO as the intermediate layer.[40] Lastly, Sun et al. developed a method to enhance the interaction between the MeO-2PACz and ITO using sp-NiOx layer with the triple-cation perovskite devices. The result shows that NiO_x passivates the ITO and prevents a direct contact between perovskite and ITO, which contributes to improving the PCE.[50] Herein, we developed a similar strategy using sp-NiO_x by coating MeO-2PACz on top of sp-NiO_x to study the surface defect of NiO_x and perovskite interfaces using different analytical techniques with the commonly used perovskite methylammonium lead iodide (MAPbI3). Despite these remarkable contributions, the application of MeO-2PACz, by modulating the crystal contact or layer between NiO_x/perovskite, requires further investigation. Therefore, the current study involves a systematic investigation of the effect of MeO-2PACz on a NiO_x layer. Second, an in-depth analysis of the defect at NiO_x and perovskite layers is conducted, where a thin layer of MeO-2PACz is inserted, as illustrated in Figure 8-1.

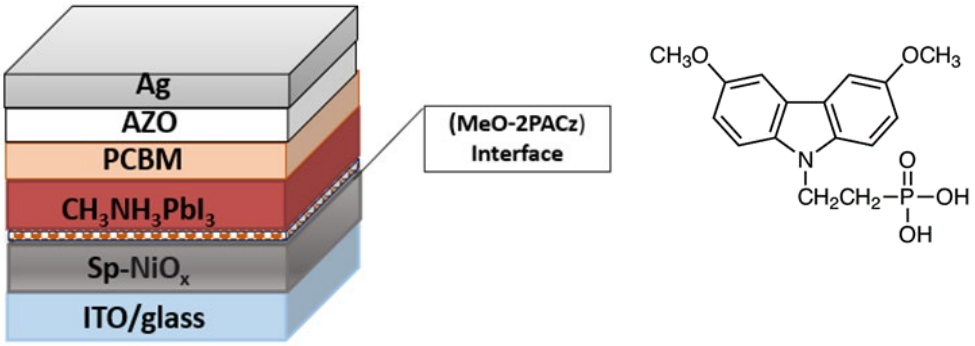

Figure 8-1. (Left) Schematic representation of the device structure and (Right) chemical structure of MeO-2PACz.

The surface functional groups of NiO_x are composed of hydroxylated groups[51,52] that react with phosphonic groups.[41,53] Hence, the three main goals of a SAM are 1) a SAM that can synchronously contribute to improving the crystallinity and stability of the perovskite layer, 2) a SAM that can passivate the defects of the interface, and 3) a SAM that can be applied to have superior interface contact properties compared to the plain NiO_x layer. The current work shows that MeO-2PACz reduces the defects in sp-NiO_x and enhances the quality of the perovskite film by enlarging the domain size, increasing the charge attraction efficiency and reducing charge recombination. In this case, PSCs with a modified sp-NiO_x/perovskite interface yielded PCEs of 17.2% with an active area of 1 cm^2 (certified efficiency of 16.25%; see Figure S8-3). Therefore, the outcome proves that it is feasible to treat the sp-NiO_x/perovskite interface because the performance of PSCs with a sp-NiO_x HTL is significantly improved.

8.3 Experimental

8.3.1 Structure of the device

The device containing the SAM interface had the following structure: ITO-coated glass/sp-NiOx/MeO-2PACz/perovskite, CH3NH3PbI3/PC61BM/AZO/Ag, as illustrated

in Figure 8-1. In this representation, sp-NiOx acts as the HTL layer, which blocks electrons, and PC61BM/AZO acts as the ETL. Materials and sample preparation are described in Chapter 3, Section 3.2.3. Experimental details about XRD, PDS and SEM can be found in Chapter 3.

8.4 Results and Discussion

8.4.1 Understanding the effect of MeO-2PACz (SAM) on the NiOx layer

A correlative investigation was conducted into the impact of the MeO-2PACz (SAM) interface on NiO_x and its influence on the performance of an SC device. Hence, the focus is to understand the properties and crystallisation of the NiO_x film and the interaction between NiO_x and MeO-2PACz.

8.4.1.1 Structural and optical characterisation of NiO_x

Treatment of NiO_x with MeO-2PACz was investigated through SEM, as shown in Figures 8-2(a) and 8-2(b). The surface morphology of the pristine NiO_x film and treated NiO_x films were investigated, where minimal changes were observed. In this case, the results depict the same domain size and good coverage. Notably, the SEM images do not show a significant difference, implying that with or without the MeO-2PACz layer, the morphological properties are retained.

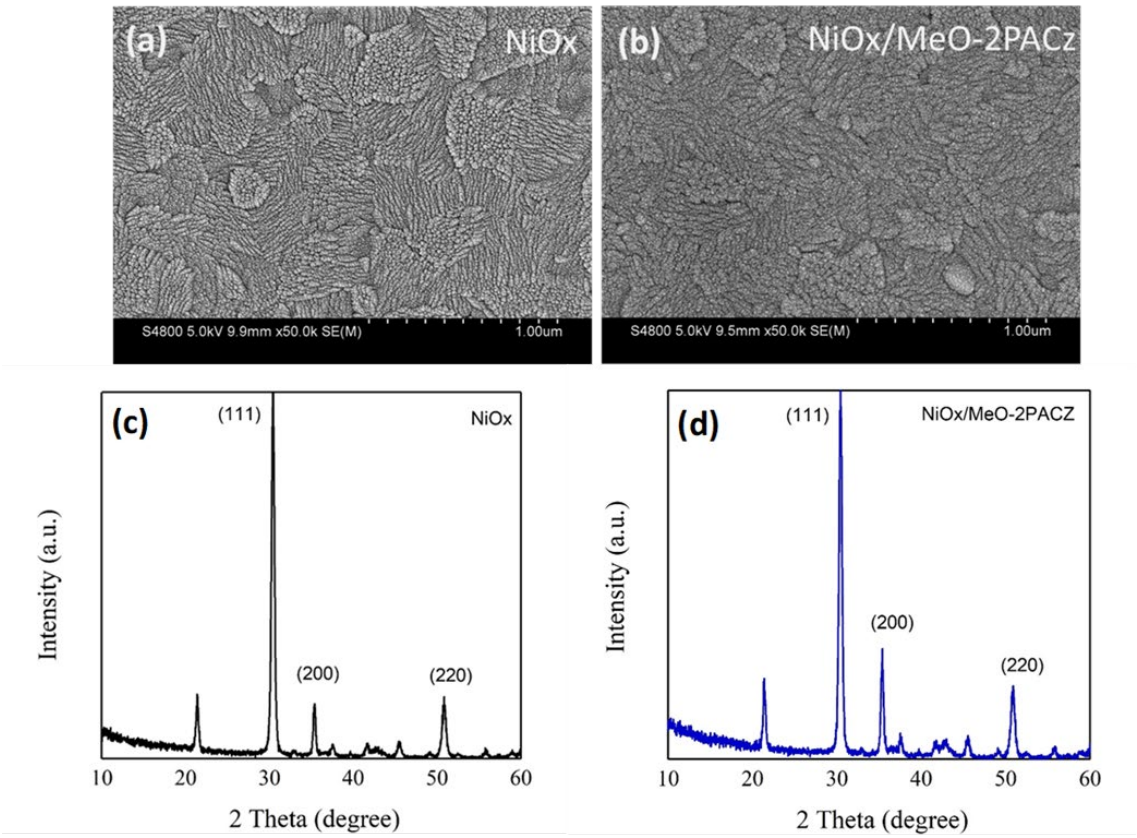

Figure 8-2. (a and b) SEM images of NiO_x before and after treatment with MeO-2PACz SAM. (c) XRD patterns for NiO_x. (d) XRD patterns for NiO_x/MeO-2PACz SAM.

The transmittance of NiO_x and NiO_x/MeO-2PACz was investigated, as shown in Figure S8-1, using UV-vis transmittance spectra. The same NiO_x substrate was measured before and after MeO-2PACz treatment to show the minimal change by the introduction of the SAM.

The crystallinity of the film was studied using XRD, and the results are presented in Figure 8-2(c) and 8-2(d), in which the evolution of the XRD patterns obtained for the NiO_x film and the field after being modified with MeO-2PACz are shown. The dominant (111), (200) and (220) peaks fit well to crystalline NiO.[54] Notably, in the two films, there are no significant changes, which means that the SAM of MeO-2PACz should not change the crystal structure of NiOx.

8.4.1.2 Surface analysis for NiO_x

XPS was conducted to investigate the properties of NiO_x. In this case, the chemical components of the pristine NiO_x film and NiO_x/MeO-2PACz were analysed. The characteristic peaks for Ni $2p_{3/2}$ and O 1s are presented in Figure 8-3. Further, decomposition of the XPS spectrum shows that the Ni 2p spectrum can be fitted by two oxidation states: Ni^{2+} and Ni^{3+}. The other two peaks are related to satellite peaks. Ni^{2+} is found at 853.7 eV and 854.1 eV for the pristine NiO_x and modified NiO_x surfaces, respectively, as shown in Figures 8-3(a) and 8-3(c). This peak corresponds to NiO_6 octahedral bonding in the cubic rock-salt NiO structure.[55] Another peak was observed at 855.3 eV for pristine NiO and at 855.7 eV for modified NiO_x, which can be attributed to Ni^{3+} comprising NiOOH[56] and Ni_2O_3.[54,57] In previous studies, this peak has been assigned to the O vacancy in NiO_x.[15] The broad peaks observed at 860.6 eV and 864.4 eV are assigned to the shake-up processes (satellites) for NiO.[56,58] After treating the NiO film, a significant decrease in the integrated area of overall Ni peaks, as summarised in Table 8-1. Notably, a shift of ~0.5 eV was observed for the dominant peaks in Ni $2p_{3/2}$ for pristine and treated NiO_x, implying that electron transfer occurs. This is similar to a previous result,[59] which showed a shift in the core component of NiO after the treatment. In conclusion, the surface passivation cannot be supported by the XPS results. Additionally, a high-resolution XP spectra for the C1s and N1s are shown in the Figure S8-2. The position for C1s peaks for pristine NiOx as the first peak was obtained at 284.9 eV and can be assigned to the C-C bond, whereas the second peak was at 286.4 eV and can be identified as representing the C-O-C bond. A third peak is found at the position of 288.3 eV, which is related to C=O. The NiOx with the MeO-2PACz layer has three C1s peaks, at 284.9 eV, 286.4 eV and 288.6 eV, related to C-C, C-O-C and C=O, respectively. The N1s spectrum was found in the NiOx with the MeO-2PACz layer at 400.1 eV, as shown in Figure S8-2.

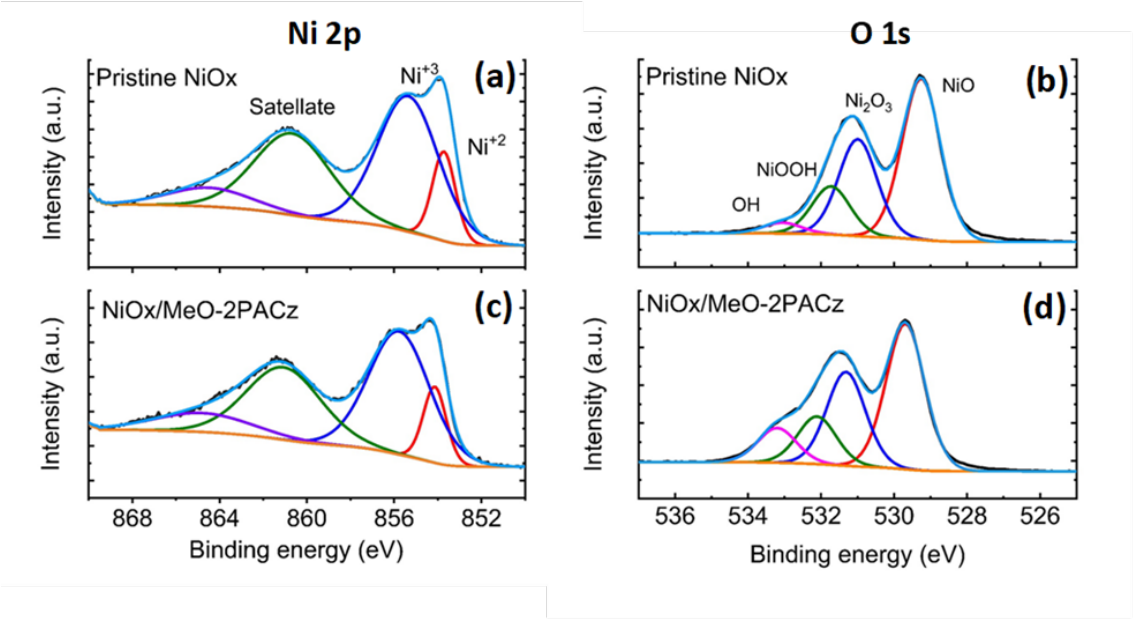

Figure 8-3. XPS surface spectra: (a) Ni $2p_{3/2}$ for pristine NiOx, (b) O 1s for pristine NiOx, (c) Ni $2p_{3/2}$ for NiOx treated with MeO-2PACz and (d) O 1s for NiOx treated with MeO-2PACz.

Table 8-1

Summary of the Relative Intensity of the Ni 2p, O 1s and P 2p Peaks Showing the Area Under the Curve for the Pristine NiOx and NiOx/MeO-2PACz Samples Obtained from XPS

ELEMENTS	Peaks	CONTROL (NIOX)		NIOX/MEO-2PACZ	
		Position (eV)	Integrated the area %	Position (eV)	Integrated the area %
NI 2P	Ni^{2+} (NiO)	853.7	2.6	854.1	1.8
	Ni^{3+} (NiOOH), Ni_2O_3	855.3	10.8	855.7	7.8
O 1 S□	NiO (Ni^{2+})	529.2	21.8	529.6	18.2
	Ni_2O_3 (Ni^{3+})	530.9	13.1	531.3	11.7
	NiOOH	531.7	6.5	532.1	5.9
	OH	533.0	1.4	533.2	4.3
P 2P	$2P_{3/2}$	-	-	133.1	1.2
	$2P_{1/2}$	-	-	133.9	0.6

The binding energy in the O 1s spectra was resolved into four main oxygen states, as shown in Figures 8-3(b) and 8-3(d). The peaks at 529.2 eV and 529.6 eV are attributed to NiO or Ni^{2+} [57] for pristine NiO_x and NiO_x/MeO-2PACz. Moreover, the peaks at 530.9 eV for pristine NiO_x and 531.3 eV for NiO_x/MeO-2PACz are assigned to O-bonded Ni_2O_3 or Ni^{3+}, as reported previously.[57] Additionally, an increased amount of Ni_2O_3 has been reported to contribute to an increased WF.[60] The peaks at 531.7 eV and 532.1 eV are related to NiOOH.[61–63] The higher binding energy at 533 eV is attributed to hydroxyl (OH) groups,[64] and the intensity of this peak increases after the treatment, which is probably because of the OH group present in the MeO-2PACz structure.

Evidence that NiO_x surface was covered with MiO-2PACz after the treatment is indicated by the P 2p peak observed for the two phosphates and metaphosphate, as shown by the

XPS spectra in Figure S8-2. Because the main P 2p binding energy is 133.1 eV, this peak is attributed to phosphate groups, which indicates a phosphorous binding state.[57]

8.4.2 Understanding the role of MeO-2PACz (SAM) on a perovskite film

Understanding the impact of MeO-2PACz (SAM) on the performance of perovskite devices requires investigating the morphology and optical properties of perovskite films. Additionally, the defect level at the NiO_x/MeO-2PACz interface and the effect of the treatment on the energy level are investigated.

8.4.2.1 Effect of surface modification on the morphology of perovskite film and the optical properties of perovskite film after treating NiO_x

SEM analysis was carried out to gain insights into the perovskite morphology on NiO_x and NiO_x/MeO-2PACz, as shown in Figure 8-4 (a–d). A significant difference in perovskite domain size when deposited onto the MeO-2PACz layer is obtained from the quantified domain size. Based on the surface SEM images, an increase in domain size is observed because of the MeO-2PACz interface layer. Hence, treating NiO_x with MeO-2PACz influences the perovskite's bulk properties with uniform perovskite crystallinity because of the passivation of the surface defect in NiO_x, leading to a slight enhancement in domain size; here, suppression of recombination is expected. SEM images of the cross-section of samples with a layered structure ITO/NiO_x/MeO-2PACz/perovskite indicate no significant morphological difference for the perovskite.

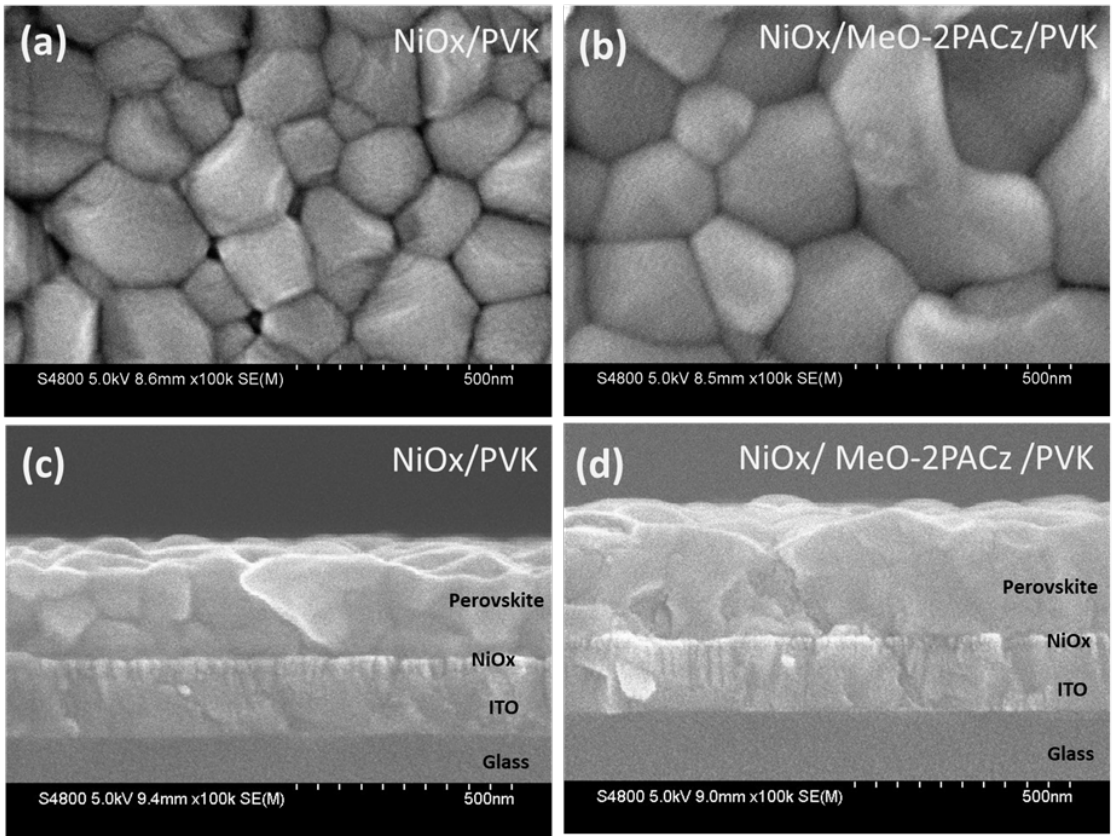

Figure 8-4. SEM images of perovskite (PVK) films: (a) top surface SEM without treatment, (b) top surface SEM with MeO-2PACz interface, (c) cross-sectional scanning image without treatment and (d) cross-sectional scanning image with a MeO-2PACz interface.

Steady-state PL and TRPL were performed to investigate the photophysical properties of perovskite films with and without the MeO-2PACz interface layer. Figure 8-5(a) shows the PL results obtained for the perovskite films. The PL intensities are increased after MeO-2PACz treatment, which indicates a significant suppression of recombination in the perovskite layer.[65] Further measurements included TRPL analysis, which aimed to understand the recombination lifetime in perovskites. The results are illustrated in Figure 8-5(b), which shows the control perovskite device and modified film with a MeO-2PACz layer. A single wavelength of 402 nm was applied as an excitation source. Figure 8-5(b) shows the firster decay reflecting the firster charge injection into the MeO-2PACz-treated interface. Effective transfer of the charge carrier was attained for the modified sample

according to the TRPL results. A higher steady-state PL indicates slightly better surface passivation; thus, the faster TRPL decay likely stems from CT and not higher non-radiative recombination.

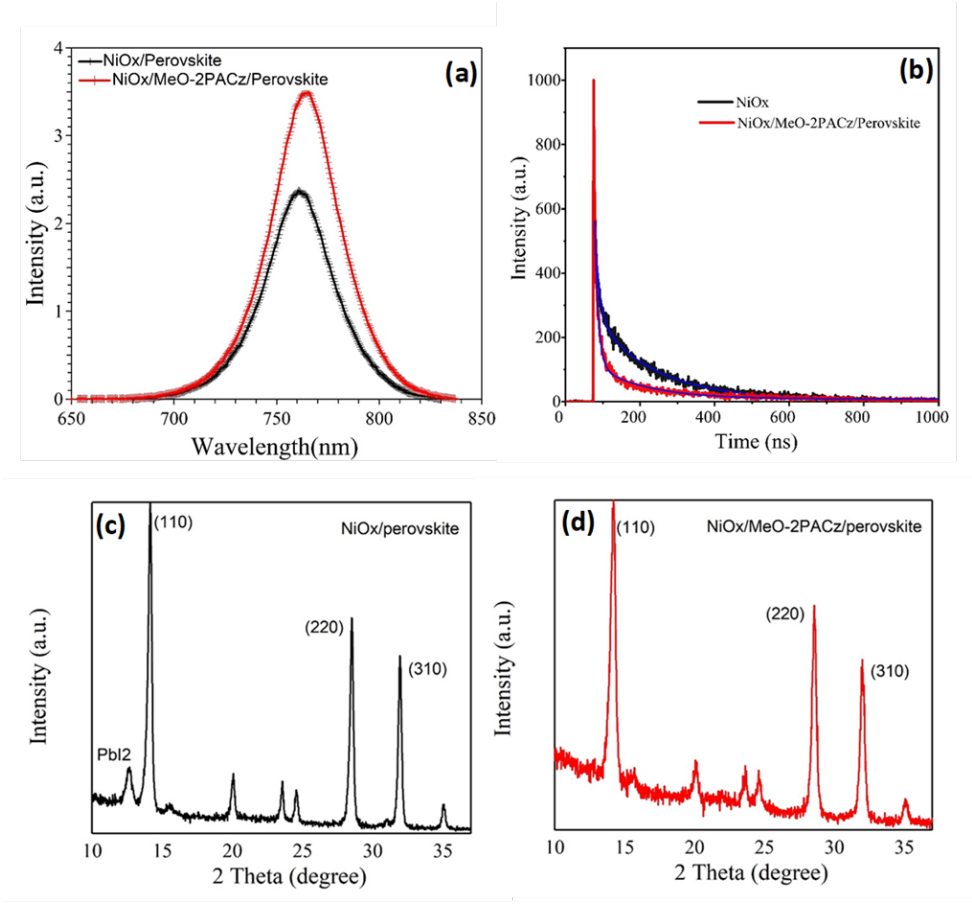

Figure 8-5. (a) Steady-state PL for perovskite films with and without treatment. (b) TRPL measured for perovskite films with and without treatment. (c) XRD patterns for perovskite films on pristine NiO_x. (d) XRD patterns for modified NiO_x.

The PL and TRPL results indicate the role of the MeO-2PACz layer in surface passivation. Hence, these results explain the enhancement of the J_{sc} for MeO-2PACz-modified PSCs, which will be discussed later.

The XRD results for perovskite films with and without the MeO-2PACz layer are presented in Figures 8-5(c) and 8-5(d), which indicates the effect of MeO-2PACz on the surface. In this case, the diffraction peaks for the perovskite layer with the MeO-2PACz

treatment are similar to the control film without a MeO-2PACz layer. However, a new diffraction peak appears at 12^0, which is attributed to PbI_2, indicating the presence of unreacted PbI_2 content in the perovskite film. Introducing the MeO-2PACz interface layer between perovskite/NiO_x results in the total disappearance of PbI_2 crystals, which can be explained by their conversion in the perovskite phase.

The XRD results obtained lead to the conclusion that NiO_x without treatment affects the perovskite film because of the improper perovskite crystallisation on NiO_x without a MeO-2PACz underlayer, resulting in the appearance of residual PbI_2 that appears unclear. However, the presence of H_2O and OH groups and interstitial oxygen on NiO_x or the presence of Ni^{3+} in NiO_x can cause improper perovskite crystallisation.[15,18,66,67] Comparatively, the device containing the MeO-2PACz interface layer shows a better passivation effect than perovskite/NiO_x. Thus, the MeO-2PACz layer was utilised to passivate the defects in the perovskite layer.

8.4.2.2 Studying the defect level at the interface

To further support our claim that the MeO-2PACz layer can passivate the NiO_x surface, PDS was used to further investigate the pristine NiO_x and NiO_x/perovskites; the results obtained are compared with MeO-2PACz-treated NiO_x, as shown in Figures 8-6(a) and 8-6(b). The intensity of the PDS signal measured for NiO_x without treatment is higher than that of the treated samples. Moreover, the slope of the spectrum depicts the structural order of the surface. A quantitative description of disorder is indicated by the Urbach energy, which is described as the inverse slope of the PDS signal. PDS signals are observed to range from 4 eV to 3.2 eV, as shown in Figure 8-6(a), and from 1.65 eV to ~1.7 eV, as shown in Figure 8-6(b), indicating a reduction of the defect level at the NiOx surfaces and NiOx/perovskite interface, respectively. Conversely, the Urbach energy shows a decline in value with treated NiO_x, indicating a reduction in the defect level.[68,69] We can conclude that the MeO-2PACz layer can passivate the surface of NiO_x, improving the crystalline quality and decreasing the number of defects.

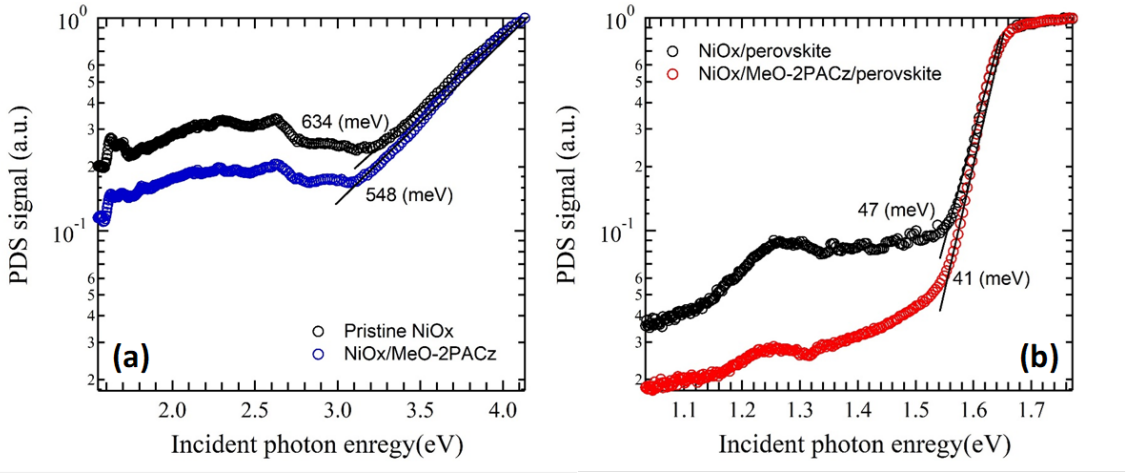

Figure 8-6. PDS spectra and the Urbach energy as determined from the inverse slope of the PDS signals for (a) NiOx and (b) perovskite.

8.4.3 Effect of surface modification on PV properties

The effects of surface modification were investigated, as shown in Figures 8-7(a) and 8-7(b). Figure 8-7(a) represents the J-V, a characteristic control for a perovskite device and a modified device with a MeO-2PACz SAM layer. Figure 8-7(b) shows the EQE spectra for the control perovskite device and modified device with the SAM layer.

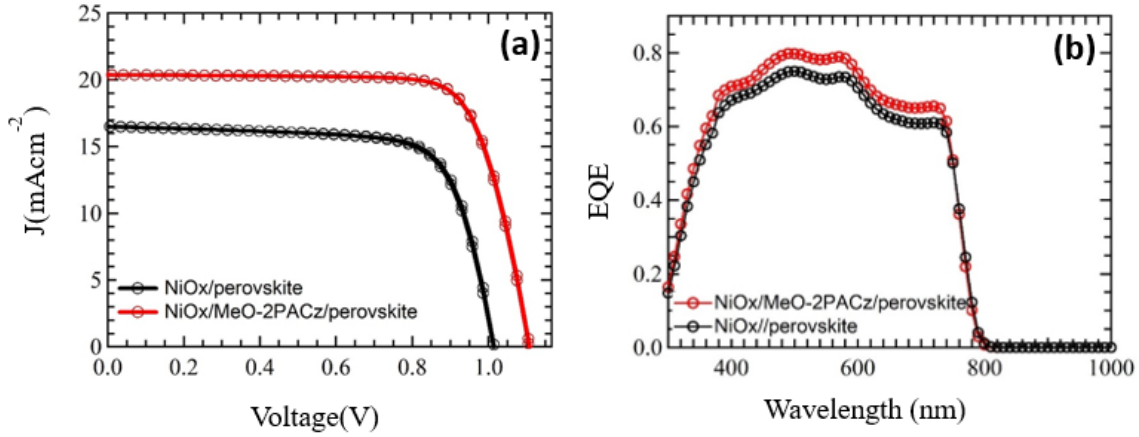

Figure 8-7. (a) Representative J-V characteristics for the control perovskite device and the device modified using the MeO-2PACz interface layer. (b) EQE spectra for the control perovskite device and the device modified with a MeO-2PACz interface layer. Integrated J_{sc} for the MeO-2PACz treated and untreated devices are 17.7 mA/cm^2 and 16.3 mA/cm^2.

The results are summarised in Table 8-2, indicating the average device parameters for PSCs, where the data for the control device and device modified with the MeO-2PACz interface layer are presented. The average results are derived from measurements for eight PSC devices for each condition (see Figure S8-6).

Table 8-2

Device Parameters for PSCs Including the Control Devices and Devices Modified Using a SAM Layer Interface

Device	J_{sc} (mA/cm^2)	V_{oc} (V)	FF (%)	R_s ($\Omega\ cm^2$)	R_{sh} ($\Omega\ cm^2$)	η (%)
Perovskite/ NiO_x	17.3 ± 0.68	1.0 ± 0.06	0.7 ± 0.03	8.7 ± 2.08	1.027.5 ± 334.78	11.9 ± 0.74
Perovskite/ MeO-2PACz/NiO_x	20.1 ± 0.18	1.11 ± 0.01	0.8 ± 0.01	4.8 ± 0.45	4.810.7 ± 437.98	17.2 ± 0.03

Note. The results are derived from the eight PSC devices for each condition.

The effect of film quality on carrier recombination was studied by comparing the PV performance of the fabricated devices with and without the MeO-2PACz treatment. The J-V characteristics with and without MeO-2PACz treatment were analysed, as shown in Figure 8-7(a). Notably, the PCEs for the devices with and without MeO-2PACz treatment were determined to be 17.2% and 11.9%. The devices were fabricated under the same conditions, and the results are summarised in Table 8-2. The results indicate a significant enhancement of V_{oc}, J_{sc}, FF and R_{sh} for the MeO-2PACz-treated device compared to the untreated device. The certified data for the MeO-2PACz-treated device are shown in Figure S8-3, with an efficiency of 16.25%. The preliminary stability testing over 100 hours was also conducted under maximum power point tracking (MPPT) conditions. The MeO-2PACz-treated and untreated devices revealed similar performance, as shown in Figure S8-4, displaying almost no reduction in the PCE.

The EQE was measured to study the efficiency of photocurrent conversion. The results show that the EQE covers the entire visible range from 300 nm to 800 nm for the treated

devices and control device, as presented in Figure 8-7(b). The results confirm that the MeO-2PACz-treated device has a higher EQE than the control device, and band gap energies for both devices are about 1.55 eV, which is a typical value for MAPI perovskites.

An analysis of the IQE measurements for the devices was conducted, and the results are presented in Figure S8-5. The values obtained correspond to the ratio of the carrier charge, which is collected by the SC, to the number of photons absorbed under illumination. The results show that the charge carriers generated and collected for SC operation are significantly higher when the perovskite device is treated with MeO-2PACz.

8.4.4 Electronic properties and energy level for perovskite films

To determine the mechanism behind this improvement, the electronic structures of NiO_x with and without a MeO-2PACz interlayer were investigated using UPS. The UPS results for NiO_x and NiO_x/MeO-2PACz, as measured under a –10 V bias for the VB, are shown in Figure 8-8(a), and the secondary electrons are shown in Figure 8-8(b). Additionally, the WF for pristine NiO_x and NiO_x covered with MeO-2PACz was determined to be 4.9 eV and 5.5 eV, respectively.

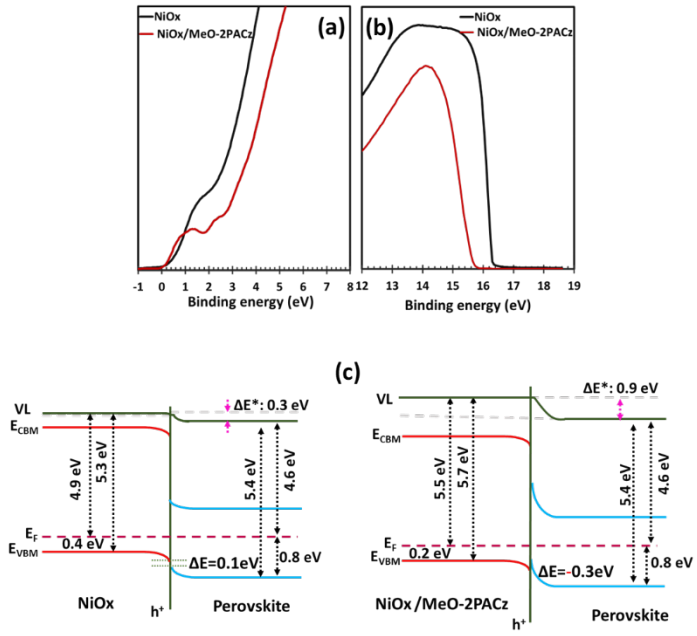

Figure 8-8. UPS spectra for NiO_x and NiO_x/MeO-2PACz, as measured under a bias of –10 V. (a) Valance band spectra for NiO_x and NiO_x/MeO-2PACz. (b) The WF (φ) is calculated using the equation φ = hv, with the secondary electron (SE) used as the cut-off. (c) The energy level diagram for pristine NiOx (left) and NiO_x/MeO-2PACz (right).

The obtained VB values for perovskite on NiO_x and NiO_x/MeO-2PACz are close to the E_f, which improves the device performance by facilitating CT between perovskites and NiO_x, as shown in Figure 8-8(c). The values of the WF and IE for the perovskite layer were taken from prior literature.[25] Before MeO-2PACz treatment, an energy gap of 0.1 eV between the VB maximum of perovskite and the VB maximum of NiO_x can be observed, which can lead to the formation of a hole trap at the interface for charge carriers with insufficient kinetic energy to overcome the gap. After treating NiO_x with MeO-2PACz, the VB maximum of perovskite exceeded the VB maximum of NiO_x. Thus, the energy gap is compensated due to an energy shift, resulting in a proper energy level alignment for hole transport over the interface. The energetic gap between the VB maximum of perovskite and NiO_x changes from +0.1 eV to –0.3 eV. More details for the extraction of these values can be found in Table S8-1.

8.5 Conclusion

In this study, we modified a HTL (NiO_x) with a MeO-2PACz (SAM) layer. Inserting the MeO-2PACz interface between a NiO_x HTL and perovskite layer helped decrease defects by passivation of NiO_x. Based on the results obtained, the MeO-2PACz on NiO_x interface significantly improves the defect level and device performance. This performance improvement can be attributed to a reduction in charge recombination, increase in extraction efficiency and enhancement of the perovskite film quality with its large domain size. The analysis further indicates that, generally, the introduction of MeO-2PACz results in the passivation of NiO_x surface defects, resulting in an enhancement of the crystallisation. In summary, interface modification leads to various positive effects, including better interfacial contact, better energy level alignment, enhanced crystallisation and an increase in the PCE. Thus, our results offer a promising mechanism for improving the performance of inorganic carrier transport layers in PSCs, which can potentially be extended to other combinations of inorganic semiconductors and functional organic molecule dopants in the future.

8.6 Acknowledgement

Amira R. M. Alghamdi and Gunther G. Andersson would like to thank the National Institute for Material Science (NIMS), Japan, and Flinders University, Adelaide, for the International Cooperative Graduate Program (ICGP) Fellowship. We also thank Dr Masatomo Sumiya for providing PDS data.

8.7 References

(1) Eperon, G. E.; Burlakov, V. M.; Goriely, A.; Snaith, H. J. Neutral Color Semitransparent Microstructured Perovskite Solar Cells. *ACS Nano* **2014**, *8* (1), 591–598.

(2) Snaith, H. J. Perovskites: The Emergence of a New Era for Low-Cost, High-Efficiency Solar Cells. *The Journal of Physical Chemistry Letters* **2013**, *4* (21), 3623–3630.

(3) Ye, S.; Rao, H.; Yan, W.; Li, Y.; Sun, W.; Peng, H.; Liu, Z.; Bian, Z.; Li, Y.; Huang, C. A Strategy to Simplify the Preparation Process of Perovskite Solar Cells by Co-Deposition of a Hole-Conductor and a Perovskite Layer. *Advanced Materials* **2016**, *28* (43), 9648–9654.

(4) Hu, L.; Wang, W.; Liu, H.; Peng, J.; Cao, H.; Shao, G.; Xia, Z.; Ma, W.; Tang, J. PbS Colloidal Quantum Dots as an Effective Hole Transporter for Planar Heterojunction Perovskite Solar Cells. *Journal of Materials Chemistry A* **2015**, *3* (2), 515–518.

(5) Xiao, Z.; Dong, Q.; Bi, C.; Shao, Y.; Yuan, Y.; Huang, J. Solvent Annealing of Perovskite-Induced Crystal Growth for Photovoltaic-Device Efficiency Enhancement. *Advanced Materials* **2014**, *26* (37), 6503–6509.

(6) Wu, Z.; Bai, S.; Xiang, J.; Yuan, Z.; Yang, Y.; Cui, W.; Gao, X.; Liu, Z.; Jin, Y.; Sun, B. Efficient Planar Heterojunction Perovskite Solar Cells Employing Graphene Oxide as Hole Conductor. *Nanoscale* **2014**, *6* (18), 10505–10510.

(7) Wang, Q.; Bi, C.; Huang, J. Doped Hole Transport Layer for Efficiency Enhancement in Planar Heterojunction Organolead Trihalide Perovskite Solar Cells. *Nano Energy* **2015**, *15*, 275–280.

(8) Nakai, H.; Sugiyama, M.; Chichibu, S. F. Ultraviolet Light-Absorbing and Emitting Diodes Consisting of a p-Type Transparent-Semiconducting NiO Film Deposited on an n-Type GaN Homoepitaxial Layer. *Applied Physics Letters* **2017**, *110* (18), 181102.

(9) Aydin, E.; Troughton, J.; De Bastiani, M.; Ugur, E.; Sajjad, M.; Alzahrani, A.; Neophytou, M.; Schwingenschlögl, U.; Laquai, F.; Baran, D. Room-Temperature-Sputtered Nanocrystalline Nickel Oxide as Hole Transport Layer for p–i–n Perovskite Solar Cells. *ACS Applied Energy Materials* **2018**, *1* (11), 6227–6233.

(10) Hu, Z.; Chen, D.; Yang, P.; Yang, L.; Qin, L.; Huang, Y.; Zhao, X. Sol-Gel-Processed Yttrium-Doped NiO as Hole Transport Layer in Inverted Perovskite Solar Cells for Enhanced Performance. *Applied Surface Science* **2018**, *441*, 258–264.

(11) Wang, S.; Zhang, B.; Feng, D.; Lin, Z.; Zhang, J.; Hao, Y.; Fan, X.; Chang, J. Achieving High Performance and Stable Inverted Planar Perovskite Solar Cells Using Lithium and Cobalt Co-Doped Nickel Oxide as Hole Transport Layers. *Journal of Materials Chemistry C* **2019**, *7* (30), 9270–9277.

(12) Liu, Z.; Chang, J.; Lin, Z.; Zhou, L.; Yang, Z.; Chen, D.; Zhang, C.; Liu, S.; Hao, Y. High-Performance Planar Perovskite Solar Cells Using Low Temperature, Solution–Combustion-Based Nickel Oxide Hole Transporting Layer with Efficiency Exceeding 20%. *Advanced Energy Materials* **2018**, *8* (19), 1703432.

(13) Li, W.; Zhang, W.; Van Reenen, S.; Sutton, R. J.; Fan, J.; Haghighirad, A. A.; Johnston, M. B.; Wang, L.; Snaith, H. J. Enhanced UV-Light Stability of Planar Heterojunction Perovskite Solar Cells with Caesium Bromide Interface Modification. *Energy & Environmental Science* **2016**, *9* (2), 490–498.

(14) Zhou, L.; Lin, Z.; Ning, Z.; Li, T.; Guo, X.; Ma, J.; Su, J.; Zhang, C.; Zhang, J.; Liu, S. Highly Efficient and Stable Planar Perovskite Solar Cells with Modulated Diffusion Passivation Toward High Power Conversion Efficiency and Ultrahigh Fill Factor. *Solar RRL* **2019**, *3* (11), 1900293.

(15) Cui, J.; Meng, F.; Zhang, H.; Cao, K.; Yuan, H.; Cheng, Y.; Huang, F.; Wang, M. CH3NH3PbI3-Based Planar Solar Cells with Magnetron-Sputtered Nickel Oxide. *ACS Applied Materials & Interfaces* **2014**, *6* (24), 22862–22870.

(16) Kim, B. G.; Jang, W.; Wang, D. H. Facile Niox Sol-Gel Synthesis Depending on Chain Length of Various Solvents Without Catalyst for Efficient Hole Charge Transfer in Perovskite Solar Cells. *Polymers* **2018**, *10* (11), 1227.

(17) Yang, H.; Park, H.; Kim, B.; Park, C.; Jeong, S.; Chae, W.-S.; Kim, W.; Jeong, M.; Ahn, T. K.; Shin, H. Unusual Hole Transfer Dynamics of the NiO Layer in Methylammonium Lead Tri-iodide Absorber Solar Cells. *The Journal of Physical Chemistry Letters* **2021**, *12* (11), 2770–2779.

(18) Yanagida, M.; Shimomoto, L.; Shirai, Y.; Miyano, K. Effect of Carrier Transport in NiO on the Photovoltaic Properties of Lead Iodide Perovskite Solar Cells. *Electrochemistry* **2017**, *85* (5), 231–235.

(19) Islam, M. B.; Yanagida, M.; Shirai, Y.; Nabetani, Y.; Miyano, K. NiO x Hole Transport Layer for Perovskite Solar Cells with Improved Stability and Reproducibility. *ACS Omega* **2017**, *2* (5), 2291–2299.

(20) Islam, M. B.; Yanagida, M.; Shirai, Y.; Nabetani, Y.; Miyano, K. Highly Stable Semi-Transparent MAPbI3 Perovskite Solar Cells with Operational Output for 4000 h. *Solar Energy Materials and Solar Cells* **2019**, *195*, 323–329.

(21) Dubey, P.; Kaurav, N.; Devan, R. S.; Okram, G.; Kuo, Y. The Effect Of Stoichiometry on the Structural, Thermal and Electronic Properties of Thermally Decomposed Nickel Oxide. *RSC Advances* **2018**, *8* (11), 5882–5890.

(22) Corani, A.; Li, M.-H.; Shen, P.-S.; Chen, P.; Guo, T.-F.; El Nahhas, A.; Zheng, K.; Yartsev, A.; Sundström, V.; Ponseca Jr, C. S. Ultrafast Dynamics of Hole Injection and Recombination in Organometal Halide Perovskite Using Nickel Oxide as p-Type Contact Electrode. *The Journal of Physical Chemistry Letters* **2016**, *7* (7), 1096–1101.

(23) Chen, W.; Wu, Y.; Fan, J.; Djurišić, A. B.; Liu, F.; Tam, H. W.; Ng, A.; Surya, C.; Chan, W. K.; Wang, D. Perovskite Solar Cells: Understanding the Doping Effect on NiO: Toward High-Performance Inverted Perovskite Solar Cells (Adv. Energy Mater. 19/2018). *Advanced Energy Materials* **2018**, *8* (19), 1870091.

(24) Chen, W.; Liu, F. Z.; Feng, X. Y.; Djurišić, A. B.; Chan, W. K.; He, Z. B. Cesium Doped NiOx as an Efficient Hole Extraction Layer for Inverted Planar Perovskite Solar Cells. *Advanced Energy Materials* **2017**, *7* (19), 1700722.

(25) Chen, W.; Zhou, Y.; Wang, L.; Wu, Y.; Tu, B.; Yu, B.; Liu, F.; Tam, H. W.; Wang, G.; Djurišić, A. B. Molecule-Doped Nickel Oxide: Verified Charge Transfer and Planar Inverted Mixed Cation Perovskite Solar Cell. *Advanced Materials* **2018**, *30* (20), 1800515.

(26) Lany, S.; Osorio-Guillén, J.; Zunger, A. Origins of the Doping Asymmetry in Oxides: Hole Doping in NiO versus Electron Doping in ZnO. *Physical Review B* **2007**, *75* (24), 241203.

(27) Zhang, K. H.; Xi, K.; Blamire, M. G.; Egdell, R. G. P-Type Transparent Conducting Oxides. *Journal of Physics: Condensed Matter* **2016**, *28* (38), 383002.

(28) Chen, W.; Wu, Y.; Yue, Y.; Liu, J.; Zhang, W.; Yang, X.; Chen, H.; Bi, E.; Ashraful, I.; Grätzel, M. Efficient and Stable Large-Area Perovskite Solar Cells with Inorganic Charge Extraction Layers. *Science* **2015**, *350* (6263), 944–948.

(29) Kim, J. H.; Liang, P. W.; Williams, S. T.; Cho, N.; Chueh, C. C.; Glaz, M. S.; Ginger, D. S.; Jen, A. K. Y. High-Performance and Environmentally Stable Planar Heterojunction Perovskite Solar Cells Based on a Solution-Processed Copper-Doped Nickel Oxide Hole-Transporting Layer. *Advanced Materials* **2015**, *27* (4), 695–701.

(30) Li, G.; Jiang, Y.; Deng, S.; Tam, A.; Xu, P.; Wong, M.; Kwok, H. S. Overcoming the Limitations of Sputtered Nickel Oxide for High-Efficiency and Large-Area Perovskite Solar Cells. *Advanced Science* **2017**, *4* (12), 1700463.

(31) Shi, J.; Xu, X.; Li, D.; Meng, Q. Interfaces in Perovskite Solar Cells. *Small* **2015**, *11* (21), 2472–2486.

(32) Wang, Q.; Chueh, C. C.; Zhao, T.; Cheng, J.; Eslamian, M.; Choy, W. C.; Jen, A. K. Effects of Self Assembled Monolayer Modification of Nickel Oxide Nanoparticles Layer on the Performance and Application of Inverted Perovskite Solar Cells. *ChemSusChem* **2017**, *10* (19), 3794–3803.

(33) Yang, X.; Ying, Z.; Yang, Z.; Xu, J. R.; Wang, W.; Wang, J.; Wang, Z.; Yao, L.; Yan, B.; Ye, J. Light-Promoted Electrostatic Adsorption of High-Density Lewis Base Monolayers as Passivating Electron-Selective Contacts. *Advanced Science* **2021**, *8* (5), 2003245.

(34) Love, J. C.; Estroff, L. A.; Kriebel, J. K.; Nuzzo, R. G.; Whitesides, G. M. Self-Assembled Monolayers of Thiolates on Metals as a Form of Nanotechnology. *Chemical Reviews* **2005**, *105* (4), 1103–1170.

(35) Ulman, A. Formation and Structure of Self-Assembled Monolayers. *Chemical Reviews* **1996**, *96* (4), 1533–1554.

(36) Ali, F.; Roldán-Carmona, C.; Sohail, M.; Nazeeruddin, M. K. Applications of Self-Assembled Monolayers for Perovskite Solar Cells Interface Engineering to Address Efficiency and Stability. *Advanced Energy Materials* **2020**, *10* (48), 2002989.

(37) Magomedov, A.; Al-Ashouri, A.; Kasparavičius, E.; Strazdaite, S.; Niaura, G.; Jošt, M.; Malinauskas, T.; Albrecht, S.; Getautis, V. Self-Assembled Hole Transporting Monolayer for Highly Efficient Perovskite Solar Cells. *Advanced Energy Materials* **2018**, *8* (32), 1801892.

(38) Caliò, L.; Follana-Berná, J.; Kazim, S.; Madsen, M.; Rubahn, H.-G.; Sastre-Santos, Á.; Ahmad, S. Cu (ii) and Zn (ii) Based Phthalocyanines as Hole Selective Layers for Perovskite Solar Cells. *Sustainable Energy & Fuels* **2017**, *1* (10), 2071–2077.

(39) Más-Montoya, M.; Gómez, P.; Curiel, D.; da Silva, I.; Wang, J.; Janssen, R. A. A Self-Assembled Small-Molecule-Based Hole-Transporting Material for Inverted Perovskite Solar Cells. *Chem. Eur. J* **2020**, *26*, 10276–10282.

(40) Phung, N.; Verheijen, M.; Todinova, A.; Datta, K.; Verhage, M.; Al-Ashouri, A.; Köbler, H.; Li, X.; Abate, A.; Albrecht, S. Enhanced Self-Assembled Monolayer Surface Coverage by ALD NiO in pin Perovskite Solar Cells. *ACS Applied Materials & Interfaces* **2021**.

(41) Bai, Y.; Chen, H.; Xiao, S.; Xue, Q.; Zhang, T.; Zhu, Z.; Li, Q.; Hu, C.; Yang, Y.; Hu, Z. Effects of a Molecular Monolayer Modification of NiO Nanocrystal Layer Surfaces on Perovskite Crystallization and Interface Contact Toward Faster Hole Extraction and Higher Photovoltaic Performance. *Advanced Functional Materials* **2016**, *26* (17), 2950–2958.

(42) Zhang, J.; Luo, H.; Xie, W.; Lin, X.; Hou, X.; Zhou, J.; Huang, S.; Ou-Yang, W.; Sun, Z.; Chen, X. Efficient and Ultraviolet Durable Planar Perovskite Solar Cells via a Ferrocenecarboxylic Acid Modified Nickel Oxide Hole Transport Layer. *Nanoscale* **2018**, *10* (12), 5617–5625.

(43) Du, Y.; Xin, C.; Huang, W.; Shi, B.; Ding, Y.; Wei, C.; Zhao, Y.; Li, Y.; Zhang, X. Polymeric Surface Modification of NiO x-Based Inverted Planar Perovskite Solar Cells with Enhanced Performance. *ACS Sustainable Chemistry & Engineering* **2018**, *6* (12), 16806–16812.

(44) Di Girolamo, D.; Di Giacomo, F.; Matteocci, F.; Marrani, A. G.; Dini, D.; Abate, A. Progress, Highlights and Perspectives on NiO in Perovskite Photovoltaics. *Chemical Science* **2020**, *11* (30), 7746–7759.

(45) Głowienka, D.; Zhang, D.; Di Giacomo, F.; Najafi, M.; Veenstra, S.; Szmytkowski, J.; Galagan, Y. Role of Surface Recombination in Perovskite Solar Cells at the Interface of HTL/CH3NH3PbI3. *Nano Energy* **2020**, *67*, 104186.

(46) Boyd, C. C.; Shallcross, R. C.; Moot, T.; Kerner, R.; Bertoluzzi, L.; Onno, A.; Kavadiya, S.; Chosy, C.; Wolf, E. J.; Werner, J. Overcoming Redox Reactions at Perovskite-Nickel Oxide Interfaces to Boost Voltages in Perovskite Solar Cells. *Joule* **2020**, *4* (8), 1759–1775.

(47) Mann, D. S.; Patil, P.; Kwon, S.-N.; Na, S.-I. Enhanced Performance of pin Perovskite Solar Cell via Defect Passivation of Nickel Oxide/Perovskite Interface with Self-Assembled Monolayer. *Applied Surface Science* **2021**, *560*, 149973.

(48) Al-Ashouri, A.; Magomedov, A.; Roß, M.; Jošt, M.; Talaikis, M.; Chistiakova, G.; Bertram, T.; Márquez, J. A.; Köhnen, E.; Kasparavičius, E. Conformal Monolayer Contacts with Lossless Interfaces for Perovskite Single Junction and Monolithic Tandem Solar Cells. *Energy & Environmental Science* **2019**, *12* (11), 3356–3369.

(49) Al-Ashouri, A.; Köhnen, E.; Li, B.; Magomedov, A.; Hempel, H.; Caprioglio, P.; Márquez, J. A.; Vilches, A. B. M.; Kasparavicius, E.; Smith, J. A. Monolithic Perovskite/Silicon Tandem Solar Cell with> 29% Efficiency by Enhanced Hole Extraction. *Science* **2020**, *370* (6522), 1300–1309.

(50) Sun, J.; Shou, C.; Sun, J.; Wang, X.; Yang, Z.; Chen, Y.; Wu, J.; Yang, W.; Long, H.; Ying, Z. NiOx-Seeded Self-Assembled Monolayers as Highly Hole-Selective Passivating Contacts for Efficient Inverted Perovskite Solar Cells. *Solar RRL* **2021**, *5* (11), 2100663.

(51) Hotchkiss, P. J.; Jones, S. C.; Paniagua, S. A.; Sharma, A.; Kippelen, B.; Armstrong, N. R.; Marder, S. R. The Modification of Indium Tin Oxide with Phosphonic Acids: Mechanism of Binding, Tuning of Surface Properties, and Potential for Use in Organic Electronic Applications. *Accounts of Chemical Research* **2012**, *45* (3), 337–346.

(52) Zhang, H.; Cheng, J.; Lin, F.; He, H.; Mao, J.; Wong, K. S.; Jen, A. K.-Y.; Choy, W. C. Pinhole-Free and Surface-Nanostructured NiO x Film by Room-Temperature Solution Process for High-Performance Flexible Perovskite Solar Cells with Good Stability and Reproducibility. *ACS Nano* **2016**, *10* (1), 1503–1511.

(53) Boehm, H. Acidic and Basic Properties of Hydroxylated Metal Oxide Surfaces. *Discussions of the Faraday Society* **1971**, *52*, 264–275.

(54) Islam, M. B.; Pant, N.; Yanagida, M.; Shirai, Y.; Miyano, K. Effect of Hydroxyl Groups in NiO x on the Open Circuit Voltage of Lead Iodide Perovskite Solar Cells. *Japanese Journal of Applied Physics* **2018**, *57* (8S3), 08RE06.

(55) Chen, W.; Wu, Y.; Fan, J.; Djurišić, A. B.; Liu, F.; Tam, H. W.; Ng, A.; Surya, C.; Chan, W. K.; Wang, D. Understanding the Doping Effect on NiO: Toward High-Performance Inverted Perovskite Solar Cells. *Advanced Energy Materials* **2018**, *8* (19), 1703519.

(56) Koushik, D.; Jošt, M.; Dučinskas, A.; Burgess, C.; Zardetto, V.; Weijtens, C.; Verheijen, M. A.; Kessels, W. M.; Albrecht, S.; Creatore, M. Plasma-Assisted Atomic Layer Deposition of Nickel Oxide as Hole Transport Layer for Hybrid Perovskite Solar Cells. *Journal of Materials Chemistry C* **2019**, *7* (40), 12532–12543.

(57) Ivan, Ş.-B.; Popescu, I.; Fechete, I.; Garin, F.; Pârvulescu, V. I.; Marcu, I.-C. The Effect of Phosphorus on the Catalytic Performance of Nickel Oxide in Ethane Oxidative Dehydrogenation. *Catalysis Science & Technology* **2016**, *6* (18), 6953–6964.

(58) Sun, Y.; Chen, W.; Wu, Y.; He, Z.; Zhang, S.; Chen, S. A Low-Temperature-Annealed and UV-Ozone-Enhanced Combustion Derived Nickel Oxide Hole Injection Layer for Flexible Quantum Dot Light-Emitting Diodes. *Nanoscale* **2019**, *11* (3), 1021–1028.

(59) Tarasov, A.; Zhang, S.; Tsai, M. Y.; Campbell, P. M.; Graham, S.; Barlow, S.; Marder, S. R.; Vogel, E. M. Controlled Doping Of Large-Area Trilayer MoS2 with Molecular Reductants and Oxidants. *Advanced Materials* **2015**, *27* (7), 1175–1181.

(60) Liu, S.; Liu, R.; Chen, Y.; Ho, S.; Kim, J. H.; So, F. Nickel Oxide Hole Injection/Transport Layers for Efficient Solution-Processed Organic Light-Emitting Diodes. *Chemistry of Materials* **2014**, *26* (15), 4528–4534.

(61) Zhang, B.; Su, J.; Guo, X.; Zhou, L.; Lin, Z.; Feng, L.; Zhang, J.; Chang, J.; Hao, Y. NiO/Perovskite Heterojunction Contact Engineering for Highly Efficient and Stable Perovskite Solar Cells. *Advanced Science* **2020**, *7* (11), 1903044.

(62) Pant, N.; Yanagida, M.; Shirai, Y.; Miyano, K. Effect of Different Surface Treatments of Sputtered NiO X on the Photovoltaic Parameters of Perovskite Solar Cells: A Correlation Study. *Applied Physics Express* **2020**, *13* (2), 025505.

(63) Jiang, S.; Wu, Y.; Fang, D.-f.; Chen, Y. Hypothermic Preconditioning but Not Ketamine Reduces Oxygen and Glucose Deprivation Induced Neuronal Injury Correlated with Downregulation of COX-2 Expression in Mouse Hippocampal Slices. *Journal of Pharmacological Sciences* **2018**, *137* (1), 30–37.

(64) Kwan, Y. C. G.; Ng, G. M.; Huan, C. H. A. Identification of Functional Groups and Determination of Carboxyl Formation Temperature in Graphene Oxide Using the XPS O 1s Spectrum. *Thin Solid Films* **2015**, *590*, 40–48.

(65) Chen, H.; Ye, F.; Tang, W.; He, J.; Yin, M.; Wang, Y.; Xie, F.; Bi, E.; Yang, X.; Grätzel, M. A Solvent- and Vacuum-Free Route to large-Area Perovskite Films for Efficient Solar Modules. *Nature* **2017**, *550* (7674), 92–95.

(66) Lee, H.; Huang, Y.-T.; Horn, M. W.; Feng, S.-P. Engineered Optical and Electrical Performance of rf–sputtered Undoped Nickel Oxide Thin Films for Inverted Perovskite Solar Cells. *Scientific Reports* **2018**, *8* (1), 1–10.

(67) Pant, N.; Kulkarni, A.; Yanagida, M.; Shirai, Y.; Miyasaka, T.; Miyano, K. Investigating the Growth of CH3NH3PbI3 Thin Films on RF-Sputtered NiOx for Inverted Planar Perovskite Solar Cells: Effect of CH3NH3+ Halide Additives versus CH3NH3+ Halide Vapor Annealing. *Advanced Materials Interfaces* **2020**, *7* (3), 1901748.

(68) Wu, S.; Li, Z.; Zhang, J.; Liu, T.; Zhu, Z.; Jen, A. K.-Y. Efficient Large Guanidinium Mixed Perovskite Solar Cells with Enhanced Photovoltage and Low Energy Losses. *Chemical Communications* **2019**, *55* (30), 4315–4318.

(69) Li, Z.; Wu, S.; Zhang, J.; Yuan, Y.; Wang, Z.; Zhu, Z. Improving Photovoltaic Performance Using Perovskite/Surface-Modified Graphitic Carbon Nitride Heterojunction. *Solar RRL* **2020**, *4* (3), 1900413.

Chapter 9: Conclusion and Future Work

9.1 Conclusion

This thesis focuses on the further development of two main classes of SCs: OPVs and PSCs. In OPVs, new organic cathode interface materials were investigated to be used for blocking the holes and transferring electrons, while PSCs demonstrated SAM as passivation interface layer. All the interfaces' materials were studied with different techniques to reveal their chemical and electronic properties, and the results were used to describe the most feasible mechanism of CT.

In Chapter 4, a new organic cathode interface, P(NDI3N-T-Br), was examined in contact with well-known active layers (TQ1 and N2200). Core electron spectroscopies showed C1s, N1s (N=C) and S 2p species energetically biased at the interface and shifted to the lower binding energy as a result of the dipole formation. The strength of the dipole formation and its electrical field distribution were further investigated by analysing the valence electron spectra and employing a decomposition algorithm. As a result, the spectra of TQ1 experienced a significant shift in the binding energy, while those of N2200 experienced only a minor shift. A full diagram of the electronic states at the P(NDI3N-T-Br)/active layer interfaces has been demonstrated and the mechanism of CT has been discussed. Alignment of energy levels between TQ1, N2200 and P(NDI3N-T-Br) is favourable and puts forward P(NDI3N-T-Br) as an effective hole-blocking material that simultaneously allows the electron transfer to the interface layer when TQ1: N2200 is applied in the active layer.

In Chapter 5, another new CIL, P(NDI3N-F8-Br), was investigated with PTB-Th: ITIC. The results showed two dipoles formed at the interfaces of active layers/P(NDI3N-F8-Br)

and across the layer thickness of the active materials. Inverted OPV using P(NDI3N-F8-Br) as a CIL demonstrated a PCE of 3.2% compared to 6.8% for conventional devices. The energy levels of the active layer PTB7-Th and ITIC with P(NDI3N-F8-Br) were determined by UPS and IPES, and it was demonstrated that P(NDI3N-F8-Br) functioned as a hole-blocking layer due to its high HOMO level. Further, P(NDI3N-F8-Br) has a high LUMO level, which blocks electrons transferring from ITIC to P(NDI3N-F8-Br). This could be a possible reason for the lower PCE. Thus, the energy level alignment at PTB7-Th/ITIC with a common inorganic interface layer (ZnO) was investigated in Chapter 6.

In Chapter 6, an additional investigation was undertaken to understand the electronic structures of PTB7-Th and ITIC with an inorganic cathode interface (ZnO). The results showed that the valance electron spectra of PTB7-Th shifted in the energy scale due to the formation of a dipole at the PTB7-Th/ZnO interface. Conversely, the components of ITIC did not show any shift in the valance electron spectra. Further, the results showed that two dipoles formed at the PTB7-Th/ZnO interface. The first dipole was formed at the PTB7-Th/ZnO interface with thin layers, while a dipole with opposite polarity was formed within thicker PTB7-Th layers further away from the interface. The energy level alignment meets the expectation of using ZnO as an interface layer in blocking the hole and transferring the electrons at the same time from ITIC, which is favourable.

In Chapter 7, the influence of AA as an additive on the composition distribution of PTB7-Th: ITIC was investigated by measuring the concentration depth profile of sulphur. The results showed overall enrichment of ITIC at the top layer of the BHJ, followed by the PTB7-Th layer, revealing an enriched layer of PTB7-Th at the substrate/BHJ interface. The difference in the ratio of the PTB7-Th at the surface and the subsurface region is related to the difference of the surface energy of PTB7-Th and ITIC. The AA additive increased the concentration of the PTB7-Th at the surface and decreased that of ITIC.

The enhancement of PTB7-Th at the surface region is beneficial for the charge transferring to the MoO_x electrode in the inverted OPV.

In Chapter 8, the SAM layer MeO-2PACz was used as a modification of sp-NiOx/perovskite interface, which can improve the crystallinity of perovskites and decrease defects by passivating NiO_x. The MeO-2PACz on NiO_x interface significantly improves the defect level and device performance. This improvement in performance can be attributed to a reduction in charge recombination, increase in extraction efficiency and enhancement of the perovskite film quality with its large domain size. The electronic structures of NiO_x with and without a MeO-2PACz interlayer were investigated, and the interlayer help in facilitating the CT between perovskites and NiO_x was detailed.

9.2 Outlook and Future Work

With the increasing effects of global warming and rising energy demands, the development and placement of renewable energy capturing devices is an urgent issue of great importance. Presently, almost 94% of all commercially available SCs are based on silicon. These commercial devices have only about 2% lower efficiency than novel devices only realised in laboratory conditions. Still, only about 1% of total global energy consumption comes from solar energy (2020 data). Assuming continuous development and remarkable potential for commercialisation, the third generation of PVs, exemplified by OPVs and PSCs, might be the technology breakthrough needed. Both device types possess a myriad of competitive advantages over presently available technologies, including lightweight, processing versatility, possible low production cost, possible large-area fabrication, positive environmental impact and compatibility with flexible and lightweight substrates. Extensive research in the last decade has significantly improved the device efficiencies of both technologies and enabled their fast development and market readiness. Nevertheless, fundamental environmental and economic issues remain to be resolved to enable effective commercialisation.

The results of OPVs in this thesis show that a dipole forms at the organic CIL P(NDI3N-T-Br) and conjugate polymer interface, forming an energy level arrangement that is energetically favourable for charge extraction/injection with the mechanism fully described. Still, the performance of a real-world device possessing this new organic CIL has yet to be tested. The optimal structure would consist of Ag/MoO3/TQ1: N2200 BHJ/P(NDI3N-T-Br)/ITO. Device performance will be measured and compared using the energy level diagram.

The energy level arrangement of the other organic CIL P(NDI3N-F8-Br) with PTB7-Th and ITIC within an inverted structure was also investigated within the thesis, indicating a mismatch in the energy levels between ITIC and P(NDI3N-F8-Br). Using a conventional configuration as a part of further work could reveal possible reasons for the decrease in device performance. Future work should measure the electronic properties of the interface of P(NDI3N-F8-Br) on top of active layers under the conditions as generated in the inverted device.

Our work in this thesis covered active layer/new organic cathode interface as part of the cell. However, the interfaces formed between distinct layers (BHJ/organic cathode interface and dipoles formed at these contacts) have not been fully studied. Analysing the role of these interfaces, which play a part in the CT of device PCE, is of considerable interest and further investigation should be undertaken.

Lastly, regarding PSC, this thesis mainly dealt with characterising the interface between the HTL and perovskite and trying to reduce the effect of defects at the interface in perovskite film. Future studies should not concentrate only on the improvement of efficiency but also on enhancing the perovskite film and dealing with remaining issues, such as ion migration in PSCs. Two questions for future research are 1) How does ion migration affect PSC efficiency, or to what extent? and 2) Are the ions accumulating at the interface, or can they permeate the adjacent ETL or HTL? Resolution of the mentioned

issues and improvement of materials' intrinsic stability resulting from ion migration prevention may play a crucial role in enhancing the long-term stability of PSCs.

Appendices

Appendix A: Supporting Information for Chapter 4

1. Synthesis of P(NDI3N-T-Br)

diBrDANDI[1] (0.6 g, 1.0096 mmol), 2,5-Thiophenediylbisboronic acid (0.1561 g, 0.9086 mmol, Eq. 0.9), tris(dibenzylideneacetone)dipalladium(0) (0.0185 g, 0.0202 mmol) and tri(*o*-tolyl)phosphine (0.0246 g, 0.0808 mmol) were added to a RBF. The flask was consequently flushed with nitrogen five times. Toluene (40 mL), water (2.02 mL) and Aliquat 336 (six drops) were added to the flask by syringe through a septum. The reaction vessel was lowered in to a 90 °C preheated oil bath and reacted for 48 hours under vigorous stirring. The polymer was endcapped, first with monoBrDANDI and then with phenylboronic acid pinacol ester (40 mg).

The reaction mixture was allowed to cool to room temperature and then poured on 150 mL of hexane. The resulting precipitate, a fine dark-orange powder, was filtered and collected. Soxhlet extraction was performed for 24 hours for each of the solvents: hexane, acetone, ethyl acetate and chloroform. The chloroform fraction was poured on hexane and the precipitated product was collected using a polymer filtration set-up with a PTFE membrane yielding a black product. Yield: 182 mg (53%).

^{1}H NMR (CDCl3, 600 MHz) δ: 8.96 (m, 1H), 7.45 (m, 1H), 4.22 (m, 4H), 2.43 (m, 4H), 2.23 (m, 12H), 1.92 (m, 4H), 1.25 (s, 2H), 0.86 (m, 2H). IR: ν_{max} = 2966sh, 2935, 2858, 2813, 2762, 2719sh, 1702, 1655, 1568, 1526, 1512sh.

2. NICISS result of N2200

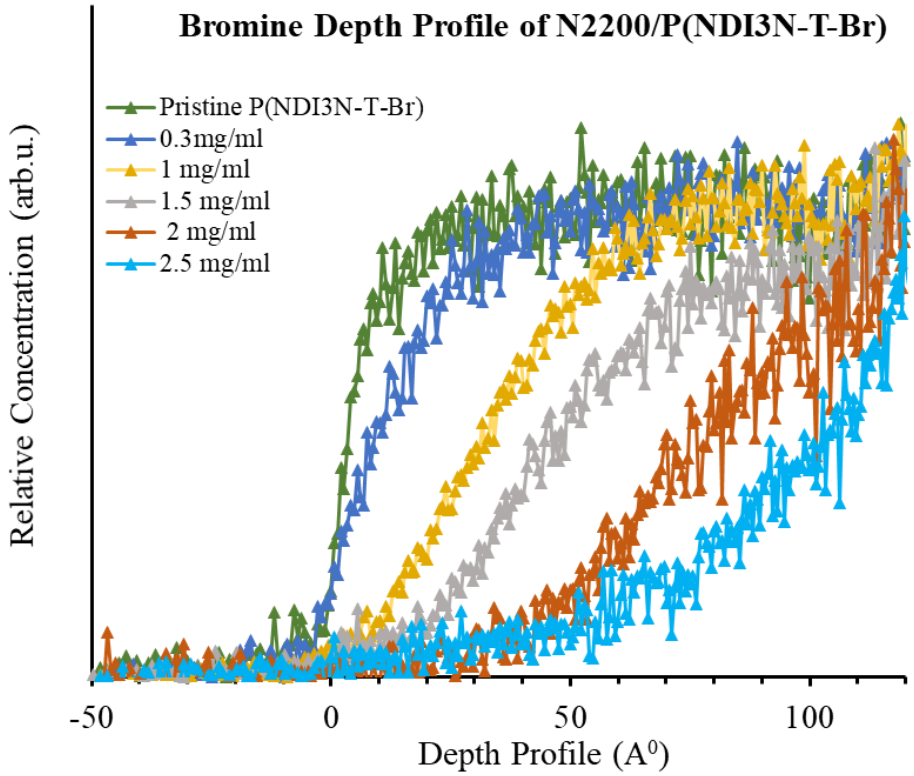

Figure S4-1. The distribution of Br in the N2200/P(NDI3N-T-BR) interface layer, with the zero mark indicating the very surface of the samples.

3. XPS result of O 1s

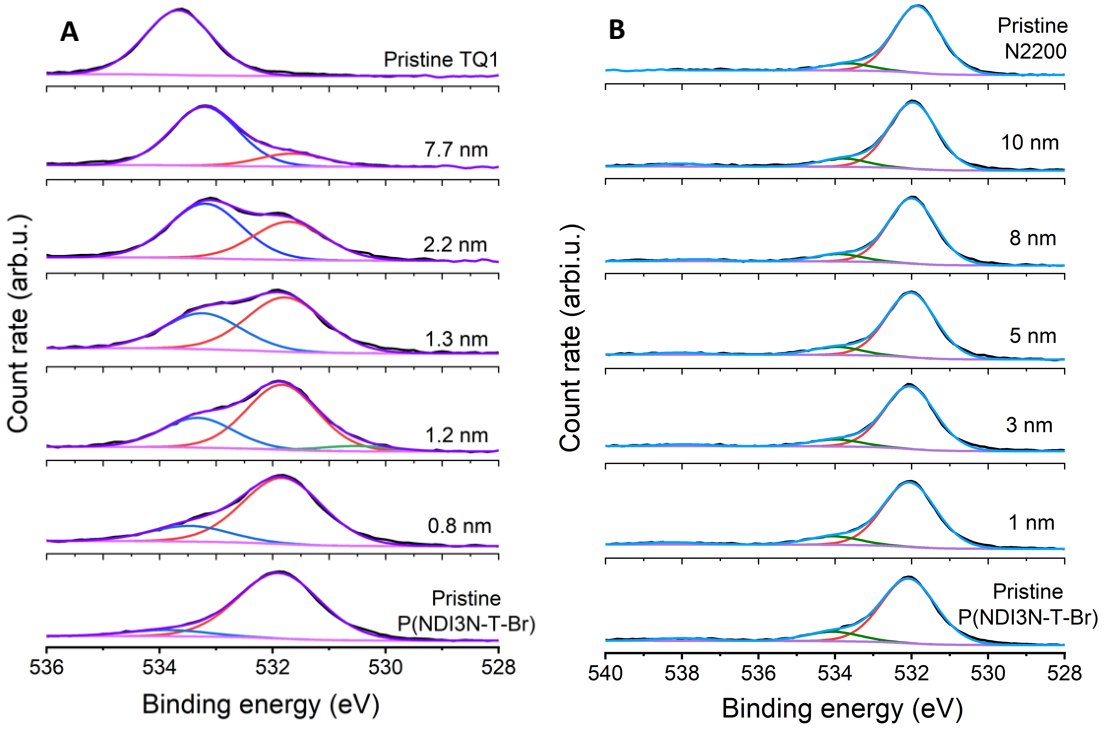

Figure S4-2. (A) High-resolution XP spectra of O 1s for different thickness of TQ1 on P(NDI3N-T-Br). (B) High-resolution XP spectra of O 1s for different thickness of N2200 on P(NDI3N-T-Br).

4. XPS result of N1s

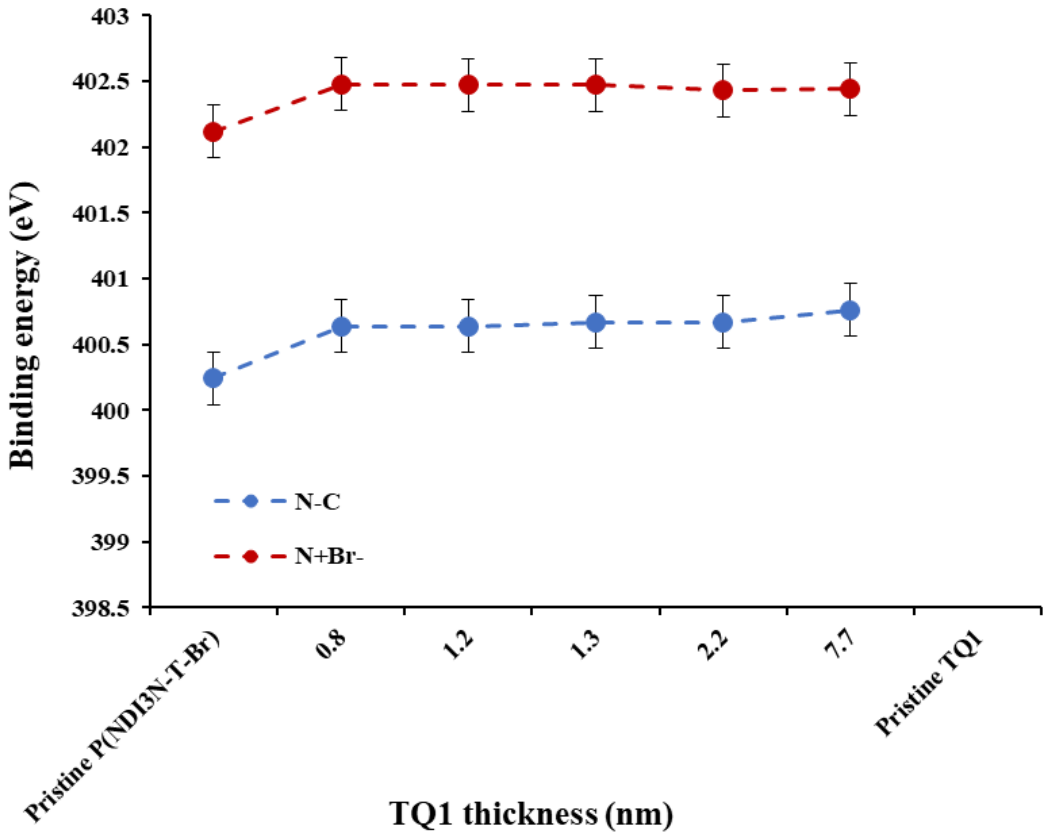

Figure S4-3. Position of N-C and $N^{+}Br^{-}$ for TQ1 deposited onto P(NDI3N-T-Br). The position of the N species of TQ1 is constant for all TQ1 thicknesses.

5. Table of the peak positions for TQ1

Table S4-1

The Peak Positions (eV) with Uncertainties of ± 0.2 or ± 0.3 for the TQ1 with Different Thicknesses

Elements	Pristine P (NDI3N-T-Br) Posi	0.8 nm Posi	1.2 nm Posi	1.3 nm Posi	2.2 nm Posi	7.7 nm Posi	Pristine TQ1 Posi
C-C	285.4	285.1	285.1	285.0	284.9	284.8	285.2
C-O	286.4	286.2	286.1	286.1	286.1	285.5	285.7
C=O	-	286.5	286.7	286.3	286.6	286.5	286.9
C-O-C	288.7	288.6	288.5	288.6	288.6	288.5	-
O-C	531.9	533.5	533.3	533.2	533.2	533.2	533.7
O2	533.9	531.8	531.8	531.8	531.7	531.6	-
O=O	338.1	-	530.5	-	-	-	-
N=C	-	399.1	399.8	399.2	399.5	399.1	399.6
N-C	400.6	400.6	400.6	400.7	400.7	400.8	-
N+Br-	402.5	402.5	402.5	402.5	402.4	402.4	-
S $2p_{3/2}$	164.2	164.9	164.1	164.1	163.9	163.9	164.3
S $2p_{1/2}$	165.4	165.4	165.3	165.3	165.2	165.1	165.7
Br $3d_{5/2}$	67.6	67.5	67.6	67.6	67.6	67.6	-
Br $23d_{3/2}$	68.7	68.5	68.7	68.7	68.7	68.7	-

6. Table of the N peak area for TQ1

Table S4-2

The Ratio of N Peaks for the TQ1 with Different Thicknesses

	TQ1 samples					
Relative concentration %	P(NDI3N-T-Br)	0.8 nm	1.2 nm	1.3 nm	2.2 nm	7.7 nm
C-N	5.5	3.9	3.7	3.1	2.0	1.0
N^+Br^-	5.1	3.5	3.2	2.9	1.9	0.8
Ratio	1.1	1.1	1.1	1.1	1.1	1.2

Note. The ratio of N peaks is not exactly 1:1 due to uncertainty within the fitting models.

7. Table of the peak positions for N2200

Table S4-3

The Peak Positions (eV) with Uncertainty of ± 0.2 or ± 0.3 for the N2200 with Different Thicknesses

Elements	Pristine P(NDI3N-T-Br) Posi	1.0 nm Posi	3.0 nm Posi	5.0 nm Posi	8.0 nm Posi	10 nm Posi	Pristine N2200 Posi
C-C	285.5	285.4	285.3	285.3	285.2	285.2	285.1
C-O	286.6	286.6	286.6	286.5	286.5	286.4	286.2
C=O	288.8	288.8	288.8	288.8	288.7	288.7	288.6
O-C	532.1	532.1	532.0	532.0	531.9	531.9	531.8
O=C	534.1	534.0	537.9	533.9	533.9	533.8	533.7
O3	537.9	538.3	533.9	538.0	537.6	538.0	-
N-C	400.8	400.8	400.9	400.8	400.8	400.8	400.7
N-O	402.8	402.7	402.7	402.8	402.8	402.8	402.5
S $2p_{3/2}$	164.5	164.5	164.5	164.4	164.4	164.4	164.3
S $2p_{1/2}$	165.6	165.7	165.6	165.6	165.6	165.6	165.5
Br $3d_{5/2}$	67.9	67.9	67.9	67.9	67.9	67.8	-
Br $3d_{3/2}$	68.9	68.9	68.9	68.9	68.9	68.9	-

8. *Analysis of MIE, UP and IPE spectra for TQ1/Pristine P(NDI3N-T-Br) interface*

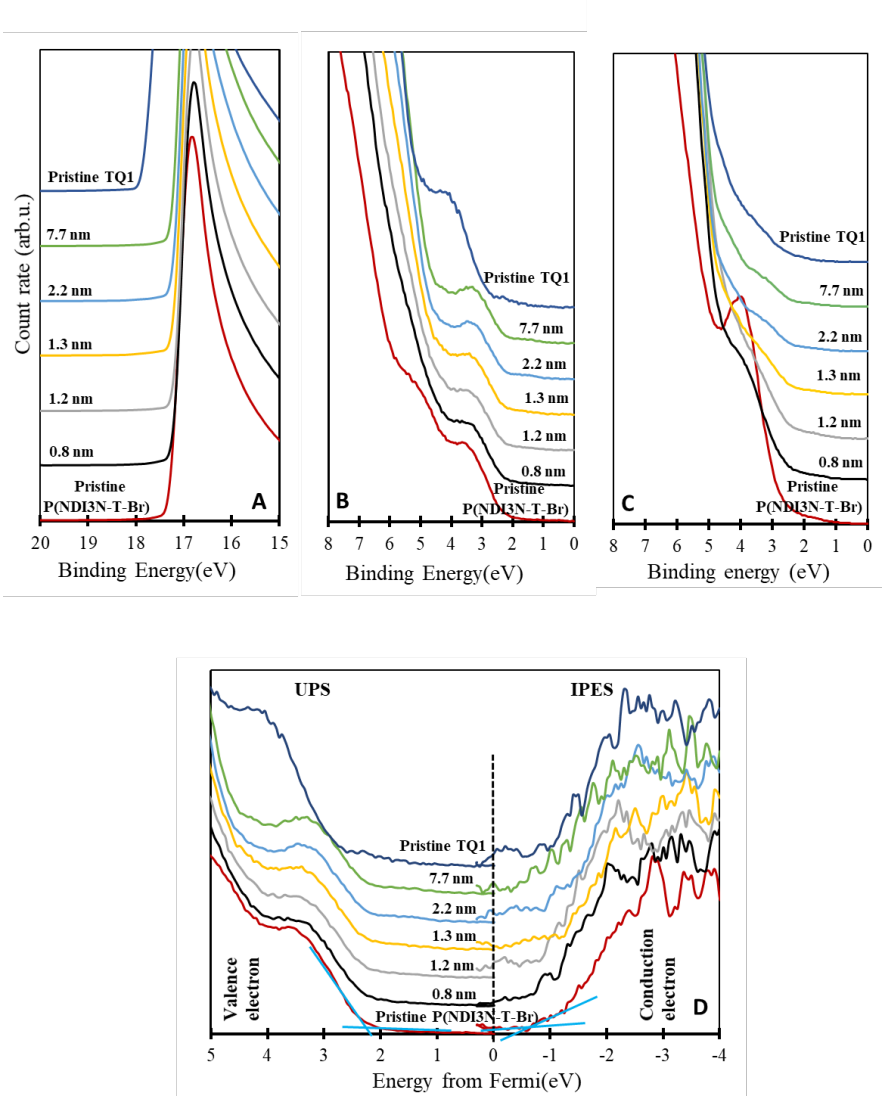

Figure S4-4. (A) SE region, (B) valence electron region of the UP spectra, (C) valence electron region of the MIES spectra of the same samples with a range of TQ1 layer thicknesses and (D) the plot of CB/E_{LUMO} and VB/E_{HOMO} region of the samples as measured via UPS and IPES.

9. *Analysis of MIE, UP and IPE spectra for N2200/Pristine P(NDI3N-T-Br) interface*

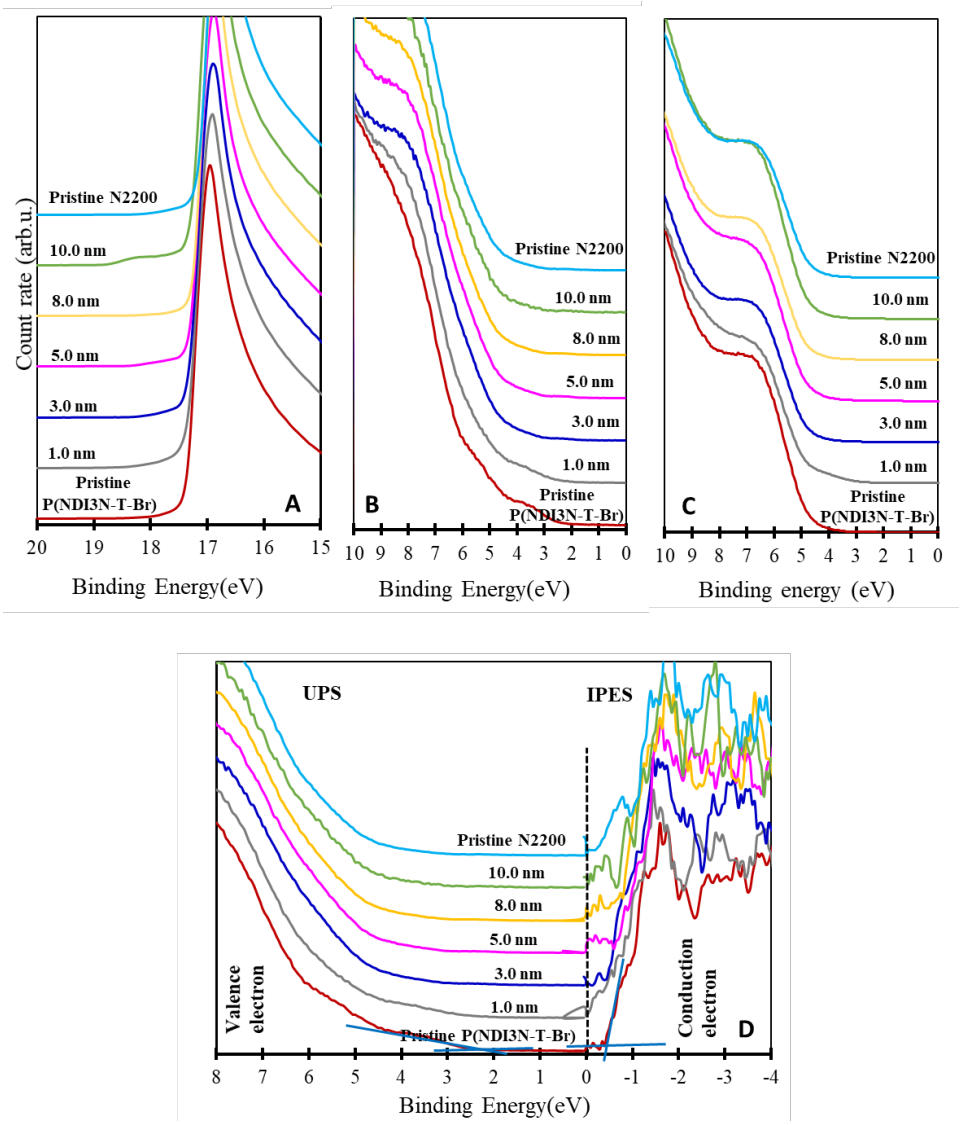

Figure S4-5. (A) SE region, (B) valence electron region of the UP spectra, (C) valence electron region of the MIES spectra of the same samples with a range of N2200 layer thicknesses and (D) the plot of CB/E_{LUMO} and VB/E_{HOMO} region of the samples as measured via UPS and IPES.

10. Full spectra of MIE and UP for TQ1/Pristine P(NDI3N-T-Br) interface

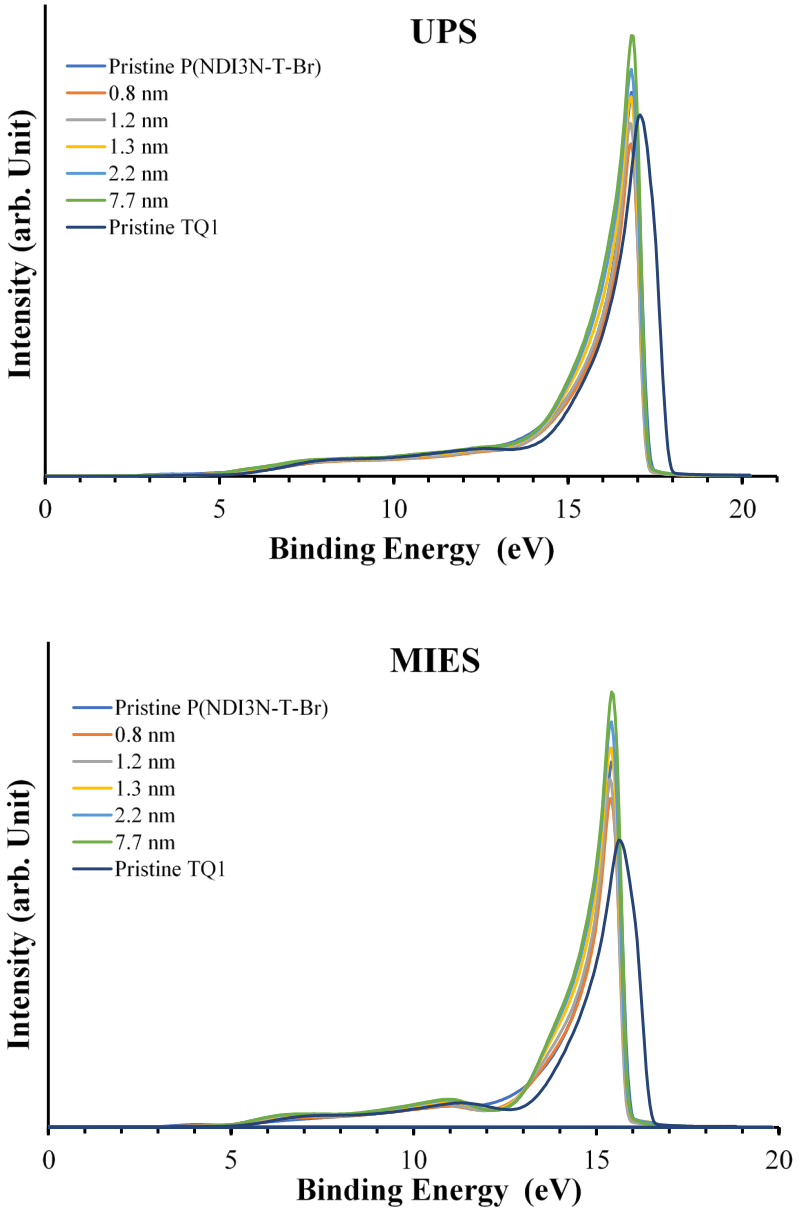

Figure S4-6. The spectra of UPS and MIES, for TQ1/P(NDI3N-T-Br) interface samples.

11. Table of the energy level values of TQ

Table S4-4

The Values of WF, VB/E_{HOMO} and CB/E_{LUMO} of the TQ1/P(NDI3N-T-Br) Samples

Concentration of TQ1 Interface TQ1/P(NDI3N-T-Br)	WF (eV) ± 0.1	VB (eV) ± 0.1	CB (eV) ± 0.1
Pristine TQ1*	3.3	1.4	–0.9
7.7 nm	3.9	2.0	–0.6
2.2 nm	3.9	2.1	–0.8
1.3 nm	3.9	2.0	–0.7
1.2 nm	3.9	2.0	–0.3
0.8 nm	3.9	2.0	–0.3
Pristine P(NDI3N-T-Br)	3.9	2.2	–0.4
ITO	4.3	2.9	–0.4

Note. All energies are indicated with a zero point at E_f. The WF of ITO is somewhat lower than that reported in the literature due to a small degree of hydrocarbon on the surface.

*The WF of TQ1 on ITO was measured twice and is lower than what can be anticipated from [2]. The reason for this discrepancy is unclear.

12. Full spectra of MIE and UP for N2200/Pristine P (NDI3N-T-Br) interface

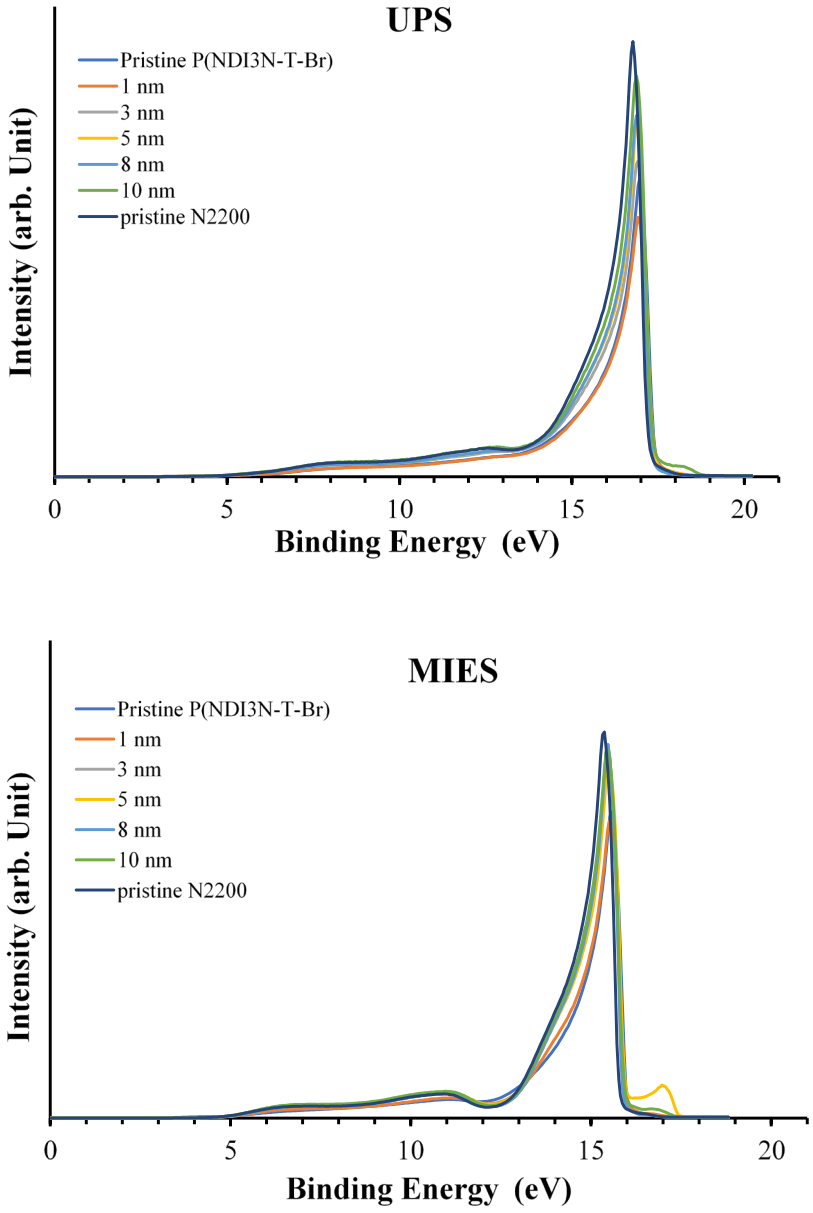

Figure S4-7. The spectra of UPS and MIES for N2200/P(NDI3N-T-Br) interface samples.

13. Table of the energy level values of N2200

Table S4-5

The Values of WF, VB/E_{HOMO} and CB/E_{LUMO} of the N2200/P(NDI3N-T-Br) Samples

Concentration of N2200 Interface N2200/P(NDI3N-T-Br)	WF (eV) ± 0.1	VB (eV) ± 0.1	CB (eV) ± 0.1
Pristine N2200	4.0	1.7	–0.8
10.0 nm	3.9	2.6	–0.6
8.0 nm	3.9	1.5	–0.6
5.0 nm	3.9	1.6	–0.6
3.0 nm	3.8	1.5	–0.3
1.0 nm	3.8	1.4	–0.3
Pristine P(NDI3N-T-Br)	3.9	2.2	–0.4
ITO	4.3	2.9	–0.4

Note. All energies are indicated with a zero point at E_f. The WF of ITO is somewhat lower than that reported in the literature due to a small degree of hydrocarbon on the surface.

14. Component analysis of valence electron spectra of UPS and MIES for TQ1

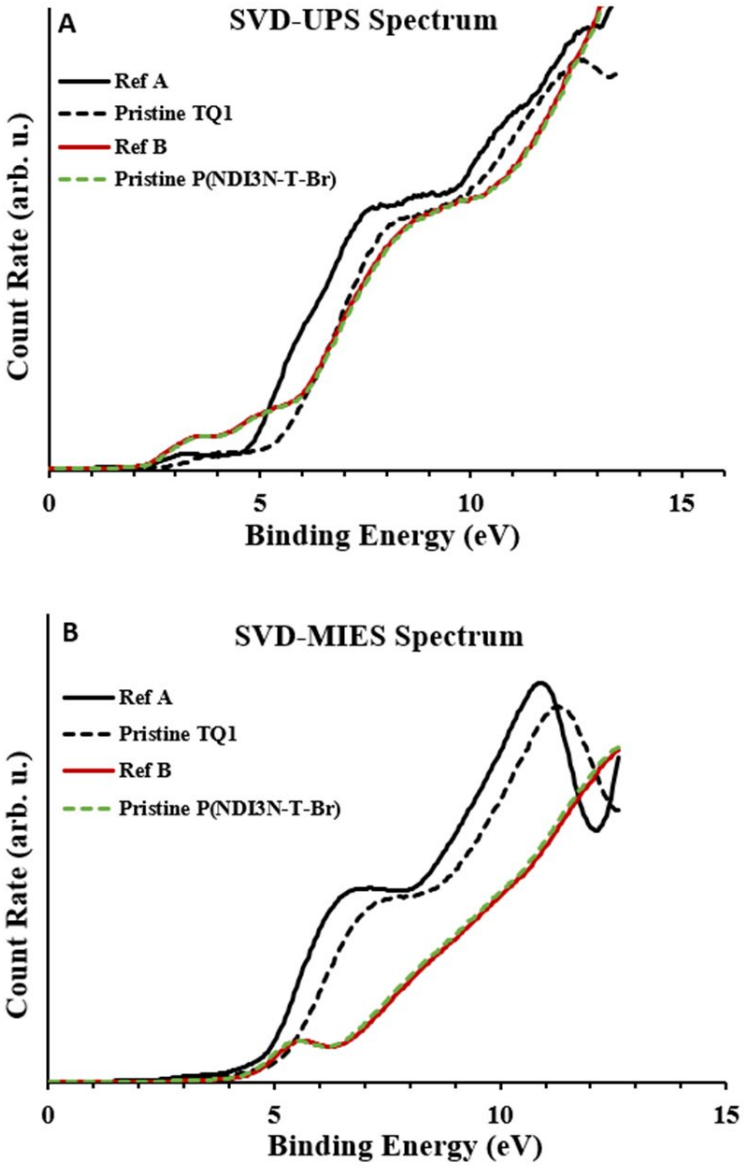

Figure S4-8. (A) and (B) The reference spectra of UPS and MIES. P(NDI3N-T-Br) does not have any shift for the TQ1/P(NDI3N-T-Br) interface.

15. Component analysis of valence electron spectra of UPS and MIES for N2200

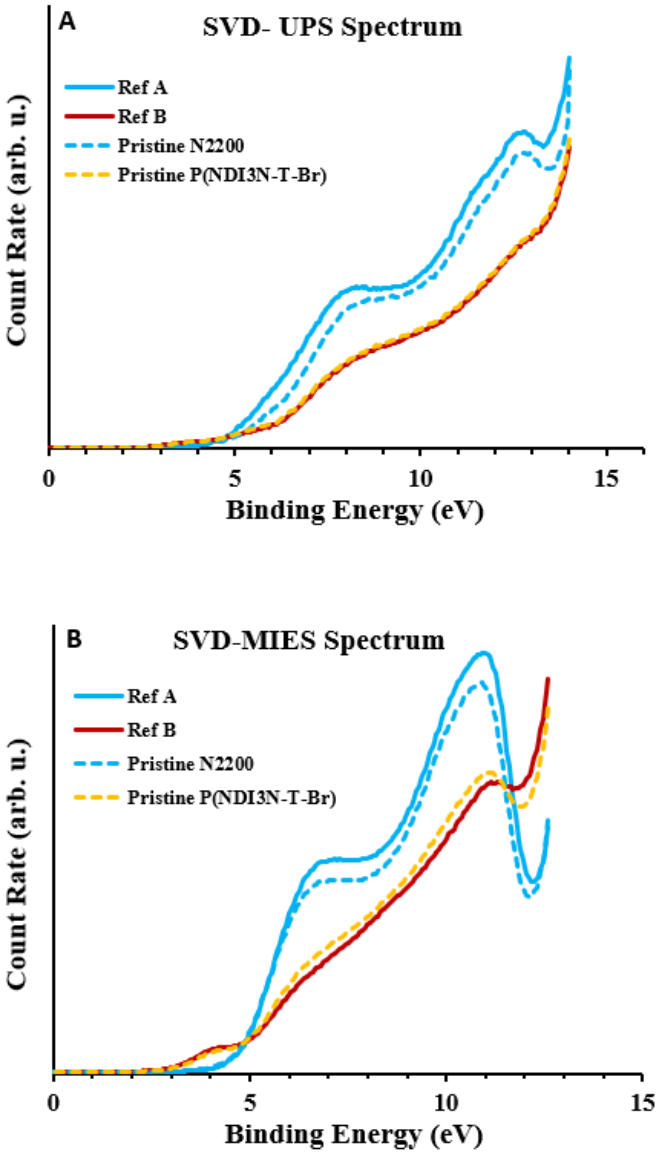

Figure S4-9. (A) and (B) The reference spectra of UPS and MIES. P(NDI3N-T-Br) does not have any shift for the N2200/P(NDI3N-T-Br) interface.

References

(1) Bjuggren, J. M.; Sharma, A.; Gedefaw, D.; Elmas, S.; Pan, C.; Kirk, B.; Zhao, X.; Andersson, G.; Andersson, M. R. Facile Synthesis of an Efficient and Robust Cathode Interface Material for Polymer Solar Cells. *ACS Applied Energy Materials* **2018**, *1*, 7130.

(2) Wang, C.; Moro, F.; Ni, S.; Zhang, G.; Pan, Q.; Yang, J.; Zhang, F.; Buyanova, I. A.; Chen, W. M.; Liu, X.; Fahlman, M. Thermal-Annealing Effects on Energy Level Alignment at Organic Heterojunctions and corresponding Voltage Losses in All-Polymer Solar Cells. *Nano Energy* **2020**, *72*, 104677.

Appendix B: Supporting Information for Chapter 5

Device preparation

The BHJ blend films of the inverted devices (PTB7-Th: ITIC inverted polymer SCs) were fabricated using a non-toxic solvent additive p-anisaldehyde and host solvent o-xylene. Devices were fabricated in a glass/ITO/P(NDI3N-F8-Br)/PTB7-Th: ITIC/MoO_X/Ag inverted device configuration. P(NDI3N-F8-Br) was deposited from MeO solution (1 mg/mL). The active layer ink was prepared by dissolving active layer materials, with a donor:acceptor weight-to-weight ratio of 1:1.3, in o-xylene (total 19.5 mg mL^{-1}). The active layer ink was mixed overnight at 75 °C under vigorous stirring. With the prepared ink, the solution was spun-coated over the P(NDI3N-F8-Br) film at 2,500 rpm for 60 seconds. After the spin coating of the active layer, the devices were vacuum dried in an evaporation chamber at 10^{-7} mbar for 1 hour. After vacuum drying, MoO_X and Ag were deposited via the following method. The MoO_X (12 nm) was thermally deposited on the BHJ layer under high vacuum using a Covap thermal evaporation system (Angstrom Engineering). This was followed by the evaporation of the Ag electrode (80 nm) using a shadow mask to define the active area to 0.1 cm^2.

For conventional devices, a thin layer of PEDOT: PSS was spin-coated onto clean ITO at 5,000 rpm for 45 seconds.

Device performance

Devices were measured using an Oriel Solar simulator fitted with a 150 W Xeon lamp (Newport), filtered to give an output of 100 mW cm^{-2} at AM 1.5 (air mass) standard and calibrated using a silicon reference cell with NIST traceable certification. Device testing was conducted under ambient conditions.

1. XPS results of PTB7-Th/P(NDI3N-F8-Br)

Table S5-1

The Peak Positions (eV) with Uncertainties of ± 0.2 or ± 0.3 for PTB7-Th with Different Thicknesses Deposited on P(NDI3N-F8-Br)

Elements	Pristine P(NDI3N-F8-Br)	0.3 (mg mL^{-1})	0.6 (mg mL^{-1})	1 (mg mL^{-1})	1.5 (mg mL^{-1})	2 (mg mL^{-1})	2.5 (mg mL^{-1})	Pristine PTB7-Th
	Posi	Posi	Posi	Posi	Posi	Posi	Posi	Posi
C-C	285.2	285.2	285.4	285.4	285.4	285.3	285.3	284.9
C-N	285.9	-	-	-	-	-	-	-
C*	286.9	-	-	-	-	-	-	-
C-S	-	286.8	286.9	286.9	287.1	287.1	287.2	287.0
C=O	289.0	289.0	288.9	288.7	289.1	289.2	289.3	289.2
O-C	530.6	-	-	-	-	-	-	-
O-N	532.3	532.3	532.3	532.2	532.3	532.3	532.1	531.9
O=C	534.1	534.5	534.2	534.1	534.0	533.9	533.9	533.7
N-C	400.9	401.0	400.9	400.9	400.8	401.1	400.8	-
N-O	403.0	403.0	402.9	402.9	402.9	403.1	403.1	-
Br $3d_{5/2}$	67.9	67.9	67.9	67.9	67.9	67.9	67.8	-
S $2p_{3/2}$	-	164.6	164.6	164.5	164.5	164.4	164.4	164.1
F	-	688.0	688.1	688.2	688.01	688.1	688.1	687.7

Note. The C* peak of P(NDI3N-F8-Br) is assigning the 10 C atoms between the O=C-N-C=O in NDI as a separate species at 285.9 eV.

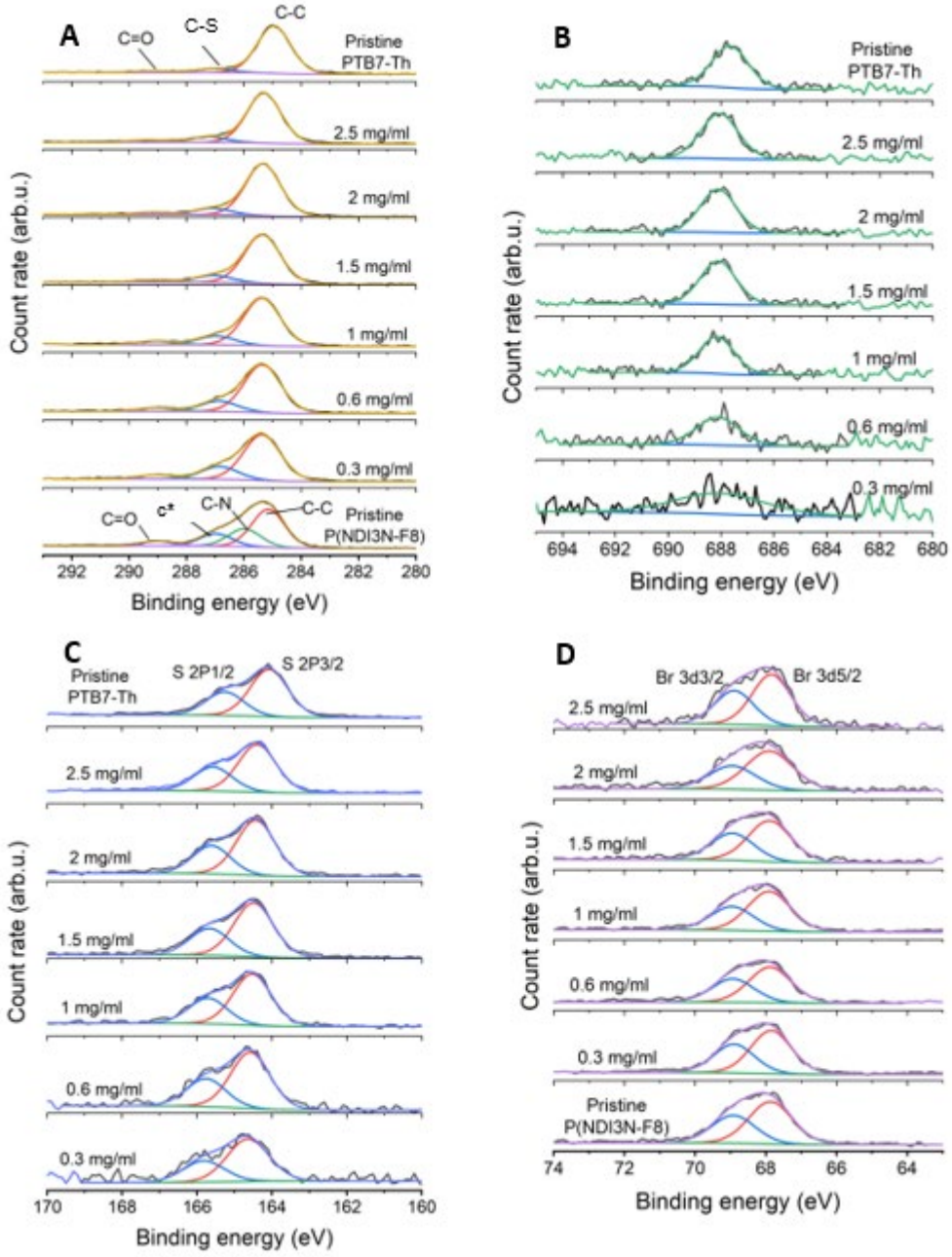

Figure S5-1. High-resolution XPS of (A) C1s, (B) F1s, (C) S 2p and (D) Br 3d for PTB7-Th layers deposited on P(NDI3N-F8-Br).

2. XPS results of ITIC/P(NDI3N-F8-Br)

Table S5-2

The Peak Positions (eV) with Uncertainties of ± 0.2 or ± 0.3 for ITIC with Different Thicknesses Deposited on P(NDI3N-F8-Br)

Elements	Pristine P(NDI3N-F8-Br)	0.05 (mg mL^{-1})	0.1 (mg mL^{-1})	0.2 (mg mL^{-1})	0.3 (mg mL^{-1})	0.6 (mg mL^{-1})	1 (mg mL^{-1})	Pristine ITIC
	Posi	Posi	Posi	Posi	Posi	Posi	Posi	Posi
C-C	285.2	285.1	285.2	285.2	285.2	285.1	284.9	284.8
C*	286.9	-	-	-	-	-	-	-
C-N	285.9	285.9	286.1	286.1	286.1	286.8	286.6	285.7
C-S	-	286.9	286.9	287.1	287.1	288.3	287.9	286.6
C=O	289.0	288.9	288.9	288.9	288.9	290.6	290.9	287.6
O1	530.6	530.7	530.8	530.6		538.5	538.8	531.9
O2	532.3	532.2	532.3	532.2	532.2	532.1	531.8	532.7
O3	534.1	533.5	533.8	533.6	534.4	534.5	534.5	535.0
O4	-	534.9	535.1	534.9	538.3	536.0	535.9	537.6
N=C	-	399.6	399.9	399.6	399.6	399.4	399.2	399.2
N-C	400.9	401.0	401.0	400.9	400.9	400.9	400.8	400.6
N-O	403.0	402.9	403.0	403.0	403.0	402.9	402.8	402.5
Br $3d_{5/2}$	67.9	67.9	67.9	67.9	67.9	67.9	67.8	-
S $2p_{3/2}$	-	164.8	164.6	164.7	164.7	164.5	164.4	164.3

Note. The C* peak of P(NDI3N-F8-Br) is assigning the 10 C atoms between the O=C-N-C=O in NDI as a separate species at 285.9 eV.

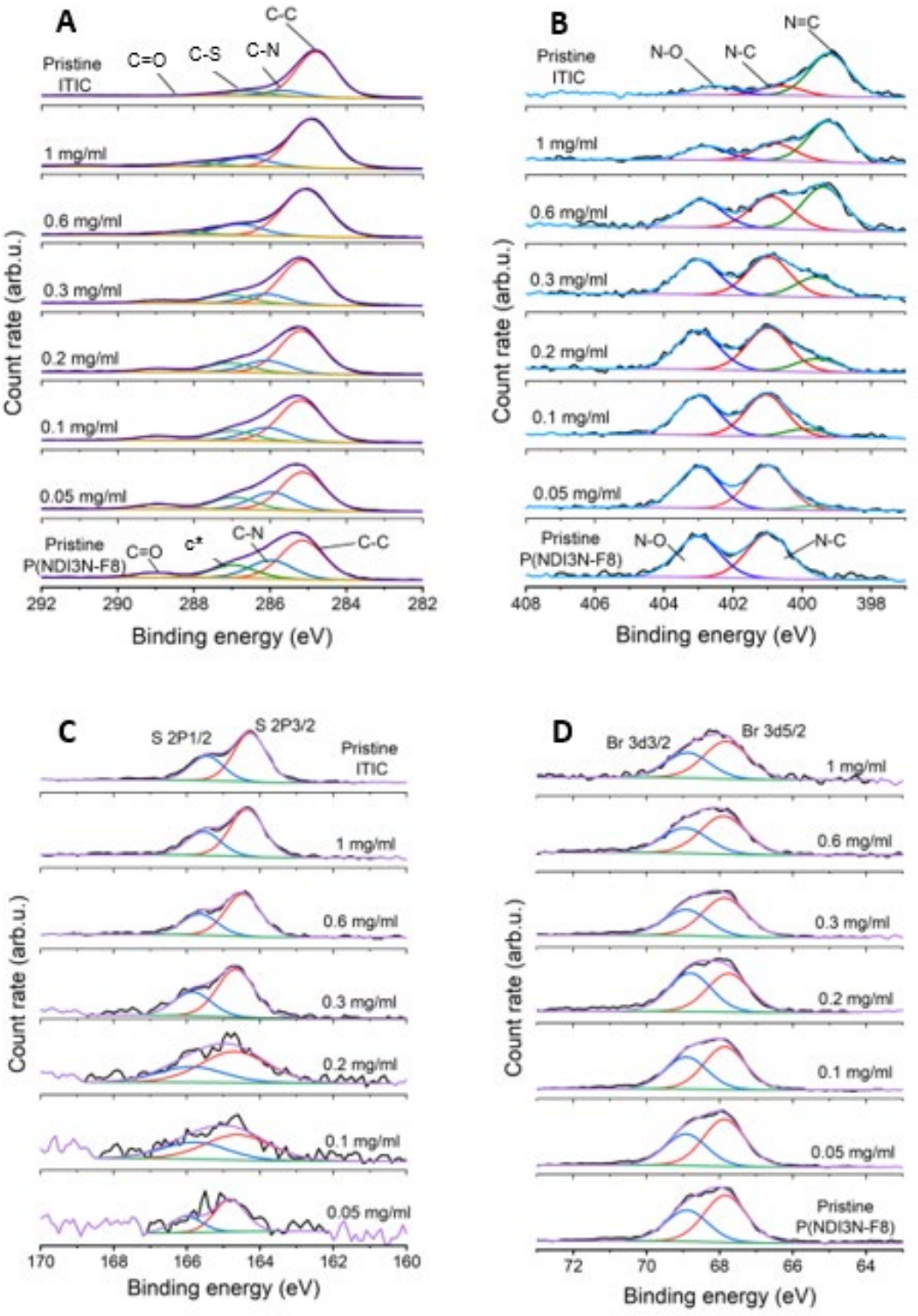

Figure S5-2. High-resolution XPS of (A) C1s, (B) N1s, (C) S 2p and (D) Br 3d for ITIC layers deposited on P(NDI3N-F8-Br).

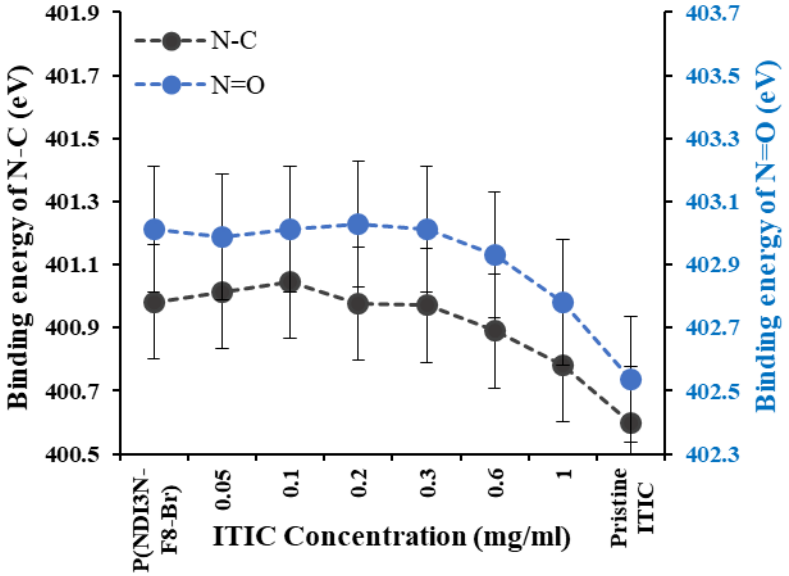

Figure S5-3. The change in the N peak positions, showing a negligible shift towards higher binding energy with decreasing concentration of ITIC.

3. *Analysis of UP and IPE Spectra of PTB7-Th/P(NDI3N-F8-Br) and ITIC/P(NDI3N-F8-Br)*

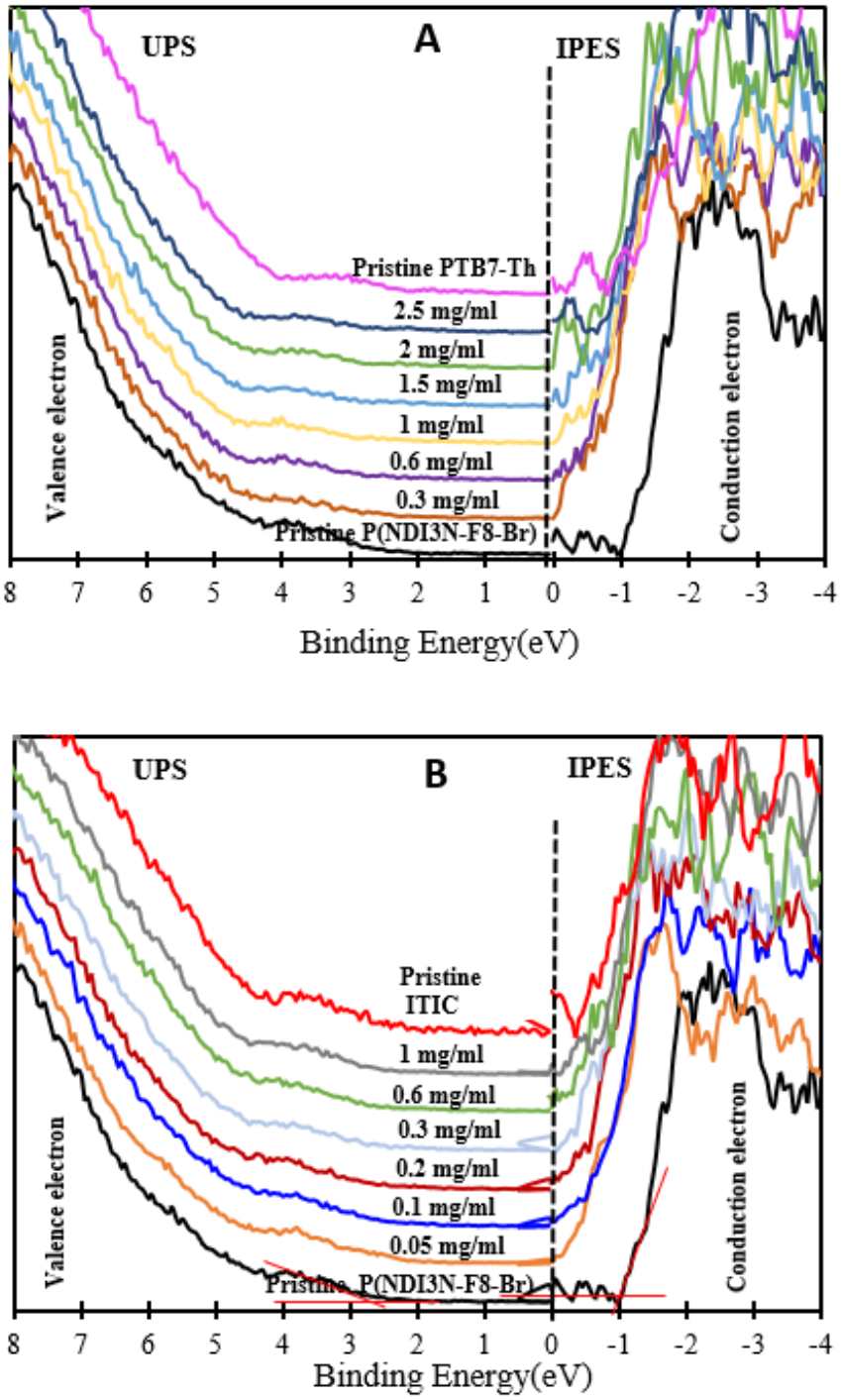

Figure S5-4. (A) The plot of VB/E_{HOMO} and CB/E_{LUMO} of the samples of different PTB7-Th layer thicknesses deposited on P(NDI3N-F8-Br) as measured by UPS and IPES. (B) The plot of VB/E_{HOMO} and CB/E_{LUMO} of the samples of different ITIC layer thicknesses deposited on P(NDI3N-F8-Br) as measured by UPS and IPES.

Table S5-3

The Values of WF, E_{HOMO} - VB and E_{LUMO} - CB of the ITIC/P(NDI3N-F8-Br) Samples

Concentration of ITIC	WF (eV) ± 0.1	VB (eV) ± 0.1	CB (eV) ± 0.1
Pristine ITIC	4.2	1.0	–0.4
1 mg/mL	3.76	1.1	–0.35
0.6 mg/mL	3.7	1.3	–0.5
0.3 mg/mL	4.0	1.7	–0.5
0.2 mg/mL	3.8	1.7	–0.5
0.1 mg/mL	3.7	1.7	–0.6
0.05 mg/mL	3.6	2.0	–0.6
Pristine P(NDI3N-F8-Br)	3.7	2.3	–0.9

Note. All energies are indicated with a zero point at Fermi Level (Ef).

Table S5-4

The Values of WF, E_{HOMO} - VB and E_{LUMO} - CB of the PTB7-Th/P(NDI3N-F8-Br) Samples

Concentration of PTB7-Th	WF (eV) ± 0.1	VB (eV) ± 0.1	CB (eV) ± 0.1
Pristine PTB7-Th	3.7	0.6	–1.0
2.5 mg/mL	3.7	0.9	–0.4
2 mg/mL	3.7	0.9	–0.5
1.5 mg/mL	3.7	0.9	–0.5
1 mg/mL	3.7	1.0	–0.5
0.6 mg/mL	3.7	1.0	–0.6
0.3 mg/mL	3.9	1.3	–0.6
Pristine P(NDI3N-F8-Br)	3.7	2.3	–0.9

Note. All energies are indicated with a zero point at Fermi Level (Ef).

Appendix C: Supporting Information for Chapter 6

1. XPS results of PTB7-Th/ZnO

Table S6-1

The Peak Positions (eV) with Uncertainties of ± 0.2 or ± 0.3 for Pristine ZnO, Pristine PTB7-Th and Different Thicknesses of PTB7-Th Deposited on ZnO

Elements	Pristine ZnO	1 (mg mL^{-1})	2.5 (mg mL^{-1})	4.5 (mg mL^{-1})	Pristine PTB7-Th
	Posi	Posi	Posi	Posi	Posi
C-C	-	285.6	285.4	285.1	284.9
C-S	-	287.7	287.4	287.3	287.0
C=O	-	290.0	289.7	289.3	289.2
O-C	531.1	531.3	531.5	531.6	531.96
O2	532.7	533.0	533.17	533.47	533.7
O=C	-	-	-	-	-
Zn	1,022.6	1,022.7	1,022.7	1,022.4	-
S $2p_{3/2}$	-	164.7	164.5	164.3	164.1
F	-	688.2	688.0	687.8	687.7

2. XPS results of ITIC/ZnO

Table S6-2

The Peak Positions (eV) with Uncertainties of ± 0.2 or ± 0.3 for Pristine ZnO, Pristine ITIC and Different Thicknesses of ITIC Deposited on ZnO

Elements	Pristine ZnO Posi	1 (mg mL^{-1}) Posi	1.3 (mg mL^{-1}) Posi	1.5 (mg mL^{-1}) Posi	Pristine ITIC Posi
C-C	-	284.9	284.8	284.8	284.8
C-N	-	-	-	-	285.7
C-S	-	286.6	286.5	286.5	286.6
C=O	-	-	-	-	287.6
O-C	531.2	531.3	531.4	531.3	531.9
O2	532.8	532.9	533.1	533.0	532.7
O3	-	-	-	-	535.0
O4	-	-	-	-	537.6
N=C	-	399.3	399.1	399.2	399.2
N-C					400.6
N-O	-	-	-	-	402.5
Zn	1,022.6	1,022.6	1,022.9	1,023.1	-
S $2p_{3/2}$	-	164.3	164.3	164.3	164.3

3. *Analysis of UP and IPE spectra of PTB7-Th/ZnO and ITIC/ZnO interfaces*

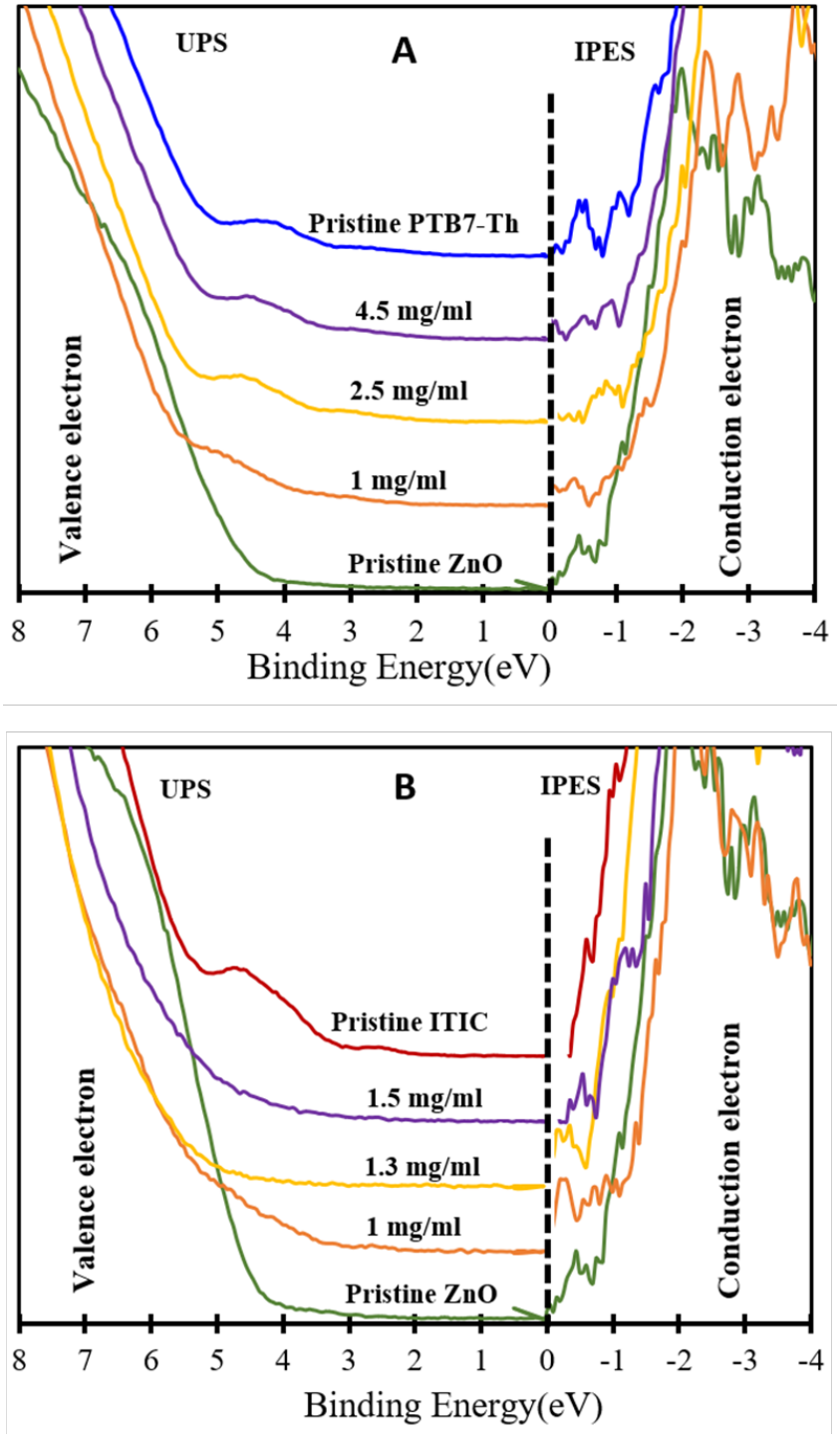

Figure S6-1. Plot of VB/E_{HOMO} and CB/E_{LUMO} (from UPS and IPES) of (A) PTB7-Th layers deposited on ZnO and (B) ITIC layers deposited on ZnO.

Table S6-3

The Values of WF, VB/E_{HOMO} and CB/E_{LUMO} of the PTB7-Th/ZnO Samples, Pristine ZnO and Pristine PTB7-Th

PTB7-Th concentrations mg/ml	WF (eV) ± 0.1	VB (eV) ± 0.1	CB (eV) ± 0.1
4.5	3.9	0.6	–1.0
2.5	3.7	0.7	–1.0
1	3.4	1.05	–0.5
Pristine PTB7-Th	3.7	0.6	–1.0
Pristine ZnO	3.8	3.1	–0.4

Note. All energies are indicated with a zero point at Fermi Level (E_f).

Table S6-4

The Values of WF, VB/E_{HOMO} and CB/E_{LUMO} of the ITIC/ZnO Samples, Pristine ZnO and Pristine ITIC

ITIC concentrations mg/ml	WF (eV) ± 0.1	VB (eV) ± 0.1	CB (eV) ± 0.1
1.5	4.0	1.2	–0.6
1.3	3.9	1.9	–0.5
1	3.8	1.2	–0.9
Pristine ITIC	4.2	1.0	–0.4
Pristine ZnO	3.8	3.1	–0.4

Note. All energies are indicated with a zero point at Fermi Level (E_f).

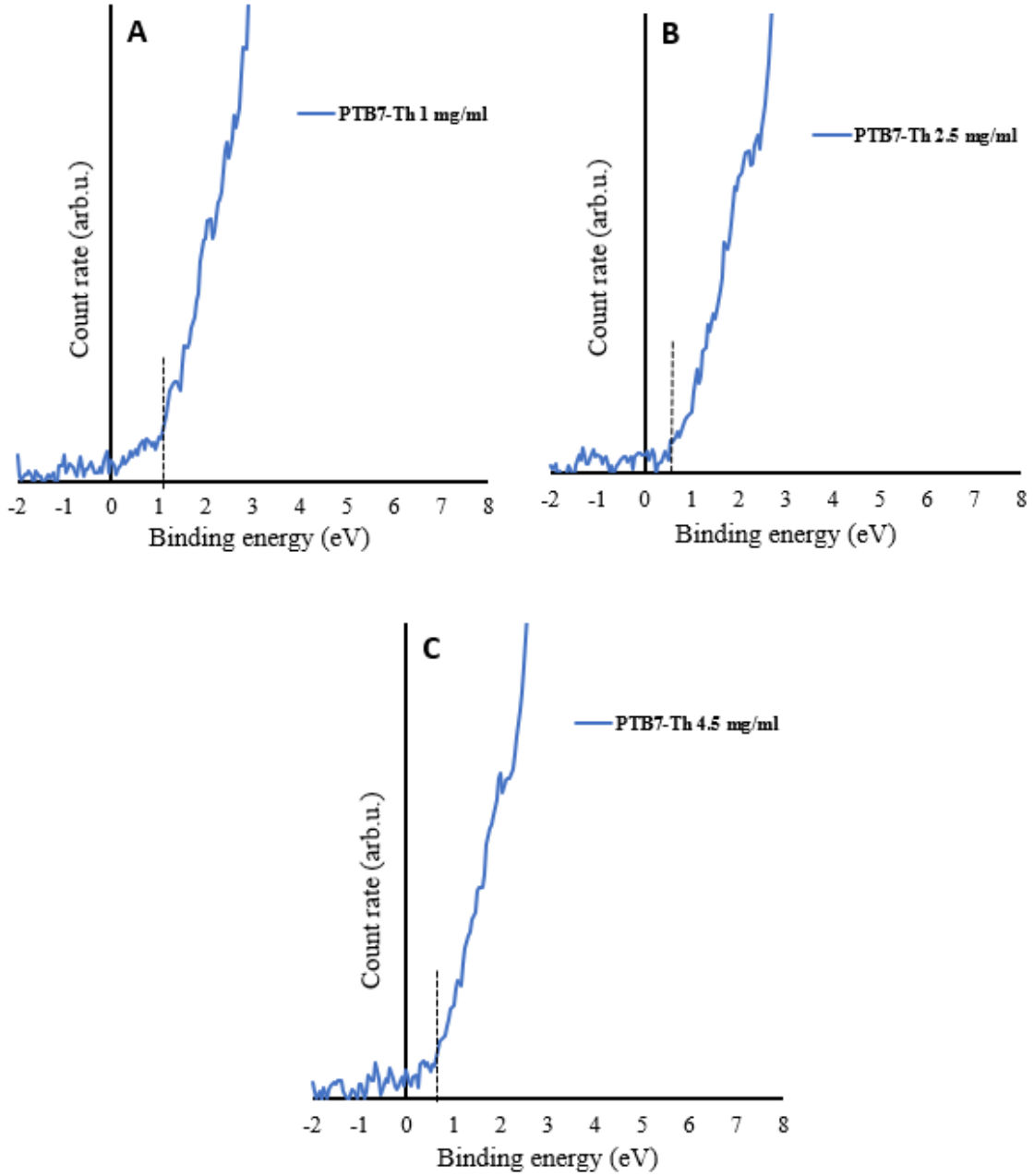

Figure S6-2. Plot of the cut-off for VB region as measured via UPS of (A) 1 mg/mL of PTB7-Th/ZnO, (B) 2.5 mg/mL of PTB7-Th/ZnO and (C) 4.5 mg/mL of PTB7-Th/ZnO.

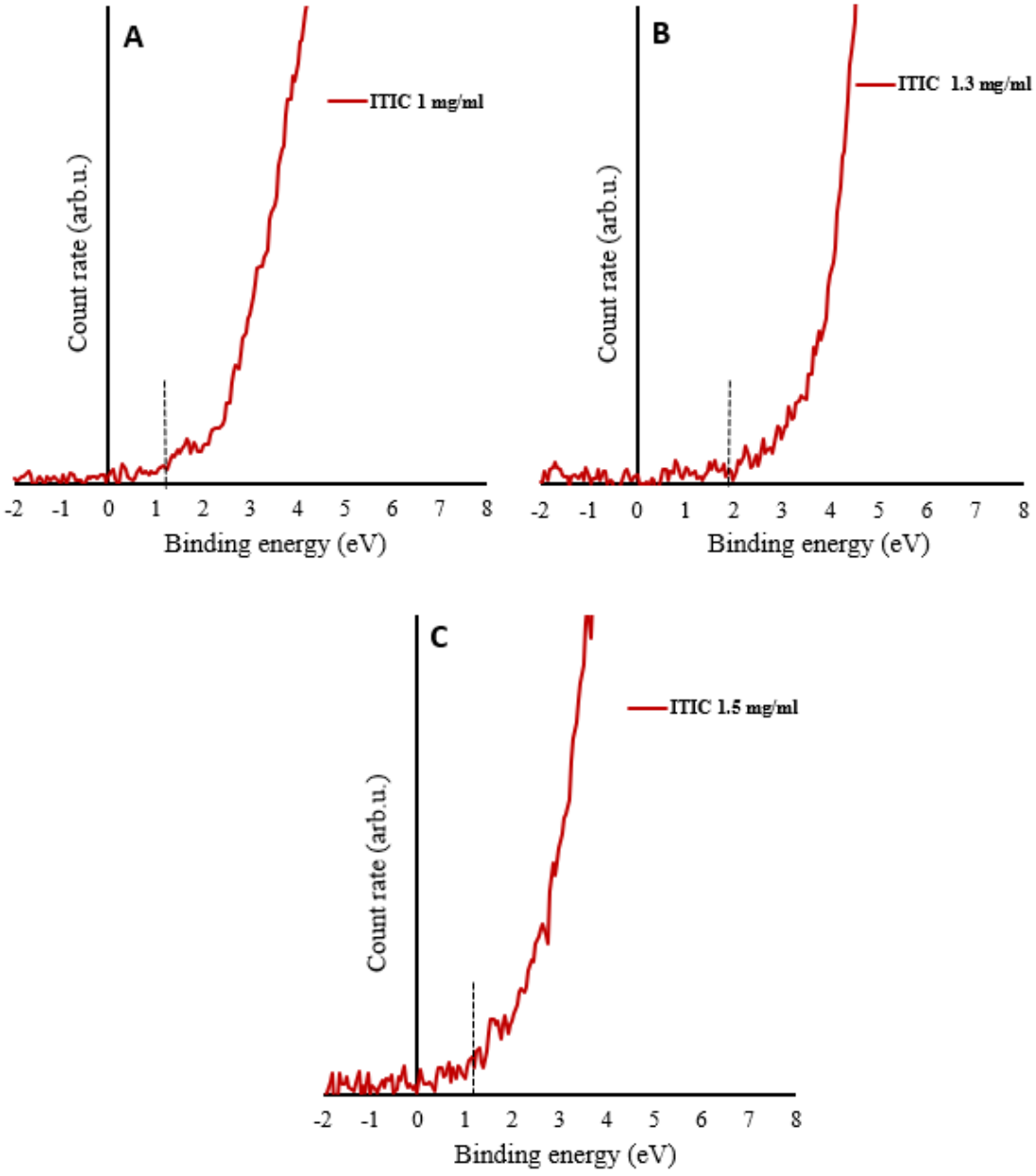

Figure S6-3. Plot of the cut-off for VB region as measured via UPS of (A) 1 mg/mL of ITIC/ZnO, (B) 1.3 mg/mL of ITIC/ZnO and (C) 1.5 mg/mL of ITIC/ZnO.

Appendix D: Supporting Information for Chapter 8

1. Results and discussion

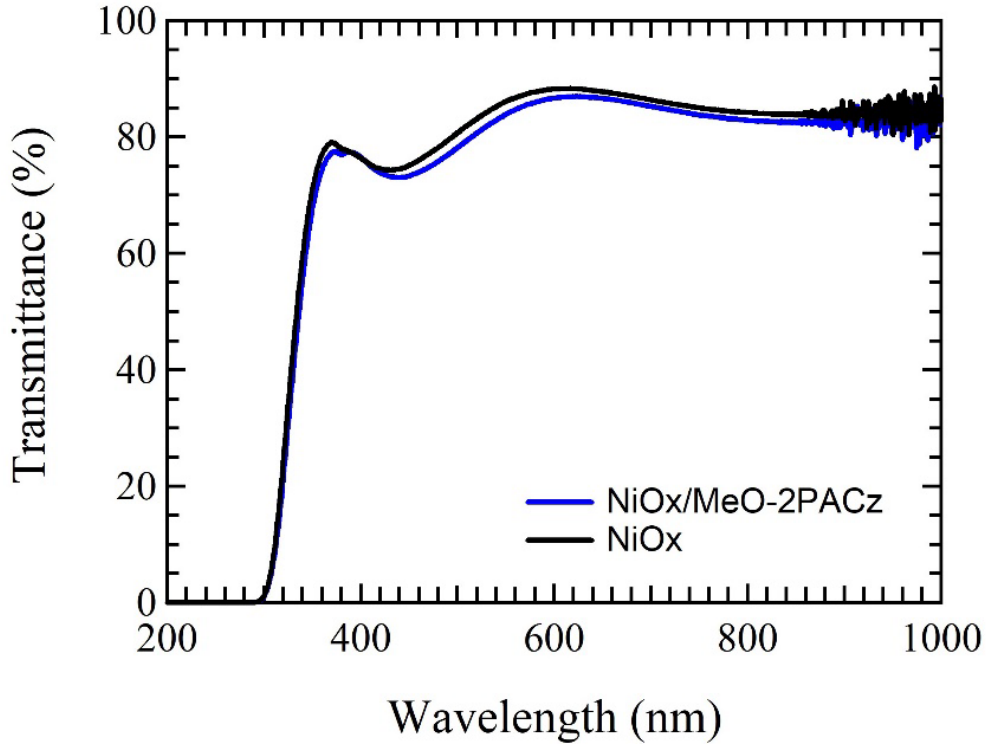

Figure S8-1. The transmittance of NiOx and NiOx/MeO-2PACz SAM.

2. *Data analysis for the XPS spectra obtained for NiOx*

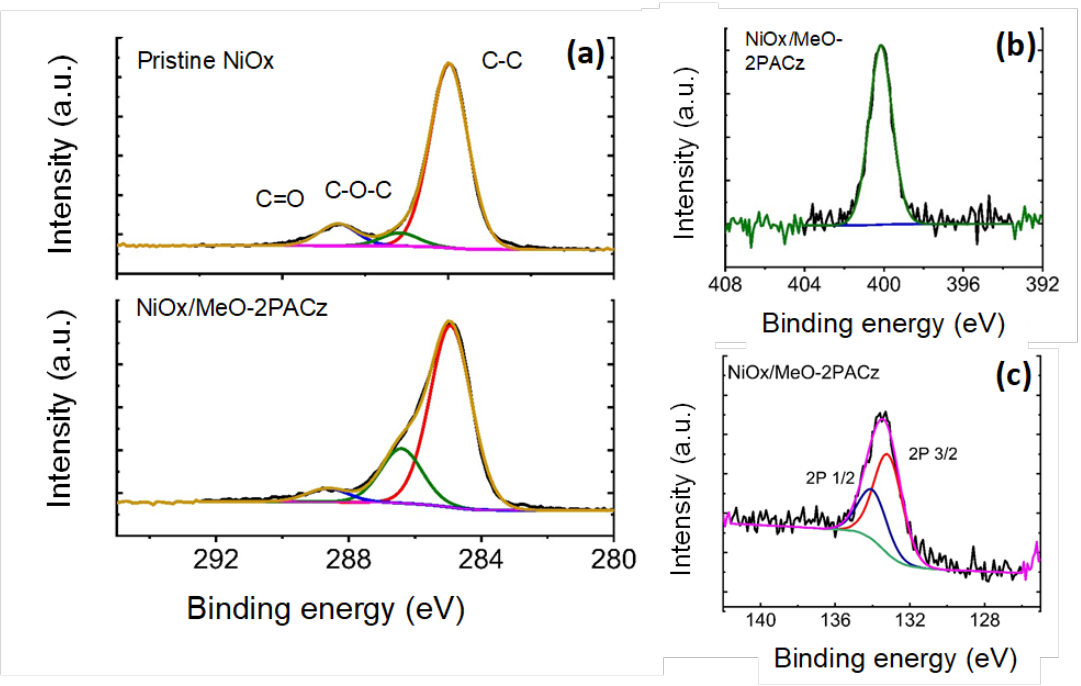

Figure S8-2. XPS surface spectra for pristine NiO_x and NiO_x treated with MeO-2PACz. (a) Top plot shows C1s peaks for pristine NiOx and bottom plot shows peaks for treated NiOx. (b) N1s peak for NiO_x treated with MeO-2PACz. (c) P 2p spectra for NiOx treated with MeO-2PACz.

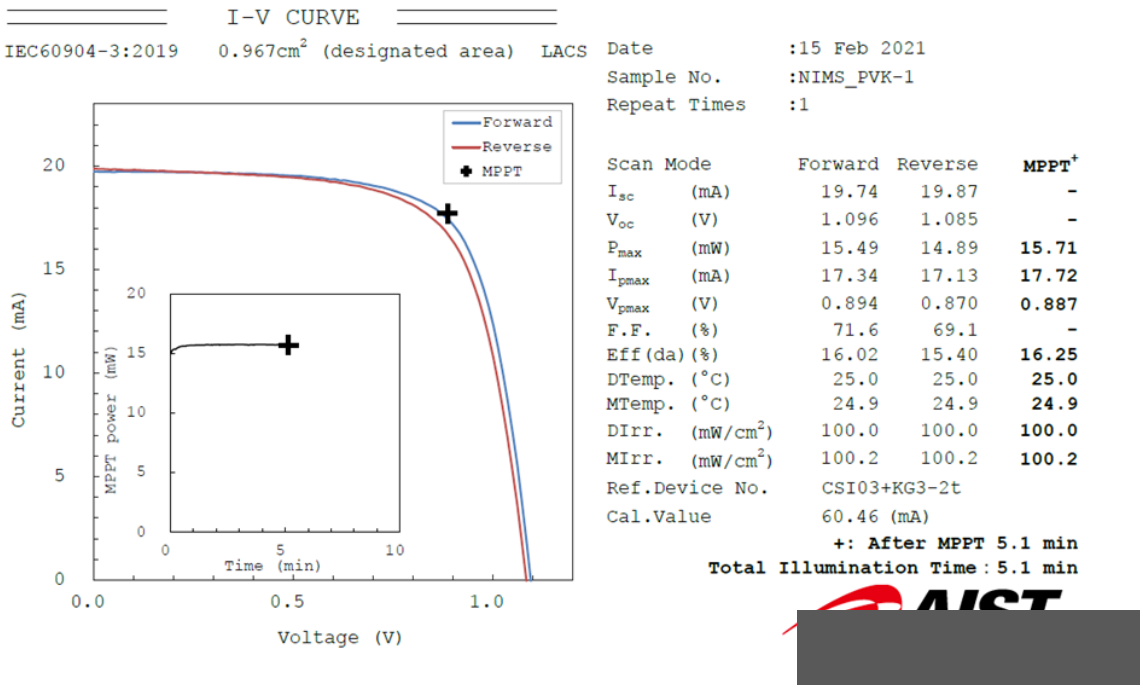

Figure S8-3. The I-V data for the NiO_x/MeO-2PACz device measured by the Calibration, Standards and Measurement Team of AIST (AIST logo was removed in accordance with the publication policies).

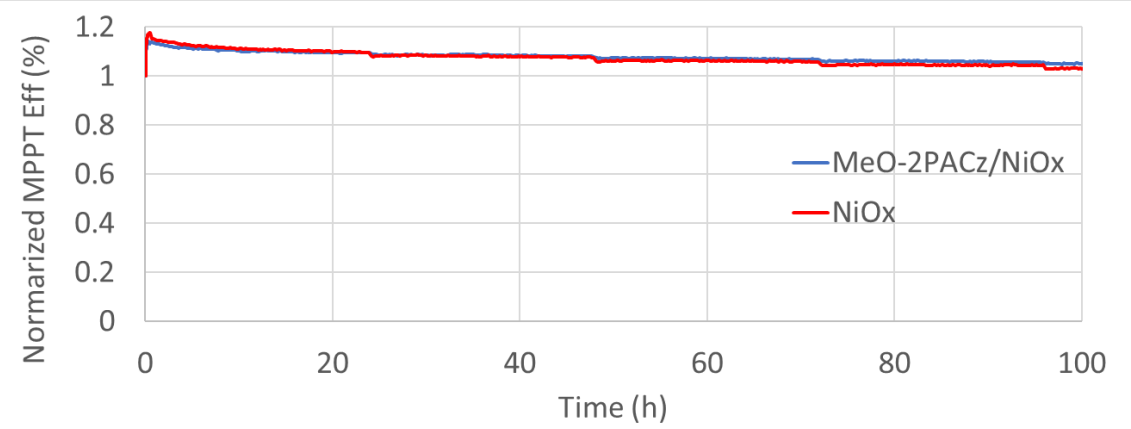

Figure S8-4. Operational stability of the glass encapsulated MeO-2PACz treated and untreated sp-NiOx devices at MPPT condition at ~60 °C in air.

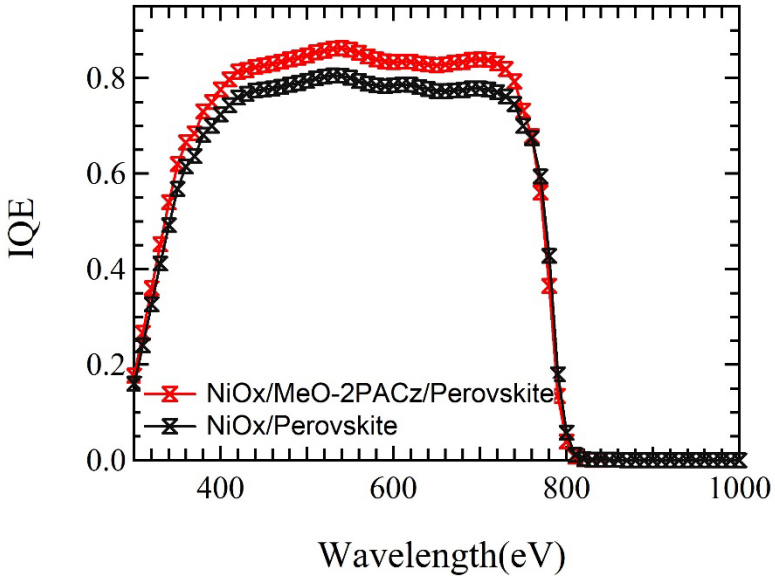

Figure S8-5. IQE spectra for the control perovskite device and device modified with a MeO-2PACz interface layer.

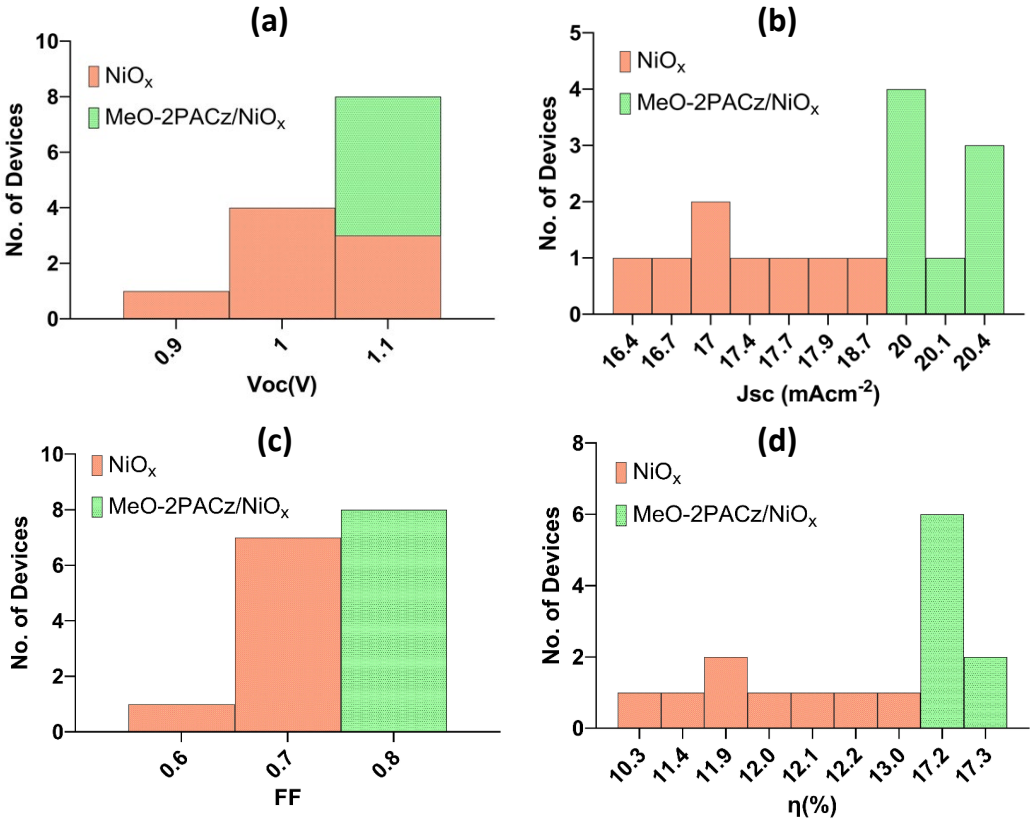

Figure S8-6. Statistics of device parameters of NiOx and MeO-2PACz/NiOx, (a) Voc, (b) J_{sc}, (c) FF and (d) efficiency (η) of the eight PSCs for each condition.

3. Electronic properties and energy level for perovskite films

As shown in the UPS spectra, the cut-off of the onset can provide information about the VB maximum, while the cut-off for the secondary electrons provides information about the WF. The WF, IE, ΔE* VL and ΔE energy gaps can be calculated as follows:

$WF = hv - E_{cut\text{-}off}$

$IE = hv - (E_{cut\text{-}off} - E_{onset})$

$\Delta E^{*}\ VL = WF_{NiOx} - WF_{pvk}$

$\Delta E\ \text{energy gap} = (IE_{pvk} - WF_{pvk}) - (IE_{NiOx} - WF_{NiOx}) - \Delta E^{*}\ VL$

Table S8-1

Electronic Properties of NiO_x and NiO_x/MeO-2PACz

Electronic structure	NiO_x	NiO_x/MeO-2PACz
WF (eV)	4.9	5.5
VB (eV)	0.4	0.2
IE (eV)	5.3	5.7
ΔE* VL (eV)	0.3	0.9
ΔE energy gap (eV)	0.1	–0.3